Understanding of Crack Growth in Single- and Bi-Material Bonded Joints with "Extra-Thick" Adhesive Bond-Lines

Lopes Fernandes, R.

DOI
10.4233/uuid:46ef8e00-d465-42c3-aeaf-0f11c814f304

Publication date
2021

Document Version
Final published version

Citation (APA)
Lopes Fernandes, R. (2021). *Understanding of Crack Growth in Single- and Bi-Material Bonded Joints with "Extra-Thick" Adhesive Bond-Lines*. [Dissertation (TU Delft), Delft University of Technology]. https://doi.org/10.4233/uuid:46ef8e00-d465-42c3-aeaf-0f11c814f304

Important note
To cite this publication, please use the final published version (if applicable).
Please check the document version above.

TU Delft

PhD Dissertation

R. Lopes Fernandes

PhD Dissertation

Understanding of Crack Growth in Single- and Bi-Material Bonded Joints with "Extra-Thick" Adhesive Bond-Lines

Romina Lopes Fernandes

Propositions

accompanying the dissertation

Understanding of crack growth in single- and bi-material bonded joints with “extra-thick” adhesive bond-lines

by

Romina LOPES FERNANDES

1. Matching the longitudinal strain distributions of adherends' surfaces in contact with the adhesive is a state of deformation needed to achieve pure mode I fracture behaviour in bi-material DCB joints (this proposition pertains to this dissertation).
2. The mode I fracture energy of DCB joints composed by high bending stiffness adherends is independent of the adherend materials and joint configuration. The mode I fracture energy is highly influenced by the adhesive thickness (this proposition pertains to this dissertation).
3. In DCB joints with adhesive bond-lines thicker than adhesive's plastic radius, the adherend-adhesive modulus mismatch and adherends thickness are the dominant terms defining the pre-crack length required for fracture onset at adhesive mid-thickness (this proposition pertains to this dissertation).
4. Test standard of fracture characterization of bi-material adhesive joints is required for scientific progress.
5. Constant re-planning is necessary when conducting research.
6. The number of publications is not a measure of success in a PhD project.
7. All big cities should have cycling infrastructure as in the cities of the Netherlands.
8. More bad news is a sign of better surveillance of suffering, not a worsening world (book “Factfulness” by Hans Rosling).
9. Due to coronavirus pandemic, we know how animals feel in zoos.
10. Vegan food is not boring.

These propositions are regarded as opposable and defendable, and have been approved as such by the promotor Prof.dr.ir. R. Benedictus.

Stellingen

behorende bij het proefschrift

Understanding of crack growth in single- and bi-material bonded joints with “extra-thick” adhesive bond-lines

door

Romina LOPES FERNANDES

1. Om puur mode I breukgedrag te bereiken in bi-materiaal DCB verbindingen is er een staat van vervorming nodig waarbij de longitudinale rekverdelingen van de substraatoppervlakken die in contact komen met de lijm op elkaar afgestemd zijn (deze stelling heeft betrekking tot dit proefschrift).
2. De mode I breukenergie van DCB verbindingen bestaande uit substraten met een hoge buigstijfheid is onafhankelijk van het materiaal van de substraten en de configuratie van de verbinding. De mode I breukenergie wordt sterk beïnvloed door de dikte van de lijmlaag (deze stelling heeft betrekking tot dit proefschrift).
3. In DCB verbindingen waarbij de dikte van de lijmlaag groter is dan de plastische radius, zijn de mismatch tussen de modulus van substraten en lijmlaag en de dikte van de substraten de dominante factoren die de lengte van de voorscheur die nodig is voor een breuk beginnend in het midden van de dikte van de lijmlaag bepalen (deze stelling heeft betrekking tot dit proefschrift).
4. Er is voor wetenschappelijke vooruitgang een testnorm nodig voor de breukkarakterisering van bi-materiaal lijmverbindingen.
5. Constante herplanning is nodig bij het doen van onderzoek.
6. Het aantal publicaties is geen maatstaf voor succes in een PhD project.
7. Alle grote steden zouden een fiets infrastructuur zoals Nederlandse steden moeten hebben.
8. Meer slecht nieuws is een teken van beter zicht op lijden, niet van een slechter wordende wereld (boek “Factfulness” door Hans Rosling).
9. Dankzij de corona pandemie weten we hoe dieren zich voelen in een dierentuin.
10. Veganistisch eten is niet saai.

Deze stellingen worden opponeerbaar en verdedigbaar geacht en zijn als zodanig goedgekeurd door de promotor Prof.dr.ir. R. Benedictus.

Understanding of crack growth in single- and bi-material bonded joints with “extra-thick” adhesive bond-lines

Understanding of crack growth in single- and bi-material bonded joints with “extra-thick” adhesive bond-lines

Dissertation

for the purpose of obtaining the degree of doctor
at Delft University of Technology,
by the authority of the Rector Magnificus Prof.dr.ir. T.H.J.J. van der Hagen,
chair of the Board for Doctorates,
to be defended publicly on
Friday 4 June 2021 at 10:00 o’clock

by

Romina LOPES FERNANDES

Master of Science in Mechanical Engineering, University of Porto, Portugal
born in Lucerne, Switzerland

This dissertation has been approved by the promotor.

Composition of the doctoral committee:

Rector Magnificus,	chairperson
Prof.dr.ir. R. Benedictus,	Delft University of Technology, promotor
Dr. S. Teixeira de Freitas,	Delft University of Technology, copromotor
Independent members:	
Prof.dr.ir. J.M.C. Mol,	Delft University of Technology
Prof.dr. T. Pardoen,	University of Louvain, Belgium
Prof.dr. A. Vassilopoulos,	École Polytechnique Fédérale de Lausanne, Switzerland
Dr. M.F.S.F. de Moura,	University of Porto, Portugal
Prof.dr.ir. R.C. Alderliesten,	Delft University of Technology, reserve member
Other members:	
Dr. M.K. Budzik,	Aarhus University, Denmark

Dr. M.K. Budzik has contributed greatly to the preparation of this dissertation.

Keywords: adhesive joints, "extra-thick" bond-line, fracture behaviour

Printed by: Ipskamp Printing (www.ipskampprinting.nl)

This research was carried out under project number S32.6.14552a – Durabond in the framework of the Partnership Program of the Materials Innovation Institute M2i (www.m2i.nl) and the Technology Foundation TTW, which is part of the Netherlands Organization for Scientific Research (www.nwo.nl). The Durabond project is linked to Joint Industry Project (JIP) set up by TNO, separately funded by *Topconsortium voor Kennis en Innovatie (TKI) HighTech Systemen & Materialen (HTSM)*.

An electronic version of this dissertation is available at http://repository.tudelft.nl/.

In memory of Francisco Saraiva.

Contents

Summary

The emergence of composite materials in shipbuilding and civil industries has driven research into structural adhesive bonding technology. Demand of increased cargo transport and renovation of bridges has created a set of challenges for which the use of a combination of steel and composite parts appears as an attractive solution. But these parts need to be joined together. Adhesive bonding can provide structural integrity without the need of fastening holes or fasteners as in mechanically fastened connections.

However, the application of adhesive bonding in these industries presents a critical difference in comparison with the reference industries, i.e. aerospace and automotive. The efficient production of large structures leads to high engineering tolerances, which corresponds in practice to adhesive bond-lines of up to 10 mm. These "extra-thick" adhesive bond-lines take the use of epoxy-based structural adhesives to a new chapter.

The geometrical length scale of the adhesive bond-line thickness imposed by shipbuilding and civil industries opens a series of questions in terms of reliability and performance of bi-material joints with thick adhesive bond-lines. There is still a long path to go through for certification of adhesive bonding as a primary joining method in these industries. The work developed in this document gives a contribution in that direction.

This dissertation deals with single- and bi-material adhesive joints with "extra-thick" bond-lines and their performance under the most critical loading mode - the opening mode. A total of four studies are performed in order to pursue the aim of this dissertation. The studies involve analytical and/or numerical work supported by laboratory experiments.

Firstly, a new design criterion to achieve mode I fracture is proposed and analysed for double-cantilever beam (DCB) bi-material adhesive joints (i.e. with dissimilar adherends). It is identified that matching the longitudinal strain distributions of the dissimilar adherends at the bond-line, instead of matching their flexural stiffness, eliminates mode II fracture component. Both the experimental and numerical results show that pure mode I can be achieved in bi-material adhesive joints designed with the proposed criterion. Mixed mode ratio is reduced by a factor of 5 when using the proposed longitudinal strain based criterion in comparison with the flexural stiffness based criterion.

In the second place, the effect of the adhesive bond-line thickness on the mode I fracture behaviour of epoxy-based steel-steel adhesive joints is investigated. The bond-line thickness ranges from 0.4 up to 10 mm. The critical mode I fracture energy of the joints is found to be similar in the range of 0.4-2.6 mm thick bond-line. The critical fracture energy increases steeply for a bond-line thickness of 4.1 mm, however this increase is followed by a decrease for joints with 10.1 mm thick

adhesive bond-line. This trend is justified by (a) the crack path, which influences the stress field ahead of the crack tip and, consequently, the size of the process zone ahead of the crack tip, and (b) the differences in the morphology of the fracture surfaces.

Thirdly, the effect of the material of the adherends on the mode I fracture behaviour of adhesive joints is pursued. The following epoxy-based adhesive joint configurations are investigated: steel-steel, GFRP-GFRP, steel-GFRP (GFRP stands for glass fibre reinforced polymer). Moreover, each configuration is produced with adhesive layer of 0.4 mm (thin bond-line) and 10.1 mm (thick bond-line). The critical mode I fracture energy shows to be independent of the adherend type and joint configuration (i.e. single- or bi-material). In the joints with thin bond-line, the results reveal a similar degree of constraint imposed to the adhesive by the high-modulus (i.e. steel) and/or relatively thick (i.e. composite) adherends. In the joints with thick bond-line, the crack grows in general along a plane close to the adhesive-adherend interface characterized by the highest material stiffness mismatch. The critical mode I fracture energy independence shows that the adhesive deforms similarly, even though the crack tip is constrained in one side by different types of adherends (i.e. either by a steel- or GFRP-adherend).

Finally, for adhesive joints with 10 mm thick bond-line, a weakness to be recognized, from both scientific and applied points of view, is the stress gradient at bi-material (adherend-adhesive) edges and corners, exacerbated by differences in materials properties. Locally, peel forces arise, which might result in local damage and fracture onset, in case external loading is applied. Within this context, the fracture onset and crack deflection in adhesive joints with thick bond-lines under mode I loading conditions is studied. An empirical relation, in terms of geometrical and material properties of the joints, that defines the transition between cohesive close to the interface and cohesive adhesive mid-thickness fracture onset is found. Above a specific pre-crack length the stress singularity at pre-crack tip rules over the stress singularity near bi-material corners, resulting in mid-adhesive thickness cohesive fracture onset. However, the cracking direction rapidly deflects out from the adhesive layer centre-line. Positive T-stress along the crack tip is one of the factors for unstable crack path.

Samenvatting

De opkomst van composietmaterialen in de scheepsbouw en civiele industrie heeft onderzoek gedreven naar structurele lijmverbindingstechnologieën. De vraag naar meer vrachtvervoer en de renovatie van bruggen heeft geleid tot een reeks uitdagingen waarvoor een combinatie van stalen en composieten onderdelen een aantrekkelijke oplossing lijkt. Maar deze onderdelen moeten worden samengevoegd. Lijmverbindingen kunnen structurele integriteit leveren zonder de noodzaak van bevestigingsgaten of bevestigingsmiddelen zoals bij mechanisch bevestigde verbindingen.
Er is echter een kritiek verschil tussen de toepassing van lijmverbindingen in deze industrieën en de toepassing in referentie-industrieën zoals de luchtvaart en automobielindustrie. De efficiënte productie van grote constructies leidt tot hoge technische toleranties. In de praktijk resulteert dit in lijmverbindingen tot 10 mm dik. Deze "extra dikke" lijmverbindingen brengen het gebruik van structurele lijmen op epoxy basis naar een nieuw hoofdstuk.
De geometrische lengteschaal van de dikte van de lijmverbindingen zoals opgelegd door de scheepsbouw en civiele industrie leidt tot vragen over de betrouwbaarheid en de prestatie van bi-materiaal verbindingen met dikke lijmlagen. Er is nog een lange weg te gaan tot de certificatie van lijmverbindingen als een primaire verbindingswijze in deze industrieën. Het werk dat uiteengezet is in dit proefschrift geeft een bijdrage in die richting.
Dit proefschrift behandelt lijmverbindingen tussen substraten van dezelfde of twee verschillende materialen (bi-materiaal) met "extra dikke" lijmlagen en hun prestatie onder de meest kritische belasting – de opening mode. In totaal zijn er vier onderzoeken uitgevoerd om het doel van deze thesis na te streven. Deze studies bestaan uit analytisch en/of numeriek werk ondersteund door experimenten.
Ten eerste is er een nieuw ontwerpcriterium om mode I breuk te bereiken voorgesteld en geanalyseerd voor double-cantilever beam (DCB) bi-materiaal lijmverbindingen (d.w.z. verschillende substraten). Er is vastgesteld dat door het matchen van de longitudinale rekverdelingen van de verschillende substraten aan de verbindingslijn, in plaats van het matchen van hun buigstijfheid, de mode II breukcomponent geëlimineerd wordt. Zowel de experimentele als de numerieke resultaten laten zien dat een pure mode I bereikt kan worden in bi-materiaal lijmverbindingen die ontworpen zijn met het voorgestelde criterium. Bij het gebruiken van het voorgestelde criterium op basis van longitudinale rekverdelingen wordt de gemengde mode ratio gereduceerd met een factor 5 ten opzichte van het criterium gebaseerd op buigstijfheid.
Ten tweede is onderzocht wat het effect is van de dikte van de verbindingslijn op mode I breukgedrag van staal-staal lijmverbindingen op epoxy basis. De lijmverbindingslijndikte is gevarieerd van 0.4 tot 10 mm. Er is gevonden dat de kritische

mode I breukenergie van de verbindingen vergelijkbaar is voor lijmdiktes tussen 0.4 – 2.6 mm. De kritische breukenergie stijgt sterk voor een verbindingslijndikte van 4.1 mm. Deze stijging wordt echter gevolgd door een daling voor verbindingen met een verbindingslijn van 10.1 mm dik. Deze trend kan verklaard worden door (a) het scheurpad, wat het spanningsveld voor de scheurpunt en daardoor de grootte van de proceszone voor de scheurpunt beïnvloedt, en (b) de verschillen in morfologie van de breuk oppervlakken.
Ten derde is het effect van het materiaal van de substraten op het mode I breukgedrag van de lijmverbindingen bekeken. De volgende op epoxy-gebaseerd lijmverbinding configuraties zijn onderzocht: staal-staal, GVK-GVK, staal-GVK (GVK staat voor glasvezelversterkte kunststof). Bovendien is elke configuratie geproduceerd met een lijmlaag van 0.4 mm (dunne verbindingslijn) en 10.1 mm (dikke verbindingslijn). De kritische mode I breukenergie blijkt onafhankelijk van het soort substraat en de verbindingsconfiguratie (d.w.z. enkel of bi-materiaal). In de verbindingen met dunne verbindingslijnen laten de resultaten een vergelijkbare mate van beperking van de lijmlaag zien door de substraten met een hoge modulus (d.w.z. staal) en/of relatief dikke substraten (d.w.z. composiet). In de verbindingen met een dikke verbindingslijn groeit de breuk over het algemeen langs een vlak dichtbij de lijm-substraat interface die gekenmerkt wordt door de hoogste mismatch in materiaalstijfheid. De onafhankelijkheid van de kritische mode I breukenergie laat zien dat de lijm vergelijkbaar vervormd, ondanks dat de scheurpunt beperkt is in een kant door de verschillende soorten substraten (d.w.z door of een stalen of een GVK substraat).
Ten slotte is voor de lijmverbindingen met een 10 mm dikke verbindingslijn de spanningsgradiënt op bi-materiaal (substraat-lijm) randen en hoeken een zwakte waar rekening mee moet worden gehouden, zowel vanuit een wetenschappelijk als een toegepast oogpunt. Deze gradiënt wordt verergerd door het verschil in materiaaleigenschappen. Lokaal treden er peelkrachten op, die kunnen resulteren in lokale schade en het begin van een breuk in het geval van externe belasting. Binnen deze context is het breuk begin en de scheurafbuiging in lijmverbindingen met dikke verbindingslijnen onder mode I belasting onderzocht. Een empirische relatie, in termen van geometrische eigenschappen en materiaaleigenschappen van de verbindingen, die de overgang tussen het begin van een cohesieve breuk, dicht bij de interface, en een cohesieve adhesieve breuk, in het midden van de dikte, is gevonden. Boven een bepaalde voorbarstlengte zal de singulariteit bij de voorbarstip de spanningssingulariteit bij bi-materiaal hoeken overheersen, dit resulteert in een cohesief breuk begin in de hartlijn van de lijmlaag. De scheurrichting zal echter snel afwijken van deze midden lijn. Een van de redenen voor een onstabiel scheurpad is een positieve T-spanning langs de scheurpunt.

Nomenclature

Latin Symbols

a	crack length	(mm)
a_{init}	initial crack length	(mm)
a_{total}	total crack length	(mm)
a_{SBT}	estimated crack length based on simple beam theory	(mm)
$a_{\text{strain gauge}}$	strain gauge position	(mm)
a_0	initially unbonded length	(mm)
$\lvert a_{\text{corr}} \rvert$	length correction for crack length according to modified beam theory	(mm)
A	crack surface area	(mm^2)
$[A]$	extensional matrix of laminate theory	(Pa.mm)
B	specimen width	(mm)
$[B]$	coupling matrix of laminate theory	(Pa.mm^2)
B_{ele}	finite element width	(mm)
c	bonded length	(mm)
C	specimen compliance	(mm/N)
C_{1-4}	constants of integration	(-)
d	distance between load line and origin	(mm)
$[D]$	flexural matrix of laminate theory	(Pa.mm^3)
E	tensile modulus of isotropic material	(MPa)
E_{a}	adhesive Young's modulus	(MPa)
E_{adher}	adherend Young's modulus	(MPa)
E_x^{f}	adherend flexural modulus	(MPa)
E_{xx}	UD lamina longitudinal, x-direction, modulus	(MPa)
E_{yy}	UD lamina transverse, y-direction, modulus	(MPa)
E_y^{adher}	adherend modulus in y-direction	(MPa)
$f(x)$	distribution of the reaction force acting on the beams	(N)
G	strain energy release rate	(N/mm)
G_{a}	adhesive shear modulus	(MPa)
G_{adher}	adherend shear modulus	(MPa)
G_{I}	mode I strain energy release rate	(N/mm)
G_{II}	mode II strain energy release rate	(N/mm)

G_{III}	mode III strain energy release rate	(N/mm)
G_{Ic}	critical mode I fracture energy	(N/mm)
$G_{\mathrm{Ic\text{-}a}}$	critical mode I fracture energy of bulk adhesive	(N/mm)
$G_{\mathrm{Ic\text{-}onset}}$	critical mode I fracture onset energy	(N/mm)
$G_{\mathrm{Ic\text{-}onset,\ bi\text{-}mat}}$	critical mode I fracture onset energy of bi-material adhesive joint	(N/mm)
$G_{\mathrm{I\text{-}CCM}}$	mode I strain energy release rate based on compliance calibration method	(N/mm)
$G_{\mathrm{I\text{-}max}}$	maximum value of mode I strain energy release rate	(N/mm)
$G_{\mathrm{I\text{-}min}}$	minimum value of mode I strain energy release rate	(N/mm)
$G_{\mathrm{I\text{-}PK}}$	mode I strain energy release rate by following PK model	(N/mm)
$G_{\mathrm{I\text{-}SBT}}$	mode I strain energy release rate based on simple beam theory	(N/mm)
$G_{\mathrm{I\text{-}PK}}^{\mathrm{bi\text{-}material}}$	mode I strain energy release rate of bi-material DCB joint by following PK model	(N/mm)
G_{xy}	UD lamina shear modulus in xy-direction	(MPa)
G_{xz}	UD lamina shear modulus in xz-direction	(MPa)
G_{yz}	UD lamina shear modulus in yz-direction	(MPa)
h	arm thickness in a homogeneous DCB specimen	(mm)
h_{adher}	adherend thickness	(mm)
h_{GFRP}^{*}	final thickness of the laminate after post-cure cycle	(mm)
I	second moment of the beam cross-section area	(mm^4)
k	foundation stiffness	(MPa)
$[\bar{k}]$	laminate curvatures	(1/mm)
k_{a}	adhesive constant defining stress state	(-)
k_{adher}	adherend constant defining stress state	(-)
K	interface corner stress intensity factor	(MPa$\sqrt{\mathrm{mm}}$)
K_{I}	stress intensity factor of opening mode	(MPa$\sqrt{\mathrm{mm}}$)
K_{II}	stress intensity factor of shear mode	(MPa$\sqrt{\mathrm{mm}}$)
K_{I}^{∞}	remote mode I *K*-field	(MPa$\sqrt{\mathrm{mm}}$)
K_{1-4}	constants of integration	(-)
l_{e}	bonded region length in elastic regime	(mm)
l_{f}	length between the loading point and the origin	(mm)
l_{p}	plastic zone length	(mm)
L	specimen length	(mm)
$L_{\mathrm{GFRP\ or\ Steel}}$	length of positive $w_{\mathrm{bon}}(x)$	(mm)
M	moment distribution over the deformed adhesive region	(N.mm)

$[M]$	applied moments per unit length	(N.mm/mm)
m_{q}	constant defining stress state in the adhesive	(-)
n	slope of log-log plot of Ω versus a	(-)
$[N]$	applied load per unit length	(N/mm)
P	applied load	(N)
P_{c}	critical load at fracture onset	(N)
$\tilde{P}$	normalized load	(-)
P_{CCM}	compliance calibration method estimated applied load	(N)
P_{max}	maximum applied load	(N)
$\tilde{P}_{\mathrm{bi\text{-}mat}}$	normalized load of bi-material adhesive joint	(-)
$\tilde{P}_{\mathrm{c}}$	normalized critical load at fracture onset	(-)
$\tilde{P}_{\mathrm{c,\ bi\text{-}mat}}$	normalized critical load at fracture onset of bi-material adhesive joint	(-)
$\tilde{P}_{\mathrm{shear}}$	normalized load by taking shear into account	(-)
$\tilde{P}_{\mathrm{shear,\ bi\text{-}mat}}$	normalized load of bi-material adhesive joint by taking shear into account	(-)
r	radial distance from the crack tip	(mm)
r_{p}	Irwin's estimate of the radius of the plastic zone	(mm)
R_{1-2}	constants of integration	(-)
S	equal to $\left(\frac{1}{E^{\mathrm{f}}_{x\text{-steel}} I_{\mathrm{steel}}} + \frac{1}{E^{\mathrm{f}}_{x\text{-GFRP}} I_{\mathrm{GFRP}}}\right)$	(1/MPa.mm^4)
S_{a}	average areal roughness	(μm)
S_{q}	root mean square deviation	(μm)
T	stress acting parallel to the crack plane	(MPa)
T_{g}	glass transition temperature	(°C)
u	longitudinal displacement (in x-direction)	(mm)
U	stored elastic energy	(N.mm)
u_{r}	longitudinal displacement (in x-direction) under the reaction force distribution	(mm)
v	vertical displacement (in y-direction)	(mm)
w	displacement in z-direction	(mm)
W	external work	(N.mm)
$w_{\mathrm{bon}}(x)$	deflection in bonded region of Penado-Kanninen's model	(mm)
$w_{\mathrm{unbon}}(x)$	deflection in unbonded region of Penado-Kanninen's model	(mm)
$w(x)$	deflection of Penado-Kanninen's model	(mm)
$w_1(x)$	deflection in region 1 of Yamada's model	(mm)

$w_2(x)$	deflection in region 2 of Yamada's model	(mm)
$w_3(x)$	deflection in region 3 of Yamada's model	(mm)
X	nodal force in x-direction	(N)
Y	nodal force in y-direction	(N)
Z	nodal force in z-direction	(N)
$2t_{\text{a}}$	adhesive bond-line thickness	(mm)
$2t_{\text{a-av.}}$	average adhesive bond-line thickness	(mm)
$2t_{\text{a-max}}$	maximum adhesive bond-line thickness	(mm)
$2t_{\text{a-min}}$	minimum adhesive bond-line thickness	(mm)

Greek Symbols

α	Dundurs parameter	(-)
β	Dundurs parameter	(-)
γ	constant related to the order of singularity	(-)
γ_{xy}	shear strain	(-)
Δ	half-opening displacement in DCB specimen	(mm)
Δa	pre-crack length	(mm)
$\Delta a_{\text{crit.}}$	critical pre-crack length	(mm)
Δa_{ele}	increment of the crack which is equal to the element size at the crack tip	(mm)
$\Delta a_{\text{exper.}}$	experimental pre-crack length	(mm)
$\Delta a_{\text{exp max}}$	maximum experimental pre-crack length	(mm)
ϵ	oscillation index	(-)
ε_{xx}	strain component in x-direction	(-)
ε_{yy}	strain component in y-direction	(-)
$[\varepsilon^0]$	laminate middle-plane strains	(-)
λ	wave number	(mm^{-1})
λ^{-1}	elastic process zone length	(mm)
$\lambda_{j\text{-exp}}^{-1}$	experimental elastic process zone length ($j = 0.4$, 1.1, 2.6, 4.1, 10.1)	(mm)
ν_{a}	adhesive Poisson's ratio	(-)
ν_{adher}	adherend Poisson's ratio	(-)
ν_{xy}	UD lamina Poisson's ratio	(-)
σ_{ultimate}	ultimate (maximum) strength	(MPa)
σ_{xx}	stress component in x-direction	(MPa)
σ_{y}	adhesive yield strength	(MPa)
σ_{yy}	stress component in y-direction	(MPa)
σ_{yy}^{∞}	remote stress component in y-direction	(MPa)

$\sigma_{yy\text{-homogeneous}}$	asymptotic stress component normal to a crack in homogeneous material	(MPa)
$\sigma_{yy\text{-interface}}$	asymptotic stress component normal to bi-material interface	(MPa)
σ_{xy}	stress component in xy-direction	(MPa)
ϕ	equal to $\left(\frac{BG_{Ic}}{n}\right)^{\frac{n}{n+1}}.\left(\frac{2}{\chi}\right)^{\frac{1}{n+1}}$	(-)
χ	compliance calibration method curve fitting parameter	(-)
ψ	equal to $\frac{B}{3}\sqrt[4]{\frac{3Eh^3}{4}}G_{Ic}^{3/4}$	(N.mm$^{\frac{1}{2}}$)
Ω	equal to $\chi^{-1}.a^{-n}$	(N/mm)
2Δ	total opening displacement in DCB specimen	(mm)
$2\Delta_{\text{bi-material}}$	total opening displacement in bi-material DCB specimen	(mm)
$2\tilde{\Delta}$	normalized displacement	(-)

Superscripts & subscripts

adher 1	adherend 1
adher 2	adherend 2
GFRP	GFRP adherend
Li	node at the crack tip
Ll and Ll^*	adjacent nodes directly behind the crack tip
steel	steel adherend

Acronyms

ASTM	American Society for Testing and Materials
ATR-FTIR	Attenuated Total Reflectance-Fourier Transform Infrared
CCM	Compliance Calibration Method
CFRP	Carbon Fibre Reinforced Polymer
CLT	Classical Laminate Theory
CTE	Coefficient of Thermal Expansion
DCB	Double-Cantilever Beam
DIC	Digital Image Correlation
FE	Finite Element
FEM	Finite Element Modelling
DOI	Digital Object Identifier
DW	Distilled Water

GFRP	Glass Fibre Reinforced Polymer
GPS	glycidoxypropyltrimethoxysilane
HTSM	*HighTech Systemen & Materialen*
ISO	International Organization for Standardization
JIP	Joint Industry Project
LED	Light Emitting Diode
MBT	Modified Beam Theory
M2i	Materials Innovation Institute
pH	potential of Hydrogen
PK	Penado-Kanninen
QE	Quadraxial E-glass
rpm	revolutions per minute
SBT	Simple Beam Theory
SEM	Scanning Electron Microscope
SERR	Strain Energy Release Rate
TKI	*Topconsortium voor Kennis en Innovatie*
TNO	Netherlands Organisation for Applied Scientific Research
TTW	Technology Foundation
UD	Unidirectional
VCCT	Virtual Crack Closure Technique

1

Introduction

Adhesive bonding is a method by which materials are joined together by an intermediate layer of adhesive to generate assemblies. An assembly made by the use of an adhesive is called an adhesive joint. Solid materials in the adhesive joint other than the adhesive are referred to as the adherends [1, 2].
With the emergence of synthetic polymers with improved mechanical properties in the early 1900s, the primary boost in the use of adhesives as a joining medium in structural applications took place. Adhesive bonding is an alternative to conventional joining methods, such as mechanical fastening or welding. All joining methods have their advantages and disadvantages and adhesive bonding is not an exception [1, 2].
One crucial difference between an adhesive joint and a mechanically fastened joint is that no holes are created in the adherends (e.g. continuous fibres in a composite part are not damaged). Moreover, assemblies produced with adhesives have reduced weight by eliminating the use of mechanical fasteners. Properly designed adhesive joints exhibit lower stress concentrations, thus the properties of the adherends can be fully utilized. Contrary to welded joints, adhesives allow dissimilar materials to adhere to one another [1–4].
Common for all adhesive joints is that they rely on adhesion for load transfer through the assembly. As adhesion is a surface physico-chemical phenomenon, the physical properties of the adhesive joints are dependent on how the adhesive interacts with the surface of the adherends. Therefore, proper surface preparation is needed for durable adhesive joints. Finally, as the adhesives are internal to the joints, in general, it is challenging to determine, without destructive testing, whether the adhesives were properly applied and, thus, to predict the joint strength [1–4].
The potential weight savings inherent in adhesive bonding are a major reason for the widespread use of this joining technology in aerospace and automotive industries. Great use of adhesive is also found in the electronics industry [1]. More recently, the adhesive bonding has appeared as a promising solution for the problems faced by the shipbuilding and civil industries.

1

1.1. Structural bonding as promising technology in shipbuilding and civil industries

The theoretical understanding and practical robustness of composites have driven research into lightweight construction in shipbuilding industry. Lighter ships imply, for instance, increased cargo transport as a result of increased volume at the same ship weight and, thus, increased transport efficiency. One possible solution for the reduction of the ships overall weight is found to be the replacement of metallic superstructures by composite ones.

In general, a bridge lifespan is 100 years. In the Netherlands, numerous bridges will achieve the end of their lifespan in 30 years [5]. The responsible parties are, therefore, looking for intermediate solutions to eliminate a peak in the construction or renovation of bridges in the future and to avoid the terrible consequences that such peak would have for the society. The replacement of old and damaged decks by composite ones might be an interesting solution.

The solutions presented, for both civil and shipbuilding cases, imply the connection between different materials: for shipbuilding, the assembly of composite superstructures with metallic hulls and for bridge engineering, the connection between composite bridge decks with metallic structural beams. The adhesive bonding technology appears as a promising joining method for both cases, as dissimilar components must be connected together.

Steel used to be the dominating material in shipbuilding industry and, thus, the different components used to be welded. The emergence of composites brought initially attention to the mechanical fastening technique and more recently to the adhesive bonding technology. As before mentioned, the mechanical fastening technique requires drilling of the components and also requires fasteners. In the adhesive bonding technique, neither fastening holes nor fasteners are needed.

For the civil case, structural adhesive bonding also appears as a promising joining technique. Besides the reasons previously mentioned, there is another critical point. In fact, most part of the components to be connected to the composite decks are not straight, enhancing the advantages of the manufacturing flexibility of adhesively bonded joints for this case.

1.2. Challenges

Adhesive bonding is widespread in aerospace (e.g. bonding of stringers to skins for fuselage and wing construction) and automotive (e.g. bonding of outer door to an inner shell, hoods are adhesively bonded) industries [1]. Although adhesive bonding is not the main joining method in shipbuilding and civil industries, it has progressively gained more importance. Compared to aerospace and automotive applications, the adhesively bonded joints in shipbuilding and civil applications present a critical difference.

Aerospace and automotive industries are known for the tight tolerances in the manufacturing processes. Adhesive layers in the range 0.1 to 2 mm are found in these industries [6–11]. In shipbuilding and civil applications, the scenario is rather different. The efficient production of large structures leads to high engineering toler-

ances, which corresponds in practice to adhesive bond-lines of up to 10 mm.
The "extra-thick" adhesive bond-lines present in shipbuilding and civil applications take the use of epoxy-based structural adhesives to a new chapter rather distinguishable from the reference cases, i.e. aerospace and automotive applications.
With 10 mm thick adhesive bond-lines, the constraint level imposed by the components on the adhesive layer decreases. It is known that constrained materials behave differently from unconstrained materials [12, 13]. Therefore, the performance of the "extra-thick" adhesive joints is distinct from the reference cases.
Common for all adhesive joints is that they contain interfaces and material discontinuities. A weakness to be recognized is the stress gradient at bi-material edges and corners, exacerbated by differences in materials properties [14–17]. Therefore, adhesive joints are often a locus of damage, which may posteriorly lead to failure.
In the shipbuilding and civil cases above described, there are two different interfaces as dissimilar components must be joined together, i.e. steel-adhesive interface and composite-adhesive interface. The steel-adhesive interface has the largest difference in materials properties and it is, in principle, the most critical one.
The "extra-thick" adhesive layers and the presence of interfaces contribute to general concerns regarding the reliability and performance of bi-material adhesive joints in shipbuilding and civil applications. As a consequence, more conservative designs are being used. As an example, all adhesive joints already implemented in ships are reinforced with mechanical fasteners. The fasteners are able to carry the load in case the bond-line fails. Unfortunately, this practice hinders the versatility of adhesive bonding technique.
Before adopting adhesive bonding to the full extent for primary applications in shipbuilding and civil applications, there is the need to fully understand the mechanical behaviour of the "extra-thick" adhesively bonded joints in order to be able to determine when they will fail.

1.3. Aim of this dissertation

For the special case of structural bonding in shipbuilding and civil applications, the geometrical length scale of the thickness of the adhesive bond-line should be taken carefully into consideration when studying the reliability and overall performance of the adhesive joints.
This dissertation is focused on the performance of joints with "extra-thick" adhesive bond-lines (i.e. 10 mm) under the most critical loading mode for an adhesive joint - the opening mode. The main research question of this dissertation is formulated as follows:

How do single- and bi-material joints with "extra-thick" adhesive bond-line behave under opening loading conditions?

In order to provide an answer to this main question, four key questions were formulated:

(1) How can pure opening mode be characterized in bi-material adhesive joints?

(2) What is the effect of the bond-line thickness on the fracture behaviour of adhesive joints under opening loading conditions?

(3) How is the fracture behaviour of adhesive joints under opening loading conditions affected by the material of the adherends?

(4) What are the parameters controlling the fracture onset locus and crack growth path in single- and bi-material joints with "extra-thick" adhesive bond-lines?

1.4. Dissertation outline

A review of the research conducted on the fracture behaviour of single- and bi-material adhesive joints under opening loading conditions is presented in Chapter 2. The currently available design criterion for bi-material double-cantilever beam (DCB) configuration is presented and its validity is discussed. Moreover, special attention is given to two key-factors influencing the behaviour of adhesive joints, i.e. the adhesive bond-line thickness and the material of the adherends. Finally, the special case of adhesive joints with "extra-thick" bond-lines, used in shipbuilding and civil industries, is also addressed in terms of the role of the interfaces on fracture onset and the methodologies available for opening mode fracture characterization.

In Chapter 3, the first research question is pursued. A new criterion is proposed to obtain pure opening mode in composite-metal adhesive joints. DCB experiments are conducted to verify the proposed criterion. A numerical analysis is carried out to investigate the applicability of the new criterion to other bi-material configurations (e.g. steel-aluminium).

The second research question is pursued in Chapter 4, where the effect of the bond-line thickness on the fracture behaviour of metal-metal adhesive joints under opening loading conditions is explored. DCB specimens with bond-line thicknesses ranging from 0.4 up to 10 mm are tested and the failure surfaces are examined.

In Chapter 5, the effect of the material of the adherends on the fracture behaviour of adhesive joints under opening loading conditions is investigated and defines the third research question. Three specimen configurations are studied: metal-metal, composite-composite, and composite-metal. The composite-metal specimen configuration is manufactured according to the design criterion proposed in Chapter 3.

In Chapter 6, the fourth and last research question is pursued, where the fracture onset and crack deflection in single- and bi-material adhesive joints with "extra-thick" bond-lines under opening loading conditions is investigated. The role of adherend-adhesive modulus mismatch and the role of pre-crack length on fracture onset are scrutinized. The parameters controlling the crack path directional stability are also discussed.

Finally, Chapter 7 presents the main conclusions of this dissertation and offers some suggestions for future work.

References

[1] A. V. Pocius, *Adhesion and adhesives technology: an introduction*, 3rd ed. (Hanser Publications, 2012).

[2] S. Heide-Jørgensen, *Mechanics and failure of structured interfaces*, Ph.D. thesis, Aarhus University (2019).

[3] X. Jiang, *Mechanical behaviour and durability of FRP-to-steel adhesively-bonded joints*, Ph.D. thesis, Technische Universiteit Delft (2013).

[4] J. A. Pascoe, *Characterisation of fatigue crack growth in adhesive bonds*, Ph.D. thesis, Technische Universiteit Delft (2016).

[5] *Rijkswaterstaat - ministerie van infrastructuur en waterstaat, richtlijnen kunstwerken (Artworks Guidelines),* (accessed: 29.01.2021).

[6] S. Marzi, A. Biel, and U. Stigh, *On experimental methods to investigate the effect of layer thickness on the fracture behavior of adhesively bonded joints,* International Journal of Adhesion and Adhesives **31**, 840 (2011).

[7] T. Carlberger and U. Stigh, *Influence of layer thickness on cohesive properties of an epoxy-based adhesive - an experimental study,* Journal of Adhesion **86**, 814 (2010).

[8] D.-B. Lee, T. Ikeda, N. Miyazaki, and N.-S. Choi, *Effect of bond thickness on the fracture toughness of adhesive joints,* Journal of Engineering Materials and Technology **126**, 14 (2004).

[9] S. R. Ranade, Y. Guan, D. C. Ohanehi, J. G. Dillard, R. C. Batra, and D. A. Dillard, *A tapered bondline thickness double cantilever beam (DCB) specimen geometry for combinatorial fracture studies of adhesive bonds,* International Journal of Adhesion and Adhesives **55**, 155 (2014).

[10] V. Cooper, A. Ivankovic, A. Karac, D. McAuliffe, and N. Murphy, *Effects of bond gap thickness on the fracture of nano-toughened epoxy adhesive joints,* Polymer **53**, 5540 (2012).

[11] T. Pardoen, T. Ferracin, C. M. Landis, and F. Delannay, *Constraint effects in adhesive joint fracture,* Journal of the Mechanics and Physics of Solids **53**, 1951 (2005).

[12] A. J. Kinloch and S. J. Shaw, *The fracture resistance of a toughened epoxy adhesive,* The Journal of Adhesion **12**, 59 (1981).

[13] K. J. Maloney, *Micro-architected adhesive joints*, Ph.D. thesis, University of Cambridge (2016).

[14] D. B. Bogy, *On the problem of edge-bonded elastic quarter-planes loaded at the boundary,* International Journal of Solids and Structures **6**, 1287 (1970).

[15] J. W. Hutchinson, M. E. Mear, and J. R. Rice, *Crack paralleling an interface between dissimilar materials,* Journal of Applied Mechanics **54**, 828 (1987).

[16] Z. Suo and J. W. Hutchinson, *Sandwich test specimens for measuring interface crack toughness,* Materials Science and Engineering: A **107**, 135 (1989).

[17] E. D. Reedy and T. R. Guess, *Interface corner failure analysis of joint strength: effect of adherend stiffness,* International Journal of Fracture **88**, 305 (1997).

2

Literature review

Fracture mechanics has become an indispensable approach for understanding and avoiding failures of structures. Recognizing that flaws exist in all materials and fabricated structures, the field of fracture mechanics seeks to quantify the driving forces available for crack propagation [1].
Fracture may occur in a pure mode or in some combination of the three propagation modes: mode I - opening crack, mode II - sliding crack, mode III - tearing crack, depicted in Fig. 2.1. Mode I arises from tension at the crack front. This fracture mode weakens the cracked material, causing further crack opening and often leading to catastrophic failure. Mode II and III are caused by in-plane and out-of-plane shearing of the crack surfaces, respectively. These modes may result in shielding of the crack tip, which retains and might even increase the toughness of the cracked material [1, 2]. The mode I fracture is the main focus of the present dissertation and will be described in greater details later.

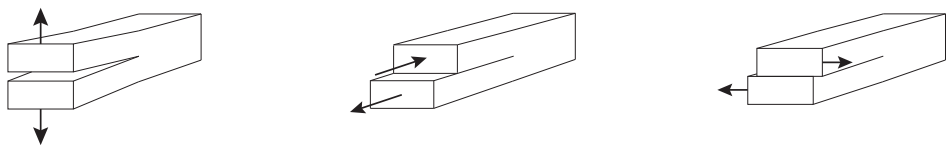

(a) Mode I: opening. (b) Mode II: in-plane shear. (c) Mode III: out-of-plane shear.

Figure 2.1: The three fracture modes.

The work of Griffith [3] and Irwin [4–6] enabled to quantify the resistance of a material against fracture. Griffith adopted an energy balance approach to determine the strength of brittle cracked materials, i.e. the critical stress, at which a crack would grow, is derived from the balance between the released strain energy from the material surrounding the crack surfaces and the consumed energy to create the

new crack surfaces. Griffith was the first to quantify the relation between material strength and crack size. Several decades later, Irwin modified this relation by considering plastic deformation in the vicinity of the crack tip.
The strain energy release rate (SERR), G, is the amount of energy per unit crack area imposed by the loading conditions and available to drive a growing crack. For systems in which dissipation is limited to the crack tip region, this relation is expressed as [1],

$$G = \frac{\partial(W - U)}{\partial A}, \tag{2.1}$$

where W is the external work, U is the stored elastic energy and A is the crack surface area. Crack growth occurs when the SERR reaches the critical value, G_c (also known as the critical fracture energy). The practicality of the SERR approach from a physical point of view resulted in broad application of it, including to bonded systems.

2.1. Mode I fracture behaviour of adhesive joints

2.1.1. Double-cantilever beam configuration

The double-cantilever beam (DCB) specimen has been an attractive configuration for the study of crack propagation in composite and in adhesively bonded materials due to its experimental and theoretical simplicity. The name originates from the work of Benbow and Roesler [8], in which each arm of the specimen is treated as a built-in cantilever beam having a length equal to the length of the crack.

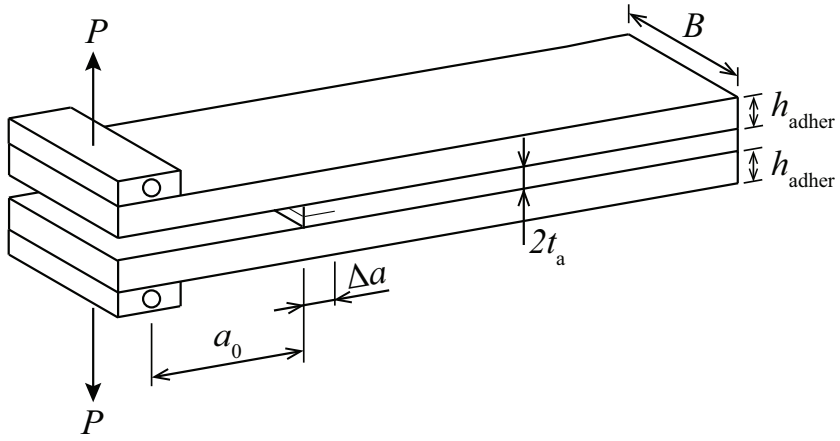

Figure 2.2: DCB configuration.

Fig. 2.2 schematically illustrates the standard DCB specimen. It consists of two uniform adherends of width B and thickness h_{adher} bonded together by an intermediate layer of adhesive of thickness $2t_a$. The unbonded part up to the load application point has a length of a_0. A pre-crack of length Δa is initially made in the adhesive layer by a razor blade, which is removed prior to testing. The initial crack has a total length of $a_0 + \Delta a$. The load P is applied to adherends in the unbonded end. The test and the data treatment incorporates easily measurable quantities

- macroscopic displacement and external force, used to establish fracture driving parameters, such as the critical mode I SERR, also referred to as the critical mode I fracture energy, G_{Ic}.

Through the last century, several theoretical models of adhesive joints have been developed. The adhesive bond-line can either be included or neglected depending on the scenario and the approach taken [2]. Some of those models are described in greater details in Chapters 3 to 6, such as the standard simple beam theory (SBT) or a beam partially free and partially supported by an elastic foundation, i.e. the Winkler foundation [9, 10].

2.1.2. Bi-material DCB adhesive joints

The standard DCB specimen configuration, from now on referred to as single-material DCB, is shown in Fig. 2.2, however different versions of it exist. For example, if the two adherends are not identical, the DCB specimen is asymmetric in terms of geometry and materials. This type of configuration is hereinafter referred to as bi-material joint type.

Currently, standard mode I fracture test methods are only available for joints with the same adherend material. Experimental and numerical work has been carried out by many researchers for standard DCB adhesive joints (i.e. adherends of same material and thickness) [11–15]. However, the fracture behaviour might be dependent on the materials of two adherends when performing fracture test of bi-material DCB joints. In this case, the standard DCB specimen must be adapted.

From open literature, it is found that, for bi-material DCB joints, the most commonly used design criterion is matching the flexural stiffness of the two adherends [16–19]. Although the deflection of the two adherends is symmetric in the bi-material DCB specimen designed with this criterion, mode II fracture component has been found [17, 18]. Ouyang et al. [20] has reported that the shear stress in the adhesive interlayer between two dissimilar adherends has to be suppressed to obtain pure mode I, otherwise mode II would be present. Zambelis et al. [21] has verified the idea of Ouyang et al. [20] with numerical simulations. Therefore, a new design criterion to achieve pure mode I in a bi-material adhesive joint is needed.

2.1.3. The role of adhesive bond-line thickness

Research on the effect of adhesive bond-line thickness on mode I fracture behaviour has mainly focused either on joints bonded with structural epoxy adhesives with bond-line thicknesses normally ranging between 0.1 and 2 mm – mostly applied to aerospace and automotive applications [7, 22–33], or on joints with flexible adhesives often with thicker bond-lines [7, 34–36]. However, limited studies were found on joints with "extra-thick" bond-lines (> 5 mm up to 10 mm) of epoxy adhesives, relevant for civil and maritime applications. The research done in the past has proved that there is a dependence of the critical fracture energy of adhesive joints on bonding thickness, regardless of the nature of the adhesives. However, there is no single trend for this dependency.

Most solid materials develop plastic strains when the yield strength is exceeded in the region near a crack tip. Structural adhesives, such as epoxies, are no exception.

The amount of plastic deformation is restricted by the surrounding material, which remains elastic during loading. As a result, a plastic zone is formed containing micro-structural defects such as dislocations and voids and it is called the crack tip plastic zone. This plastic deformation occurs in a small region (small-scale yielding) and is considered as responsible of dissipating majority of external loading. In a bulk adhesive specimen, when tensile loaded, is assumed that this zone has a circular shape of diameter equal to $2r_p$, where r_p is Irwin's estimation of the radius of the plastic zone (more on that later, in Chapter 4). In a bonded joint, the physical constraints of the adherends affect the stress field at the crack tip and, consequently, the shape and size of the plastic deformation zone. The influence of the adherends on the geometry of the plastic zone varies with the bond-line thickness [37, 38].

In a bonded joint with a thin adhesive layer, the role of the interphases becomes dominant on the fracture behaviour of the joint. The term interphase relates to the adhesive volume adjacent to the surface of the adherend, which is assumed to possess properties different from those of the adhesive when cured in the absence of an adherend. It has been reported that epoxide based adhesives form interphases with an extension of up to 100 μm from the adherends surfaces [39, 40]. Geiss et al. [39] experimentally measured the local deformation of the adhesive layer and its interphases in shear-loaded adhesive joints. The results showed that, in the elastic regime, the properties of the interphases were similar to those in the centre of the adhesive joint. Nevertheless, the interphases revealed to be more sensitive to strain-induced softening, which was triggered once the polymer's yield point was exceeded.

Bascom et al. [24] investigated the effect of bond-line thickness on mode I fracture behaviour of aluminium joints with an epoxy adhesive and the toughening effects of adding elastomer particles to the epoxy adhesive (i.e. 15% of the weight of the epoxy adhesive). The critical fracture energy of the joints with the unmodified epoxy was not affected by the bond-line thickness in the studied range (i.e. from 0.25 mm up to 2 mm), while a sharp increase of almost 30 times was observed in the joints bonded with the elastomer-modified epoxy. Moreover, the G_{Ic} of the joints with the elastomer-modified epoxy was found to be strongly dependent upon the thickness of the adhesive layer. The G_{Ic} was maximized when the bond-line thickness was about the size of the plastic zone formed at the crack tip (i.e. bond-line thickness of 0.25-0.5 mm). The maximum critical fracture energy was higher than the one from bulk adhesive.

Wang et al. [41] numerically predicted the stresses in the near field of the crack tip in adhesive joints as a function of adherends/adhesive modulus ratio and adhesive thickness. The results showed that when the bond-line thickness decreased, a shoulder developed on the local tensile stress distribution with the result that higher stresses extended along a larger distance ahead of the crack tip. This distance increased as the bond-line thickness was decreasing.

The work of Kinloch and Shaw [26] supported the findings of Bascom et al. [24], however via a slightly modified argument based on the work of Wang et al. [41]. By assuming a stress singularity at the crack tip, Kinloch and Shaw supposed that

the yield strength of the adhesive would be overreached in some zone ahead of the crack tip. Due to the fact that higher stresses spread out along a larger distance ahead of the crack tip as the bond-line thickness decreased, Kinloch and Shaw assumed that the yield criterion would be exceeded at further distances from the crack tip. Consequently, this would result in more elongated plastic zones. Their theory suggested that there is a peak in the critical fracture energy of an adhesive joint when the adhesive bond-line thickness approaches the diameter of the plastic zone of a growing crack in a bulk adhesive specimen. In this case, the height of the plastic zone is, therefore, as predicted from the bulk adhesive specimen but its length ahead of the crack tip may be greater due to constraint from the adherends. Consequently, the volume of the plastic zone should be larger in the adhesive joint than its volume in bulk adhesive specimens. Moreover, the critical fracture energy of adhesive joints decreases at bond-lines thinner than the bulk adhesive plastic zone diameter. Although the presence of stiff adherends extends the plastic zone length, the volume of the plastic zone is always smaller due to thinner bond-lines. On the other hand, in joints with bond-line thicknesses greater than the bulk adhesive plastic zone diameter, the constraint level from the adherends is lower, resulting in a reduction of the length of the plastic zone, and, thus, in lower values of the critical fracture energy of the joints (tending towards the critical fracture energy of the bulk adhesive).

The results of other researchers further supported the proposals of Bascom et al. [24] and Kinloch and Shaw [26], regarding the role of the plastic zone size on the critical fracture energy-adhesive thickness relation of adhesive joints. Hunston et al. [22] conducted fracture experiments on adhesive joints composed by aluminium adherends and an elastomer-modified epoxy adhesive. Bonded joints with adhesive thicknesses of 0.38, 1 and 2 mm were tested and the stress-whitening that occurred at the crack tip was used to evaluate the size and shape of the plastic zone. The results showed that the plastic zone changes with the bond-line thickness due to the physical constraint of the adherends and the stress field at the crack tip. The maximum value of the critical mode I fracture energy was found to occur at a specific thickness where the height of the plastic zone was equal to the bond-line thickness.

Maloney [7] investigated the mode I fracture behaviour of aluminium joints bonded with a structural epoxy adhesive (Araldite 2015, Huntsman®), with bond-line thicknesses ranging from 0.2 to 4.0 mm. Failure of the joints was observed to occur by cohesive propagation of a single crack. Evidence of plastic damage mechanisms occurring at the tip of the growing crack was found along the failure surfaces, such as stress whitening. The critical mode I fracture energy, G_{Ic}, of joints with bond-line thicknesses of 0.2 and 0.3 mm was found to be much lower than the one of the bulk adhesive specimens, while the G_{Ic} of the 4.0 mm thick bond-line joints was similar to the critical fracture energy of the bulk adhesive specimens. The joints with a finite adhesive bond-line thickness of 1 mm presented the highest G_{Ic} value. This maximum occurred at a bond-line thickness nearly equal to the size of the plastic zone.

As mentioned earlier, there is no single trend to describe the dependence of the

critical fracture energy of adhesive joints on bonding thickness and in some cases the proposals of Bascom et al. [24] and Kinloch and Shaw [26] do not correlate well with the experimental results. Ranade et al. [29] have studied the effect of the bond-line thickness on the critical fracture energy under mode I loading conditions of aluminium specimens bonded with a structural epoxy adhesive. The bond-line thickness varied from 0.02 up to 4.5 mm. The fracture energies increased with an increase in the bond-line thickness up to about 2 mm and remained constant out to the maximum bond-line thickness of about 4.5 mm. An estimate of the plastic zone length was obtained by testing bulk adhesive specimens and the result was compared to the experimental bond-line thicknesses. The estimated plastic zone length was about one-fourth the bond-line thickness value of 2 mm (where a plateau of G_{Ic} was achieved). No detailed analysis of the crack path was reported and, consequently, the critical fracture energy-adhesive bond-line thickness relation could not be fully understood.

Daghyani et al. [32, 33] investigated the effect of bond thickness on the mode I fracture toughness of aluminium adhesive joints. A rubber-toughened adhesive was used. The critical fracture energy increased gradually up to 1 mm thick bond-line, tending to a plateau afterwards. For bond-line thicknesses larger than 4 mm, there was a sharp increase in the critical fracture energy towards the critical fracture energy of the bulk adhesive material. The authors concluded that the relationship between the critical fracture energy and the adhesive bond-line thickness is mainly controlled by the plastic deformation of the adhesive around the crack tip as may be influenced by the constraint imposed by the adherends. Tough fracture mechanisms were observed in thick bonds and their presence became more pronounced with increasing adhesive bond-line thickness.

Cooper et al. [30] performed a combined experimental-numerical study of the fracture behaviour of a rubber-toughened epoxy adhesive. Metallic adhesive joints with various bond-line thicknesses ranging from 0.25 to 2.5 mm were tested. The fracture energies increased steadily from 2.6 N/mm at 0.25 mm bond-line thickness to 5.8 N/mm at 1.3 mm and remained almost constant for larger bond-line thicknesses. The authors argued that most of the energy dissipation occurs locally in the plastic zone formed ahead of the crack tip and that the intensity of local plasticity is the main factor in determining the critical fracture energy and not only the size of the plastic zone.

As aforementioned, in bonded joints with flexible adhesives, the adhesive bond-line thickness also plays a role in mode I fracture behaviour and some studies have focused on this topic [7, 34, 36]. Maloney [7] performed experiments with adhesive joints consisting of aluminium adherends and an elastomeric adhesive (a silyl-modified polymer). Two bond-line thicknesses were tested: 1.1 and 4.1 mm. The critical mode I fracture energy increased with the adhesive bond-line thickness. In order to better understand the damage mechanisms occurring during the crack growth, the adhesive layer was scanned by computed tomography. The joints of a bond-line of 1.1 mm presented a higher concentration of voids near each interface than along the mid-plane of the adhesive layer. However, the voids along the mid-plane tended to be larger than those near each interface. The adhesive along the

free surfaces of the joints often failed in the last place, after the adhesive in the inner region has failed by cavitation due to a critical state of hydrostatic stress. Similar failure mechanisms were observed in joints with bond-line thicknesses of 4.1 mm. These joints also displayed voids along narrow strips of adhesive in the central region around 3 mm from any free surface, probably where the hydrostatic stress reached a critical value.

2.1.4. The role of material of adherends

The subject of the effect of the material of the adherends on the failure of adhesive joints has been mainly investigated for the shear loading case, namely with lap-shear tests [42–50]. These studies addressed the effect of the material of the adherends in two distinct ways: by considering single-material adhesive joints with different adherend thicknesses, or by considering bi-material adhesive joints. Looking at the effect of the material of the adherends on the mode I fracture behaviour of adhesive joints, some studies are available [31, 32, 51–55]. However, these studies commonly address the effect of the material of the adherends by considering single-material adhesive joints with different adherend thicknesses.

Kawashita et al. [54] investigated the effect of the adherend thickness on the critical mode I fracture energy of metallic joints, bonded with a rubber toughened epoxy adhesive (bond-line thickness of 0.25 mm). Three different adherend thicknesses were considered: 0.5, 1, 1.5 mm. It is reported that the lowest value of G_{Ic} corresponds to the lowest adherend thickness, while its value shows independence for thicker adherends. The lowest value of G_{Ic} is justified by the failure type in these specimens. Evidence of interfacial failure was found on the fractured surfaces.

Kafkalidis et al. [51] performed fracture experiments with steel-steel and aluminium-aluminium DCB adhesive joints. Three different adherend thicknesses were studied. The critical fracture energy of the adhesive joints was found to be independent of the thickness of the adherends and the adherend material type. The peak stress and the critical displacement for failure supported by the adhesive varied with the constraint level in such a manner that the critical fracture energy remained approximately constant.

Martiny et al. [55] conducted a numerical study on the effects of the adherend stiffness on the fracture behaviour of adhesively-bonded joints, consisting of metallic adherends and an epoxy-based structural adhesive. Two adherend materials were considered: steel and aluminium. In addition, different adherend thicknesses were studied. At a given value of the adhesive layer thickness, the predicted values of G_{Ic} varied by only about 10%, regardless of the adherend material and thickness. The authors explained these results by the higher degree of constraint that is imposed to the adhesive by employing high-modulus and/or relatively thick adherends.

Daghyani et al. [32] investigated the constraint effect on the fracture behaviour of a rubber-modified epoxy, via compact tension adhesive joints. The numerically predicted values of G_{Ic} decreased as the adherend stiffness increased. The greater degree of constraint with increasing adherend stiffness led to a lower extent of the plastic energy dissipation.

Blackman et al. [53] performed mode I fracture tests with single-material DCB

adhesive joints. Two adherend materials were studied: an unidirectional carbon-fibre reinforced plastic (CFRP) and a mild steel (grade EN24). These adherends were bonded with the same structural epoxy-paste adhesive. The thickness of the bond-line was 0.4 mm. All samples failed cohesively, no interfacial failure was observed. The critical mode I fracture energy appeared to be dependent on the adherend material used. The autors concluded that the different values of the glass transition temperature, T_g, of the cured adhesive in the different adhesive joints were the potential cause of the dependence of G_{Ic} with the adherend material. Low volumes of water diffused from the CFRP adherends into the adhesive. The water diffusion interfered with the formation of rubber-particulate separated-phase during the cure of the epoxy adhesive, affecting the T_g and, consequently, the G_{Ic} of the CFRP-CFRP adhesive joints [52].

The research carried on up to now addressed the effect of the material of the adherends on the critical fracture energy of adhesive joints by solely considering single-material adhesive joints with different adherend thicknesses. Besides, the studies available are based in standard reduction schemes, which do not take entirely into account the geometric and material properties of the adhesive joints, like adhesive bond-line thickness and out-of-plane stiffness of the adherends. Moreover, to the author's best knowledge, no studies investigating the possible changes on the critical fracture energy of bi-material adhesive joints are found in open literature.

2.2. The special case of adhesive joints with “extra-thick” bond-lines

The use of adhesive bonding technology in civil and shipbuilding industries results in bonded regions characterized by adhesive layers with a thickness of up to 5 and 10 mm, respectively. Such adhesive thicknesses are imposed by in-situ or manufacturing [56] constraints. With such thicknesses, a weakness to be recognized, from both the scientific and applied points of view, is stress gradient at bi-material edges and corners, exacerbated by differences in materials properties [57–61]. Locally, peel forces arise and might result in local damage and fracture onset, in case the bonded region is subjected to external loading, being the mode I loading case the most critical.

Moreover, structural epoxy adhesives are often indicated, by the shipbuilding and civil engineers, to be used in the bi-material joints. Their elastic-plastic material characteristics, in addition to the aforementioned geometric length scale of the thickness of the adhesive layer, introduces a material length scale of a plastic radius [38]. When the yield strength of the adhesive is exceeded in the region near a crack tip, plastic deformation occurs in a small region, as it is restricted by the surrounding material, which remains elastic. This plastic deformation is considered as responsible for dissipation of the majority of the external loading. Control over e.g. the number, the localization and size of the plastic regions is highly desired and in principle could increase both reliability and overall performance of the adhesive joint in sustaining external loading.

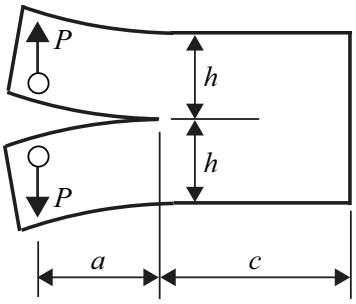

(a) Kanninen [10]: homogeneous DCB specimen modelled by considering a finite length beam which is partially free and partially supported by an elastic foundation.

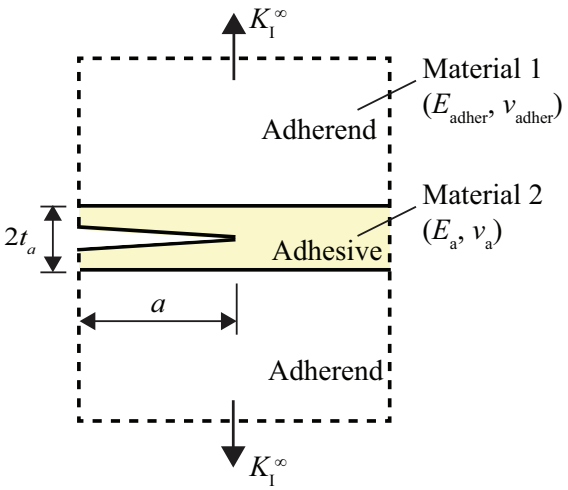

(b) F. Van Loock, M.D. Thouless, N.A. Fleck (2019) [62]: adhesive joint with semi-infinite crack subjected to a remote mode I *K*-field.

Figure 2.3: Comparison of mode I geometries used to analyse adhesive joints.

The theoretical description of the DCB configuration has been modified and extended to cover the effects of various parameters (e.g. bond-line thickness or shear deformation of adherends). As aforementioned in section 2.1, Benbow and Roesler [8] were the first to theoretically model a DCB specimen by following the simple beam theory to model the cracked parts of the adherends as built-in cantilever beams. In this model, the bonded (intact) part of the joint was assumed as completely rigid, which overestimated the stiffness of the joint.

Kanninen [10] developed the “augmented DCB model” for crack propagation analysis of a homogeneous specimen as shown in Fig. 2.3(a). The model takes direct account of the region behind the crack by considering a finite length beam which is partially free (representing the unbonded part of the specimen) and partially supported by an elastic foundation (representing the bonded region). The mathematical description of the model is based on the simplest theories: the Euler-Bernoulli beam theory and the Winkler foundation. This model remarkably gives information about the region in front of the crack, in particular the elastic process zone, λ^{-1}, which is interpreted as the distance (from the crack tip) over which the positive peel stress is distributed. Therefore, this model can form a phenomenological basis for cohesive zone models as crack tip opening displacements and stress are incorporated. However, this analysis, which can be considered as meso-scale, was intended for fracture of homogeneous materials and, therefore, did not include an adhesive layer. Later on, Penado extended Kanninen's analysis to adhesive joints, by including the adhesive layer in the analysis [63]. Moreover, Yamada modelled the bonded region by considering a beam on an elastic-plastic foundation [64].

At this stage, it seems reasonable to postulate that the limit of applicability of various models is related to the adhesive thickness. As the adhesive thickness tends to

zero, like in laminated materials, either Benbow and Roesler [8] or Kanninen [10] approximations will suffice. For sufficiently thick bond-lines, as shown in Fig. 2.4, local stress gradients at interfaces should be expected, however, meso- and local-scale analysis should be used, such as Penado's and Yamada's analyses [63, 64]. Finally, once adhesive thickness tends to infinity, in the presence of a embedded crack, stress intensity asymptotic analysis will be necessary [38].

Following the early works of Dundurs and Bogy [65, 66], it has been recognized that the so-called basic interface problem (two dissimilar materials bonded along shared interface under remote loading) introduces local stress gradients duo to the material properties mismatch. Such singular stress field, in case of materials containing a crack, comes as complementary to the crack tip stress field.

In 1987, Hutchinson et al. [58] investigated competition between the crack tip singular field and materials mismatch induced stress gradient near the interface, leading to formulation of conditions for a sub-interface crack growth. Here, authors noted that the stable sub-interface crack growth is unlikely and once the crack front onsets in cohesive manner within any of the two joined materials, configurational (≡ directional) stability of the crack follows another criterion (Cotterell-Rice theory [67]). From this work, we learn that only a negative non-singular term at the crack tip (which refers specifically to the so-called T-stress explained at a later stage in Chapter 6) can guarantee stable crack growth. The basic interface problem enriched by the presence of an interface crack was pursued by Suo and Hutchinson [68, 69]. The classic square root dependence of the stresses on the distance away from the crack tip remains, however, material mismatch enforces use of complex variables and adds additional term to the power dependence of the stress on the distance from the crack tip.

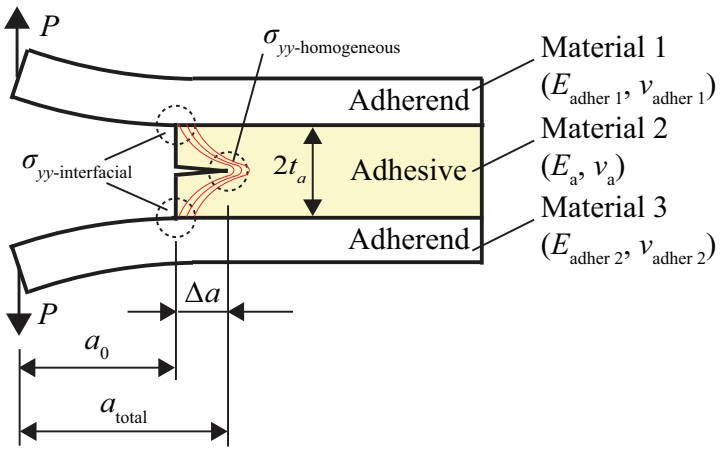

Figure 2.4: Adhesive joint with thick bond-line: geometry idealization to avoid local stress peaks at interfaces (more on that later in Chapter 6).

Recently, F. Van Loock et al. [62] studied adhesive joints subjected to a remote mode I K-field of magnitude K^{∞}. The joints, composed by an elastic adhesive layer of thickness $2t_a$ sandwiched between two elastic adherends, contained a semi-

infinite crack as shown in Fig. 2.3(b). The normal stress component σ_{yy} distribution (perpendicular to the crack plane and within the adhesive layer) ahead of the crack tip was determined by finite element analysis for different values of modulus-mismatch ratio $\frac{E_a}{E_{adher}}$ (E_a and E_{adher} being the Young's modulus of the adhesive and adherend, respectively). σ_{yy} is shielded by the presence of stiffer adherend material. As the mismatch in modulus increases (decreasing $\frac{E_a}{E_{adher}}$), the stress distribution tends to the solution for a semi-infinite crack in an adhesive layer between two rigid adherends and subjected to an uniform opening displacement. The stress is predicted to be independent of crack length and decreases with an increase in bond-line thickness [70].

A certain gap between different approaches exists, specially when it comes to implementation into the DCB-like geometries where the bond-line is once used as a crack and once as containing the crack. In fact, the standard DCB procedure skips adhesive thickness (as in ASTM D 5528 [9]), implying that the same models could be used for thin and thick bond-lines. Use of composites and bonded materials is associated with carrying a bending-type of loading, while most of the geometries investigated use idealized, remotely applied tensile loading. Such approach ultimately omits important length scale introduced by bending as outlined by the analysis of Kanninen in [10]. The load acting over the crack region cannot be treated as uniform, contrary to the case of remotely applied tensile loading as in [62]. Effects of plastic radius are barely investigated within the outlined framework, however role of this region is known as critical [71].

2.3. Summary and knowledge gaps

A review of the research conducted on mode I fracture behaviour of single- and bi-material DCB joints has been given. The currently available design criterion for bi-material DCB configuration was presented and its validity was discussed. Moreover, special attention was given to two key-factors influencing the behaviour of adhesive joints, i.e. the adhesive bond-line thickness and the material of the adherends. Finally, the special case of adhesive joints with "extra-thick" bond-lines, used in shipbuilding and civil industries, was also addressed in terms of the role of the interfaces on fracture onset and the methodologies available for mode I fracture characterization.

The standard DCB configuration consists of two identical adherends bonded together by an intermediate layer of adhesive. However, different versions of it exist. For example, if the two adherends are not identical, the DCB specimen is asymmetric in terms of geometry and materials. This is the so-called bi-material joint configuration. Consequently, a design criterion must be followed to guarantee pure mode I fracture behaviour in this type of adhesive joint. Currently, the most used design criterion for bi-material DCB joints is matching the flexural stiffness of both adherends. Although the deflection of the two adherends is symmetric in the bi-material DCB specimen designed with this criterion, mode II fracture component has been reported in open literature. Therefore, a new design criterion to achieve pure mode I in a bi-material adhesive joint is needed.

The properties of an adhesive joint are often different from the properties of the bulk adhesive. A variety of factors may play a role in this difference, such as the constraint applied by the adherends on the adhesive material, which is dependent on the thickness of the bond-line. Research on the effect of the adhesive bond-line thickness on mode I fracture behaviour has mainly focused either on joints with epoxy adhesives and with bond-line thicknesses in the range of 0.1-2 mm or on joints with flexible adhesives often with thicker bond-lines. The studies performed have shown that there is a dependence of the critical mode I fracture energy of adhesive joints on bonding thickness, regardless of the nature of the adhesives. However, there is no single trend for this dependency.

Part of the studies conducted with epoxy-adhesive joints have found a local peak in the critical fracture energy of the joints, corresponding to an adhesive bond-line thickness nearly equal to the size of the plastic zone. In general, the critical fracture energy increased with increasing bond-line thickness up to the peak value. For bond-line thickness greater than the plastic zone, the critical fracture energy decreased towards the critical fracture energy of the bulk adhesive specimen. However, this trend did not always occurred. Some authors have reported that the critical mode I fracture energy of epoxy-based adhesive joints increased gradually up to a specific bond-line thickness (not related with the plastic zone size), tending to a plateau for greater bond-line thicknesses. The increasing presence of tough fracture mechanisms with increasing adhesive thickness and the intensity of plasticity in the plastic zone (instead of only the size of this zone) were some of the factors used to justify the results. Experimental and numerical work in this area with joints with "extra-thick" bond-lines (10 mm) of epoxy adhesives, relevant for civil and maritime applications, are quite limited.

The research carried on up to now addressed the effect of the material of the adherends on the critical fracture energy of adhesive joints by solely considering single-material adhesive joints with different adherend thicknesses. Besides, the studies available are based in standard reduction schemes, which do not take entirely into account the geometric and material properties of the adhesive joints, like adhesive bond-line thickness and out-of-plane stiffness of the adherends. Moreover, to the author's best knowledge, no studies investigating the possible changes on the critical fracture energy of bi-material adhesive joints are found in open literature.

The use of adhesive bonding technology in civil and shipbuilding industries results in bonded regions characterized by adhesive layers with a thickness of up to 10 mm. With such thicknesses, a weakness to be recognized, from both the scientific and applied points of view, is stress gradient at bi-material edges and corners, exacerbated by differences in materials properties. Locally, peel forces arise, which might result in local damage and fracture onset. It is, therefore, crucial to develop an approach that eliminates the phenomenon of stress gradient at bi-material interfaces on the fracture onset process in adhesive joints under mode I loading conditions. The literature available shows that a proper analysis of DCB joints characterized by dissimilar materials and thick adhesive bond-lines with small crack length, which are representative of engineering applications, is missing.

References

[1] D. A. Dillard, *Advances in structural adhesive bonding* (Woodhead Publishing Limited, 2010).

[2] S. Heide-Jørgensen, *Mechanics and failure of structured interfaces*, Ph.D. thesis, Aarhus University (2019).

[3] A. A. Griffith, *The phenomena of rupture and flow in solids,* Philosophical Transactions of the Royal Society A: Mathematical, Physical and Engineering Sciences **221**, 163– (1921).

[4] G. R. Irwin, *Fracture dynamics,* Fracturing of Metals, American Society for Metals , 147 (1948).

[5] G. R. Irwin, *Relation of stresses near a crack to the crack extension force,* Proceedings of the International Congresses of Applied Mechanics **8**, 245– (1957).

[6] G. R. Irwin, *Analysis of stresses and strains near the end of a crack traversing a plate,* Journal of Applied Mechanics **24**, 361– (1957).

[7] K. J. Maloney, *Micro-architected adhesive joints*, Ph.D. thesis, University of Cambridge (2016).

[8] J. J. Benbow and F. C. Roesler, *Experiments on controlled fractures,* Proceedings of the Physical Society B **70**, 201 (1957).

[9] *ASTM D 5528 - Standard test method for mode I interlaminar fracture toughness of unidirectional fiber-reinforced polymer matrix composites,* (2013).

[10] M. F. Kanninen, *An augmented double cantilever beam model for studying crack propagation and arrest,* International Journal of Fracture **9**, 83 (1973).

[11] S. Azari, A. Ameli, M. Papini, and J. K. Spelt, *Analysis and design of adhesively bonded joints for fatigue and fracture loading: a fracture-mechanics approach,* Journal of Adhesion Science and Technology **27**, 1681 (2013).

[12] G. Ji, Z. Ouyang, G. Li, S. Ibekwe, and S.-S. Pang, *Effects of adhesive thickness on global and local mode-I interfacial fracture of bonded joints,* International Journal of Solids and Structures **47**, 2445 (2010).

[13] M. M. Shokrieh, M. Heidari-Rarani, and M. R. Ayatollahi, *Interlaminar fracture toughness of unidirectional DCB specimens: A novel theoretical approach,* Polymer Testing **31**, 68 (2012).

[14] M. Cabello, A. Turon, J. Zurbitu, J. Renart, C. Sarrado, and F. Martínez, *Progressive failure analysis of DCB bonded joints using a new elastic foundation coupled with a cohesive damage model,* European Journal of Mechanics - A/Solids **63**, 22 (2017).

[15] M. S. Bin Mohamed Rehan, J. Rousseau, S. Fontaine, and X. J. Gong, *Experimental study of the influence of ply orientation on DCB mode-I delamination behavior by using multidirectional fully isotropic carbon/epoxy laminates,* Composite Structures **161**, 1 (2017).

[16] Z. Jiang, S. Wan, and Z. Wu, *Calculation of energy release rate for adhesive composite/metal joints under mode-I loading considering effect of the non-uniformity,* Composites Part B: Engineering **95**, 374 (2016).

[17] M. Khoshravan and F. Asgari Mehrabadi, *Fracture analysis in adhesive composite material/aluminum joints under mode-I loading; experimental and numerical approaches,* International Journal of Adhesion and Adhesives **39**, 8 (2012).

[18] R. G. Boeman, D. Erdman, L. Klett, and R. Lomax, *A practical test method for mode I fracture toughness of adhesive joints with dissimilar substrates,* in *SAMPE-ACCE-DOE Advanced Composites Conference* (1999) pp. 358–366.

[19] X. J. Gong, F. Hernandez, and G. Verchery, *Fracture toughness of adhesive bonded composite joints under mixed mode loading,* in *12th International Conference on Composites (ICCM12 Conference)* (1999).

[20] Z. Ouyang, G. Ji, and G. Li, *On approximately realizing and characterizing pure mode-I interface fracture between bonded dissimilar materials,* Journal of Applied Mechanics **78**, 031020 (2011).

[21] G. Zambelis, T. D. S. Botelho, O. Klinkova, I. Tawfiq, and C. Lanouette, *Evaluation of the energy release rate in mode I of asymmetrical bonded composite/metal assembly,* Engineering Fracture Mechanics **190**, 175 (2018).

[22] D. L. Hunston, A. J. Kinloch, and S. S. Wang, *Micromechanics of fracture in structural adhesive bonds,* The Journal of Adhesion **28**, 103 (1989).

[23] M. B. Ouezdou and A. Chudnovsky, *Stress and energy analysis of toughness measurement for adhesive bonds,* Engineering Fracture Mechanics **29**, 253 (1988).

[24] W. D. Bascom, R. L. Cottington, R. L. Jones, and P. Peyser, *The fracture of epoxy- and elastomer-modified epoxy polymers in bulk and as adhesives,* Journal of Applied Polymer Science **19**, 2545 (1975).

[25] S. Marzi, A. Biel, and U. Stigh, *On experimental methods to investigate the effect of layer thickness on the fracture behavior of adhesively bonded joints,* International Journal of Adhesion and Adhesives **31**, 840 (2011).

[26] A. J. Kinloch and S. J. Shaw, *The fracture resistance of a toughened epoxy adhesive,* The Journal of Adhesion **12**, 59 (1981).

[27] T. Carlberger and U. Stigh, *Influence of layer thickness on cohesive properties of an epoxy-based adhesive - an experimental study,* Journal of Adhesion **86**, 814 (2010).

[28] D.-B. Lee, T. Ikeda, N. Miyazaki, and N.-S. Choi, *Effect of bond thickness on the fracture toughness of adhesive joints,* Journal of Engineering Materials and Technology **126**, 14 (2004).

[29] S. R. Ranade, Y. Guan, D. C. Ohanehi, J. G. Dillard, R. C. Batra, and D. A. Dillard, *A tapered bondline thickness double cantilever beam (DCB) specimen geometry for combinatorial fracture studies of adhesive bonds,* International Journal of Adhesion and Adhesives **55**, 155 (2014).

[30] V. Cooper, A. Ivankovic, A. Karac, D. McAuliffe, and N. Murphy, *Effects of bond gap thickness on the fracture of nano-toughened epoxy adhesive joints,* Polymer **53**, 5540 (2012).

[31] T. Pardoen, T. Ferracin, C. M. Landis, and F. Delannay, *Constraint effects in adhesive joint fracture,* Journal of the Mechanics and Physics of Solids **53**, 1951 (2005).

[32] H. R. Daghyani, L. Ye, and Y. W. Mai, *Mode-I fracture behaviour of adhesive joints. Part II. Stress analysis and constraint parameters,* The Journal of Adhesion **53**, 163 (1995).

[33] H. R. Daghyani, L. Ye, and Y. W. Mai, *Mode-I fracture behaviour of adhesive joints. Part I. Relationship between fracture energy and bond thickness,* The Journal of Adhesion **53**, 149 (1995).

[34] M. D. Banea, L. F. Da Silva, and R. D. Campilho, *The effect of adhesive thickness on the mechanical behavior of a structural polyurethane adhesive,* Journal of Adhesion **91**, 331 (2014).

[35] M. Cabello, J. Zurbitu, J. Renart, A. Turon, and F. Martínez, *A general analytical model based on elastic foundation beam theory for adhesively bonded DCB joints either with flexible or rigid adhesives,* International Journal of Solids and Structures **94-95**, 21 (2016).

[36] A. Biel and U. Stigh, *Cohesive zone modelling of nucleation, growth and coalesce of cavities,* International Journal of Fracture **204**, 159 (2017).

[37] C. T. Sun and Z. H. Jin, *Fracture Mechanics* (Academic Press, 2012).

[38] N. Perez, *Fracture mechanics* (Springer, 2017).

[39] P. L. Geiss and M. Schumann, *Investigation of the mechanical properties of interphases in adhesively bonded epoxy-aluminum joints by localized micro extensometry,* The Journal of Adhesion **88**, 941 (2012).

[40] W. Possart, J. K. Krüger, C. Wehlack, U. Müller, C. Petersen, R. Bactavatchalou, and A. Meiser, *Formation and structure of epoxy network interphases at the contact to native metal surfaces,* Comptes Rendus Chimie **9**, 60 (2006).

[41] S. S. Wang, J. F. Mandell, and F. J. McGarry, *An analysis of the crack tip stress field in DCB adhesive fracture specimens,* International Journal of Fracture **14**, 39 (1978).

[42] L. Dorn and W. Liu, *The stress state and failure properties of adhesive-bonded plastic/metal joints,* International Journal of Adhesion and Adhesives **13**, 21 (1993).

[43] M. D. Aydin, A. Özel, and e. Temiz, *The effect of adherend thickness on the failure of adhesively-bonded single-lap joints,* Journal of Adhesion Science and Technology **19**, 705 (2005).

[44] M. S. Seong, T. H. Kim, K. H. Nguyen, J. H. Kweon, and J. H. Choi, *A parametric study on the failure of bonded single-lap joints of carbon composite and aluminum,* Composite Structures **86**, 135 (2008).

[45] G. Di Bella, G. Galtieri, E. Pollicino, and C. Borsellino, *Mechanical characterization of adhesive joints with dissimilar substrates for marine applications,* International Journal of Adhesion and Adhesives **41**, 33 (2013).

[46] K. Gültekin, S. Akpinar, and A. Özel, *The effect of moment and flexural rigidity of adherend on the strength of adhesively bonded single lap joints,* Journal of Adhesion **91**, 637 (2015).

[47] V. Anes, R. Pedro, E. Henriques, M. Freitas, and L. Reis, *Bonded joints of dissimilar adherends at very low temperatures - an adhesive selection approach,* Theoretical and Applied Fracture Mechanics **85**, 99 (2016).

[48] F. Ascione, M. Lamberti, A. G. Razaqpur, and S. Spadea, *Strength and stiffness of adhesively bonded $GFRP$ beam-column moment resisting connections,* Composite Structures **160**, 1248 (2017).

[49] M. El Zaroug, F. Kadioglu, M. Demiral, and D. Saad, *Experimental and numerical investigation into strength of bolted, bonded and hybrid single lap joints: effects of adherend material type and thickness,* International Journal of Adhesion and Adhesives **87**, 130 (2018).

[50] A. G. Razaqpur, F. Ascione, M. Lamberti, S. Spadea, and M. Malagic, *$GFRP$ hollow column to built-up beam adhesive connection: mechanical behaviour under quasi-static, cyclic and fatigue loading,* Composite Structures **224** (2019), 10.1016/j.compstruct.2019.111069.

[51] M. S. Kafkalidis, M. D. Thouless, Q. D. Yang, and S. M. Ward, *Deformation and fracture of adhesive layers constrained by plastically-deforming adherends,* Journal of Adhesion Science and Technology **14**, 1593 (2000).

[52] B. R. K. Blackman, A. J. Kinloch, and M. Paraschi, *The effect of the substrate material on the value of the adhesive fracture energy, G_c: further considerations,* Journal of Materials Science Letters **20**, 265 (2001).

[53] B. R. Blackman, A. J. Kinloch, M. Paraschi, and W. S. Teo, *Measuring the mode I adhesive fracture energy, G_{Ic}, of structural adhesive joints: the results of an international round-robin,* International Journal of Adhesion and Adhesives **23**, 293 (2003).

[54] L. F. Kawashita, A. J. Kinloch, D. R. Moore, and J. G. Williams, *The influence of bond line thickness and peel arm thickness on adhesive fracture toughness of rubber toughened epoxy-aluminium alloy laminates,* International Journal of Adhesion and Adhesives **28**, 199 (2008).

[55] P. Martiny, F. Lani, A. J. Kinloch, and T. Pardoen, *A multiscale parametric study of mode I fracture in metal-to-metal low-toughness adhesive joints,* International Journal of Fracture **173**, 105 (2012).

[56] I. A. of Classification Societies, *No . 47 Shipbuilding and repair quality standard (Rev. 7 June 2013)*, Tech. Rep. 1996 (2013).

[57] D. B. Bogy, *On the problem of edge-bonded elastic quarter-planes loaded at the boundary,* International Journal of Solids and Structures **6**, 1287 (1970).

[58] J. W. Hutchinson, M. E. Mear, and J. R. Rice, *Crack paralleling an interface between dissimilar materials,* Journal of Applied Mechanics **54**, 828 (1987).

[59] Z. Suo and J. W. Hutchinson, *Sandwich test specimens for measuring interface crack toughness,* Materials Science and Engineering: A **107**, 135 (1989).

[60] E. D. Reedy and T. R. Guess, *Interface corner failure analysis of joint strength: effect of adherend stiffness,* International Journal of Fracture **88**, 305 (1997).

[61] A. R. Akisanya and C. S. Meng, *Initiation of fracture at the interface corner of bi-material joints,* Journal of the Mechanics and Physics of Solids **51**, 27 (2003).

[62] F. Van Loock, M. D. Thouless, and N. A. Fleck, *Tensile fracture of an adhesive joint: the role of crack length and of material mismatch,* Journal of the Mechanics and Physics of Solids **130**, 330 (2019).

[63] F. E. Penado, *A closed form solution for the energy release rate of the souble cantilever beam specimen with an adhesive layer,* Journal of Composite Materials **27**, 383 (1993).

[64] S. E. Yamada, *Elastic/plastic fracture analysis for bonded joints,* Engineering Fracture Mechanics **27**, 315 (1987).

[65] J. Dundurs, *Effect of elastic constants on stress in a composite under plane deformation,* Journal of Composite Materials **1**, 310 (1967).

[66] D. B. Bogy, *Two edge-bonded elastic wedges of different materials and wedge angles under surface tractions,* Journal of Applied Mechanics **38**, 377 (1971).

[67] B. Cotterell and J. R. F. Rice, *Slightly curved or kinked cracks,* International Journal of Fracture **16**, 155 (1980).

[68] Z. Suo and J. W. Hutchinson, *Interface crack between two elastic layers,* International Journal of Fracture **43**, 1 (1990).

[69] J. W. Hutchinson and Z. Suo, *Mixed mode cracking in layered materials,* (Elsevier, 1991) pp. 63–191.

[70] C. H. Wang, *Analysis of cracks in constrained layers,* International Journal of Fracture **83**, 1 (1997).

[71] B. R. K. Blackman, A. J. Kinloch, and M. Paraschi, *The determination of the mode II adhesive fracture resistance, G_{IIc}, of structural adhesive joints: an effective crack length approach,* Engineering Fracture Mechanics **72**, 877 (2005).

3

Pure mode I fracture in bi-material adhesive joints

An essential question to predict the structural integrity of bi-material adhesive joints is how to obtain their fracture properties under pure mode I. From the literature review in Chapter 2, it is found that the most commonly used design criterion to test mode I fracture is matching the flexural stiffness of the two adherends in a DCB adhesive joint. However, the material asymmetry in such designed joints results in mode II fracture as well. In this chapter, a new design criterion is proposed to obtain pure mode I fracture in adhesively bonded bi-material DCB joints by matching the longitudinal strain distributions of the two adherends at the bond-line - the longitudinal strain based criterion. A test program and finite element modelling have been carried out to verify the proposed design criterion using composite-metal DCB adhesive joints. Both the experimental and numerical results show that pure mode I can be achieved in bi-material joints designed with the proposed criterion. Mixed mode ratio is reduced by a factor of 5 when using the proposed longitudinal strain based criterion in comparison with the flexural stiffness based criterion.

Parts of this chapter have been published in Composites Part B: Engineering **153**, 137 (2018) [1].

3.1. Introduction

Currently, standard mode I fracture test methods are only available for joints with the same adherend material and thickness. From open literature, it is found that for bi-material DCB adhesive joints the most commonly used design criterion is matching the flexural stiffness of the two adherends [2–5]. Although the deflection of two adherends is symmetric in the bi-material DCB specimen designed with this criterion, mode II fracture component has been found [3, 4]. Ouyang et al. [6] has reported that the shear stress in the adhesive interlayer between two dissimilar adherends has to be suppressed to obtain pure mode I, otherwise mode II would be present. Zambelis et al. [7] has verified the idea of Ouyang with numerical simulation. Therefore, a new design criterion to achieve pure mode I in a bonded bi-material joint is needed.

In this chapter, a new design criterion is proposed to obtain pure mode I fracture in adhesively bonded bi-material DCB joints by matching the longitudinal strain distributions of the two adherends at the bond-line - the longitudinal strain based criterion. This criterion is validated with an experimental and numerical case study using adhesively bonded composite-metal DCB joints.

3.2. Proposed approach

Considering cohesive failure in bonded bi-material DCB joints, the crack is embedded within the adhesive layer between two adherends. In order to develop a method of achieving pure mode I in an adhesive joint, with the adhesive layer embracing a crack, it is crucial to examine the deformation of the cracked adhesive layer especially around the crack tip.

3.2.1. Analysis of the deformation of the cracked adhesive layer in a bi-material DCB specimen

In a DCB specimen, the loading applied to the adhesive layer is introduced by the deformation of the two adherends. In Fig. 3.1, a general DCB specimen with dissimilar adherends is schematically illustrated. The flexural modulus and thickness of the upper and lower beams are denoted as $E_x^{\text{f-adher 1}}$, $h_{\text{adher 1}}$ and $E_x^{\text{f-adher 2}}$, $h_{\text{adher 2}}$, respectively. The two beams open up under a pair of opening loading, P, however the two beams are not perfectly cantilevered at the crack tip [8]. A portion of adhesive is deformed in front of the crack tip. The deformation of the adhesive layer containing the crack is governed by the displacement of the lower surface of the upper beam and the displacement of the upper surface of the lower beam, as illustrated in the close-up crack picture shown in Fig. 3.1.

It is, therefore, crucial to analyse the deformation of the two beams of the DCB joint to extract the displacements of the faying surfaces. In the proposed approach, it is assumed that linear elastic fracture mechanics is applicable. Therefore, the classic beam theory is employed to derive the deformations of the two beams. The origin of the x-y coordinates is set at the point where the two beams are built-in, see Fig. 3.1. The exact location is unknown, since it is highly dependent on the mechanical properties of the adhesive system, but it is not required to explain the fracture

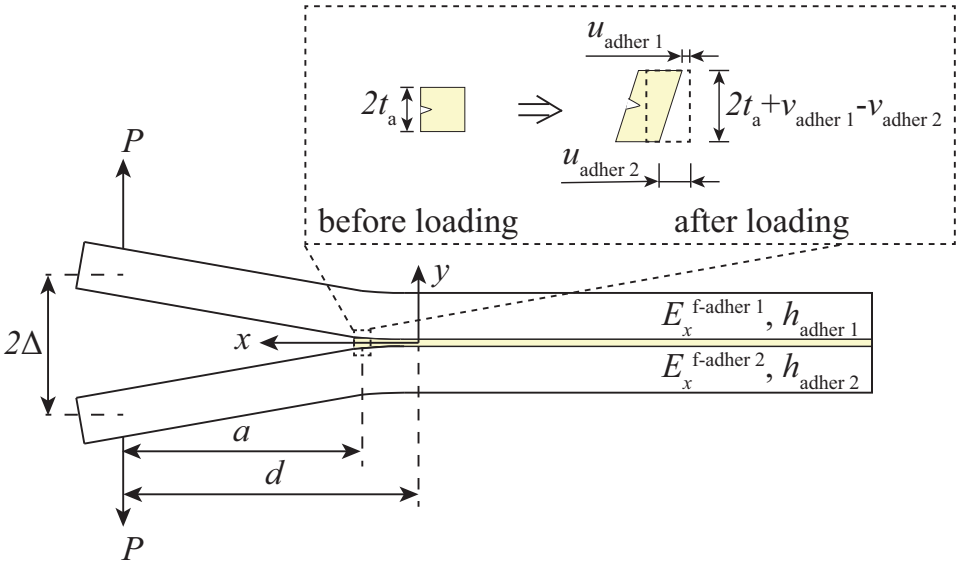

Figure 3.1: Deformation of the cracked adhesive in DCB specimen.

modes in the adhesive layer.
The longitudinal displacement in x-direction and vertical displacement in y-direction of the lower surface of the upper beam developed from the simple beam theory are given by,

$$u_{\text{adher 1}} = \frac{h_{\text{adher 1}} x P}{2E_x^{\text{f-adher 1}} I_{\text{adher 1}}}(d-x), \tag{3.1}$$

$$v_{\text{adher 1}} = \frac{P}{E_x^{\text{f-adher 1}} I_{\text{adher 1}}}\left(\frac{dx^2}{2} - \frac{x^3}{6}\right), \tag{3.2}$$

and similarly the corresponding displacements of the upper surface of the lower beam are expressed as,

$$u_{\text{adher 2}} = \frac{h_{\text{adher 2}} x P}{2E_x^{\text{f-adher 2}} I_{\text{adher 2}}}(d-x), \tag{3.3}$$

$$v_{\text{adher 2}} = -\frac{P}{E_x^{\text{f-adher 2}} I_{\text{adher 2}}}\left(\frac{dx^2}{2} - \frac{x^3}{6}\right), \tag{3.4}$$

where subscripts "adher 1" and "adher 2" refer to the upper and lower beams respectively, P is the applied load, d is the distance between the load line and y-axis, I is the second moment of the beam cross-section area of width B and thickness h_{adher} and is given by,

$$I = \frac{1}{12} B h_{\text{adher}}^3. \tag{3.5}$$

With the small deformation assumption, the normal strain, ε_{yy}, and shear strain, γ_{xy}, of the adhesive layer can be derived respectively as following,

$$\varepsilon_{yy} = \frac{v_{\text{adher 1}} - v_{\text{adher 2}}}{2t_{\text{a}}}, \tag{3.6}$$

$$\gamma_{xy} = \frac{u_{\text{adher 1}} - u_{\text{adher 2}}}{2t_{\text{a}}}, \tag{3.7}$$

where $2t_{\text{a}}$ denotes the thickness of the adhesive layer. Eq. 3.6 indicates that the adhesive layer containing a crack deforms in opening mode. While Eq. 3.7 shows that an in-plane-shear mode could occur. These strains are illustrated schematically in Fig. 3.1.

It is evident that the reaction forces from the adhesive on the beams are not considered in calculating the displacements of the faying surfaces. Consequently the above obtained strains are a first approximation of strains of the adhesive. Nevertheless, they provide the tendency of how the cracked adhesive layer could deform. The significance of accounting the reaction forces in the calculation is discussed in the next subsection.

3.2.2. Criterion to achieve pure mode I

Based on the analysis of the deformation of the cracked adhesive layer in a general bi-material DCB specimen, it was shown that the existence of shear deformation of the adhesive layer with a crack introduces in-plane shear fracture mode, i.e. mode II. In order to obtain pure mode I in such a DCB specimen, the shear strain in the cracked adhesive should be eliminated, i.e. $\gamma_{xy} = 0$. The following equation can then be obtained based on Eq. 3.7,

$$u_{\text{adher 1}} = u_{\text{adher 2}}. \tag{3.8}$$

The longitudinal strain distributions of the faying surfaces can be determined by the displacement distribution with Eq. 3.8. Eq. 3.8 can be rewritten in terms of strain, which is expressed as Eq. 3.10,

$$\varepsilon = \frac{\partial u}{\partial x}, \tag{3.9}$$

$$\varepsilon_{\text{adher 1}} = \varepsilon_{\text{adher 2}}. \tag{3.10}$$

In order to eliminate the shearing mode in the DCB specimen, the longitudinal strain distributions at the two faying surfaces should be identical. If this criterion is fulfilled, only pure mode I fracture will develop in the adhesive with the crack. If this criterion is not satisfied, the mismatch of strains of the faying surfaces will lead to mode II fracture behaviour [9].

The DCB specimen with dissimilar adherends should be designed to meet this criterion under a pair of applied loads. Substituting Eq. 3.1, Eq. 3.3 and Eq. 3.5 into Eq. 3.8, one can obtain the following equation,

$$E_x^{\text{f-adher 1}} h_{\text{adher 1}}^2 = E_x^{\text{f-adher 2}} h_{\text{adher 2}}^2. \tag{3.11}$$

If a bi-material DCB specimen is designed according to Eq. 3.11, the faying surfaces of the two beams under a pair of applied load, as illustrated in Fig. 3.1, would have identical longitudinal displacements and strain distributions. There is no tendency of loading the adhesive layer in shear mode. The adhesive layer is expected to deform only in y-direction. Consequently, the reaction forces from the adhesive layer on the beams are in y-direction only.

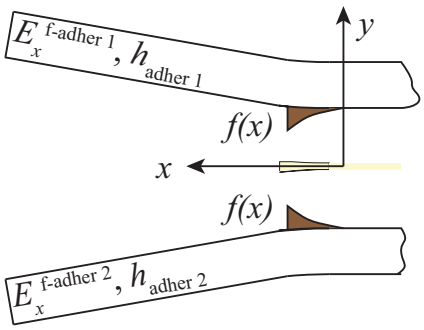

Figure 3.2: Illustration of the reaction force distributions from the adhesive layer on the beams of the DCB specimen.

Assuming that the reaction forces acting on the beam surfaces follow a similar distribution $f(x)$, as illustrated in Fig. 3.2, the moment distributions over the deformed adhesive layer region for the two beams can be given by,

$$-M_{\text{adher 1}} = M_{\text{adher 2}} = \int_0^x f(x)dx. \tag{3.12}$$

Under the reaction force distributions from the adhesive, the longitudinal displacements can be given by,

$$u_{\text{r-adher 1}} = \frac{h_{\text{adher 1}} x M_{\text{adher 1}}}{2E_x^{\text{f-adher 1}} I_{\text{adher 1}}} = -\frac{6x\int_0^x f(x)dx}{E_x^{\text{f-adher 1}} h_{\text{adher 1}}^2 B}, \tag{3.13}$$

$$u_{\text{r-adher 2}} = -\frac{h_{\text{adher 2}} x M_{\text{adher 2}}}{2E_x^{\text{f-adher 2}} I_{\text{adher 2}}} = -\frac{6x\int_0^x f(x)dx}{E_x^{\text{f-adher 2}} h_{\text{adher 2}}^2 B}. \tag{3.14}$$

Giving the fact that Eq. 3.11 is valid, these two longitudinal displacements caused by the reaction forces are identical. Based on the analysis above, no shearing could be involved. It has been proven that pure mode I in the DCB specimen with two beams of different materials could be obtained when the design criterion of Eq. 3.11 is met.

The two beams of a DCB specimen with the matched strain distributions do not necessarily deflect symmetrically under a pair of opening load. In order to have symmetric deformation of the DCB beams, the flexural stiffness of the two beams should be equal, then $E_x^{\text{f-adher 1}} h_{\text{adher 1}}^3 = E_x^{\text{f-adher 2}} h_{\text{adher 2}}^3$ is satisfied. However, this configuration involves mode II fracture behaviour [3, 4].

If DCB specimens are made of the same material, pure mode I can be obtained if the thickness of the two beams is the same, because $E_x^{\text{f-adher 1}} h_{\text{adher 1}}^2 = E_x^{\text{f-adher 2}} h_{\text{adher 2}}^2$

and $E_x^{\text{f-adher 1}} h_{\text{adher 1}}^3 = E_x^{\text{f-adher 2}} h_{\text{adher 2}}^3$ are equally met. However for bi-material DCB specimens, these two criteria cannot be met simultaneously. In this case, the strain-based criteria is the one to be chosen if one aims for pure mode I.

3.2.3. Design of composite adherend

In the preceding sub-sections, the flexural modulus of the adherend is used. For isotropic materials, such as metals, the flexural modulus is equal to the material Young's modulus. However, for composite laminates this is not the case. Here, the effective flexural modulus of composite laminates is determined using the Classic Laminate Theory (CLT).

According to the CLT, an ABD-matrix can be developed for a composite laminate [10]. The ABD-matrix can be used to calculate the midplane strains $[\varepsilon^0]$ and curvatures $[k]$ as a result of applied line loads $[N]$ and moments $[M]$ as following,

$$\begin{bmatrix} \varepsilon^0 \\ k \end{bmatrix} = \begin{bmatrix} A & B \\ B & D \end{bmatrix}^{-1} \begin{bmatrix} N \\ M \end{bmatrix} = \begin{bmatrix} A^* & B^* \\ C^* & D^* \end{bmatrix} \begin{bmatrix} N \\ M \end{bmatrix}, \tag{3.15}$$

and the laminate strains throughout thickness can be calculated as,

$$\begin{bmatrix} \varepsilon_x \\ \varepsilon_z \\ \gamma_{xz} \end{bmatrix} = \begin{bmatrix} \varepsilon_x^0 \\ \varepsilon_z^0 \\ \gamma_{xz}^0 \end{bmatrix} + y \begin{bmatrix} k_x \\ k_z \\ k_{xz} \end{bmatrix}, \tag{3.16}$$

where y is in the direction of thickness with its origin at the midplane and x and z are longitudinal and transverse axes, respectively. The strains at the faying surface of the composite adherend need to be determined. For this, $y = h_{\text{adher}}/2$ should be substituted into Eq. 3.16 to obtain the corresponding strains.

Based on Eq. 3.15, the relation between the curvature k_x and moment M_x is

$$k_x = D_{11}^* M_x, \tag{3.17}$$

where D_{11}^* is the element at the first row and first column of $[D^*]$. Therefore, the effective flexural modulus, E_x^{f}, can be derived,

$$E_x^{\text{f}} = \frac{12 M_x}{k_x h^3} = \frac{12}{h^3 D_{11}^*}. \tag{3.18}$$

The effective flexural modulus E_x^{f} is only valid for symmetric laminates. Analogous to the calculation of the longitudinal strain throughout thickness for isotropic metals, the longitudinal strain of symmetric composite laminate can then be easily determined by,

$$\varepsilon_x = \frac{M_x y}{E_x^{\text{f}} I}. \tag{3.19}$$

Based on Eq. 3.18, the proposed criterion expressed as Eq. 3.11 can be used to obtain the desirable layup of composite adherend.

For an asymmetric composite laminate, the longitudinal strain cannot be calculated directly using Eq. 3.19. This is attributed to the fact that $[\varepsilon^0] \neq [0]$. In this case, Eq. 3.16 has to be used to obtain the longitudinal strain of an asymmetric laminate, such that the longitudinal strain at the faying surface is equal to the strain at the faying surface of the opposite adherend.

3.3. Case study

A test program was carried out in order to validate the proposed approach of achieving pure mode I in DCB specimens made of dissimilar materials. The DCB specimens were made out of steel strips bonded to glass fibre reinforced polymer (GFRP) laminates. Two DCB configurations were manufactured: one batch following the strain based design criterion - $E_x^{\text{f-adher 1}} h_{\text{adher 1}}^2 = E_x^{\text{f-adher 2}} h_{\text{adher 2}}^2$, and one batch following the flexural based criterion - $E_x^{\text{f-adher 1}} h_{\text{adher 1}}^3 = E_x^{\text{f-adher 2}} h_{\text{adher 2}}^3$. Both specimens configurations were tested and numerically modelled.

Furthermore, symmetric steel-steel DCB specimens were manufactured in order to have a reference test. The fracture surfaces of the bi-material specimens were analysed and compared with the reference case.

3.3.1. Materials and preparation

Materials used

Fig. 3.3 shows the DCB test specimen geometry, which is characterised by adherends height h_{steel} and $h_{\text{composite}}$, adherends length L and width B, and an initial crack of length a_{init}.

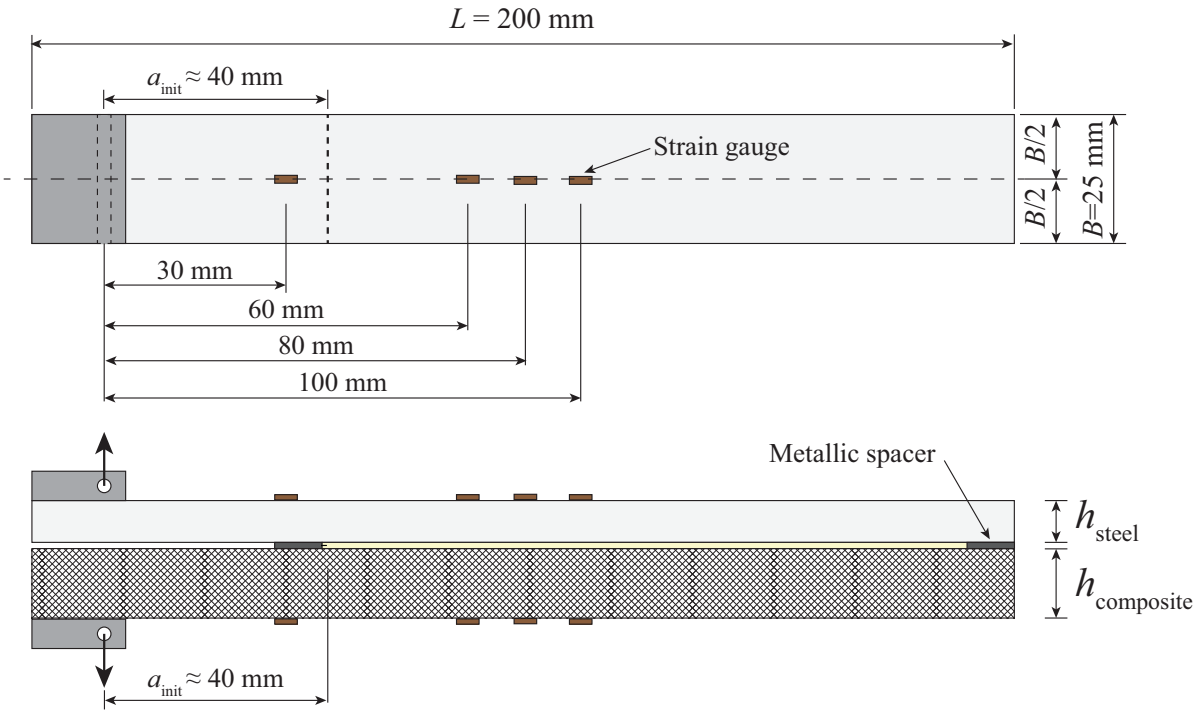

Figure 3.3: Steel-composite DCB test specimen.

The DCB specimens were manufactured by bonding steel S690 and GFRP laminates using the structural epoxy adhesive Araldite 2015 (Huntsman®). The GFRP laminates were manufactured with quadraxial E-glass (QE) fabric (nominal thickness of 0.9 mm), which consists of a stacking of four unidirectional (UD) layers of E-glass lamina with the orientations 0°/+45°/90°/-45°. A rubber modified epoxy based vinyl ester resin was used to impregnate the E-glass fabric stacking sequence. The GFRP laminate was manufactured by vacuum infusion. After a period of 24h at laboratory temperature (≈ 23°C), the laminate was post-cured at 60°C during 12h in an oven, following supplier's specifications. The mechanical properties of UD-0° lamina, steel and the epoxy adhesive are summarized in Table 3.1. The mechanical properties of the UD-0° lamina were experimentally determined and the steel properties were taken from the supplier's technical data-sheet.

Table 3.1: Materials mechanical properties.

Material	E_{xx} (MPa)	E_{zz} (MPa)	G_{xz} (MPa)	ν_{xz}
UD-0° lamina	38070	11160	3951	0.28
Steel S690	210000		-	0.3
Epoxy adhesive [11]	2000		-	0.33
Axis x: longitudinal/fibres direction; Axis z: transverse direction				

Assumption concerning symmetry of the bi-material specimen

As aforementioned, two DCB configurations were manufactured: one following the strain based design criterion and another following the flexural based design criterion. In order to provide a better comparison of the results of the two configurations, the steel adherend was kept the same for all tested configuration and the GFRP adherend was designed to meet the individual design criterion by changing the stacking sequence of the GFRP laminates.

Table 3.2 shows the lay-up and thicknesses of the two configurations. The steel thickness of 3 mm was selected to avoid yielding during quasi-static fracture testing (this was numerically verified). For this given thickness of steel, the lay-up of the GFRP corresponding to each criterion is given in Table 3.2, row number 2. Unfortunately, neither criteria can be perfectly satisfied due to the fixed stacking sequence and thickness of the quadraxial E-glass fabric and available steel plate. The final laminate thickness after curing is listed in Table 3.2, row number 3 (the final thickness is smaller than the nominal one due to the manufacturing process constraints). Finally, the theoretical thickness of the steel adherend which matches perfectly to the real laminate configuration and the corresponding criterion is also provided in Table 3.2 (theoretical thickness).

Table 3.2: GFRP laminates: lay-up stacking for each design criterion (the lay-up is defined from the bottom to the top of the laminate).

Criterion	Strain based	Flexural based
Lay-up	$[0° +45° 90° -45°]_5/[+45° 90° -45° 0°]_5$	$[0° +45° 90° -45°]_4/[+45° 90° -45° 0°]_3$
h^*_{GFRP} (mm)	8.60	6.06
h_{steel} (mm) (theoretical thickness)	3.00 (2.72)	3.00 (2.84)
E^f_x (MPa)	21014	21609
h^*_{GFRP} - final thickness of the laminate after post-cure cycle		
$E^f_x = \frac{12}{h^3_{GFRP} J_{44}}$ for non-symmetric laminate (matrix $[J]$ is equal to the inverse of ABD-matrix)		

Surface preparation and bonding

The surfaces of the steel adherends were grit blasted using aluminium oxide (Corublast Super Z-EW nr. 100). Before and after the grit blasting, the surfaces were cleaned with a clean cloth soaked with acetone. Afterwards, the steel surfaces were immersed in a potassium hydroxide solution (alkaline cleaner), which was stirred at 300 rpm and heated to 60°C. The immersion in the solution lasted 10 min. As a final step prior to bonding, the cleaned steel surfaces were immersed in a silane γ-glycidoxypropyltrimethoxysilane (γ-GPS) solution for 20 seconds in order to strengthen the adhesion of the adhesive at the interfaces. The steel adherends were then oven cured for 1 hour at 150°C. The silane solution was prepared in three steps according to Li et al. [12]. Firstly, the γ-GPS was hydrolysed in distilled water (DW)-methanol mixture. The volume ratios of γ-GPS/DW/methanol were 10/80/10, respectively. Secondly, the pH was set to 5-5.5 by adding acetic acid to keep the solution's stability. Finally, the solution was magnetically stirred for 48h at 300 rpm at room temperature.

The surfaces of the GFRP laminate were manually abraded with sandpaper (grid 180). During this process, care was taken to not affect the fibres of the laminate. Before and after the sanding, the GFRP surfaces were cleaned with a clean cloth soaked with isopropanol.

A manual applicator gun with a static-mixing nozzle was used to mix and apply the two component epoxy paste adhesive, Araldite® 2015. In order to have a correct mixture of both components, a small quantity of adhesive was first discarded. Metallic spacers of approximately 0.4 mm were used to obtain an uniform adhesive bond-line, as shown in Fig. 3.3. Two metallic strips and a sharp razor blade were used to build the spacers. These components were bonded by a fast curing adhesive. While the metallic strips designated the length of initially unbonded zone and the distance from the load application point - a_0, the razor blade placed in between the metallic strips created an additional pre-crack of length Δa at the mid thickness of the adhesive bond-line. To facilitate post-bonding removal, the spacers were covered with a release agent. After the bonding process, curing took place at 80°C for 1 hour according to manufacturer's specifications. An even bond-line thickness was obtained by making use of weights to uniformly compress the specimens. After curing the specimens, the excess of adhesive on the sides was removed by abra-

sion. The total thickness of the specimens was measured at three locations along the specimen length and the average was calculated in accordance with the ASTM D5528-13 [8].

Strains gauges were used in order to measure the longitudinal strains at the free surfaces of the specimens. A total of eight strain gauges were glued on each specimen (four on the steel adherend (type: KFG-5-120-C1-23), and the another four on the GFRP adherend (type: KFG-5-120-C1-11)). They were placed in specific locations as showed in Fig. 3.3.

Finally, prior to testing, a thin layer of white paint was applied to the side of the specimens in order to enhance visibility of the crack. Vertical lines every 1 mm were marked on the side in order to provide a length scale for the crack length measurements.

Symmetric steel-steel DCB specimens were also manufactured in order to obtain the fracture morphology of the adhesive under pure mode I loading. The bonding process described previously was followed.

3.3.2. Test set-up

Mechanical tests on DCB specimens were conducted based on ASTM standard test method D5528-13 [8]. The quasi-static tests were performed on a 20 kN (load-cell precision of 0.5%) Zwick tensile test machine under displacement control, with a fixed displacement rate of 1 mm/min (the displacement was measured by the testing machine itself and by two extensometers placed closer to the grips). The tests were carried out to failure at laboratory conditions (temperature of 23°C and relative humidity of 55%). The crack length was measured by means of a camera placed at the side of the specimen. Pictures were taken every second after the load application.

The crack length was defined as the straight and horizontal line distance between the load line and the crack tip, where the load line is assumed to be coincident with the centreline of the pins of the grips. The displacement used in all calculations is the grip-to-grip displacement measured by the extensometers. It is assumed that any displacement occurring in the loading blocks is negligible compared to the deformation of the arms of the specimens.

Fig. 3.4 shows an overview of the experimental test set-up and a close-up view of the specimen under loading. It is possible to observe the extensometers, the loading blocks and the crack length at that moment of the test.

3.4. Finite element modelling (FEM)

3D models were built in Abaqus® to model the fracture behaviour of the tested DCB joints. The virtual crack closure technique (VCCT) was used for calculation of the fracture parameters at the crack tip. The concept behind VCCT is based on the following - see Fig. 3.5: the strain energy released when the crack grows by the length of one element (Δa_{ele}) is assumed to be equal to the energy required to close the crack by the same length. This energy is found by considering the work done by the forces at the crack tip node (node i, F_i) when displaced over a distance

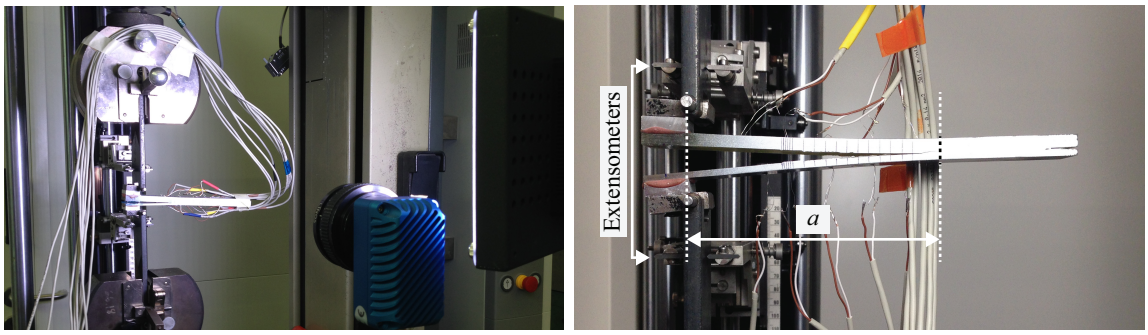

(a) Overview. (b) Close-up view of the experiment.

Figure 3.4: Test set-up.

equal to the displacement of the nodes directly behind the crack tip (nodes j and k, U_j and U_k)[13, 14].

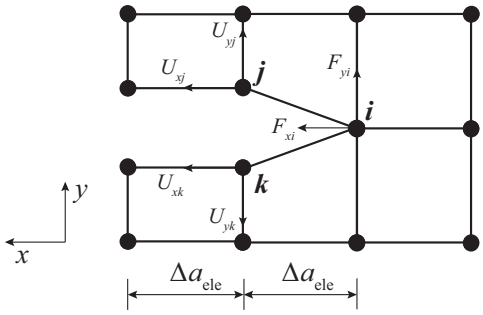

Figure 3.5: Nodes at the crack tip for VCCT in 2D FEM [14].

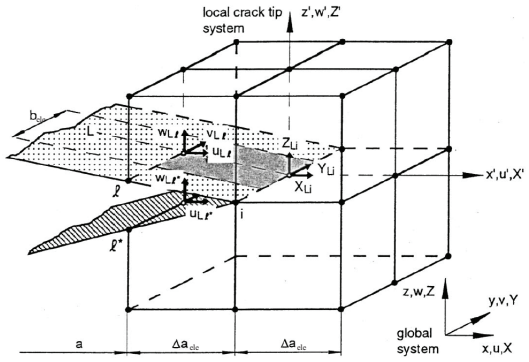

Figure 3.6: VCCT for 8-noded solid elements (lower surface forces are not represented for visual clarity) [15].

For a model with 8-noded 3D solid elements as shown in Fig. 3.6, the fracture components G_{I}, G_{II} and G_{III} are calculated as,

$$G_{\mathrm{I}} = \frac{1}{2\Delta a_{\mathrm{ele}}.B_{\mathrm{ele}}}[Z_{Li}(w_{Ll} - w_{Ll^*})], \tag{3.20}$$

$$G_{\mathrm{II}} = \frac{1}{2\Delta a_{\mathrm{ele}}.B_{\mathrm{ele}}}[X_{Li}(u_{Ll} - u_{Ll^*})], \tag{3.21}$$

$$G_{\mathrm{III}} = \frac{1}{2\Delta a_{\mathrm{ele}}.B_{\mathrm{ele}}}[Y_{Li}(v_{Ll} - v_{Ll^*})], \tag{3.22}$$

where X_{Li}, Y_{Li} and Z_{Li} are the nodal forces at the node Li at the crack tip, and u_{Ll}, v_{Ll}, w_{Ll},u^*_{Ll}, v^*_{Ll}, w^*_{Ll} are the displacements of the top face and lower face adjacent nodes Ll and Ll^*, respectively. Δa_{ele} is the increment of the crack which is equal to the element size at the crack tip and B_{ele} is the width of the elements [14–16].

VCCT is implemented as a crack propagation tool in Abaqus® which means that propagation only occurs when a certain criterion, e.g. Benzeggagh-Kenane law, exceeds a certain value, e.g. 1.0. In this study the FE model is used to obtain the fracture components at the crack tip line. Fracture energies values are given along the width of the specimen at the crack tip location for the three modes: mode I, II and III. The crack propagation prediction is not part of this study, since the aim is to evaluate the crack loading mode and not predict the damage progression. Hence, very high values were entered for the critical fracture components. This assured that the crack growth criterion would not reach the value of 1.0. A similar approach was used by Zarouchas and Alderliesten [17] where VCCT was employed to study how the size and the position of a defect alters the mode-mix ratio when an adhesively bonded stiffened panel is subjected to compression loading.

Fig. 3.7(a) shows a representation of the boundary conditions applied in the model. In order to simulate the real constraints during a DCB test, the following boundary conditions and loading were applied: the right end of the upper edge of the bottom adherend was constrained from all displacements. Rotations were not constrained. A load was applied on the right end of the upper edge of the top adherend, equal to the load taken from the experimental tests at specific crack length points ($\mathrm{Load}_i = f(a_i)$).

The specimens were modelled using 8 node linear brick elements (C3D8). In a 3D model, the Abaqus® integrated VCCT capability is only compatible with linear elements. The adhesive layer thickness was not explicitly modelled due to its negligible contribution to the overall specimen's stiffness in comparison with the adherends. All materials were modelled as linear elastic, using the materials properties given in Table 3.1.

The number of elements in thickness direction of the GFRP adherends was defined by one element per quadraxial fabric. Taking into account each lay-up of the GFRP laminates, the following was defined: 10 elements for the strain based approach, and 7 elements for the flexural based approach. For the steel adherends, 8 elements were used in thickness direction for both criteria. The element size in width and length directions was set to $0.001B$ (B is the specimen width). A mesh convergence study was performed to guarantee mesh in-dependency of the numerical results. A 3D-mesh overview is shown in Fig. 3.7(b).

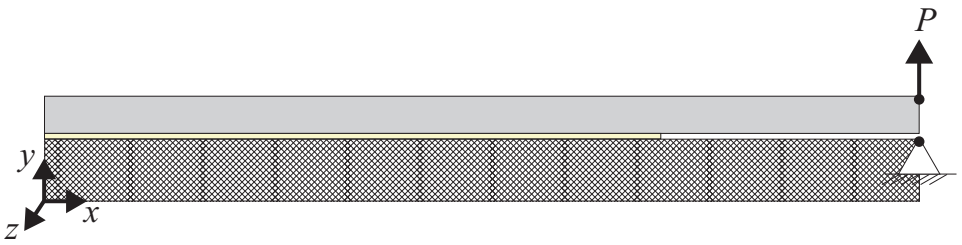

(a) Schematic representation of the boundary conditions (the adhesive layer thickness is presented just for illustration purposes).

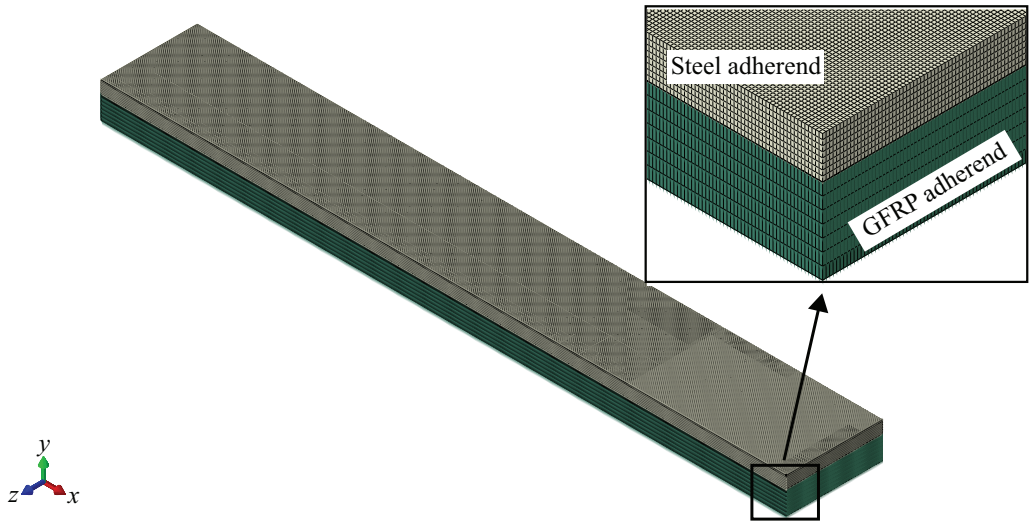

(b) Typical mesh of the numerical model, including a zoom of the specimen thickness.

Figure 3.7: DCB finite element model: boundary conditions and mesh overview.

3.5. Results and discussion

3.5.1. Experimental results and FEM validation

Fig. 3.8 shows the load-displacement curves of the flexural based and strain based criteria obtained during experiments. The linear part of these curves is compared with the linear elastic stiffness obtained from the numerical models. The FE model followed a similar stiffness as in the experiments.

There is an acceptable scatter in the experimental load-displacement curves for both configurations. One can also see that the maximum load of the strain based specimens is higher than that of the flexural based specimens. This difference was expected since the flexural stiffness of the composite adherend in the strain based criterion is higher than that in the flexural based criterion.

In order to further validate the FE model, the longitudinal strain values recorded by the strain gauges during experiments were compared to the correspondent numerical values obtained from the models. The results are presented in Figs. 3.9 and 3.10 for flexural and strain based specimens, respectively. Three loading cases and correspondent crack lengths were considered for each criterion. These are represented in Fig. 3.8 by the points $P_{i=1\text{-}6}$. The x-position is defined from the

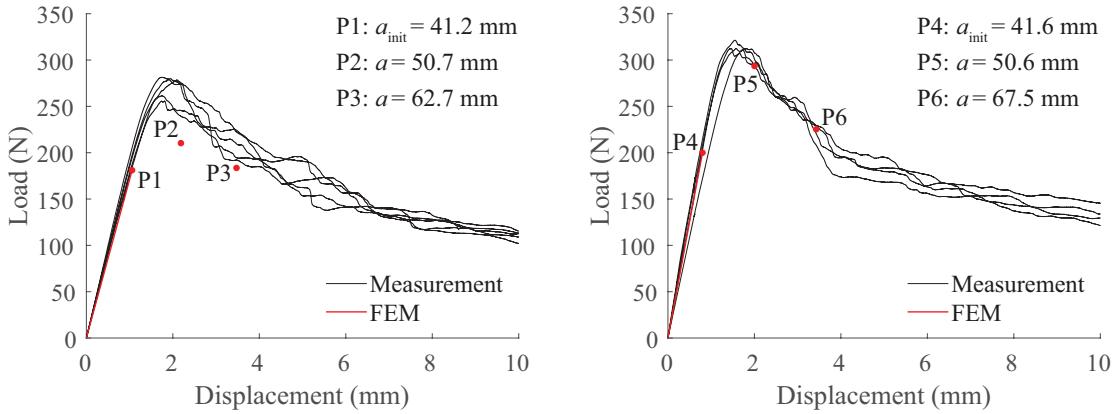

(a) Flexural based configuration.

(b) Strain based configuration.

Figure 3.8: FEM validation by using the initial linear part of the load-displacement experimental curves for both configurations.

load application point, as shown in the insert of Fig. 3.9(a). It can be observed that there is a good matching between the numerical and experimental longitudinal strain results.

Looking into more detail to the results presented in Figs. 3.9 and 3.10, one can observe two special features. Firstly, the longitudinal strains of both adherends did not become zero right in front of the crack tip. This shows that the two adherends were not perfectly cantilevered at the crack tip. The strains become zero about 10 mm ahead of the crack tip. Most likely the adhesive has deformed in this region. The second feature is related with the differences in the strain distributions of the two criteria. For the flexural based specimens (Fig. 3.9), a great discrepancy in the strain distributions between the two adherends can be observed. Moreover, it is also shown that there was still some discrepancy in front of the crack tip, giving the indication that the adhesive in that region was loaded under shear mode. As expected, the strain distributions were quite similar on both adherends for the proposed criterion (of matching the longitudinal strains at the bonded surfaces) - see Fig. 3.10. The slight difference still observed is attributed to the thickness manufacturing constraints inherent to both adherends.

This discussion is further supported with the fractography results of the two tested bi-material configurations, which are described in the next subsection.

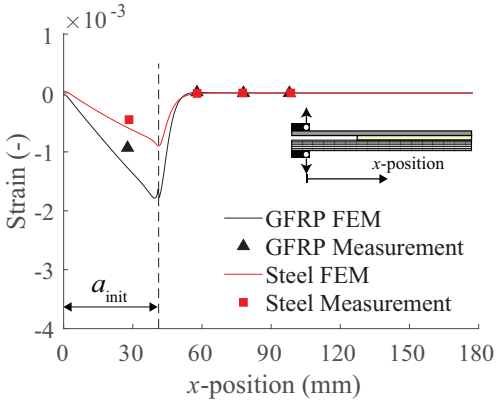

(a) **Point 1**: P = 181.09 N, a_{init} = 41.2 mm.

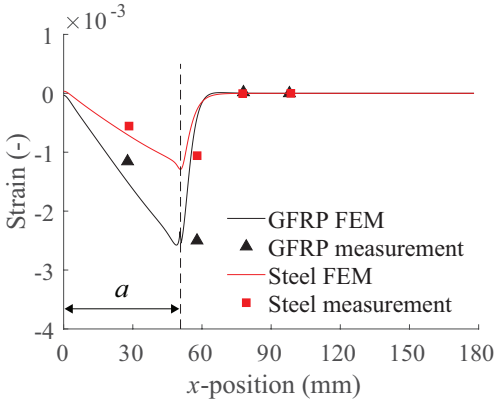

(b) **Point 2**: P = 210.32 N, a = 50.7 mm.

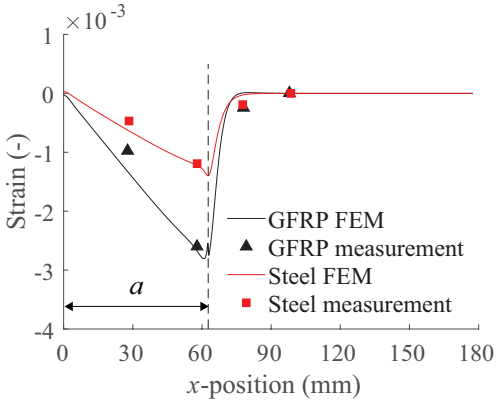

(c) **Point 3**: P = 183.59 N, a = 62.7 mm.

Figure 3.9: Flexural based criterion: longitudinal strains as a function of the x-position for 3 different loading cases, numerical vs. experimental results.

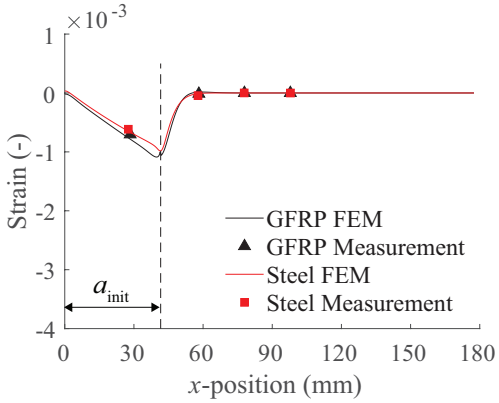

(a) **Point 4**: P = 200 N, a_{init} = 41.6 mm.

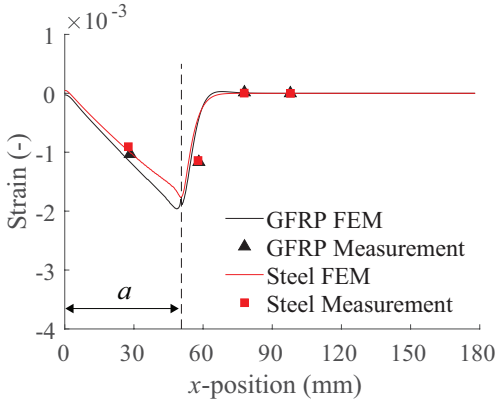

(b) **Point 5**: P = 293.48 N, a = 50.6 mm.

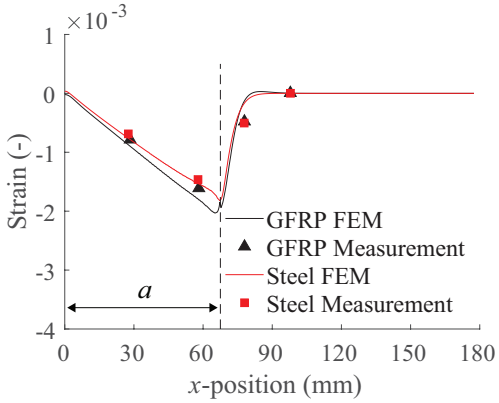

(c) **Point 6**: P = 225.26 N, a = 67.5 mm.

Figure 3.10: Strain based criterion: longitudinal strains as a function of the x-position for 3 different loading cases, numerical vs. experimental results.

3.5.2. Analysis of the fracture surfaces

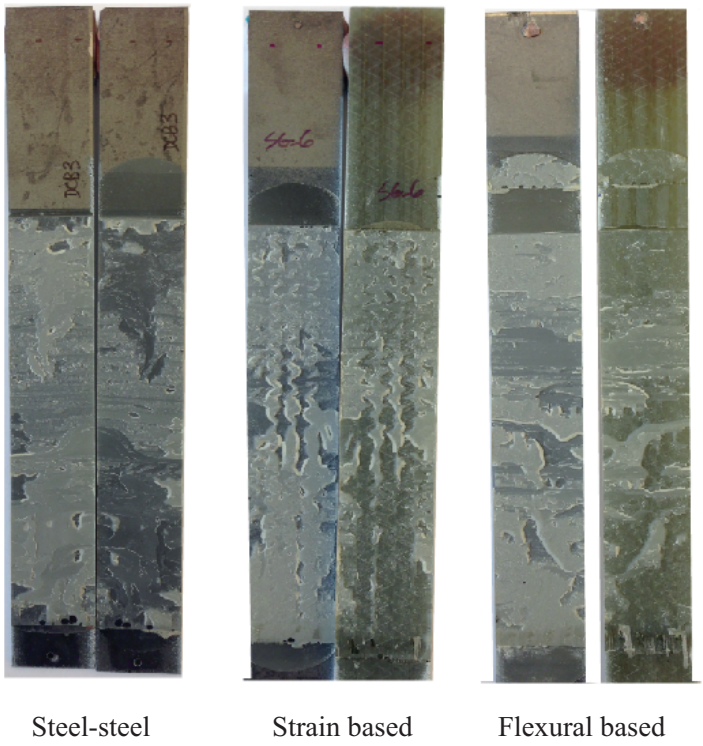

Figure 3.11: Representative macroscopic view of the fracture surfaces.

After testing, no delamination has been observed in the composite laminate. The fracture surfaces of all three tested configurations were analysed. A macroscopic view of the representative fracture surfaces is provided in Fig. 3.11. As it can be seen, adhesive residues are clearly present on the pairs of adherends of all tested configurations, proving that all the specimens experienced cohesive failure during testing.

The fracture surfaces were also characterized at a microscopic level using JEOL JSM-7500F field emission scanning electron microscope (SEM) (JEOL, Tokyo, Japan). This fractographic analysis was conducted to determine the failure modes in the tested DCB specimens. Prior to the SEM characterization, the fracture surface was visually observed and areas of interest were selected using optical microscopy. These areas were dissected from the adherends and inspected with SEM. Fig. 3.12 shows typical SEM microscopic fracture surfaces of all tested configurations (5.0 kV acceleration voltage, low angle secondary electron detector – LEI): steel-steel, steel-composite strain based and steel-composite flexural based.

The failure took place in the bulky adhesive layer containing toughening particles, making interpretation of the fracture morphology more challenging [18]. The fracture morphology of such an adhesive system under pure mode I loading is extracted from the steel-steel DCB specimen, as shown in Fig. 3.12(a). This fracture surface is provided as a reference for pure mode I morphology features. The toughening particles were pulled apart directly from the resin without smearing it. Clear impressions of the toughening particles can be observed at the fracture surface shown

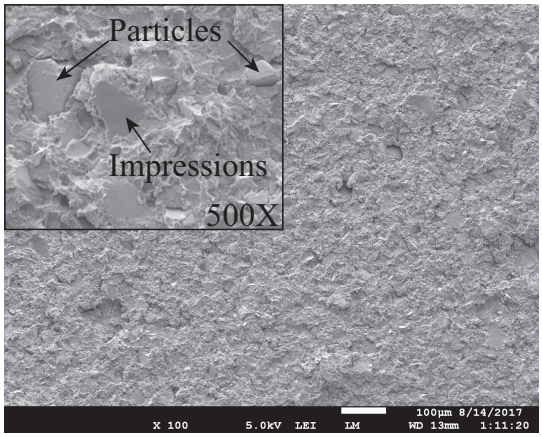

(a) Fracture surface of steel-steel specimen.

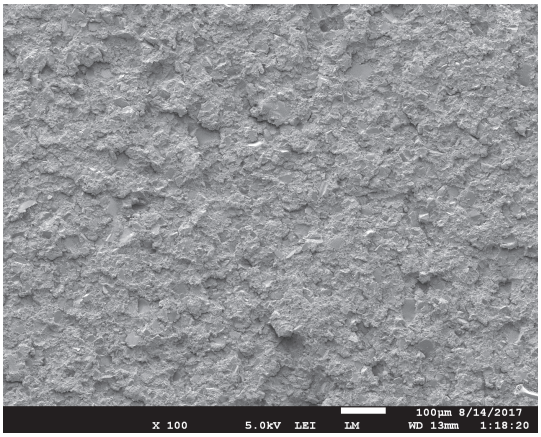

(b) Fracture surface of strain based specimen.

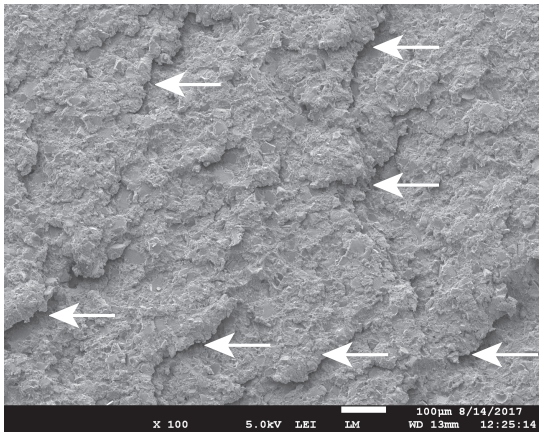

(c) Fracture surface of flexural based specimen.

Figure 3.12: Fractography analysis. All pictures were taken at the magnification of 100x.

in Fig. 3.12(a). These observations are clear evidences of the occurrence of pure mode I fracture [18].

Fig. 3.12(b) shows the typical fracture morphology of the strain based specimens and Fig. 3.12(c) shows the typical fracture morphology of the flexural based specimens. As can be seen, the fracture surface of the strain based specimen, shown in Fig. 3.12(b), is quite similar to that of the steel-steel specimen, whereas the fracture morphology of the flexural based specimen exhibits distinctly different features. Tilted cracks into the fracture surface indicated with white arrows in Fig. 3.12(c) can be observed. The occurrence of such tilted cracks indicates that mixed-mode failure took place in the flexural based specimens. The peeling stress and shear stress result in a principle tensile stress inclined at a certain angle to the global fracture surface, leading to tilted crack growth into the adhesive. The occurrence of shear stress can be explained with the difference in the strain distributions of the two adherends of flexural based specimens. Such features are hardly observed in Fig. 3.12(b), demonstrating the absence of mode II fracture in the strain based

specimen.
The fractography analysis shows that the failure modes in the strain based specimen comprise mode I while in the flexural based specimen comprise mode I and mode II. This analysis of the failure modes in the two configurations reaches the same conclusion discussed in sub-section 3.5.1.

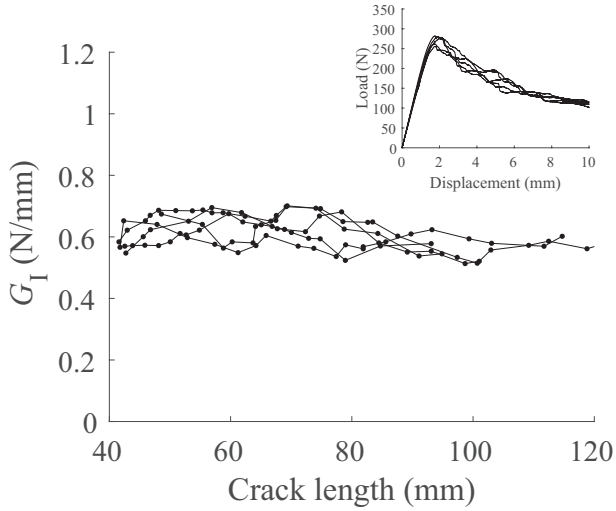

Figure 3.13: *Resistance*-curve of the flexural based specimens.

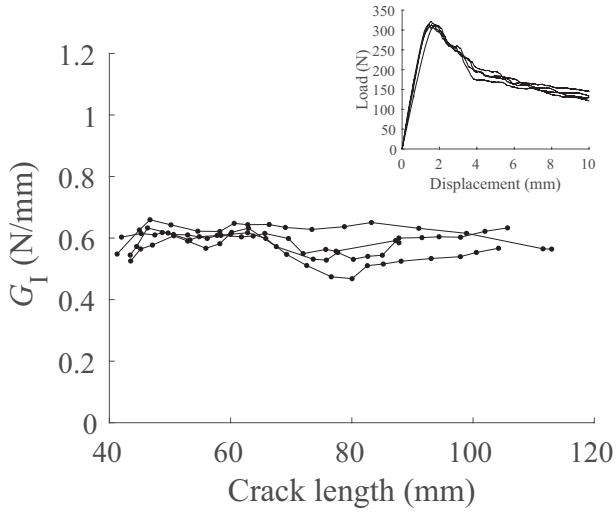

Figure 3.14: *Resistance*-curve of the strain based specimens.

3.5.3. Critical fracture energy results

The mode I strain energy release rate of each tested DCB configuration was determined with the modified beam theory (MBT), according to ASTM D5528-13 [8], and is given by,

$$G_{\mathrm{I}} = \frac{3P2\Delta}{2B(a + |a_{\mathrm{corr}}|)}, \tag{3.23}$$

where $|a_{corr}|$ is an experimentally determined crack length. According to the MBT, $|a_{corr}|$ denotes a portion of crack length which should be included into the actual crack length a when performing the calculation of G_I [8]. Experimentally determined, $|a_{corr}|$ is around 10 mm (at least 15 points were used to calculate $|a_{corr}|$ with an average R^2 of 0.9985 $\pm$ 0.0007).

For all the specimens, a *Resistance*-curve, also called *R*-curve, was obtained. This curve presents G_I as a function of the crack length. The experimental *R*-curves are presented in Figs. 3.13 and 3.14 for the flexural based criterion and for the strain based criterion, respectively. The critical fracture energy was taken from the plateau on the *R*-curve. This plateau correspond to a stable crack propagation. As can be seen from Figs. 3.13 and 3.14, the critical fracture energy for each configuration is around 0.6 N/mm. Due to the experimental scatter, it is hard to conclude that there is a well-marked difference in the values of critical fracture energy between the two configurations. However, it is understood so far that the flexural based specimens experienced mixed-mode fracture, and hence its critical fracture energy parameters should not be carelessly calculated using Eq. 3.23.

Fig. 3.15 and 3.16 present the numerically calculated fracture components for both criteria, flexural based and strain based respectively. For both configurations, mode I is dominant. On the other hand, mode II component is less pronounced and closer to 0 in the strain based specimens when compared to the flexural based specimens. The numerical results show that the strain based criterion can provide better pure mode I in bi-material DCB specimens.

Due to the material limitation, it was unachievable to satisfy either criterion using the tested GFRP lay-up and steel. However, each criterion can be exactly met with the theoretical thickness of steel adherend provided in Table 3.2. A numerical analysis was performed in order to examine the discrepancy in the G_{II}/G_I ratios for both criteria when considering the experimental adherends' thicknesses (i.e. h_{GFRP} and h_{steel}) and the theoretical ones (i.e. h_{GFRP} and theoretical h_{steel}). A load of 200 N was applied and a crack of 41.6 mm was considered in both criteria. The results are presented in Fig. 3.17. One could see that by using the theoretical thicknesses, there is a reduction of mode II component. The G_{II}/G_I ratio decreased from 6.1% to 3.5% for the strain based criterion when considering the real and theoretical thicknesses, respectively. For the flexural based case, these ratios are, as expected, higher (G_{II}/G_I of 22.3% for the real thicknesses and G_{II}/G_I of 18.6% for the theoretical ones). It is evident that the G_{II}/G_I ratio is dramatically reduced, by a rough factor of 5, when the strain based criterion is followed to design the GFRP-steel joint.

3.6. Applications and limitations of the strain based criterion

From the experimental and numerical results, one could see that, for the bi-material adhesive joint studied, the mode II component is significantly suppressed by applying the strain based criterion. In order to further investigate the applicability of this criterion to other bi-material joints, the authors have performed

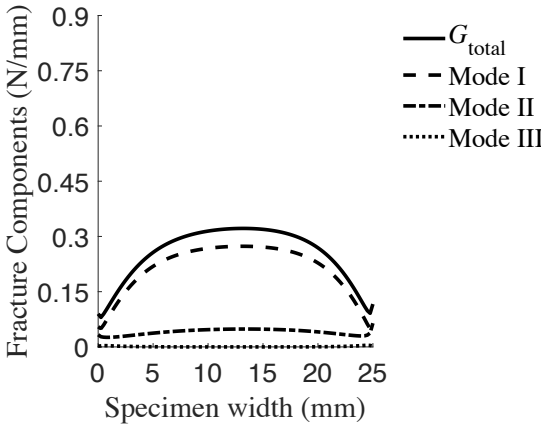

(a) **Point 1**: P = 181.09 N, a_{init} = 41.2 mm.

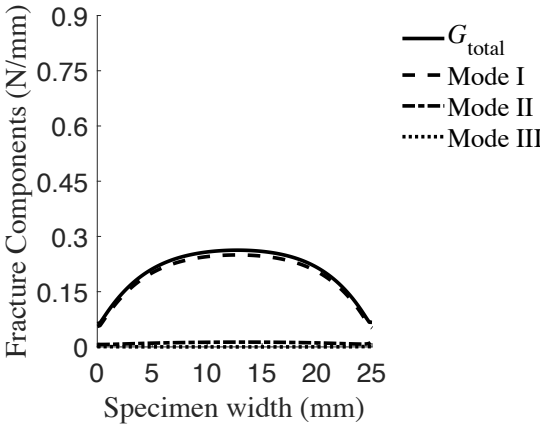

(a) **Point 4**: P = 200 N, a_{init} = 41.6 mm.

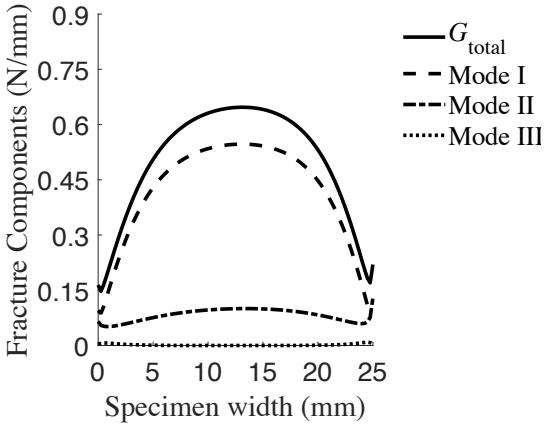

(b) **Point 2**: P = 210.32 N, a = 50.7 mm.

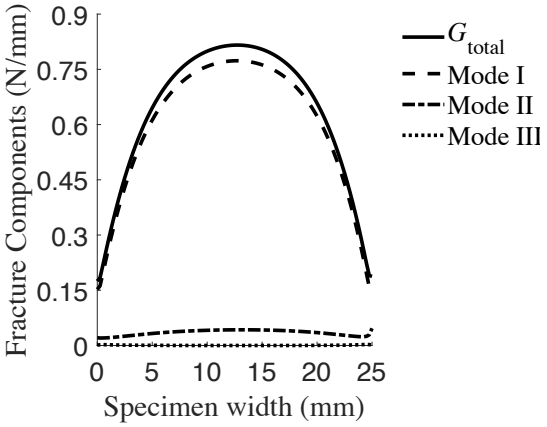

(b) **Point 5**: P = 293.48 N, a = 50.6 mm.

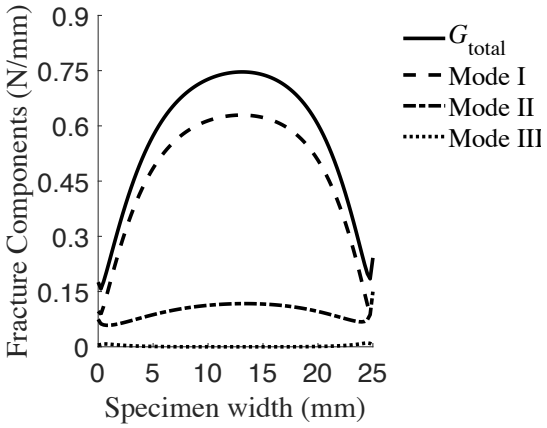

(c) **Point 3**: P = 183.59 N, a = 62.7 mm.

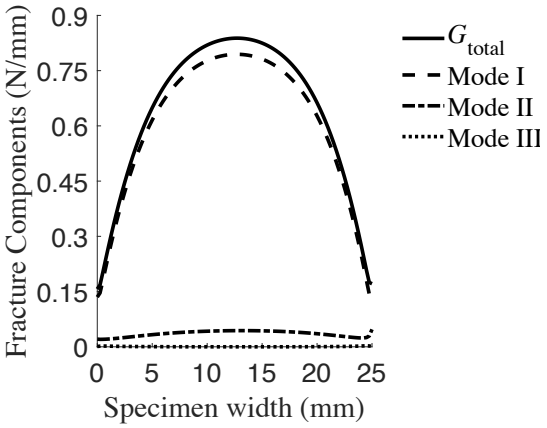

(c) **Point 6**: P = 225.26 N, a = 67.5 mm.

Figure 3.15: Flexural based criterion: fracture components as a function of the specimen width for 3 different loading cases.

Figure 3.16: Strain based criterion: fracture components as a function of the specimen width for 3 different loading cases.

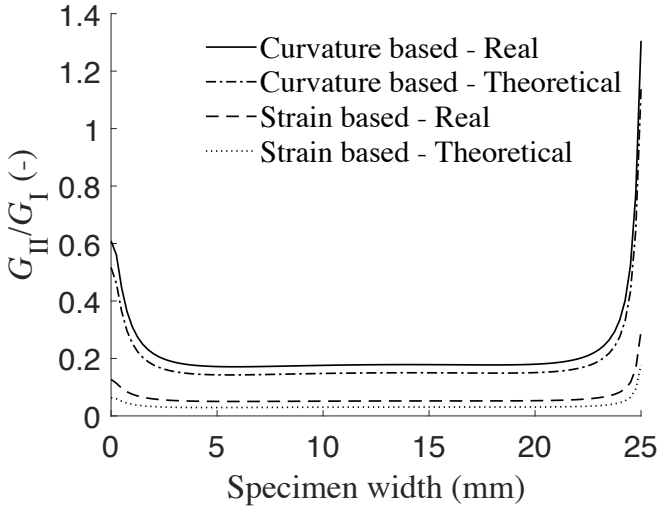

Figure 3.17: Comparison of the G_{II}/G_I ratio for both criteria considering the real and theoretical thicknesses of the adherends.

a numerical study to verify the influence of the adherend material on the G_{II}/G_I ratio.

The studied cases are summarized in Table 3.3. All cases have the same steel adherend (adherend 1). The other adherend (adherend 2) varies from isotropic metal to anisotropic composite materials. All joints are designed following the strain based criterion. The primary mechanical parameters are summarized in Table 3.3. The G_{II}/G_I ratios of the studied cases are presented in Fig. 3.18. It is noted that the G_{II}/G_I ratio is dependent on the material of the adherend 2. Compared to the asymmetric composite adherend, the symmetric unidirectional composite adherend provides lower G_{II}/G_I ratio in the bi-material joint. This might be attributed to the elimination of the in-plane shear deformation. It is also observed that the G_{II}/G_I ratio is lower for joints where the difference in the flexural stiffness of the two adherends is smaller, as for example for the steel-aluminium in comparison with steel-uni 0° GFRP. For the steel-aluminium joint, the G_{II}/G_I ratio is almost zero. This also shows that the criterion is not only for composite-metal, but also metal-metal bi-material adhesive joints.

Table 3.3: Applicability of the strain based criterion: joint types, materials, thicknesses and properties considered in the numerical models.

	Joint type	Benchmark	Asymmetric (iso.-iso.)	Asymmetric (iso.-sym. composite)	Asymmetric (iso.-asym. composite)
	Materials	Steel-steel	Steel-aluminium	Steel-uni 0° GFRP	Steel-QE GFRP
Adherend 1	Thickness	2.72046	2.72046	2.72046	2.72046
	Properties	$E = 210$ GPa $\nu = 0.3$	$E = 210$ GPa $\nu = 0.3$	$E = 210$ GPa $\nu = 0.3$	$E = 210$ GPa $\nu = 0.3$
Adherend 2	Thickness	2.72046	4.63323	6.38942	8.60000
	Properties	$E = 210$ GPa $\nu = 0.30$	$E = 74.2$ GPa $\nu = 0.33$	$E_x^f = 38.07$ GPa $\nu_{12} = 0.28$	$E_x^f = 21.014$ GPa $\nu_{12} = 0.28$
	Iso. = Isotropic; Sym. = Symmetric; Asym. = Asymmetric				

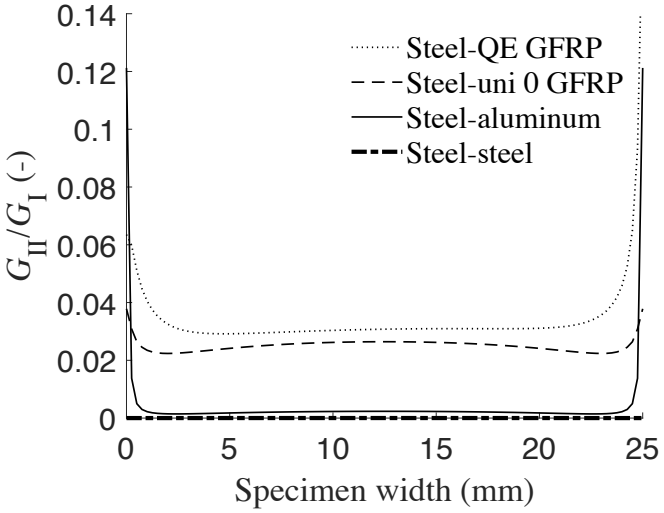

Figure 3.18: G_{II}/G_I ratio of different bi-material adhesive joints.

The authors are aware of certain limitations of the proposed strain based design criterion. First of all, the criterion does not account for the residual stresses in the adhesive interlayer due to the thermal coefficients mismatch of bonded bi-material adherends where the adhesive needs to be cured at higher temperature. The residual stresses may introduce certain mode-mixity. Another limitation is with regards to the in-plane shear deformation induced by the asymmetric lay-up of a composite adherend. It is suggested to use symmetric composite lay-up for testing bi-material joints. One more limitation is that non-zero G_{II} is obtained in spite of the fact that the G_{II}/G_I ratio is almost zero. This might be attributed to the inherent limitations of the simple beam theory employed in the derivation of the proposed criterion.

Nevertheless, the proposed strain based criterion is very concise, simple and physically sound when designing bi-material adhesive joints for mode I fracture testing. It is envisioned to be applicable for composite-composite, composite-metal and metal-metal bi-material joints.

3.7. Conclusions

A new design method to achieve mode I fracture is proposed and analysed for DCB adhesive joints with two dissimilar adherends. It is identified that matching the longitudinal strain distributions of the two dissimilar adherends at the bond-line eliminates mode II, and thus it provides pure mode I in the specimen.

The case study presented in this chapter comprises two DCB configurations. In one of the configurations, the dissimilar adherends are designed to possess identical longitudinal strain distributions at the surfaces bonded with adhesive. The other configuration has two dissimilar adherends of the same flexural stiffness. VCCT technique is applied to model the fracture behaviour of the two DCB configurations, which is validated with experimental data. Both the experimental and modelling results show that approximately pure mode I is achieved by matching the longitudinal

strain distributions. By contrast, the DCB configuration with matched flexural stiffness presents mode II fracture mode. The $G_{\mathrm{II}}/G_{\mathrm{I}}$ ratio is reduced by a factor of 5 when using the proposed longitudinal strain based criterion in comparison with the flexural stiffness based criterion.

The DCB configuration with identical flexural stiffness of the two adherends provides false critical mode I fracture energy values, as involved mode II fracture is overlooked in calculating the critical fracture energy according to the ASTM D5528-13 standard. The critical mode I fracture energy obtained can be, therefore, misleading. Matching the longitudinal strain distribution in the DCB specimen with dissimilar adherends is a general and more accurate approach to achieve pure mode I.

To minimize the mode II component in bi-material adhesive joints where composite adherend is used, it is suggested to apply symmetric lay-up and minimize the difference in the flexural stiffness of the two adherends.

3.8. Data availability

The data required to reproduce these findings are available at:
https://doi.org/10.4121/UUID:32C09DA7-3FD5-48E7-8711-82B1740B7A62

References

[1] W. Wang, R. Lopes Fernandes, S. Teixeira de Freitas, D. Zarouchas, and R. Benedictus, *How pure mode I can be obtained in bi-material bonded DCB joints: a longitudinal strain-based criterion,* Composites Part B: Engineering **153**, 137 (2018).

[2] Z. Jiang, S. Wan, and Z. Wu, *Calculation of energy release rate for adhesive composite/metal joints under mode-I loading considering effect of the non-uniformity,* Composites Part B: Engineering **95**, 374 (2016).

[3] M. Khoshravan and F. Asgari Mehrabadi, *Fracture analysis in adhesive composite material/aluminum joints under mode-I loading; experimental and numerical approaches,* International Journal of Adhesion and Adhesives **39**, 8 (2012).

[4] R. G. Boeman, D. Erdman, L. Klett, and R. Lomax, *A practical test method for mode I fracture toughness of adhesive joints with dissimilar substrates,* in *SAMPE-ACCE-DOE Advanced Composites Conference* (1999) pp. 358–366.

[5] X. J. Gong, F. Hernandez, and G. Verchery, *Fracture toughness of adhesive bonded composite joints under mixed mode loading,* in *12th International Conference on Composites (ICCM12 Conference)* (1999).

[6] Z. Ouyang, G. Ji, and G. Li, *On approximately realizing and characterizing pure mode-I interface fracture between bonded dissimilar materials,* Journal of Applied Mechanics **78**, 031020 (2011).

[7] G. Zambelis, T. D. S. Botelho, O. Klinkova, I. Tawfiq, and C. Lanouette, *Evaluation of the energy release rate in mode I of asymmetrical bonded composite/metal assembly,* Engineering Fracture Mechanics **190**, 175 (2018).

[8] *ASTM D 5528 - Standard test method for mode I interlaminar fracture toughness of unidirectional fiber-reinforced polymer matrix composites,* (2013).

[9] J. G. Williams, *On the calculation of energy release rates for cracked laminates,* International Journal of Fracture **36**, 101 (1988).

[10] A. K. Kaw, *Mechanics of composite materials*, 2nd ed. (CRC Press, 2006).

[11] R. D. S. G. Campilho, A. M. G. Pinto, M. D. Banea, R. F. Silva, and L. F. M. da Silva, *Strength improvement of adhesively-bonded joints using a reverse-bent geometry,* Journal of Adhesion Science and Technology **25**, 2351 (2011).

[12] G. Li, X. Wang, A. Li, W. Wang, and L. Zheng, *Fabrication and adhesive properties of thin organosilane films coated on low carbon steel substrates,* Surface and Coatings Technology **201**, 9571 (2007).

[13] J. A. Pascoe, *Delamination of bonded repairs*, Master thesis, Delft University of Technology (2012).

[14] Y. Zhang, A. P. Vassilopoulos, and T. Keller, *Mode I and II fracture behavior of adhesively-bonded pultruded composite joints,* Engineering Fracture Mechanics **77**, 128 (2010).

[15] R. Krueger, *Virtual crack closure technique: history, approach, and applications,* Applied Mechanics Reviews **57**, 109 (2004).

[16] S. Moslem, P. V. Anastasios, and K. Thomas, *Modelling effects of asymmetry and fiber bridging on mode I fracture behavior of bonded pultruded composite joints,* Engineering Fracture Mechanics **99**, 335 (2013).

[17] D. Zarouchas and R. Alderliesten, *The effect of disbonds on stability aspects of adhesively bonded aluminum panels during compression loading,* Thin-Walled Structures **96**, 372 (2015).

[18] E. S. Greenhalgh, *Chapter 4 - Delamination-dominated failures in polymer composites,* in *Failure Analysis and Fractography of Polymer Composites* (Woodhead Publishing, 2009) pp. 164–237.

4

From thin to “extra-thick” adhesive bond-lines

The bond-line thickness plays a role on the fracture behaviour of adhesive joints as it is explained in Chapter 2. The effect of the adhesive bond-line thickness, varying from 0.4 to 10.1 mm, on the mode I fracture behaviour of steel-steel joints bonded with a structural epoxy adhesive is investigated in this chapter. An experimental test campaign of double-cantilever beam (DCB) specimens was carried out in laboratory conditions. Five bond-line thicknesses were studied: 0.4, 1.1, 2.6, 4.1 and 10.1 mm. The critical mode I SERR, G_{Ic}, presented similar values for the specimens with adhesive bond-line thicknesses of 0.4, 1.1 and 2.6 mm (G_{Ic} = 0.71, 0.61, 0.63 N/mm, respectively). However, it increased by approximately 63% for 4.1 mm (G_{Ic} = 1.16 N/mm) and decreased by about 10% (in comparison with 4.1 mm) for the 10.1 mm (G_{Ic} = 1.04 N/mm). The trend of the G_{Ic} in relation to the bond-line thickness is explained by the combination of three factors: the crack path location, the failure surfaces features and the stress field ahead of the crack tip.

Parts of this chapter have been published in Engineering Fractures Mechanics **218**, 106607 (2019) [1].

4.1. Introduction

Research on the effect of the adhesive bond-line thickness on mode I fracture behaviour has mainly focused either on joints bonded with structural epoxy adhesives with bond-line thicknesses normally ranging between 0.1 and 2 mm - mostly applied to aerospace and automotive applications [2–14], or on joints with flexible adhesives often with thicker bond-lines [5, 15–17]. However, limited studies were found on joints with “extra-thick” bond-lines (10 mm) of epoxy adhesives, relevant for civil and shipbuilding applications. The research done in the past has proved that there is a dependence of the critical fracture energy of adhesive joints on bonding thickness, regardless of the nature of the adhesives. However, there is no single trend for this dependency.

The study presented herein focuses on the adhesive bond-line thickness effect on mode I fracture behaviour of steel-steel joints bonded with a structural epoxy adhesive by using the double-cantilever beam (DCB) test. The range of adhesive bond-line thickness considered was 0.4 mm to 10 mm. Standard (i.e. the simple beam theory (SBT), the compliance calibration method (CCM)) and non-standard (i.e. the Penado-Kanninen (P-K) model) reduction methods were applied to the experimental load-displacement curves to evaluate the mode I strain energy release rate (SERR). The stress field ahead of the crack tip was assessed for the range of adhesive bond-line thicknesses studied. The mode I SERR-adhesive bond-line thickness relation was explained by the crack path location and the features found on the failure surfaces in conjunction with the stress field ahead of the crack tip.

4.2. Experimental

4.2.1. Materials and preparation

Materials used

The DCB specimens (see Fig. 4.1) were made of S690 steel adherends, with a thickness of 3.0 mm, bonded with a structural two-component epoxy paste adhesive, Araldite 2015 (Huntsman®). Five adhesive bond-line thicknesses were studied: 0.4, 1.1, 2.6, 4.1 and 10.1 mm.

The mechanical properties of the steel S690 and the epoxy adhesive are given in Table 4.1. The steel properties were taken from the supplier's technical datasheet, while the adhesive's mechanical properties were experimentally measured from tensile dog bone specimens with a thickness of 2 mm in accordance with ISO 527 [18]. The representative engineering stress-stress curve of the epoxy adhesive Araldite 2015 is shown in Fig. 4.2.

Surface preparation and bonding

The details of surface preparation and bonding are described in Chapter 3, subsection 3.3.1. Here, a recall is made. Metallic spacers of 5 different thicknesses (approximately, 0.4, 1.1, 2.6, 4.1 and 10.1 mm) were used to obtain an uniform adhesive bond-line, as shown in Fig. 4.1.

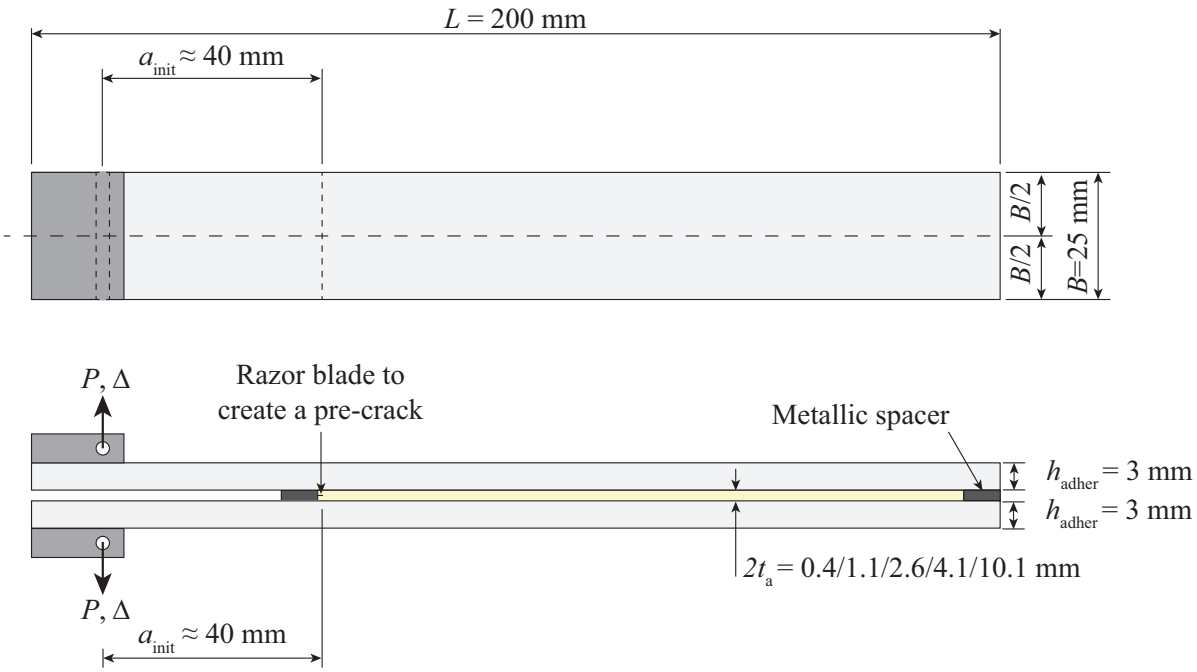

Figure 4.1: Double-cantilever beam (DCB) specimen.

Table 4.1: Mechanical properties of steel S690 and epoxy adhesive Araldite 2015.

Material	E (MPa)	ν	σ_y^{***} (MPa)	$\sigma_{ultimate}$ (MPa)
Steel S690	210000	0.30	770	832
Epoxy adhesive*	2000 ± 300	0.33**	16.1 ± 1.9	28.8 ± 0.7

* experimentally measured from dog bone specimens cured 1 hour at 80°C

** supplier's technical data-sheet

*** Steel: yield strength 0.2% offset; Adhesive: yield strength 0.1% offset

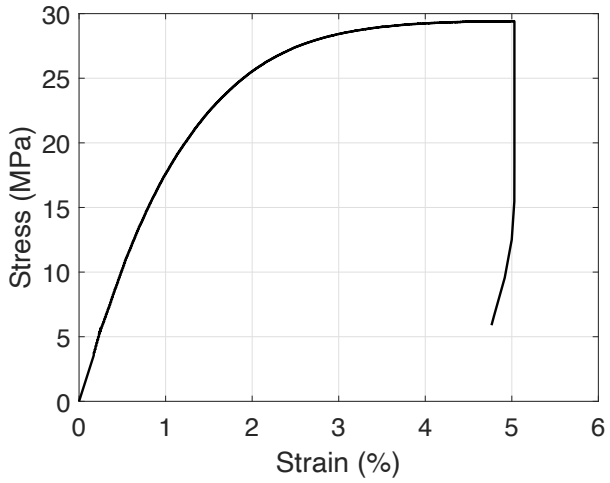

Figure 4.2: Engineering stress-strain curve: Araldite 2015 cured 1 hour at 80°C.

4.2.2. Test set-up

The details of test set-up are described in Chapter 3, sub-section 3.3.2.

4.2.3. Analysis of fracture surfaces

In order to evaluate the crack path location and to investigate the features of the fracture surfaces, a three-dimensional measuring microscope and a fringe projection scanner (Keyence VR-3200, Japan) were used. The scanner is characterized by <100 nm out-of-the plane resolution with up to a 200x200 mm^2 measuring area.

4.3. Data reduction methods

Using the Irwin-Kies compliance formula, the mode I strain energy release rate (SERR), i.e. the driving force for steady-state crack growth, can be expressed as

$$G_{\mathrm{I}} = \frac{P^2}{2B}\frac{dC}{da}, \tag{4.1}$$

where P is the applied load, C is the specimen compliance, B is the specimen width and da is the instantaneous crack length extension. A straight crack front is assumed. Standard methods for the mode I energy release calculation are based on Eq. 4.1, differing only in the way in which the derivative dC/da is obtained [19].

4.3.1. Standard methods

Literature suggests different methods to determine the specimens' compliance, C. Some methods are based on an analytical calculation, such as the simple beam theory (SBT), while others are based on direct curve fitting of the measured compliance to the measured crack length, such as the compliance calibration method (CCM) [20]. The adhesive layer thickness effect on G_{I} is indirectly taken into account in these methods when considering the experimental specimens' compliance. Indeed, the finite stiffness of the system, including the effects of the bond-line, are effectively taken into account when experimental compliance is used, although the adhesive bond-line thickness does not explicitly appear in the expression of G_{I}.

The simple beam theory

The mode I strain energy release rate based on the SBT is given by,

$$G_{\text{I-SBT}} = \frac{P^2a^2}{BEI} = \frac{3P}{Bh_{\text{adher}}}\sqrt[3]{\frac{4P\Delta^2}{BE}}. \tag{4.2}$$

where a represents the crack length, E is the Young's modulus of an isotropic beam, Δ is half of the total displacement and $I = \frac{Bh_{\text{adher}}^3}{12}$ defines the second moment of the beam cross-section area [20].

At fracture, the driving force equals the critical fracture energy, $G_{\mathrm{I}} = G_{\mathrm{Ic}}$, denoting the crack onset in the adhesive. The initial linear relation between load and

displacement turns to a non-linear one during crack steady-state propagation. Assuming that G_{Ic} is constant during propagation, P and Δ scale as,

$$P = \frac{B}{3}\sqrt[4]{\frac{3Eh_{adher}^3}{4}}G_{Ic}^{3/4}.\Delta^{-1/2} = \psi.\Delta^{-1/2}. \tag{4.3}$$

Eq. 4.3 provides a power-law for the steady-state, self-similar crack growth process [21].

The compliance calibration method

From an empirical analysis, in the compliance calibration method (CCM), the relation between P, 2Δ and a is expressed as [22],

$$P_{CCM} = (\chi^{-1}.a^{-n}).2\Delta = \Omega.2\Delta. \tag{4.4}$$

The mode I strain energy release rate based on the CCM is expressed as,

$$G_{I\text{-}CCM} = \frac{nP\Delta}{Ba} = \frac{nP\Delta}{B\left(\frac{2\Delta}{P\chi}\right)^{1/n}} = \frac{n}{2^{1/n}B}.\chi^{1/n}.P^{\frac{n+1}{n}}.\Delta^{\frac{n-1}{n}}, \tag{4.5}$$

where n equals the slope of the log-log plot of Ω versus a (i.e. $\log\Omega = -\log\chi - n\log a$). According to the SBT, n should be equal to 3 [22].
Similarly, as explained in SBT, at crack onset and post-propagation, the driving force equals the critical fracture energy, $G_I = G_{Ic}$. Assuming that G_{Ic} is constant during the crack growth process, the load, P, as a function of Δ is given by,

$$P = \left(\frac{BG_{Ic}}{n}\right)^{\frac{n}{n+1}}.\left(\frac{2}{\chi}\right)^{\frac{1}{n+1}}.\Delta^{-\frac{(n-1)}{(n+1)}} = \phi.\Delta^{-\frac{(n-1)}{(n+1)}}. \tag{4.6}$$

4.3.2. Penado-Kanninen model: the Euler-Bernoulli beam on the Winkler elastic foundation

In the SBT, the bonded region is considered infinitely stiff. The crack tip opening displacement is, thus, 0, so it is the root rotation, and the presence of the fracture process zone ahead of the crack tip is disregarded. However, in reality, the scenario is rather different. In fact, the beams are not fixed at the crack tip due to the flexibility of the adhesive layer. Indeed, this flexibility may lead to some vertical displacement of the beams within the bonded zone, inducing root rotation of the beams near the crack tip region. The Winkler elastic foundation was seemingly the first approach developed to depict the root rotation effect [23, 24].
The Winkler correction for DCB specimens with softer and thicker interlayers was subject of the study of several researchers [25–28]. Penado [28] developed a method to determine the compliance and the energy release rate of the DCB specimen with an adhesive layer based on modifying the Kanninen's "augmented DCB model" [25] for crack propagation analysis of a homogeneous specimen. The Penado-Kanninen (P-K) model is obtained by considering a finite length beam, which

is partially free (representing the unbonded part of the specimen) and partially supported by an elastic foundation (representing the bonded region), see Fig. 4.3. The DCB specimen is symmetric about the x-axis along the centreline of the adhesive layer. Only half of the specimen is represented in Fig. 4.3 (bond-line of thickness t_a). The simplest theories are used: the Euler-Bernoulli beam theory and the Winkler foundation for the free and the bonded regions, respectively [21].

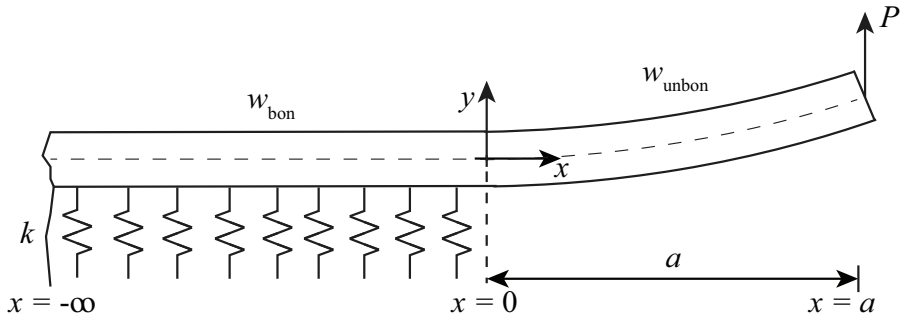

Figure 4.3: DCB specimen modelled according to Kanninen-Penado model [21].

The solution of the displacement of the Penado-Kanninen beam model is given by,

$$w(x) = \frac{P}{6EI\lambda^3}\begin{cases}(3a\lambda^3x^2 - \lambda^3x^3 + 6a\lambda^2x + 3\lambda a + 3\lambda x + 3) & 0 \leqslant x \leqslant a \\ 3e^{\lambda x}[\cos(\lambda x)a\lambda + a\sin(\lambda x)\lambda + \cos(\lambda x)] & -\infty \leqslant x \leqslant 0\end{cases} \tag{4.7}$$

where λ is the wave number, an inverse of which defines the elastic process zone length. The process zone length, λ^{-1}, in the context of the elastic foundation is interpreted as the distance (from the crack tip) over which the positive peel stress is distributed. The λ^{-1} length exits beyond the crack tip due to the flexibility of the adhesive. The λ is defined as,

$$\lambda = \sqrt[4]{\frac{k}{4EI}} \quad \text{where} \quad k = m_q\left(\frac{E_a}{t}\right)B, \tag{4.8}$$

where E is the adherends' elastic modulus, E_a is the Young's modulus of the adhesive, t_a is half of the thickness of the adhesive layer, and B is the specimen width. Moreover, k is the foundation modulus describing the stiffness of the springs and depends on the geometry and material properties of the adhesive. Finally, constant m_q (q=1-3) allows for the arbitrary formulation of the stress state at the crack front. Specifically, m_q is expressed as,

$$m_1 = 1 \tag{4.9}$$

for plane stress conditions in all directions (3D plane stress state) [29];

$$m_2 = \frac{1}{(1-\nu_a^2)} \tag{4.10}$$

for in-plane strain conditions and plane stress conditions in the transverse direction (2D plane strain state) [30];

$$m_3 = \frac{(1-\nu_a)}{[(1-2\nu_a)(1+\nu_a)]} \tag{4.11}$$

for the plane strain conditions in all directions (3D plane strain state) [31]. ν_a is the Poisson's ratio of the adhesive, presenting elastic or elasto-plastic behaviour. In the case of an (incompressible) elastomeric adhesive, the foundation modulus should be modelled differently and, hence, the interested reader is referred to [16, 32] for more details.
The strain energy release rate is determined using the compliance method. The beam displacement at $x = a$ is given by,

$$\Delta = w_{\text{unbon}}(x=a) = \frac{P}{EI\lambda^3}\left(\frac{1}{3}\lambda^3 a^3 + \lambda^2 a^2 + \lambda a + \frac{1}{2}\right). \tag{4.12}$$

The displacement given by Eq. 4.12 corresponds to half of the specimen. Therefore, the whole specimen displacement is equal to 2Δ. The strain energy release rate, G_{I}, is then given by,

$$G_{\text{I-P-K}} = \frac{P^2}{2B}\frac{dC}{da} = \frac{P^2}{BEI\lambda^2}\left(\lambda^2 a^2 + 2\lambda a + 1\right). \tag{4.13}$$

Eq. 4.8 seems of fundamental importance revealing an inherent effect of the adhesive thickness on the elastic process zone length, λ^{-1}. The foundation modulus k decreases as the adhesive layer thickness increases, leading to smaller values of λ. As the elastic process zone length is the inverse of λ, its value increases with increasing adhesive layer thickness. The strain energy release rate is directly affected by the increase of the adhesive layer thickness.

4.3.3. Mode I SERR: the relation between the simple beam theory and the Penado-Kanninen model

The mode I energy release rate was previously derived from the simple beam theory and the Penado-Kanninen model, and is expressed as,

$$G_{\text{I-SBT}} = \frac{P^2 a^2}{BEI}, \tag{4.14}$$

$$G_{\text{I-P-K}} = \frac{P^2}{BEI\lambda^2}\left(\lambda^2 a^2 + 2\lambda a + 1\right). \tag{4.15}$$

Eq. 4.15 can be re-written as,

$$G_{\text{I-P-K}} = G_{\text{I-SBT}}.\left(1 + \frac{2}{\lambda a} + \frac{1}{\lambda^2 a^2}\right). \tag{4.16}$$

Eq. 4.16 reveals that the value of $G_{\text{I-P-K}}$ tends to the value of $G_{\text{I-SBT}}$ when $\lambda a \to \infty$, which means that the bonded region would be infinitely stiff and, consequently, the opening displacement, as well as the root rotation at the crack tip, would be null.

4.4. Results

4.4.1. Load-displacement curves

The test results corresponding to the representative specimens of each bond-line thickness are shown in Fig. 4.4. The experimental load-displacement, $P-2\Delta$, curves are consistent for each specimen within the same test series. In fact, the initial stiffness and peak load were similar in each of them as well as the post-peak region, from the crack onset up to complete failure. The average peak load is summarized in Table 4.2.
Moreover, in Fig. 4.4 are also plotted analytical predictions of the experimental curves. The initial linear part of the $P-2\Delta$ curve is predicted based on the SBT $\left(P=\frac{3}{2}EI\frac{2\Delta}{a_0^3}\right)$ and the P-K model (from Eq. 4.12). The propagation region is predicted from the SBT and the CCM. For each representative specimen, the average values of G_{I} by applying the SBT and the CCM are determined and used as G_{Ic} in Eqs. 4.3 and 4.6, respectively. Concerning the SBT prediction, please note that the estimated crack length $\left(a_{\mathrm{SBT}}=\sqrt[3]{\frac{3}{2}EI\frac{2\Delta}{P}}\right)$ is used to calculate G_{I} as reported by [24] and [33]. Finally, the experimentally measured crack lengths are plotted as a function of the displacement (the crack length range is restricted by the area analysed by the acquisition image system). The points highlighted in Fig. 4.4 are used in section 4.5 for P-K model validation.

Table 4.2: Average peak load and corresponding standard deviation per bond-line thickness.

$2t_{\mathrm{a}}$	0.4 mm	1.1 mm	2.6 mm	4.1 mm	10.1 mm
Peak Load	311 $\pm$ 18.2	304 $\pm$ 12.7	308 $\pm$ 18.2	413 $\pm$ 8.4	380 $\pm$ 15.8

4.4.2. Failure surfaces

The failure surfaces of the representative specimen of each bond-line thickness are shown in Fig. 4.5, which exhibit cohesive failure (i.e. the crack propagated within the adhesive layer). In order to evaluate the crack path location and to investigate the features of these surfaces, a three-dimensional measuring microscope and a fringe projection scanner (Keyence VR-3200, Japan) were used. These measurements are presented in Fig. 4.6 (only one of the two failure surfaces is shown). The colour bar refers to the height of the adhesive remaining on the adherend surface. The bare steel regions (dark blue) were defined as the reference surface. There is some variation on the average bond-line thickness within each set of specimens per bond-line thickness, which leads in some cases to average bond-line thicknesses higher than the average nominal thickness. However, unique features can be found on each set of the steel-steel DCB specimens. Even inside each set, different waviness and corresponding roughness profiles can be noticed on the failure surfaces, which explains the non-smooth behaviour of each $P-2\Delta$ curve. The average areal roughness, S_{a}, and the root mean square deviation, S_{q}, of the entire failure surface (Area Total) and some arbitrary regions (Areas 1-4 in Fig. 4.6) of

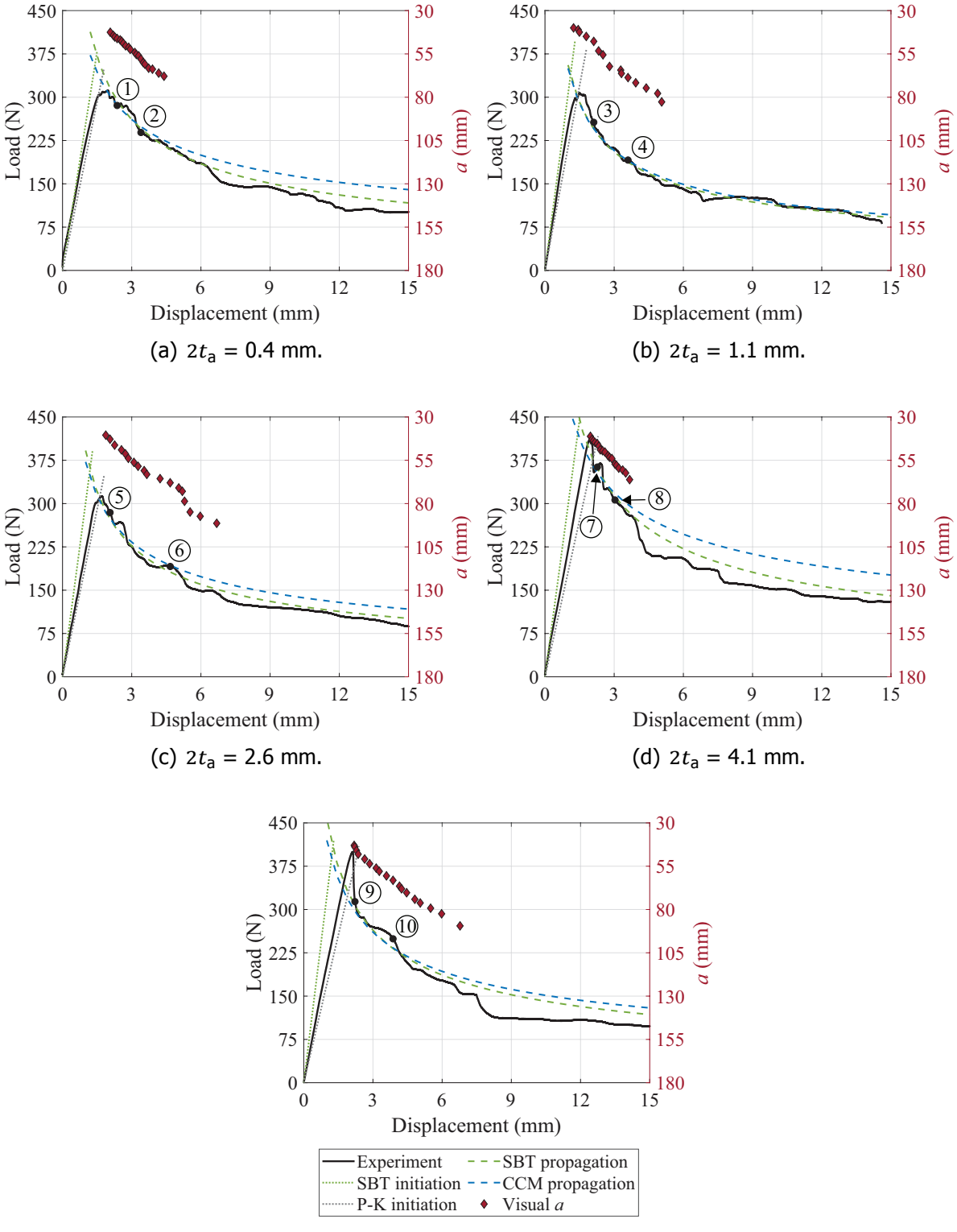

(a) $2t_a$ = 0.4 mm. (b) $2t_a$ = 1.1 mm.

(c) $2t_a$ = 2.6 mm. (d) $2t_a$ = 4.1 mm.

(e) $2t_a$ = 10.1 mm.

Figure 4.4: Load-displacement curves (experiment vs. predictions) and experimentally measured crack lengths. The points highlighted are used in section 4.5 for P-K model validation.

each representative specimen are given in Table 4.3 (a Gaussian filter is applied according to ISO 25178-2:2012. S_a is the arithmetic average of the absolute values of the profile height deviations from the mean line (defined by the waviness), S_q is the root mean square of the profile height deviations from the mean line).

Table 4.3: The average areal roughness, S_a, and the root mean square deviation, S_q, of the representative specimen of each test series. Area Total corresponds to the entire fracture surface, excluding the edges. The other areas are represented on each representative specimen in Fig. 4.6.

		Area Total	Area 1	Area 2	Area 3	Area 4
$2t_a = 0.4$ mm	S_a (μm)	93.79	123.71	52.14	88.92	129.64
	S_q (μm)	115.45	140.91	65.25	107.36	146.76
$2t_a = 1.1$ mm	S_a (μm)	279.89	161.63	-	349.55	307.21
	S_q (μm)	358.76	183.42	-	400.66	364.42
$2t_a = 2.6$ mm	S_a (μm)	381.28	244.40	-	371.18	119.44
	S_q (μm)	469.29	307.96	-	393.06	146.44
$2t_a = 4.1$ mm	S_a (μm)	459.06	226.87	-	237.49	260.00
	S_q (μm)	536.19	281.62	-	287.01	307.61
$2t_a = 10.1$ mm	S_a (μm)	2687.75	148.60	417.37	741.79	244.24
	S_q (μm)	2970.89	209.84	506.24	869.02	301.07

Fig. 4.7 presents the longitudinal profiles of the failure surfaces of the representative specimens and thus the overall crack path profile. The height profile of the remaining adhesive layer on the failure surface in respect to the reference surfaces (dark blue regions in Fig. 4.6) is plotted along the specimens length direction, more precisely at three specific values of the specimen width, namely at z'= 5, 12.5 and 20 mm. In fact, Fig. 4.7 shows that the height profiles of all specimens do not coincide along the specimen's width, being the more uniform the representative specimen with the thickest bond-line of 10.1 mm. This means that the failure surfaces are not symmetric along the width and, therefore, the crack front did not propagate uniformly along the width direction.

In the representative specimen with the thinnest bond-line (i.e. approximately of 0.4 mm), the failure surface is, in the initial part (from the initial crack length up to 70 mm), characterized by some peaks, as is highlighted in Fig. 4.6(a). This region is followed by a smoother one, where the crack seems to propagate in the mid-thickness of the bond-line (i.e. perfectly cohesive propagation). This feature can also be observed in Fig. 4.7(a). More heavy peaks appear afterwards, for crack lengths larger than 100 mm. The S_a and S_q were determined in some arbitrary regions and the results corroborate the description presented previously, see Table

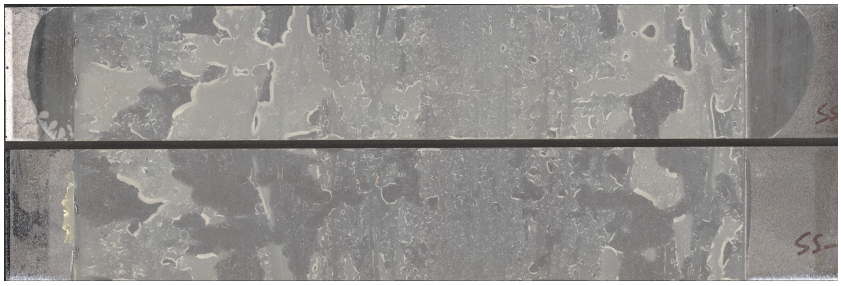

(a) $2t_a$ = 0.4 mm.

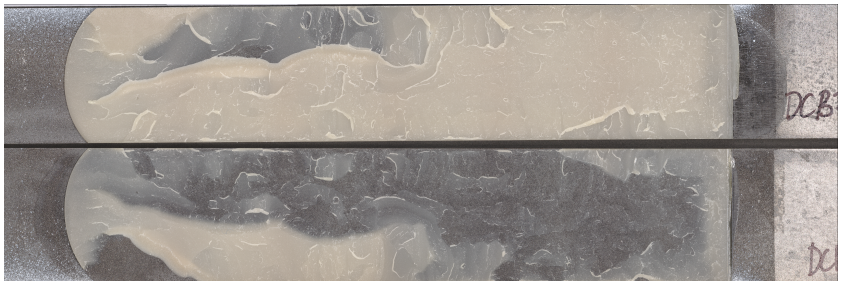

(b) $2t_a$ = 1.1 mm.

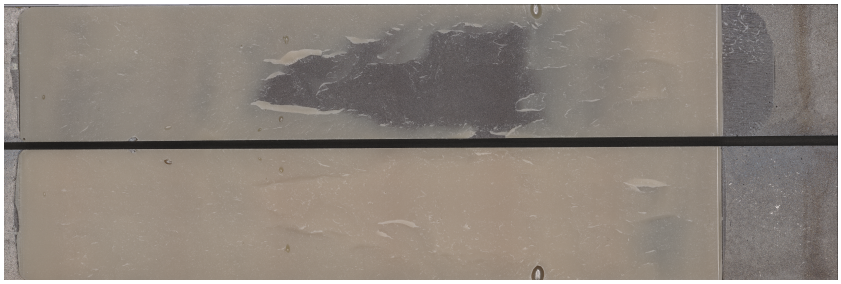

(c) $2t_a$ = 2.6 mm.

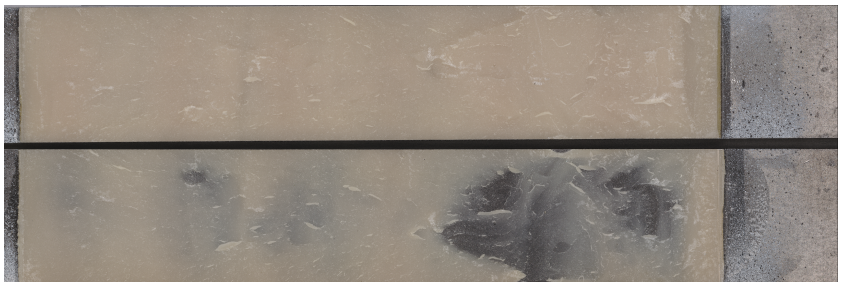

(d) $2t_a$ = 4.1 mm.

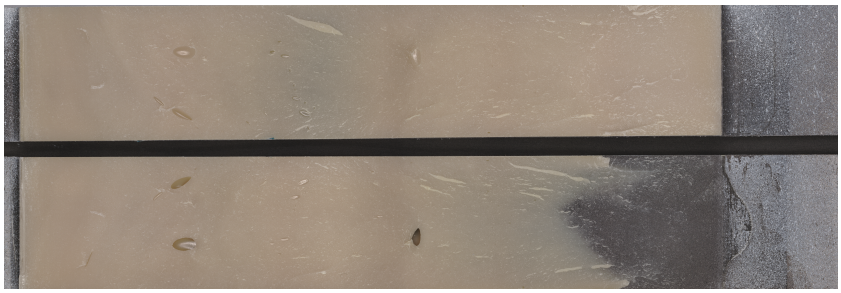

(e) $2t_a$ = 10.1 mm.

Figure 4.5: Failure surfaces of the representative specimens per bond-line thickness - optical view.

4.3. By increasing the adhesive bond-line thickness up to 1.1 mm, the crack kept propagating inside the adhesive layer, however in a plane more remote from the mid-bond-line thickness plane. Although the crack path approached regions really close to the epoxy-steel interface, it should be noticed that interfacial failure did not take place (a thin layer of adhesive is found on the complementary failure surface). As can be seen in Figs. 4.6(b) and 4.7(b), for crack lengths larger than 80 mm, two different regions can be observed and the failure surface asymmetry along the width direction becomes more pronounced.

In the representative specimens with bond-lines of 2.6 and 4.1 mm, the crack started propagating in the mid-thickness of the adhesive layer, as shown in Figs. 4.7(c) and 4.7(d), respectively. However, its locus direction changed towards regions close to one of the epoxy-steel interfaces, afterwards. As previously commented, interfacial failure never took place. In the final region of the failure surface of the 2.6 mm thick bond-line specimen, the crack propagated in a more central plane (i.e. near the mid-thickness of the adhesive layer). The average areal roughness and corresponding standard deviation were determined in arbitrary regions (Figs. 4.6(c) and 4.6(d)) to show the changes on the local average roughness and the results are presented in Table 4.3. Finally, in the thickest specimens, with a bond-line thickness of 10.1 mm, the crack onset moved towards the steel-epoxy interface due to geometry singularity (Figs. 4.6(e) and 4.7(e)) [34, 35]. This change on the crack initiation location led to propagation along one of the steel interfaces. The presence of a thin layer of adhesive on these regions of the failure surfaces is indicative of the non-occurrence of adhesive failure. During the crack growth, the crack propagated through the weakest regions throughout the thickness and longitudinal directions of the bonded area, leading to a change on the crack propagation plane. For instance, in Fig. 4.6(e) is shown that the crack propagated from a region close to one interface to a region close to the second interface in the crack length range of 60 to 120 mm.

The fact that the average areal roughness, S_a, does not provide any information on the shape, size or frequency of surface features is worthy of comment. The critical fracture energy of an adhesive joint is dependent on the parameters mentioned in the last sentence. For example, the average areal roughness of Area 1 of the representative specimens with a bond-line thickness of 0.4 and 1.1 mm is 123.71 and 161.63 μm, respectively. In the former specimen, this area is characterized by several peaks, whereas in later specimen a smoother area is found. The surface with the higher frequency of peaks is expected to lead to higher critical fracture energy as the total surface area is larger and thus more external work is needed for crack growth.

4.4.3. *Resistance*-curves

The *Resistance*-curves, also called as *R*-curves, of the representative specimens of two adhesive bond-line thicknesses are presented in Fig. 4.8. Three curves are shown, which are determined based on: the SBT (Eq. 4.2), the CCM (Eq. 4.5) and the Penado-Kanninen model (Eq. 4.13). It is important to call attention to the fact that the experimentally measured crack lengths are plotted in Fig. 4.4,

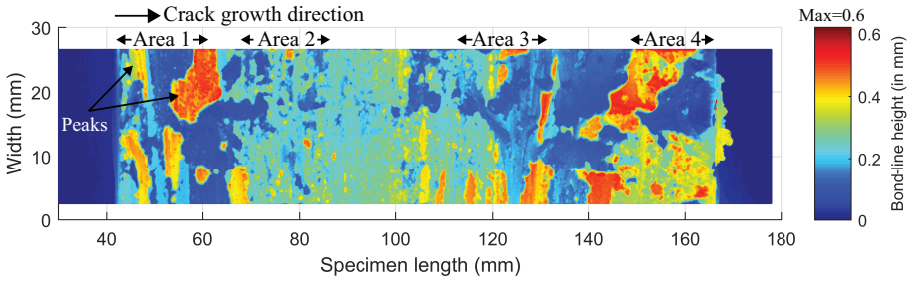

(a) $2t_a$ = 0.4 mm.

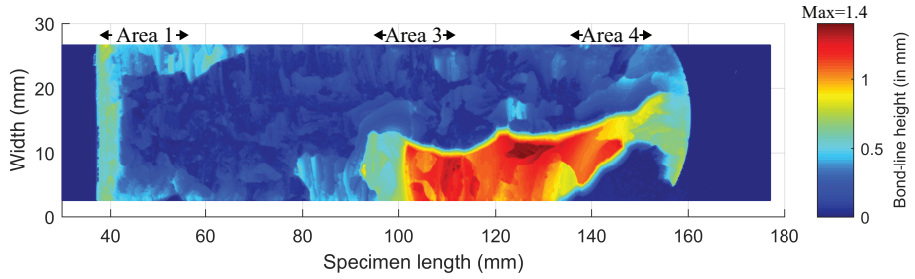

(b) $2t_a$ = 1.1 mm.

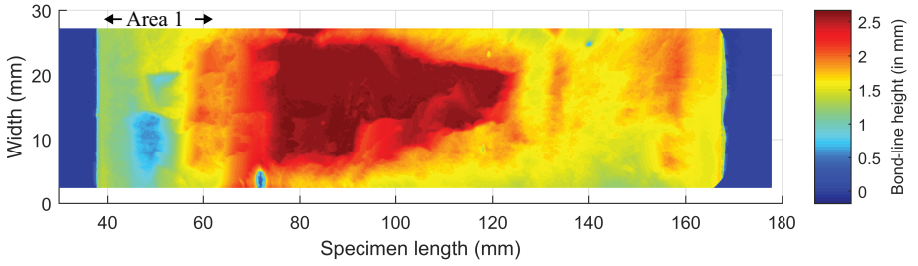

(c) $2t_a$ = 2.6 mm.

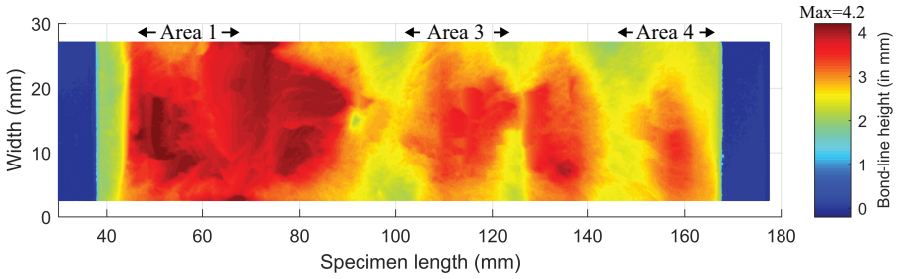

(d) $2t_a$ = 4.1 mm.

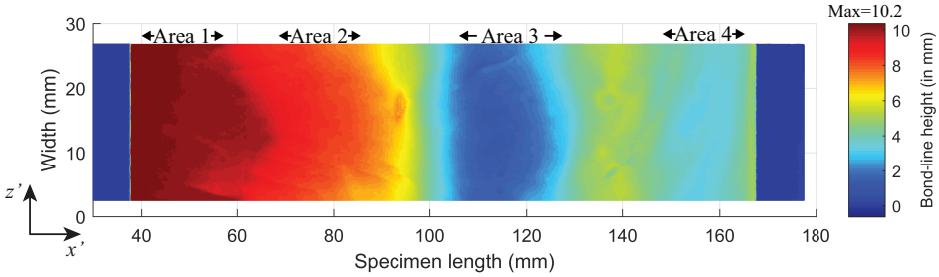

(e) $2t_a$ = 10.1 mm.

Figure 4.6: Failure surfaces of the representative specimens per bond-line thickness - height view. The colour bar refers to the height of the adhesive remaining on the adherend surface. The bare steel regions (dark blue) were defined as the reference surface.

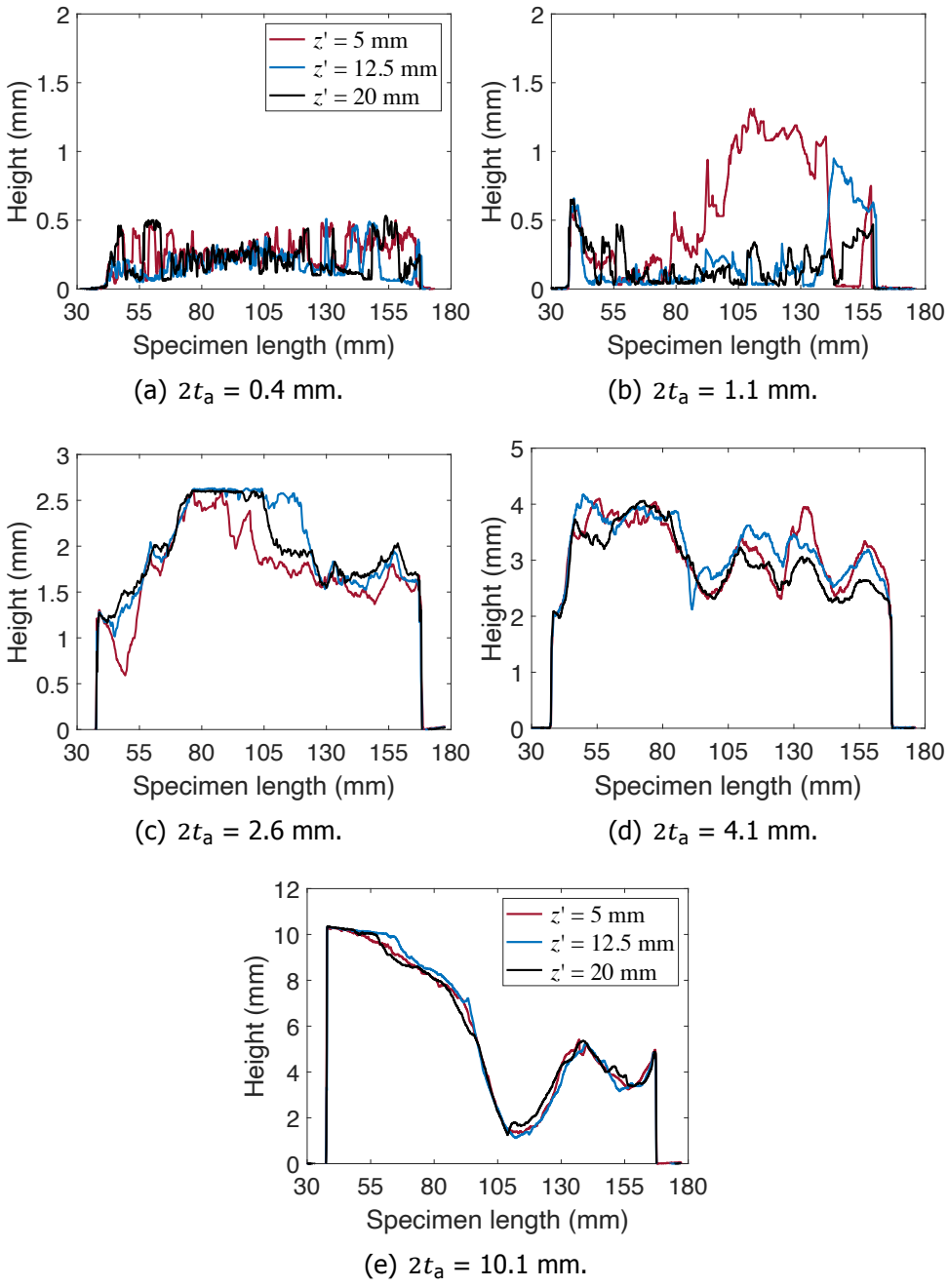

Figure 4.7: Height profile of the remaining adhesive layer on the failure surface in respect to the reference surfaces (dark blue regions in Fig. 4.6) along the specimen's length direction of the representative specimens: a) bond-line thickness ($2t_a$) of 0.4 mm; b) $2t_a$ = 1.1 mm; c) $2t_a$ = 2.6 mm; d) $2t_a$ = 4.1 mm; e) $2t_a$ = 10.1 mm. The height profile is plotted at z'= 5, 12.5 and 20 mm.

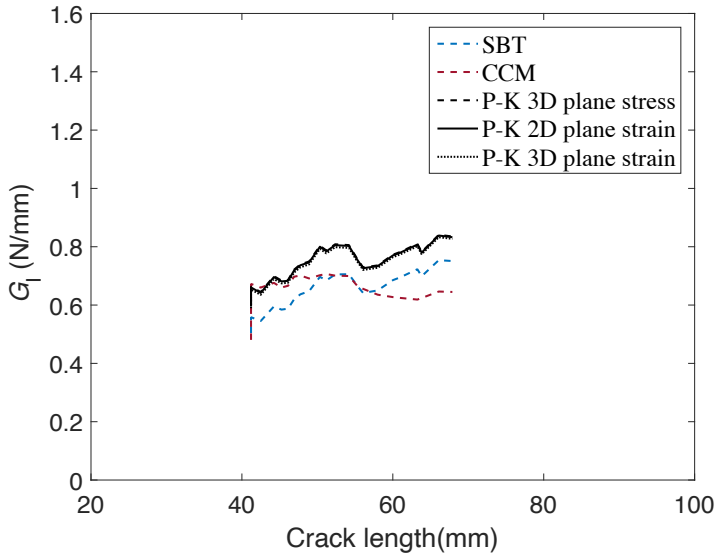

(a) $2t_a$ = 0.4 mm.

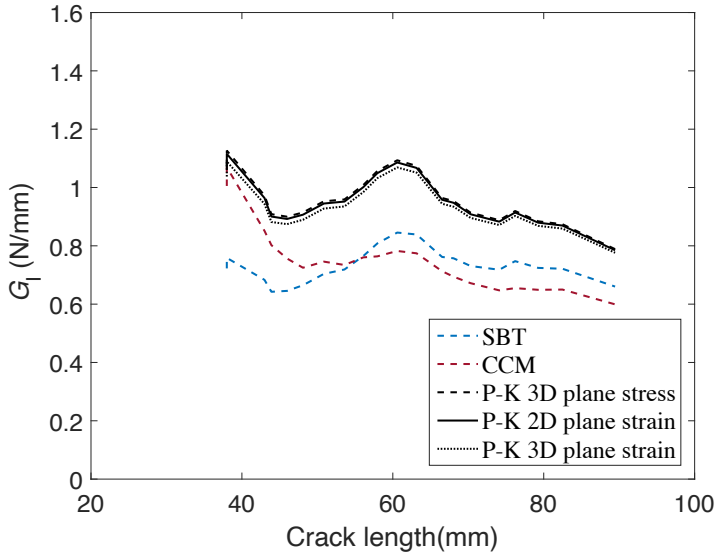

(b) $2t_a$ = 10.1 mm.

Figure 4.8: *Resistance*-curves of the representative specimens of two bond-line thicknesses.

allowing the correlation between the *R*-curves and the corresponding $P-2\Delta$ curves. Moreover, the effect of the stress state at the crack tip on G_{I} is also evaluated by using three different m_{q} coefficients to calculate $G_{\mathrm{I\text{-}P\text{-}K}}$. Regardless of the bond-line thickness, the three curves (i.e. P-K plane stress, P-K plane strain 2D, and P-K plane strain 3D) present almost identical results. Table 4.4 summarizes the effect of the stress state at the crack tip, of the Poisson's ratio ν_{a} and of the adhesive bond-line thickness, $2t_{\mathrm{a}}$, on the foundation modulus and the wave number, k and λ, respectively. The correction made in order to allow for plane strain conditions at the crack tip is not negligible for adhesives with high Poisson's ratio (for example, $\nu_{\mathrm{a}} = 0.4$). Indeed, for such adhesive, the value of k by considering 3D plane strain

conditions is almost twice the value of k given by the 3D plane stress conditions, regardless of the bond-line thickness. However, as the studied adhesive, Araldite 2015, has a Poisson's ratio of 0.33, the correction for the plane strain conditions is not necessary.

Table 4.4: Penado-Kanninen model: the effect of the stress state at the crack tip, of the adhesive's Poisson's ratio ν_a and of the bond-line thickness on the coefficient m_q, the foundation modulus k and the wave number λ.

	$2t_a$	0.2 mm		10.1 mm	
ν_a (-)	m_q (-)	k (GPa)	λ (mm^{-1})	k (GPa)	λ (mm^{-1})
0.33	$m_1 = 1.00$	250	0.27	10	0.12
	$m_2 = 1.12$	281	0.28	11	0.12
	$m_3 = 1.48$	370	0.30	15	0.13
0.4	$m_1 = 1.00$	250	0.27	10	0.12
	$m_2 = 1.19$	298	0.28	12	0.13
	$m_3 = 2.14$	536	0.33	21	0.15

$E_a = 2$ GPa; $E = 210$ GPa; $B = 25$ mm; $h_{steel} = 3$ mm

The $G_{I\text{-}P\text{-}K}$ gives higher values than the $G_{I\text{-}SBT}$, which is expected according to Eq. 4.16, and the difference between the SBT and the P-K curves gets larger as the adhesive bond-line increases. The thicker the bond-line, the higher the amount of energy dissipated by plastic deformation in the adhesive layer in the region ahead of the crack tip due to larger plastic deformation zones. In fact, the foundation modulus varies inversely with the bond-line thickness, and, consequently, an increase in the bond-line thickness leads to a smaller k and a smaller value of λ (from Eq. 4.8) - see Table 4.4. Therefore, as λ appears as a denominator in the terms inside the parentheses in Eq. 4.16, the factor, by which $G_{I\text{-}SBT}$ is multiplied to obtain $G_{I\text{-}P\text{-}K}$, increases leading to a higher offset between the *R*-curves of both methods. Regardless of the adhesive bond-line thickness (and the methodology employed), the *R*-curves are characterized by a peaked or “saw-tooth” appearance, which shows that no steady-state, self-similar regime was reached (i.e. G_I is not constant in the propagation region). Indeed, in sub-section 4.4.2 was demonstrated that the crack did not always propagate along the same plane (i.e. along the same adhesive layer height). These changes on the crack path position along the adhesive layer thickness are also reflected in the experimental $P - 2\Delta$ curves by the non-smooth behaviour (see Fig. 4.4). Looking at the crack locus, this means that its direction has several times changed during the crack growth process and, consequently, it has affected the plastic zone size and shape. As energy dissipation mainly occurs in the plastic deformation zone, the non self-similar regime in the *R*-curves is then attributed to the alteration of the size of this zone. More details about the variation of G_I on each bond-line thickness are given in section 4.5.
Hereinafter, only the results considering m_3 are reported because the mode I strain

energy release rate results kept independent of the stress state considered, see Fig. 4.8.

4.4.4. Analytical load-displacement curves

As aforementioned, analytical predictions of the initial linear part and crack growth region are shown in Fig. 4.4. By considering a $G_{\mathrm{I}} = G_{\mathrm{Ic}} = const.$ during the propagation process, an analytical $P - 2\Delta$ curve can be obtained from the SBT and the CCM. For each representative specimen, the average values of G_{I} by applying the SBT and the CCM are determined and used as G_{Ic} in Eqs. 4.3 and 4.6, respectively. Concerning the SBT prediction, please note that the estimated crack length $\left(a_{\mathrm{SBT}} = \sqrt[3]{\frac{3EI2\Delta}{2P}}\right)$ is used to calculate G_{I} as reported by [24] and [33]. Two examples of the $\log\Omega$-$\log a$ relation are shown in Fig. 4.9 and the average value of the exponent n determined for each representative specimen is presented in Table 4.5.

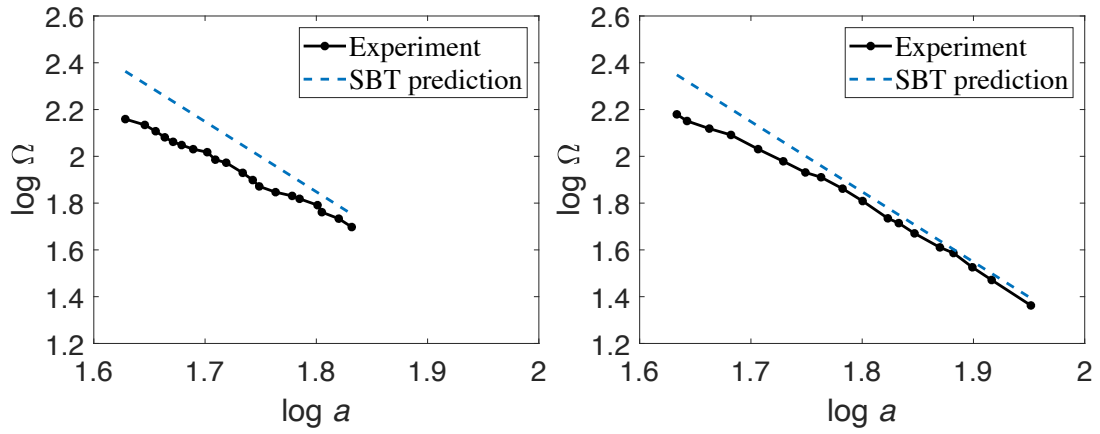

(a) $2t_{\mathrm{a}}$ = 0.4 mm. (b) $2t_{\mathrm{a}}$ = 10.1 mm.

Figure 4.9: $\log\Omega$-$\log a$ relation (experiment vs. prediction).

Table 4.5: Average value of the exponent n of each representative specimen per bond-line thickness.

$2t_{\mathrm{a}}$	0.4 mm	1.1 mm	2.6 mm	4.1 mm	10.1 mm
n	2.2686	2.8196	2.4876	2.1666	2.5346

The initial linear part of the experimental $P - 2\Delta$ curves (see Fig. 4.4) is estimated from the SBT ($P = \frac{3EI2\Delta}{2a_0^3}$) and the P-K model (from Eq. 4.12). The SBT prediction matches well the DCB specimens with thin adhesive bond-lines (i.e. $2t_{\mathrm{a}} = 0.4$-1.1 mm). By increasing $2t_{\mathrm{a}}$, the level of agreement between the analytical and experimental curves gets lower. On the other hand, the P-K model predicts the behaviour rather well in the range of bond-line thicknesses of $0.4 - 2.6$ mm. For thicker bond-lines (i.e. of 4.1 and 10.1 mm thick), the predicted compliance by the P-K model is higher than the experimental as the crack has propagated asymmetrically close

to one of the two interfaces for both cases. These results were expected because the SBT does not allow for flexibility of the adhesive joint near the crack front (the beams are assumed to be fixed at the crack front), leading to an overestimation of the experimental stiffness. This flexibility effect becomes more meaningful as the bond-line thickness gets thicker and thicker.

In the propagation region (see Fig. 4.4), the SBT gives better predictions than the CCM. Good agreement between experimental data and the theoretical SBT relation was also shown by Budzik et al. [24] and Salem et al. [33]. Eq. 4.3 provides a power-law for steady-state, self-similar crack growth. However, the experimental results display non-smooth behaviour and, as shown previously in the *R*-curves of each representative specimen, a steady-state condition was not reached during the experiments. This fact explains the differences between the analytical and experimental $P-2\Delta$ curves. Finally, the accuracy of the CCM predictions depends on the evaluation of the parameters n and χ, which gets more precise for a larger number of data (i.e. when the range of crack lengths experimentally measured is larger, there will be a better fitting of the entire propagation region). For a better agreement of the CCM predictions, n and χ should be updated for every increment of a. However, by using the average values of these two parameters (i.e. n and χ), good predictions are obtained in the range of the experimentally measured crack lengths. Alternatively, the critical fracture energy or the ψ (from Eq. 4.3) could be updated for the SBT model, which would allow considering the more local character of G_{Ic}.

4.5. Adhesive bond-line thickness effect on critical fracture energy

Fig. 4.10 shows the trend of G_{I} based on the P-K model, Eq. 4.13, considering m_3 - 3D plane strain (note that only these results are plotted because G_{I} results kept independent of the stress state considered, see Fig. 4.8) as a function of the adhesive bond-line thickness. The maximum (“$\triangle$” symbol) and minimum (“∇” symbol) values of G_{I} of each single specimen are represented and plotted against the average thickness of the corresponding bond-line (the bond-line was measured three times along the specimen length and the average was calculated). Two error bars are also plotted, giving the range of scatter on the thickness and G_{I} results of each bond-line thickness. The average value of G_{I}, G_{Ic}, which is represented by a bullet point, “•”, corresponds to the mean of all points (maximum and minimum) plotted for each bond-line thickness. The deformation zone length ahead of the crack tip of each bond-line thickness is also plotted, i.e. $2r_{\mathrm{p}}+\lambda^{-1}_{j\text{-exp}}$ where $j=$ 0.4, 1.1, 2.6, 4.1, 10.1 mm and $\lambda^{-1}_{j\text{-exp}}$ corresponds to the value of the experimental λ^{-1} of thickness of j mm (more details about the calculation of $2r_{\mathrm{p}}$ and $\lambda^{-1}_{j\text{-exp}}$ are shown later in this section). For clarity, the deformation zone length comprises both the plastic zone length and the elastic fracture process length, $\lambda^{-1}_{j\text{-exp}}$. The energy dissipation mainly occurs in the plastic deformation zone. However, the elastic process length also contributes to the work done by the external applied displacement.

Overall, a good agreement between the minimum and maximum values of G_{I} was found (i.e. the minimum and maximum values of G_{I} form two distinct groups), as can be seen in Fig. 4.10. The results of the specimens with a bond-line thickness of 0.4 mm were the exception, which is justified by the different waviness and corresponding roughness profiles found out in the failure surfaces of each specimen. The critical mode I fracture energy, G_{Ic}, presented similar values for the specimens with adhesive bond-line thicknesses of 0.4, 1.1 and 2.6 mm ($G_{\mathrm{Ic}} = 0.71$, 0.61, 0.63 N/mm, respectively). However, it increased by approximately 63% for 4.1 mm ($G_{\mathrm{Ic}} = 1.16$ N/mm), and it decreased by about 10% (in comparison with 4.1 mm) for the 10.1 mm ($G_{\mathrm{Ic}} = 1.04$ N/mm).
In a bulk adhesive specimen, the plastic deformation zone for a growing crack assumes a rounded shape of diameter equal to $2r_{\mathrm{p}}$, which is given by [7],

$$2r_{\mathrm{p}} = \frac{1}{\pi}\frac{E_{\mathrm{a}}.G_{\mathrm{Ic\text{-}a}}}{\sigma_{\mathrm{y}}^2} \quad \text{for in-plane stress conditions,} \tag{4.17}$$

$$2r_{\mathrm{p}} = \frac{1}{3\pi}\frac{E_{\mathrm{a}}.G_{\mathrm{Ic\text{-}a}}}{\sigma_{\mathrm{y}}^2}\frac{1}{(1-\nu_{\mathrm{a}}^2)} \quad \text{for in-plane strain conditions,} \tag{4.18}$$

where ν_{a} is the adhesive Poisson's ratio, $G_{\mathrm{Ic\text{-}a}}$ is the critical mode I fracture energy of the bulk adhesive, and σ_{y} is the yield strength of the adhesive. The stress state near the crack tip varies from plane stress in the edge regions to plane strain in the central regions of the adhesive joints. The tensile stress necessary for yielding is higher under the influence of plane strain conditions, leading to a smaller plastic zone, as can be deducted from Eqs. 4.17 and 4.18.
The length $2r_{\mathrm{p}}$ for the epoxy adhesive here studied is presented in Table 4.6. The plane stress and plane strain conditions are considered. Moreover, the plane strain plastic zone length, $2r_{\mathrm{p}}$, is represented by means of a dashed red line in Fig. 4.10. For determining $2r_{\mathrm{p}}$ in Eqs. 4.17 and 4.18, a σ_{y} of 16.1 MPa is used (from Table 4.1). The average value of $G_{\mathrm{I\text{-}P\text{-}K}}$ of 4.1 mm thick bond-line is considered as the critical mode I fracture energy of the bulk adhesive, $G_{\mathrm{Ic\text{-}a}}$. Considering the scenario that the maximum critical mode I fracture energy for the specimen geometry and materials used in the present study is attained for a bond-line thickness of 4.1 mm thick bond-line, the bulk adhesive mode I energy would be smaller as shown by [5, 7]. Consequently, by considering $G_{\mathrm{I\text{-}P\text{-}K}}$ of 4.1 mm thick bond-line as the critical mode I fracture energy of the bulk adhesive, $G_{\mathrm{Ic\text{-}a}}$, the prediction of $2r_{\mathrm{p}}$ is overestimated. However, for the purpose of the discussion of the results, the tendency between the length of the analytical plastic zone and the theoretically one would remain the same, as it is described in sub-section 4.5.2.

Table 4.6: $2r_{\mathrm{p}}$ - The plastic process zone length, Eqs. 4.17 and 4.18.

	Plane stress	Plane strain
$2r_{\mathrm{p}}$ (mm)	2.88	1.08

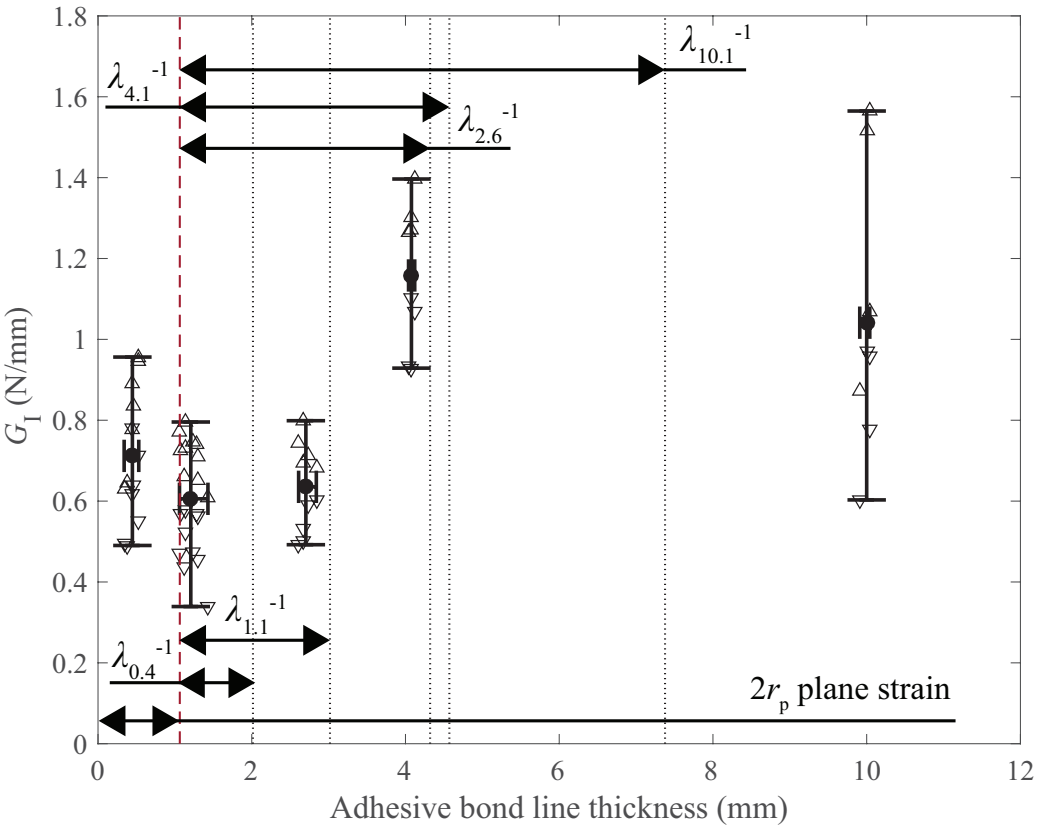

Figure 4.10: Adhesive bond-line thickness effect on G_I: P-K model results, considering 3D plane strain conditions. The maximum (“$\triangle$”) and minimum (“∇”) values of G_I of each specimen are plotted against the average thickness of the corresponding bond-line. Two error bars are also plotted, giving the range of scatter on the thickness and G_I results of each bond-line thickness. The average value of G_I (i.e. “$\bullet$” symbol) corresponds to the mean of all points (maximum and minimum) plotted for each bond-line thickness. The red dashed line gives the limit of $2r_p$ considering plane strain conditions. The black dashed lines give the limit of $2r_p + \lambda_{j\text{-exp}}^{-1}$, where j = 0.4, 1.1, 2.6, 4.1, 10.1 mm.

4.5.1. Displacement & stress field ahead the crack tip

Figs. 4.11(a), 4.11(c), 4.11(e), 4.12(a) and 4.12(c) present the prediction of the transverse displacement in the bonded region, w_{bon}, for all studied bond-line thicknesses based on the P-K model. The crack tip is located at $x = 0$. The points used for model validation are represented in Fig. 4.4. These points were selected from the propagation region (after P_{max}). The peel stresses profile, σ_{yy}, in the adhesive layer is shown in Figs. 4.11(b), 4.11(d), 4.11(f), 4.12(b) and 4.12(d). The calculations are based on the displacement field, $w(x)$, determined by the P-K model, Eq. 4.7,

$$\sigma_{yy} = \frac{E_a.w_i(x)}{t_a} \quad -\infty \leqslant x \leqslant 0, \tag{4.19}$$

where i = 1-10 and represents the points chosen in the propagation region of the representative specimens. An upper limit from the yield strength of the bulk

adhesive, from Table 4.1, is also plotted in Figs. 4.11(b), 4.11(d), 4.11(f), 4.12(b) and 4.12(d) to define the length of λ^{-1}, which is the distance over which the positive elastic peel stress is distributed up to the yield strength, σ_y. In addition, both the plane strain and plane stress plastic zone length are plotted in Figs. 4.11(b), 4.11(d), 4.11(f), 4.12(b) and 4.12(d). The region under peel stresses, σ_{yy}, higher than the adhesive's yield strength, σ_y, is the so-called plastic zone.

Table 4.7: $2w_{unbon}(x = a)$: Experimental vs. analytical results, considering m_3. The reader is referred to Fig. 4.4 to identify the location of the Point i on the corresponding $P - 2\Delta$ curve.

$2t_a$	Point i	P_i	a_i	$2\Delta_i$	$2w_{unbon}$ $(x = a_i)$	% Error
0.4 (mm)	1	285.69	46.11	2.37	1.95	-18
	2	238.94	57.99	3.40	3.11	-9
1.1 (mm)	3	256.51	47.77	2.11	2.05	-3
	4	191.13	68.67	3.60	4.19	16
2.6 (mm)	5	284.50	42.84	2.06	1.80	-13
	6	191.06	67.98	4.67	4.26	-9
4.1 (mm)	7	363.27	45.46	2.27	2.80	23
	8	306.23	57.17	3.04	4.36	43
10.1 (mm)	9	313.67	43.91	2.22	2.31	4
	10	249.23	63.15	3.87	4.97	28

The values of $2w_{unbon,i}(x = a_i)$ were compared with the experimental ones, $2\Delta_i$. The results using m_3 - 3D plane strain are summarized in Table 4.7. Reasonable agreement is found between the analytical and the experimental displacements regardless of the adhesive bond-line thickness, as shown in Table 4.7. However, the deviations from the experimental results are higher in the thicker specimens, namely the ones with a bond-line thickness of 4.1 and 10.1 mm, as is shown in Table 4.7. In these specimens, the change of the crack path location along the adhesive layer thickness affects the total displacement, 2Δ, which is not taken into account in the P-K model. The P-K model assumes that the crack is located at the mid-thickness of the adhesive layer. Moreover, in the derivation of the P-K model is assumed that the stiffness of the adhesive layer can be neglected in the unbonded region of the specimen when $\frac{E_a}{E} \leq 0.05$ and the adhesive layer is thin. When that is not the case, in order to have more accurate predictions, an effective adherend height, which takes the adhesive's stiffness in consideration, should be implemented [28, 33].

The elastic fracture process zone length, λ_{exp}^{-1}, was determined from the experimental results (i.e. from the $w_{unbon} - a$ curve computed using the experimental data P_i, a_i). As aforementioned, λ_{exp}^{-1} is defined as the distance over which the positive peel stress is distributed up to the yield strength of the bulk adhesive, see Figs. 4.11(b), 4.11(d), 4.11(f), 4.12(b) and 4.12(d). The values of λ_{exp}^{-1} are summarized

in Table 4.8. As expected, the elastic fracture process zone length increases with the adhesive bond-line thickness. Concerning the region of σ_{yy} in the plastic domain, its length is overestimated by the plane stress plastic zone length (the light grey shaded region length up to $x = 0$ in Figs. 4.11(b), 4.11(d), 4.11(f), 4.12(b) and 4.12(d)), which is expected as the plane stress conditions are representative of the edge regions. There is a better agreement between the theoretical (Table 4.6) and the experimental predictions of the length of the plastic region when considering plane strain conditions (the light blue shaded region length in Figs. 4.11(b), 4.11(d), 4.11(f), 4.12(b) and 4.12(d)). Indeed, the stress state near the crack tip in the central regions of the adhesive joints are better represented by the plane strain conditions.

Table 4.8: λ_{exp}^{-1}: Experimental results, considering m_3.

$2t_a$ (mm)	0.4	1.1	2.6	4.1	10.1
λ_{exp}^{-1}	0.95	1.95	3.26	3.51	6.31

4.5.2. Discussion

According to Kinloch and Shaw findings [7], the specimens with a bond-line thickness of 1.1 mm would be the tougher ones as $2t_a \approx 2r_p$ (plane strain conditions) - see Table 4.6. Although this is not the case for the adhesive investigated in this study, their theory can still support the overall trend of G_I as a function of the bond-line thickness. Moreover, Irwin [36] showed that in a tensile loaded panel, the plastic deformation zone has a circular shape of diameter equal to $2r_p$. In an adhesive joint, the physical constraints of the adherends affect the shape and size of the plastic deformation zone and, consequently, the critical fracture energy of the joint. The influence of the adherends on the geometry of this region varies with the bond-line thickness and is discussed hereafter.

In the specimens with thin bond-lines of 0.4 mm, the effect of the adherends constraint is more pronounced, leading to higher confinement of the crack tip and higher local peel stresses, as shown in Fig. 4.11(b). The adherends' constraint effect seems to expand the plastic deformation zone as the length of this region is higher than $2r_p$ (plane strain conditions), resulting in a more elongated deformation zone with an elliptical shape, as reported by Kinloch and Shaw [7] and Wang et al. [37]. By increasing the bond-line thickness up to 2.6 mm, the adherends' constraint effect gets smaller, and, consequently, the plastic deformation zone length decreases and it seems to converge to the length of the plane strain $2r_p$, as can be seen in Fig. 4.11(f). In the range of bond-line thicknesses of 0.4 to 2.6 mm, it would be expected an increase on the average value of G_I as the physical constraint becomes less pronounced for thicker bond-lines and, naturally, the deformation zone becomes larger in volume. However, the experimental results show a different trend. Similar average G_I values are obtained in the range of 0.4 to 2.6 mm thick adhesive layer. The high deviations from the average G_I on each of these bond-lines affect the final result. Indeed, as shown in sub-sections 4.4.1

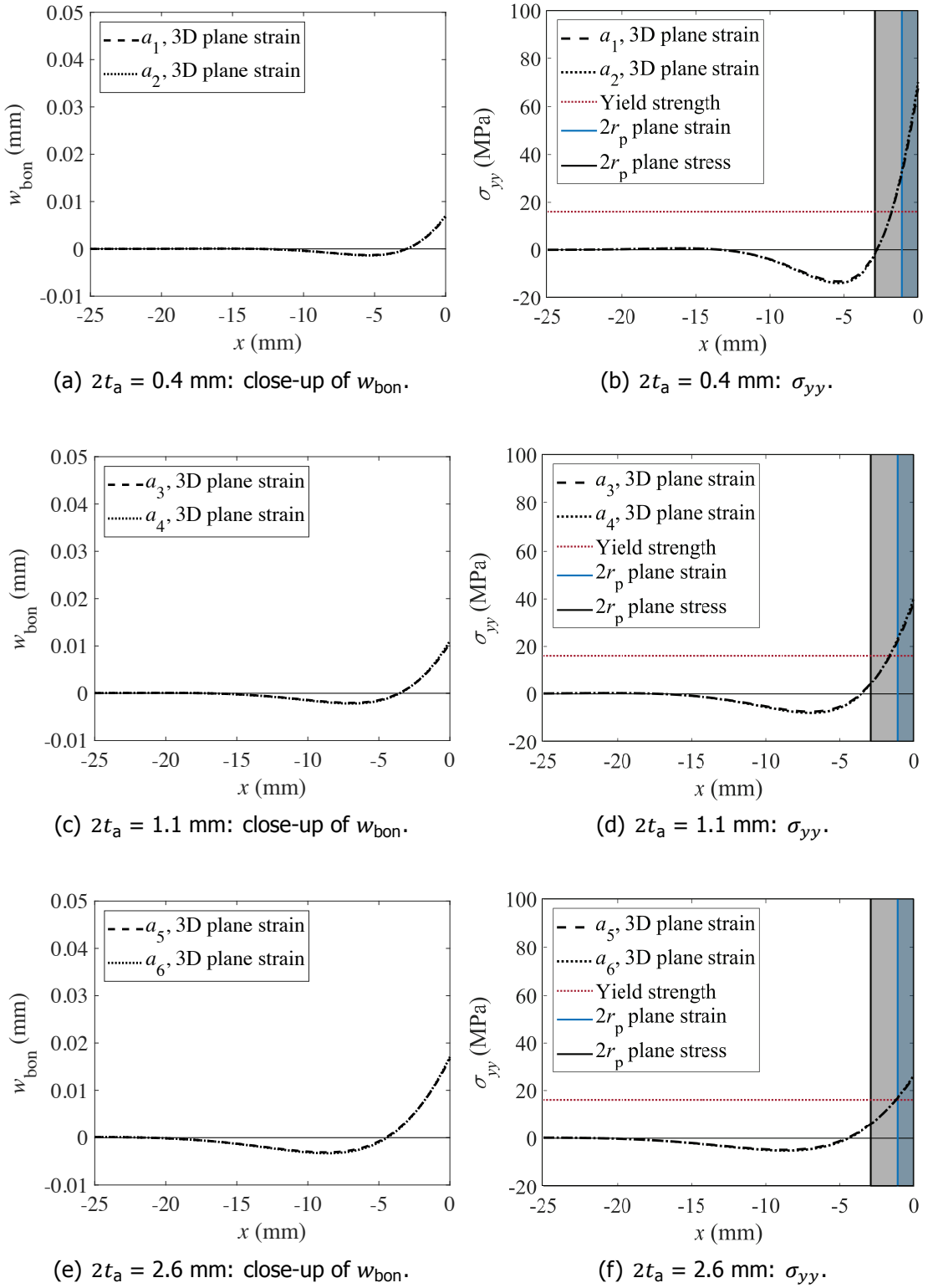

(a) $2t_a$ = 0.4 mm: close-up of w_{bon}.

(b) $2t_a$ = 0.4 mm: σ_{yy}.

(c) $2t_a$ = 1.1 mm: close-up of w_{bon}.

(d) $2t_a$ = 1.1 mm: σ_{yy}.

(e) $2t_a$ = 2.6 mm: close-up of w_{bon}.

(f) $2t_a$ = 2.6 mm: σ_{yy}.

Figure 4.11: Displacement & stress field ahead of the crack tip based on the P-K model, considering m_3 ($-\infty \leqslant x \leqslant 0$). The crack tip is located at x = 0. Two arbitrary points in the propagation region were selected for each representative specimen: a_i, P_i (i = 1-6) - see Fig. 4.4.

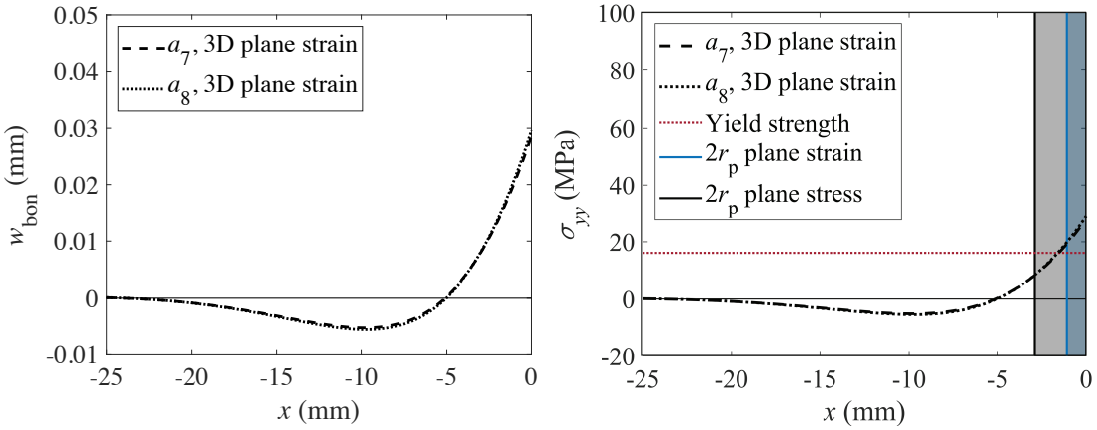

(a) $2t_a$ = 4.1 mm: close-up of w_{bon}. (b) $2t_a$ = 4.1 mm: σ_{yy}.

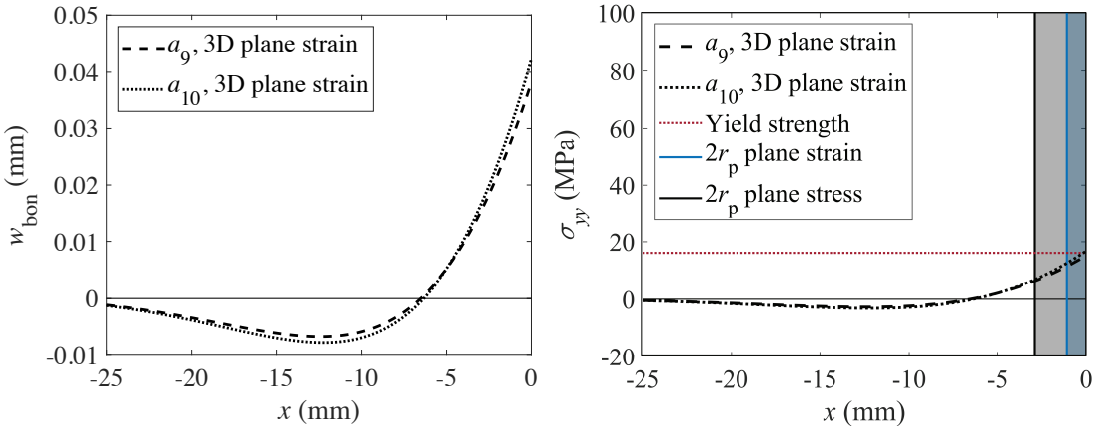

(c) $2t_a$ = 10.1 mm: close-up of w_{bon}. (d) $2t_a$ = 10.1 mm: σ_{yy}.

Figure 4.12: Displacement & stress field ahead of the crack tip based on the P-K model, considering m_3 ($-\infty \leqslant x \leqslant 0$). The crack tip is located at x = 0. Two arbitrary points in the propagation region were selected for each representative specimen: a_i, P_i (i = 7-10) - see Fig. 4.4.

and 4.4.2, the joint strength slightly decreased in the specimens with a bond-line of 1.1 and 2.6 mm in comparison with the thinnest ones with a bond-line thickness of 0.4 mm. Furthermore, the failure surfaces and crack paths present some differences. In the thinnest specimens, the surfaces are characterized by several peaks (Fig. 4.6(a)). For the thicker specimens of a bond-line of 1.1 and 2.6 mm, the failure surfaces appear smoother and the changes on the crack path plane location might have prevented the full development of the deformation zone, leading in the end to similar results of G_I. Table 4.8 shows that λ_{exp}^{-1} increases with the bond-line thickness. However, it did not seem to affect the average value of G_I in the bond-line thicknesses range of 0.4-2.6 mm, which shows that energy dissipation mainly occurs in the plastic deformation zone.

In the specimens with a bond-line of 4.1 mm, the adherends' constraining effect is supposed to be even lower due to the total thickness of the bond-line. Therefore,

the deformation zone should be fully developed, leading to higher energy dissipation before crack propagation, and consequently, to higher G_{I} values. In fact, there was a rise of approximately 84% in the average value of G_{I} from a bond-line of 2.6 mm to a bond-line of 4.1 mm. The joint strength was the highest amongst the studied bond-line thicknesses, as is shown in Fig. 4.4(d). According to Kinloch and Shaw [7], the plastic deformation zone for this bond-line thickness should have height equal to $2r_{\mathrm{p}}$ and length longer than $2r_{\mathrm{p}}$. The results in Fig. 4.12(b) agree with Kinloch and Shaw theory regarding the increase in the length of the deformation zone. Nevertheless, the P-K model assumes perfectly cohesive crack propagation (i.e. at the mid-thickness of the bond-line), which is not representative of the real crack path profile of the 4.1 mm thick adhesive bond-line specimens (see Fig. 4.6(d)). In fact, the change on the crack plane might have affected the shape, size and direction of the deformation zone, namely in the regions where the crack propagated close to one of the interfaces. Consequently, the real deformation zone length might be slightly different from the estimated by the P-K model. However, despite the real crack path, it seems that the deformation zone could develop more in the specimens with a bond-line thickness of 4.1 mm than in the ones with 2.6 mm thick adhesive bond-line as it is shown by the higher average G_{I} value obtained.

Finally, in the specimens with a bond-line of 10.1 mm, the crack grew alternating between the two interfaces (but always within the adhesive layer). Consequently, the propagation occurred most likely under mixed mode conditions, because no geometrical and material symmetries were observed during crack propagation. As a consequence of the crack path location, the deformation zone was physically constrained just in one side (by the adherend), which might have reduced its size, and, subsequently, the critical mode I fracture energy. The estimation of $\lambda_{\mathrm{exp}}^{-1}$ and the plastic deformation zone from Fig. 4.12(d) might not be representative of the experiment due to the crack plane location. As aforementioned, in the P-K model is assumed that the crack is located at the mid-thickness of the bond-line. The deeper understanding of possible reasons behind alternating crack path are distinct from the core objective of this chapter, and hence the interested reader is referred to [38–42] for more details.

Although the same adhesive was used in the present study and on the study of Maloney [5], two different trends of the critical mode I fracture energy as a function of the adhesive bond-line thickness were obtained. Maloney's results show an increase on the critical fracture energy from a bond-line thickness of 0.2 mm up to 1.1 mm ($G_{\mathrm{Ic}} = 0.19$ and $G_{\mathrm{Ic}} = 0.73 \pm 0.07$ N/mm, respectively). At this thickness, a maximum on the critical fracture energy is observed. For thicknesses higher than the optimum, the critical mode I fracture energy tends to the bulk adhesive critical fracture energy, $G_{\mathrm{Ic}} = 0.64 \pm 0.07$ N/mm. The reader should note that Maloney's specimens were cured 16 hours at 60°C, while the specimens manufactured for the present study were cured 1 hour at 80°C. By comparison of the experimental stress-strain curves of both cured systems, a more flexible behaviour is found on the system cured at 80°C with an average failure strain of about 5%, while the system cured at 60°C presents a failure strain of about 3%.

The research done in the past has proved that there is a dependence of the critical

fracture energy of adhesive joints on bonding thickness, regardless of the nature of the adhesives. However, there is no single trend for this dependency. Some studies [2, 4, 5, 7] affirm that the critical mode I fracture energy is directly related to the size of the process zone forming in the adhesive material ahead of the crack tip and its variation with adhesive layer thickness is determined by the constraint effect from the adherends. In the present study, the critical mode I fracture energy, G_{Ic}, presented similar values for the specimens with adhesive bond-line thicknesses in the range of 0.4 mm to 2.6 mm, and it increased by approximately 63% for the joints of 4.1 mm thick bond-line. Further increase in the thickness of the adhesive layer led to a decrease of about 10% in G_{Ic} (in comparison with 4.1 mm thick bond layer). These results show that the increase in bond thickness does not always lead to an increase in the critical fracture energy. The reasons for the trend of these results are attributed to: (a) the crack path, which influences the stress field ahead of the crack tip and, consequently, the size of the deformation zone, and (b) the differences in the fracture surfaces'morphology.

4.6. Conclusions

The effect of the adhesive bond-line thickness, varying from 0.4 to 10.1 mm, on the mode I fracture behaviour of steel to steel joints bonded with a structural epoxy adhesive was investigated. This range of bond-line thicknesses is relevant for maritime applications, where the efficient production of the superstructures leads to required thicker bonds than for aerospace applications. An experimental test campaign of double-cantilever beam (DCB) specimens was carried out in laboratory conditions. Five bond-line thicknesses were studied: 0.4, 1.1, 2.6, 4.1 and 10.1 mm.

Analytical predictions of the experimental load-displacement curves were performed based on the Simple Beam Theory (SBT), the Compliance Calibration Method (CCM) and the Penado-Kanninen (P-K) model. The P-K model was used to determine the mode I strain energy release rate (SERR). The critical mode I SERR, G_{Ic}, presented similar values for the specimens with adhesive bond-line thicknesses of 0.4, 1.1 and 2.6 mm ($G_{\mathrm{Ic}} = 0.71$, 0.61, 0.63 N/mm, respectively). However, it increased by approximately 63% for 4.1 mm ($G_{\mathrm{Ic}} = 1.16$ N/mm), and decreased about 10% (in comparison with 4.1 mm) for the 10.1 mm ($G_{\mathrm{Ic}} = 1.04$ N/mm). The trend of the G_{Ic} in relation to the bond-line thickness is explained by the combination of three factors: the crack path location, the failure surfaces features and the stress field ahead of the crack tip.

In all tested specimens, the crack has propagated cohesively (regardless of the bond-line thickness). However, the crack showed a tendency to propagate with an alternating trajectory (i.e. the crack grew along an alternating path along the bond-line thickness). This behaviour affects the stress field ahead of the crack tip and, consequently, the extent of the deformation zone ahead of it (i.e. crack propagation in the mid-thickness of the adhesive layer allows the full development of the process zone, while propagation in a plane more remote from the specimen mid-plane restricts the development of this zone). Among all tested bond-line thicknesses, it seems that the alternating crack path pattern affected the least the thinnest bond-

line of 0.4 mm, leading to similar values of the average G_{I} in the range of 0.4 to 2.6 mm. Moreover, the average joint strength was higher and the failure surfaces were rougher in the bond-line of 0.4 mm than in the specimens with bond-lines of 1.1 and 2.6 mm. Although the alternating (wavy) pattern on the crack path was also present in the specimens with an adhesive layer thickness of 4.1 mm, it is thought that the deformation zone could develop further than in the bond-line thickness of 2.6 mm, which is corroborated by the higher G_{Ic} value obtained. Finally, in the thickest specimens (10 mm), the crack onset moved towards the steel-epoxy interface due to geometry singularity. The crack grew alternating between the two interfaces. As a consequence of the crack path location, the deformation zone was physically constrained just on one side, which might have decreased its size, and, subsequently, the critical mode I fracture energy.

The critical mode I fracture energy-bond-line thickness trend presented in this study shows that the increase in bond thickness does not always lead to a rise in the critical fracture energy. The reasons for this trend are attributed to: (a) the crack path, which influences the stress field ahead of the crack tip and, consequently, the size of the deformation zone, and (b) the differences in the fracture surfaces'morphology.

4.7. Data availability

The data required to reproduce these findings are available at:
https://doi.org/10.4121/uuid:b3fe805b-3833-42a9-bcd8-de39c2211ca7

References

[1] R. Lopes Fernandes, S. Teixeira de Freitas, M. K. Budzik, J. A. Poulis, and R. Benedictus, *From thin to extra-thick adhesive layer thicknesses : fracture of bonded joints under mode I loading conditions,* Engineering Fracture Mechanics **218** (2019), 10.1016/j.engfracmech.2019.106607.

[2] D. L. Hunston, A. J. Kinloch, and S. S. Wang, *Micromechanics of fracture in structural adhesive bonds,* The Journal of Adhesion **28**, 103 (1989).

[3] M. B. Ouezdou and A. Chudnovsky, *Stress and energy analysis of toughness measurement for adhesive bonds,* Engineering Fracture Mechanics **29**, 253 (1988).

[4] W. D. Bascom, R. L. Cottington, R. L. Jones, and P. Peyser, *The fracture of epoxy- and elastomer-modified epoxy polymers in bulk and as adhesives,* Journal of Applied Polymer Science **19**, 2545 (1975).

[5] K. J. Maloney, *Micro-architected adhesive joints*, Ph.D. thesis, University of Cambridge (2016).

[6] S. Marzi, A. Biel, and U. Stigh, *On experimental methods to investigate the effect of layer thickness on the fracture behavior of adhesively bonded joints,* International Journal of Adhesion and Adhesives **31**, 840 (2011).

[7] A. J. Kinloch and S. J. Shaw, *The fracture resistance of a toughened epoxy adhesive,* The Journal of Adhesion **12**, 59 (1981).

[8] T. Carlberger and U. Stigh, *Influence of layer thickness on cohesive properties of an epoxy-based adhesive - an experimental study,* Journal of Adhesion **86**, 814 (2010).

[9] D.-B. Lee, T. Ikeda, N. Miyazaki, and N.-S. Choi, *Effect of bond thickness on the fracture toughness of adhesive joints,* Journal of Engineering Materials and Technology **126**, 14 (2004).

[10] S. R. Ranade, Y. Guan, D. C. Ohanehi, J. G. Dillard, R. C. Batra, and D. A. Dillard, *A tapered bondline thickness double cantilever beam (DCB) specimen geometry for combinatorial fracture studies of adhesive bonds,* International Journal of Adhesion and Adhesives **55**, 155 (2014).

[11] V. Cooper, A. Ivankovic, A. Karac, D. McAuliffe, and N. Murphy, *Effects of bond gap thickness on the fracture of nano-toughened epoxy adhesive joints,* Polymer **53**, 5540 (2012).

[12] T. Pardoen, T. Ferracin, C. M. Landis, and F. Delannay, *Constraint effects in adhesive joint fracture,* Journal of the Mechanics and Physics of Solids **53**, 1951 (2005).

[13] H. R. Daghyani, L. Ye, and Y. W. Mai, *Mode-I fracture behaviour of adhesive joints. Part II. Stress analysis and constraint parameters,* The Journal of Adhesion **53**, 163 (1995).

[14] H. R. Daghyani, L. Ye, and Y. W. Mai, *Mode-I fracture behaviour of adhesive joints. Part I. Relationship between fracture energy and bond thickness,* The Journal of Adhesion **53**, 149 (1995).

[15] M. D. Banea, L. F. Da Silva, and R. D. Campilho, *The effect of adhesive thickness on the mechanical behavior of a structural polyurethane adhesive,* Journal of Adhesion **91**, 331 (2014).

[16] M. Cabello, J. Zurbitu, J. Renart, A. Turon, and F. Martínez, *A general analytical model based on elastic foundation beam theory for adhesively bonded DCB joints either with flexible or rigid adhesives,* International Journal of Solids and Structures **94-95**, 21 (2016).

[17] A. Biel and U. Stigh, *Cohesive zone modelling of nucleation, growth and coalesce of cavities,* International Journal of Fracture **204**, 159 (2017).

[18] *ISO 527: Plastics - Determination of tensile properties,* (2012).

[19] M. F. S. F. de Moura, R. D. S. G. Campilho, and J. P. M. Gonçalves, *Crack equivalent concept applied to the fracture characterization of bonded joints under pure mode I loading,* Composites Science and Technology **68**, 2224 (2008).

[20] *ASTM D 5528 - Standard test method for mode I interlaminar fracture toughness of unidirectional fiber-reinforced polymer matrix composites,* (2013).

[21] S. Heide-Jørgensen and M. K. Budzik, *Crack growth along heterogeneous interface during the DCB experiment,* International Journal of Solids and Structures **120**, 1339 (2017).

[22] J. P. Berry, *Determination of fracture energies by the cleavage technique,* Journal of Applied Physics **34**, 62 (1963).

[23] M. Budzik, J. Jumel, and M. E. R. Shanahan, *Adhesive compliance effect in mode I separation: profilometry approach,* International Journal of Adhesion and Adhesives **31**, 135 (2011).

[24] M. Budzik, J. Jumel, K. I. Imielińska, and M. E. R. Shanahan, *Effect of adhesive compliance in the assessment of soft adhesives with the wedge test,* Journal of Adhesion Science and Technology **25**, 131 (2011).

[25] M. F. Kanninen, *An augmented double cantilever beam model for studying crack propagation and arrest,* International Journal of Fracture **9**, 83 (1973).

[26] D. R. Lefebvre, D. A. Dillard, and H. F. Brinson, *The development of a modified double-cantilever-beam specimen for measuring the fracture energy of rubber to metal bonds,* Experimental Mechanics **28**, 38 (1988).

[27] M. B. Ouezdou, A. Chudnovsky, and A. Moet, *Re-evaluation of adhesive fracture energy,* The Journal of Adhesion **25**, 169 (1988).

[28] F. E. Penado, *A closed form solution for the energy release rate of the souble cantilever beam specimen with an adhesive layer,* Journal of Composite Materials **27**, 383 (1993).

[29] C. L. Chow, C. W. Woo, and J. L. Sykes, *On the determination and application of cod to epoxy-bonded aluminium joints,* Journal of Strain Analysis **14**, 37 (1979).

[30] S. Krenk, *Energy release rate of symmetric adhesive joints,* Engineering Fracture Mechanics **43**, 549 (1992).

[31] J. Jumel, M. K. Budzik, and M. E. R. Shanahan, *Beam on elastic foundation with anticlastic curvature: application to analysis of mode I fracture tests,* Engineering Fracture Mechanics **78**, 3253 (2011).

[32] D. A. Dillard, B. Mukherjee, P. Karnal, R. C. Batra, and J. Frechette, *A review of Winkler's foundation and its profound influence on adhesion and soft matter applications,* Soft Matter **14**, 3669 (2018).

[33] N. B. Salem, M. K. Budzik, J. Jumel, M. E. Shanahan, and F. Lavelle, *Investigation of the crack front process zone in the double cantilever beam test with backface strain monitoring technique,* Engineering Fracture Mechanics **98**, 272 (2013).

[34] A. R. Akisanya and N. A. Fleck, *Analysis of a wavy crack in sandwich specimens,* International Journal of Fracture **55**, 29 (1992).

[35] A. R. Akisanya and C. S. Meng, *Initiation of fracture at the interface corner of bi-material joints,* Journal of the Mechanics and Physics of Solids **51**, 27 (2003).

[36] S. K. Maiti, *Linear elastic fracture mechanics,* in *Fracture mechanics: fundamentals and applications* (Cambridge University Press, 2015) 1st ed., Chap. 2, pp. 6–64, arXiv:arXiv:1408.4413v1 .

[37] S. S. Wang, J. F. Mandell, and F. J. McGarry, *An analysis of the crack tip stress field in DCB adhesive fracture specimens,* International Journal of Fracture **14**, 39 (1978).

[38] L. Banks-Sills and D. Ashkenazi, *A note on fracture criteria for interface fracture,* International Journal of Fracture **103**, 177 (2000).

[39] N. A. Fleck, J. W. Hutchinson, and Z. Suo, *Crack path selection in a brittle adhesive layer,* International Journal of Solids and Structures **27**, 1683 (1991).

[40] B. Chen and D. A. Dillard, *Numerical analysis of directionally unstable crack propagation in adhesively bonded joints,* International Journal of Solids and Structures **38**, 6907 (2001).

[41] A. G. Evans, B. J. Dalgleish, M. He, and J. W. Hutchinson, *On crack path selection and the interface fracture energy in bimaterial systems,* Acta Metallurgica **37**, 3249 (1989).

[42] B. Chen and D. A. Dillard, *The effect of the T-stress on crack path selection in adhesively bonded joints,* International Journal of Adhesion and Adhesives **21**, 357 (2001).

5

Role of adherend material on the fracture of adhesive joints

After addressing the bond-line thickness effect on the mode I fracture behaviour of adhesive joints in Chapter 4, the next logical step is to investigate the effect of the material of the adherends as it influences the constraint level of the adhesive material. Both single-material (i.e. steel-steel and composite-composite) and bi-material (i.e. steel-composite) joints bonded with a structural epoxy adhesive are studied in this chapter. Additionally, two different adhesive bond-line thicknesses are considered: 0.4 mm (thin bond-line) and 10.1 mm (thick bond-line). The results show that the critical mode I fracture energy, G_{Ic}, is independent of the adherend type and joint configuration (i.e. single or bi-material) for each bond-line thickness. For the joints with the thin adhesive layer, G_{Ic} shows average values between 0.60-0.72 N/mm, while for the joints with the thick adhesive layer average values between 0.90-1.10 N/mm are determined. In the joints with a thin adhesive layer, the failure is cohesive and the similar degree of constraint that is imposed to the adhesive by the high-modulus (i.e. steel) and/or relatively thick (i.e. composite) adherends results in similar values of G_{Ic} for both single- and bi-material joint types. In all joints with a thick adhesive layer, the crack grows closer to one of the adhesive-adherend interfaces, but still within the adhesive. The results of the critical mode I fracture energy show that the adhesive could deform similarly, although the crack has been constrained in one side by different types of adherends (i.e. either by a steel- or composite-adherend).

Parts of this chapter have been published in Composite Structures **252**, 112643 (2020) [1].

5.1. Introduction

The research carried on up to now addressed the effect of the material of the adherends on the critical fracture energy of adhesive joints by solely considering single-material adhesive joints with different adherend thicknesses. Besides, the studies available are based in standard reduction schemes, such as corrected beam theory or compliance calibration method, which do not take entirely into account the geometric and material properties of the adhesive joints, like adhesive bond-line thickness and out-of-plane stiffness of the adherends. Moreover, to the author's best knowledge, no studies investigating the possible changes on the critical fracture energy of bi-material adhesive joints are found in open literature.
Therefore, the primary objective of this chapter is to investigate the effect of the material of the adherends on the mode I fracture behaviour of adhesively bonded joints by testing single-material (i.e. steel-steel and GFRP-GFRP) and bi-material (i.e. steel-GFRP) joints bonded with a structural epoxy adhesive under DCB fracture test conditions. Moreover, two adhesive bond-line thicknesses are considered: 0.4 mm (thin bond-line) and 10.1 mm (thick bond-line). Some specimens are instrumented with strain gauges to assess the crack growth process. The Penado-Kanninen (PK) reduction scheme is outlined and applied to evaluate the mode I strain energy release rate, G_{I}. The morphology of the fracture surfaces is examined by an optical profiler and their chemical composition is analysed by a spectrometer. The results are discussed and conclusions are drawn.

5.2. Experimental

5.2.1. Materials and preparation

Materials used

Fig. 5.1 shows the three DCB configurations tested. The specimens were made of either S690 steel adherends, with a thickness of 3.0 mm, or glass fibre reinforced polymer (GFRP) laminate adherends, with a thickness of 8.6 mm, bonded with a structural two-component epoxy paste adhesive, Araldite 2015 (Huntsman®). Two adhesive bond-line thicknesses were studied: 0.4 mm (thin adhesive layer) and 10.1 mm (thick adhesive layer).
The mechanical properties of the UD-0° lamina were experimentally determined and are given in Table 5.1. The mechanical properties of the steel S690 and the epoxy adhesive are listed in Table 5.2. The steel properties were taken from the supplier's technical datasheet, while the adhesive's mechanical properties were evaluated from tensile dog bone specimens with a thickness of 2 mm in accordance with ISO 527 [2].

Assumption concerning symmetry of the bi-material specimen

The bi-material steel-GFRP DCB specimens were manufactured by following the longitudinal strain based design criterion developed in Chapter 3 to guarantee pure mode I loading at the crack tip. The strain based criterion is given by,

$$E_x^{\text{f-adher 1}} h_{\text{adher 1}}^2 = E_x^{\text{f-adher 2}} h_{\text{adher 2}}^2, \tag{5.1}$$

where $E_x^{\text{f-adher 1,2}}$ is the flexural modulus of adherend 1 and 2, respectively. Here, steel and GFRP adherends are used. Therefore, for the steel adherend, $E_x^{\text{f-steel}}$ is equal to the Young's modulus (see Table 5.2). The effective flexural modulus of the GFRP laminate, $E_x^{\text{f-GFRP}}$, is calculated by applying the classical lamination theory (CLT) [3]. In the case of a non-symmetric lay-up, $E_x^{\text{f-GFRP}}$ is equal to,

$$E_x^{\text{f-GFRP}} = \frac{12}{h_{\text{GFRP}}^3 J_{44}}, \tag{5.2}$$

where J_{44} component is obtained from matrix $[J]$,

$$[J] = \left[\begin{array}{c|c} A & B \\ \hline B & D \end{array}\right]^{-1}. \tag{5.3}$$

The $[A]$, $[B]$, and $[D]$ are the extensional, coupling and flexural matrices of the GFRP laminate, respectively [3].

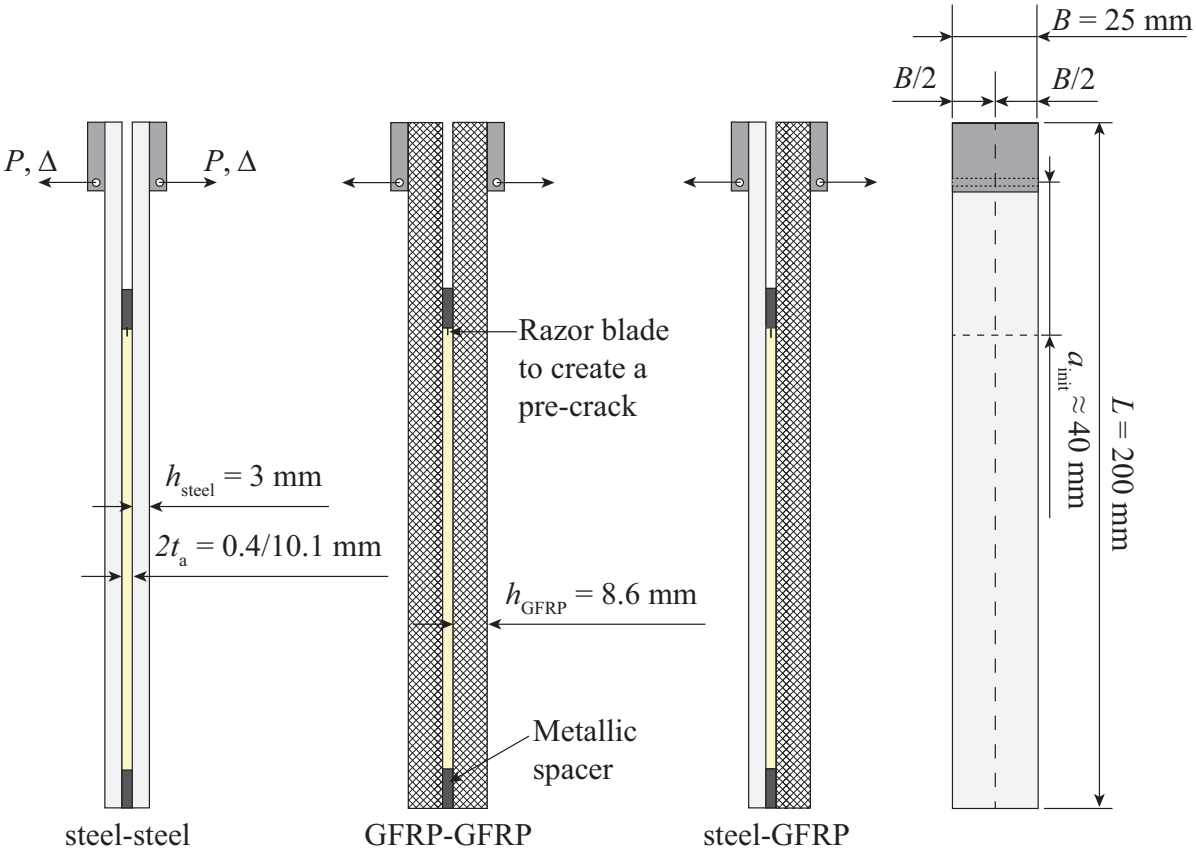

Figure 5.1: DCB specimen: the three tested configurations.

By considering the steel adherend thickness, h_{steel}, equal to 3 mm, the GFRP adherend is designed to meet the longitudinal strain based criterion. The lay-up of the GFRP laminate is given in Table 5.3 as well as $E_x^{\text{f-GFRP}}$ and the final thickness of the laminate after post-curing. For more details about the longitudinal strain based criterion and laminate stacking definition, the interested reader is referred to Chapter 3.

Table 5.1: Mechanical properties of the UD-0° lamina.

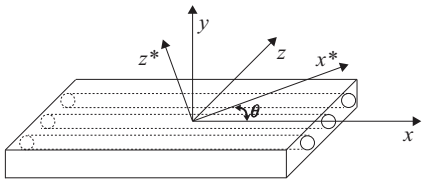

E_{xx} (MPa)	E_{zz} (MPa)	G_{xz} (MPa)	G_{xy} (MPa)	G_{zy} (MPa)	ν_{xz}
37861	12047	5003	4125	3692	0.252

Table 5.2: Mechanical properties of steel S690 and epoxy adhesive Araldite 2015.

Material	E (MPa)	ν	σ_y^{***} (MPa)	$\sigma_{ultimate}$ (MPa)
Steel S690	210000	0.30	770	832
Epoxy adhesive*	2000 $\pm$ 300	0.33**	16.1 $\pm$ 1.9	28.8 $\pm$ 0.7

* experimentally measured from dog bone specimens cured 1 hour at 80°C

** supplier's technical data-sheet

*** Steel: yield strength 0.2% offset; Adhesive: yield strength 0.1% offset

Table 5.3: GFRP laminate: lay-up based on the strain based criterion (the lay-up is defined from the bottom to the top of the laminate).

Lay-up	h^*_{GFRP} (mm)	$E_x^{f\text{-}GFRP}$ (MPa)
$[0° +45° 90° -45°]_5/[+45° 90° -45° 0°]_5$	8.60	21996

h^*_{GFRP} - final thickness of the laminate after post-cure cycle

Surface preparation and bonding

The details of surface preparation and bonding are described in Chapter 3, sub-section 3.3.1. Here, a recall is made. Small metallic spacers of 2 different thicknesses (approximately, 0.4 and 10.1 mm) were used to obtain an uniform adhesive bond-line, as shown in Fig. 5.1.

5.2.2. Test set-up

The details of test set-up are described in Chapter 3, sub-section 3.3.2. Here, a recall is made. Four GFRP-GFRP and four steel-GFRP DCB adhesive joints with thin adhesive layer were instrumented with strain gauges (Kyowa micro-measurements reference KFG-5-120-C1-11 and KFG-5-120-C1-23 with 120Ω nominal resistance for steel and GFRP adherends, respectively) to measure the adherends backface longitudinal strain. The strain gauges were bonded along the mid-line of the outer face of the adherends. In each specimen, the strain gauges were bonded at the same positions along the length direction in both adherends in order to assess the symmetry of the test. The distance between strain gauges from the applied force

is: 1) GFRP-GFRP joints = {30, 60, 80, 100, 120 mm}; 2) steel-GFRP joints = {30, 60, 80, 100 mm}. Fig. 5.2 shows an instrumented GFRP-GFRP specimen being tested. Please note that solely the GFRP-GFRP and steel-GFRP adhesive joints were instrumented with strain gauges because of their high complexity due to either the anisotropy of the GFRP adherends or the asymmetry of the bi-material joint, respectively.

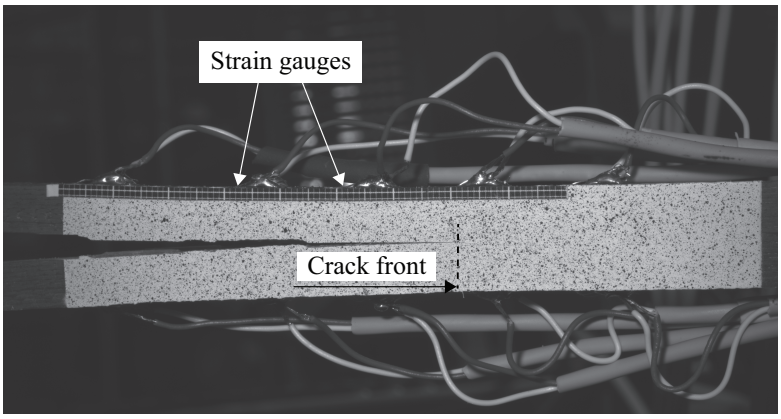

Figure 5.2: Close-up view of a GFRP-GFRP specimen instrumented with strain gauges.

5.2.3. Analysis of the fracture surfaces by a scanning microscope

All fracture surfaces of the DCB joints were examined in a Keyence VR-3200 3D optical profiler. This device is composed of a three-dimensional measuring microscope and a fringe projection scanner. The scanner is characterized by <100 nm out-of-the plane resolution with up to a 200x200 mm^2 measuring area.

5.2.4. Attenuated total reflectance-Fourier transform infrared (ATR-FTIR)

The fracture surfaces of the representative adhesive joints were analysed by the ATR-FTIR technique. The experiments were carried out by a PerkinElmer Spectrum 100 spectrometer equipped with the Universal ATR accessory. The spectrum was obtained by setting the accumulations required to 8 scans and the spectral range between 4000-600 cm^{-1} with a resolution of 4.0-7.99 cm^{-1}.

5.3. Data analysis: Penado-Kanninen model

Penado [4] developed a method to evaluate the compliance and the strain energy release rate of the DCB specimen with an adhesive layer by modifying Kanninen's "augmented DCB model" [5] for crack propagation analysis of a homogeneous specimen. The Penado-Kanninen (PK) model is obtained by considering a finite length beam, which is partially free (representing the unbonded part of the specimen) and partially supported by an elastic foundation (representing the bonded region), see Fig. 5.3. The DCB specimen is assumed to be symmetric about

the x-axis along the centreline of the adhesive layer. Only half of the specimen is represented in Fig. 5.3 (bond-line of thickness t_a). The simplest theories are used: the Euler-Bernoulli beam theory and the Winkler foundation for the free and the bonded regions, respectively [6].
It should be noted that the Winkler correction for DCB specimens with softer and thicker interlayers was subject of the study of several researchers [4, 5, 7, 8]. This approach remarkably allows the incorporation of the process zone at the crack tip. Indeed, the beams are not fixed at the crack tip due to the flexibility of the adhesive layer, which may lead to some vertical displacement of the beams within the bonded zone [9, 10].

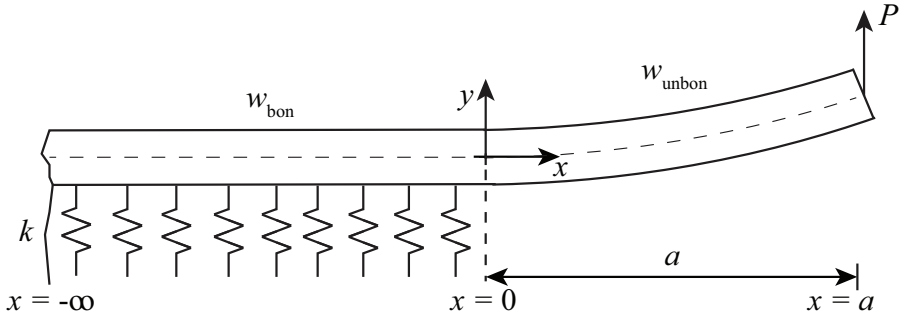

Figure 5.3: DCB specimen modelled according to Penado-Kanninen model [6].

The solution of the displacement of the Penado-Kanninen beam model is given by,

$$w(x) = \frac{P}{6E_x^{\text{f-adher}} I \lambda^3} \begin{cases} (3a\lambda^3 x^2 - \lambda^3 x^3 + 6a\lambda^2 x + 3\lambda x + 3\lambda a + 3) & 0 \leqslant x \leqslant a \\ 3e^{\lambda x}[a\lambda\cos(\lambda x) + a\lambda\sin(\lambda x) + \cos(\lambda x)] & -\infty \leqslant x \leqslant 0 \end{cases} \tag{5.4}$$

$E_x^{\text{f-adher}}$ is the flexural modulus of the adherend (in case of an isotropic adherend, $E_x^{\text{f-adher}} = E$; in case of an anisotropic adherend, $E_x^{\text{f-adher}}$ is determined by the CLT), $I = \frac{Bh_{\text{adher}}^3}{12}$ is the second moment of the beam cross-section area, and λ is the wave number, the inverse of which defines the elastic process zone length. The process zone length, λ^{-1}, in the context of the elastic foundation is interpreted as the distance (from the crack tip) over which the positive peel stress is distributed. The λ^{-1} length exits beyond of the crack tip due to the finite rigidity of the adhesive. λ is defined as,

$$\lambda = \sqrt[4]{\frac{k}{4E_x^{\text{f-adher}} I}}, \tag{5.5}$$

where k is the total foundation modulus describing the stiffness of the springs. It is assumed that the adhesive and the adherend act as springs in series. Therefore, assuming that k_{adher} and k_{adhes} represent the individual contributions, the total foundation modulus, k, is given by [4],

$$k = \frac{1}{\frac{1}{k_{\text{adher}}} + \frac{1}{k_{\text{adhes}}}}, \tag{5.6}$$

where

$$k_{\text{adher}} = \frac{4E_y^{\text{adher}} B}{h_{\text{adher}}}, \tag{5.7}$$

and

$$k_{\text{adhes}} = \left(\frac{E_{\text{a}}}{t_{\text{a}}}\right) B, \tag{5.8}$$

where E_y^{adher} is the adherend modulus in the *y*-direction (i.e. the out-of-plane tensile modulus), h_{adher} is the thickness of the adherend, E_{a} is the Young's modulus of the adhesive, t_{a} is half of the thickness of the adhesive layer, and B is the specimen width.

In the case of an isotropic adherend, $E_y^{\text{adher}} = E$. It should be noted that for a composite laminate composed of non-crimp fabric, as used in the present study, E_y^{adher} is dominated by the resin of the laminate, i.e. $E_y^{\text{adher}} \approx E_{\text{yy}}$ of a single UD-0° lamina.

The strain energy release rate is determined using the compliance method. The beam displacement at $x = a$ is given by,

$$\Delta = w_{\text{unbon}}(x = a) = \frac{P}{E_x^{\text{f-adher}} I \lambda^3}\left(\frac{1}{3}\lambda^3 a^3 + \lambda^2 a^2 + \lambda a + \frac{1}{2}\right). \tag{5.9}$$

Eq. 5.9 does not include the effect of the shear deformation in the unbonded part of the specimen. A correction for shear can be added,

$$\Delta = w_{\text{unbon}}(x = a) = \frac{P}{E_x^{\text{f-adher}} I \lambda^3}\left(\frac{1}{3}\lambda^3 a^3 + \lambda^2 a^2 + \lambda a + \frac{1}{2}\right) + \frac{3Pa}{2BG_{xy}^{\text{adher}} h_{\text{adher}}}, \tag{5.10}$$

where G_{xy}^{adher} is the shear modulus of the adherend in the *xz*-plane. For an isotropic adherend, $G = G_{xy}^{\text{adher}} = \frac{E}{2(1+\nu_{\text{adher}})}$, while for a composite material, the shear modulus G_{xy}^{adher} is estimated by using a smearing scheme. An example of a smearing scheme is the laminate homogenization method of Hyer and Knott [11].

The displacement given by Eq. 5.10 corresponds to half of the specimen. Therefore, for a single-material specimen, the total displacement is equal to 2Δ. The mode I strain energy release rate, $G_{\text{I-PK}}$, is then given by,

$$G_{\text{I-PK}} = \frac{P^2}{2B}\frac{dC}{da} = \frac{P^2}{BE_x^{\text{f-adher}} I \lambda^2}\left(\lambda^2 a^2 + 2\lambda a + 1\right) + \frac{3P^2}{2B^2 G_{xy}^{\text{adher}} h_{\text{adher}}}, \tag{5.11}$$

where P is the applied load, C is the specimen compliance, B is the specimen width and da is the instantaneous crack length extension. A straight crack front is assumed. Eq. 5.11 seems of fundamental importance revealing an inherent effect of the adhesive thickness on the elastic process zone length, λ^{-1}. The mode I strain energy release rate is directly affected by the increase of the adhesive layer thickness.

5.3.1. Adaptation to bi-material adhesive joints

The bi-material DCB adhesive joints are designed by following the longitudinal strain based criterion (see Eq. 5.1). This design criterion is achieved by matching the longitudinal strain distributions of the surfaces in contact with the adhesive layer. Therefore, the two adherends do not deflect symmetrically and, thus, the total opening displacement is given by the sum of the displacement of each arm,

$$2\Delta_{\text{bi-material}} = w_{\text{unbon}}^{\text{adher 1}}(x=a) + w_{\text{unbon}}^{\text{adher 2}}(x=a). \tag{5.12}$$

The mode I strain energy release rate of the bi-material adhesive joints, $G_{\text{I-PK}}^{\text{bi-material}}$, is then expressed as,

$$G_{\text{I-PK}}^{\text{bi-material}} = \frac{P^2}{2B}\left[\frac{\lambda_{\text{adher 1}}^2 a^2 + 2\lambda_{\text{adher 1}} a + 1}{E_x^{\text{f-adher 1}} I_{\text{adher 1}} \lambda_{\text{adher 1}}^2} + \frac{3}{2BG_{xy}^{\text{adher 1}} h_{\text{adher 1}}} + \frac{\lambda_{\text{adher 2}}^2 a^2 + 2\lambda_{\text{adher 2}} a + 1}{E_x^{\text{f-adher 2}} I_{\text{adher 2}} \lambda_{\text{adher 2}}^2} + \frac{3}{2BG_{xy}^{\text{adher 2}} h_{\text{adher 2}}}\right]. \tag{5.13}$$

5.4. Results

5.4.1. Fracture surfaces

In Fig. 5.4, optical scans of the fracture surfaces of the representative specimens of all bonded joint types with thin adhesive layer (of approximately 0.4 mm) are presented. These scans were taken from the fracture surfaces post-mortem with the Keyence VR-3200 3D optical profiler (see sub-section 5.2.3). These adhesive joints present unique features depending on the joint type. Looking at Fig. 5.4, the fracture surfaces of the representative:

- steel-steel adhesive joint show regions that are characterized by peaks and valleys, and regions with a smoother appearance, where the crack seems to propagate at the mid-thickness of the bond-line (i.e. perfectly cohesive propagation), see Fig. 5.4(a).
- GFRP-GFRP joint present some peaks and valleys, as shown in Fig. 5.4(b). Overall, the fracture surfaces reveal the tendency of the crack to grow closer to one of the adhesive-adherend interfaces, but within the adhesive. For example, in the representative specimen (see Fig. 5.4(b)), the crack propagated in the adhesive region nearby the interface with arm 2.

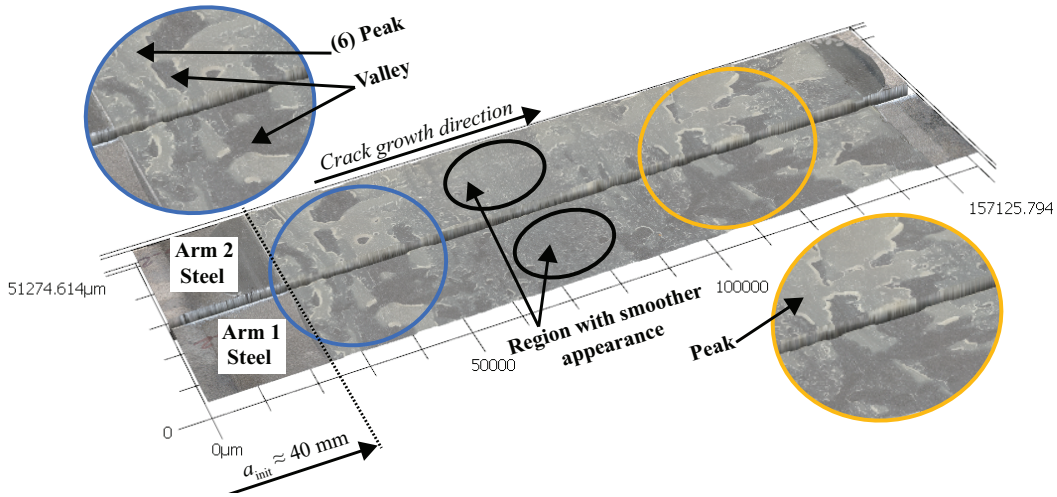

(a) Single-material steel-steel adhesive joint.

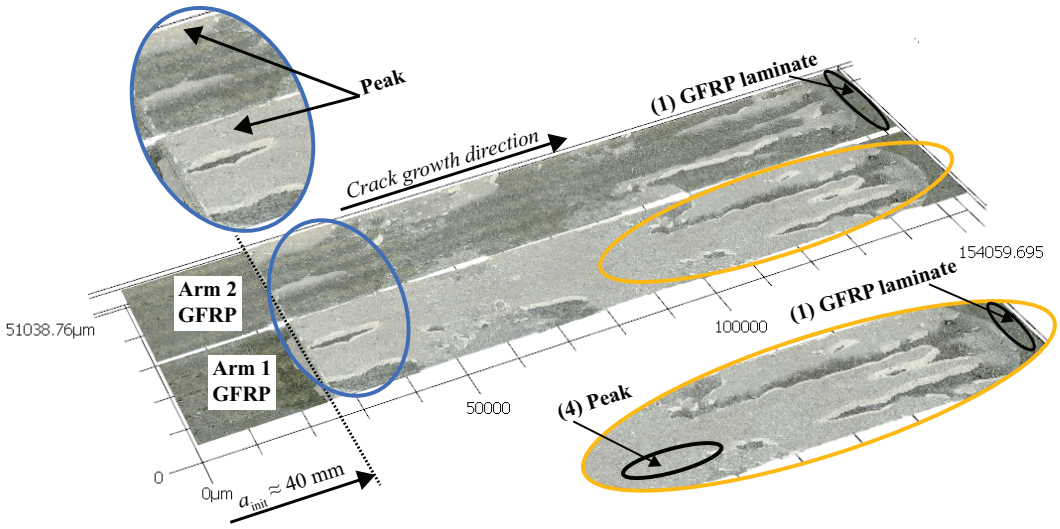

(b) Single-material GFRP-GFRP adhesive joint.

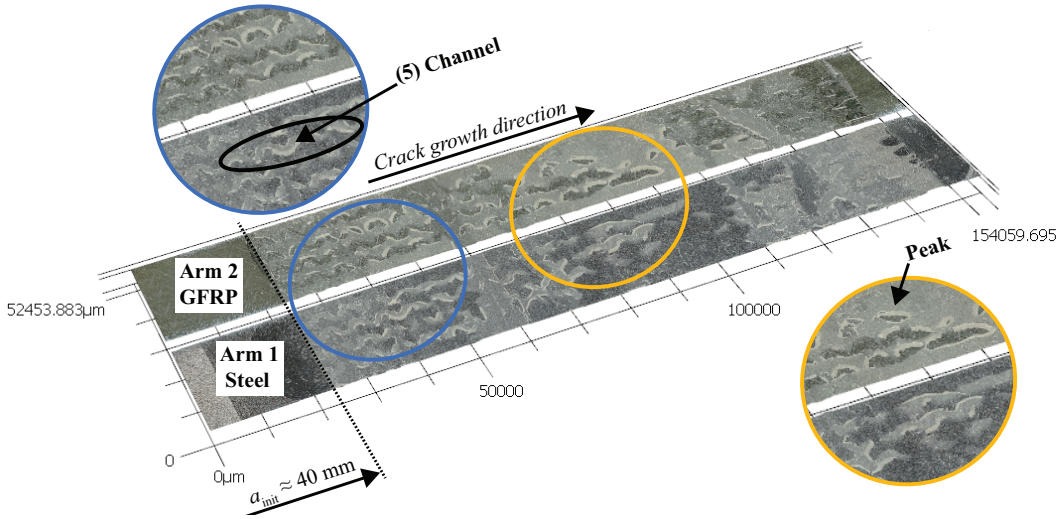

(c) Bi-material steel-GFRP adhesive joint.

Figure 5.4: Representative adhesive joints with thin adhesive layer: optical scans of the entire fracture surface of both adherends obtained by a scanning microscope.

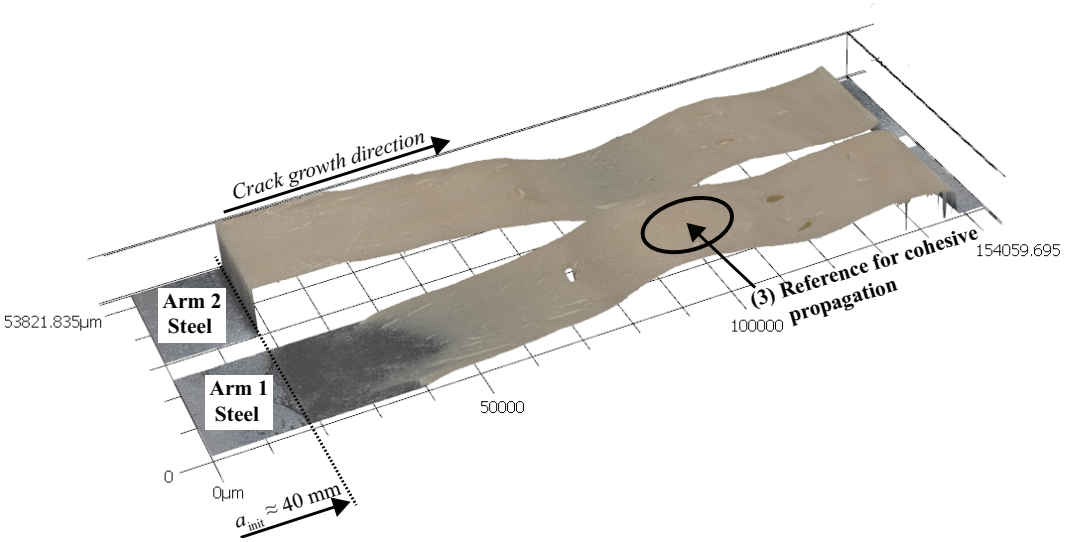

(a) Single-material steel-steel adhesive joint.

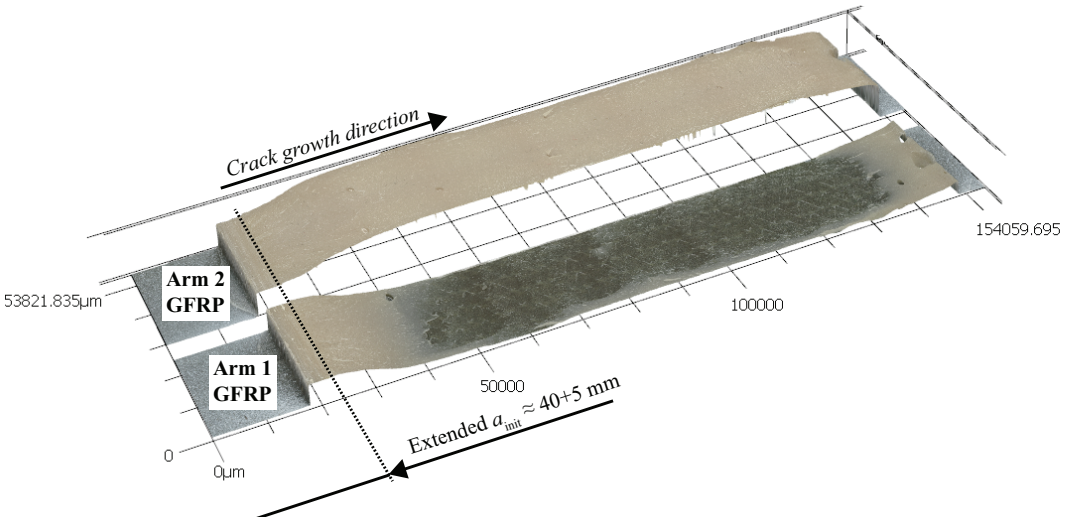

(b) Single-material GFRP-GFRP adhesive joint.

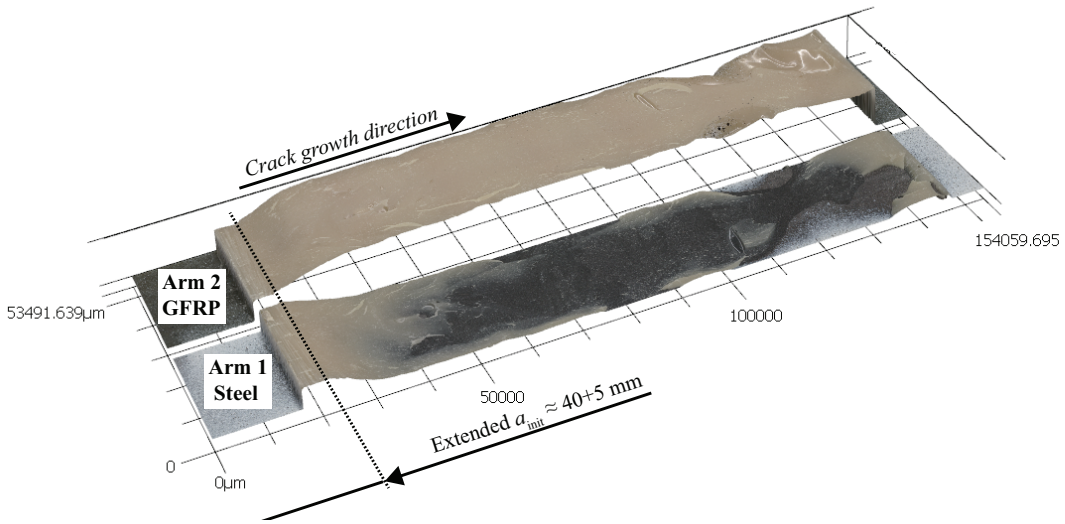

(c) Bi-material steel-GFRP adhesive joint.

Figure 5.5: Representative adhesive joints with thick adhesive layer: optical scans of the entire fracture surface of both adherends obtained by a scanning microscope.

- bi-material steel-GFRP adhesive joint show rather different fracture features. These surfaces present "adhesive channels", which are noticeable in Fig. 5.4(c), and regions where the crack jumps to planes distant from the mid-plane of the adhesive thickness. The stitching line of the GFRP laminate seems to have an influence on the development of the so-called "adhesive channels".

In Fig. 5.5, optical scans of the fracture surfaces of the representative specimens of all adhesive joint types with thick adhesive layer (of approximately 10.1 mm) are shown. Regardless of the adhesive joint type, the crack has mostly propagated in an asymmetric manner (i.e. no geometric symmetry during crack growth). Two different trends are identified at the crack initiation locus:

- in all adhesive joints with the initial pre-crack length, a_{init}, the failure initiation took place at an arbitrary plane close to one of the interfaces, but within the adhesive layer (see Fig. 5.5(a)). The mismatch in the stiffness of the materials at the interfaces (i.e. adherend and adhesive), leads to a peak of the stresses in this region of the specimen as reported by Bogy et al. and Goncalves et al. [12, 13]. The higher the mismatch, the higher the stresses. In the bi-material adhesive joints, the failure initiation took place nearby the steel adherend because the stiffness mismatch at the steel-adhesive interface is higher in comparison to the mismatch at the GFRP-adhesive interface. Overall, for longer crack lengths, the crack has propagated along the same plane, being the exception the steel-steel configuration. In steel-steel adhesive joints, an alternating crack path within the adhesive layer was observed, although the crack did run closer to one interface than the other in some segments of the bonded regions (see Fig. 5.5(a)).

- in some cases, a_{init} was extended, leading to failure initiation at the mid-plane of the adhesive layer (see Figs. 5.5(b) and 5.5(c)). However, as the crack propagated further, the crack jumped to the plane closer to one of the interfaces. In the bi-material adhesive joints, the crack grew nearby the steel interface. The extension of the pre-crack length in some specimens is worthy of comment. This extension was an attempt to experimentally observe the effect of increasing pre-crack length. Indeed, an extension of a_{init} forces the crack to stably propagate at the mid-thickness of the adhesive layer because the slope $\frac{dP}{d\Delta}$ decreases with increasing crack length [14]. However, the crack propagates in the same manner afterwards, travelling towards one of the interfaces.

Attenuated total reflectance-Fourier transform infrared (ATR-FTIR) analysis

The fracture surfaces of the representative adhesive joints were analysed by ATR-FTIR technique to evaluate the failure type (cohesive, adhesive failure or interlaminar in the GFRP adherend). The ATR-FTIR measurements performed on the fracture surfaces of the joints with the thicker adhesive layer were in agreement with the visual inspection, i.e. adhesive was found on both arms of the joints by naked eye. Concerning the joints with the thinner adhesive layer, there was

uncertainty regarding their failure type by visual inspection. However, the ATR-FTIR measurements show that the failure is cohesive regardless the adhesive joint type. Therefore, the results of the joints with thinner bond-line are presented and discussed in the subsequent paragraphs.

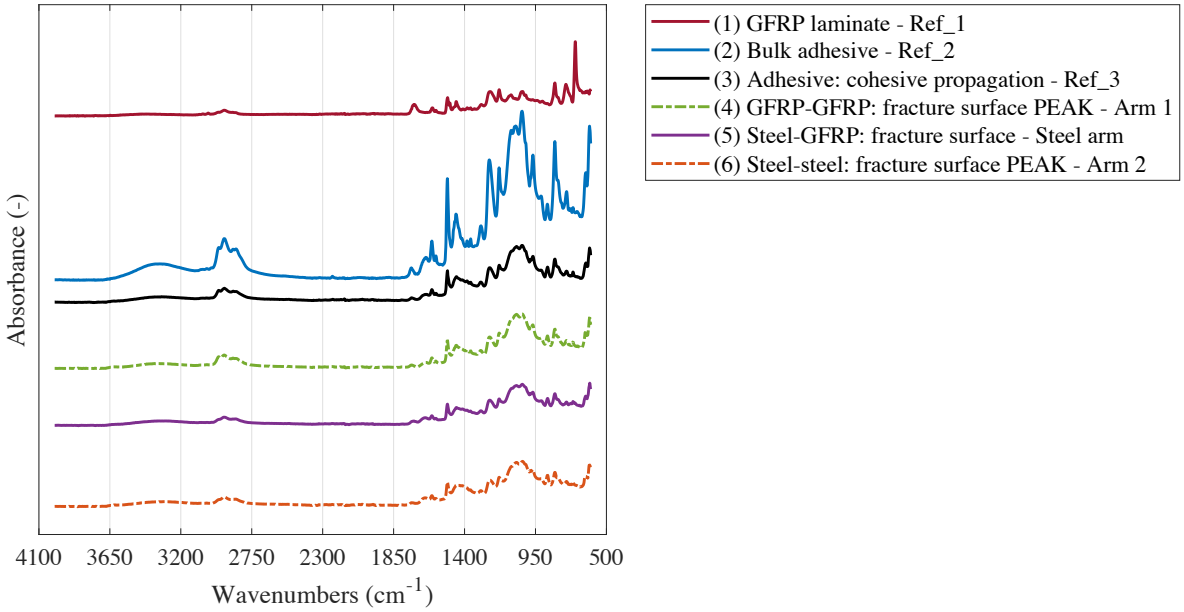

Figure 5.6: ATR-FTIR spectra: qualitative comparison.

In all adhesive joints with thin adhesive layer, the ATR-FTIR measurements were performed on characteristic areas, such as peaks and "adhesive channels" where the crack propagated in a region remote from the mid-thickness plane. ATR-FTIR measurements were performed in six different areas: (1) sanded GFRP laminate (i.e. GFRP laminate prior to bonding) - Reference 1 (Ref_1), (2) bulk adhesive (from a bulk adhesive plate cured at 80°C during one hour) - Reference 2 (Ref_2), (3) fracture area of bare adhesive (area of cohesive propagation, i.e. the propagation took place within the adhesive layer) - Reference 3 (Ref_3), (4) fracture areas of the representative GFRP-GFRP adhesive joint, (5) fracture areas of the representative steel-GFRP adhesive joint, (6) fracture areas of the representative steel-steel adhesive joint. Areas (1) and (4) are represented in Fig. 5.4(b). The areas analysed in the bi-material adhesive joint are highlighted in Fig. 5.4(c), while area (3) is represented in Fig. 5.5(a). Finally, areas (6) are shown in Fig. 5.4(a).
The ATR-FTIR spectra of the six analysed areas are shown in Fig. 5.6. A qualitative comparison is made. The spectra measured on areas (3-6) resemble the spectrum of the bulk adhesive, Ref_2. The similarity on the spectra is evidence of adhesive presence on the analysed fracture surfaces. The shape of the spectrum of the sanded GFRP laminate presents different peaks in comparison to the bulk adhesive spectrum, Ref_1 and Ref_2, respectively. The difference in the spectra is expected and is justified by the nature of the polymers studied. The GFRP laminate is composed of a rubber modified epoxy based vinyl ester resin, while Araldite 2015 is an epoxy adhesive.
Qin et al. [15] have conducted ATR-FTIR measurements on samples of bulk adhe-

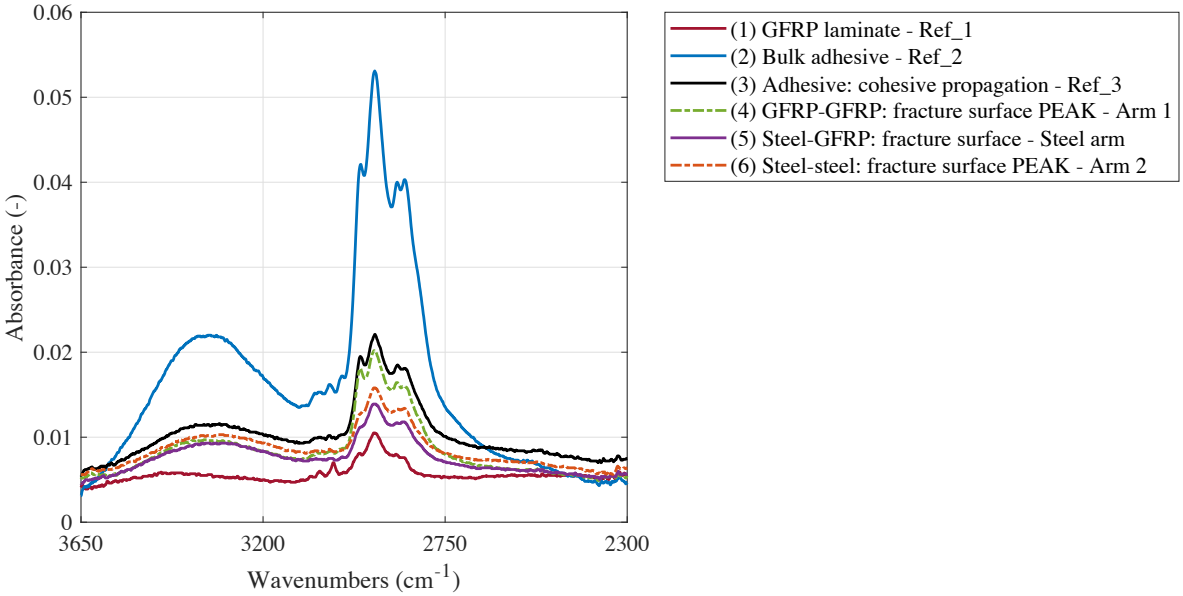

(a) Close-up of the wavenumbers in the range of 3650-2300 cm^{-1}.

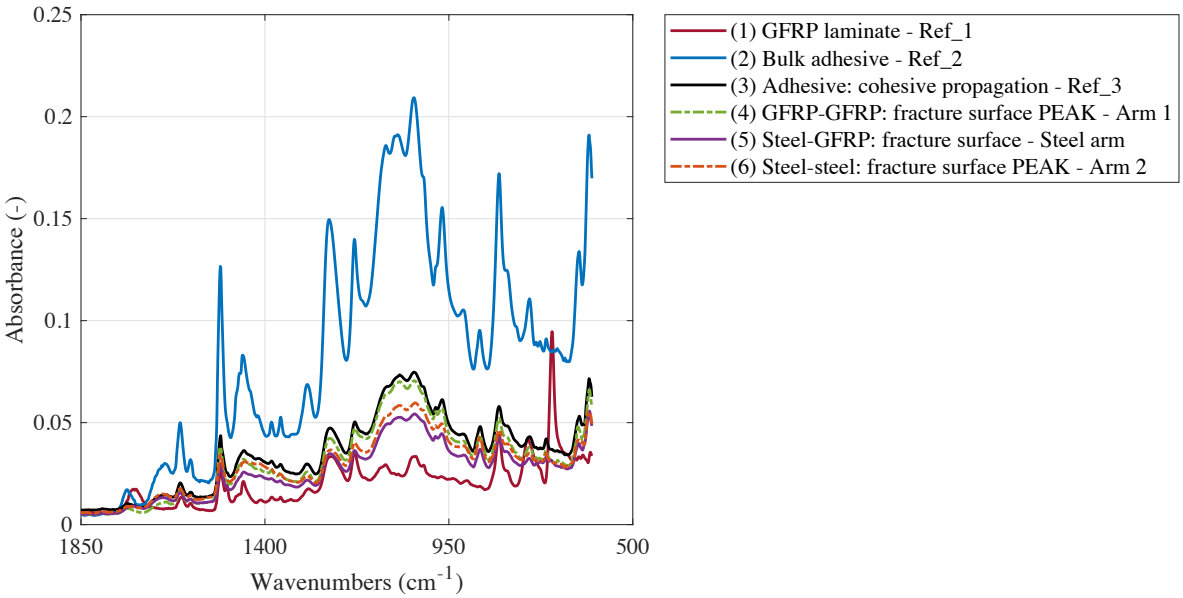

(b) Close-up of the wavenumbers in the range of 1850-500 cm^{-1}.

Figure 5.7: ATR-FTIR spectra.

sive Araldite 2015. The spectra of the adhesive here presented were qualitatively compared with the results of Qin et al. [15]. The same characteristic absorptions (peaks) were observed. The understanding of the functional groups associated with each absorption peak is distinct from the core objective of this chapter, and hence the interested reader is referred to [15] for more details.

A closer look at the spectra is presented in Fig. 5.7. These results show the same absorption peaks for the adhesive reference samples, Ref_2 and Ref_3 , and for the fracture surfaces of the adhesive joints. The occurrence of those peaks in the

fracture surfaces of the adhesive joints with the thinner bond-line is clear proof that adhesive has remained on them, indicating that cohesive propagation took place.

Finally, the spectrum of the sanded GFRP laminate (Ref_1) stands out from the other spectra (see Fig. 5.7, specially in the wavenumbers range of 1850-500 cm^{-1} (Fig. 5.7(b)). The differences in the spectra are indicative of the presence of different types of materials. As none of the fracture surfaces presented resemblances with Ref_1, it is therefore concluded that crack propagation in the GFRP laminate has not occurred.

5.4.2. Load-displacement curves and PK model validation

Figs. 5.8 and 5.9 show the representative load-displacement curves of the single-material steel-steel and the bi-material steel-GFRP bonded joints with thin (approximately 0.4 mm) and thick adhesive layer (approximately 10.1 mm), respectively. Only the representative curves are presented as the experimental load-displacement curves are consistent for each specimen within the same test series. Figs. 5.8 and 5.9 also present the theoretical estimations of the load-displacement curves based on the PK model.

The experimental displacement was predicted by the Penado-Kanninen model. Eq. 5.10 is used to estimate the displacement of the single-material DCB configurations (please note that the total displacement is equal to 2Δ), while Eq. 5.12 is used for the bi-material DCB configuration. The displacement is calculated for each data set: experimental load P_i and visually measured crack length a_i, where i is the number of data points available for each specimen (black dots on top of the experimental load-displacement curves in Figs. 5.8 and 5.9). Half-adhesive thickness, t_a, is used as an input to predict the displacement, see *PK: crack growth at mid-adhesive layer* results in Figs. 5.8 and 5.9. For the adhesive joints with thick adhesive layer, the real crack growth path is also used as an input in the PK model. The model is updated for each point to capture the alternating crack path observed in these joints, leading to a better approximation of the real case. For each a_i, the average adhesive thickness along the specimen width is used in the PK model, see *PK: real crack growth path* results in Fig. 5.9. The results concerning the GFRP-GFRP configuration are not presented in this chapter, as the trend of the theoretical estimations is similar to the one found on the steel-steel configuration regardless the bond-line thickness.

Looking at the adhesive joints with the thinner bond-line (Fig. 5.8), good agreement is observed between the experimental and the theoretical estimations based on the PK model, though no perfectly cohesive propagation occurred (the crack locus deviated from the adhesive layer mid-thickness). These results show that the changes in the crack locus direction seem to not significantly affect the plastic zone ahead of the crack tip. As the bond-line is thin, the development of this zone is controlled by the physical constraint from the adherends [16–24].

The trend between the experimental and the theoretical results is rather different in the adhesive joints with the thicker bond-line (Fig. 5.9). Although the model gives an approximation of the overall form of the load-displacement curves, that approximation is in general an overestimation of the experimental results. The analysis of the theoretical results should be divided in two groups: initial propagation re-

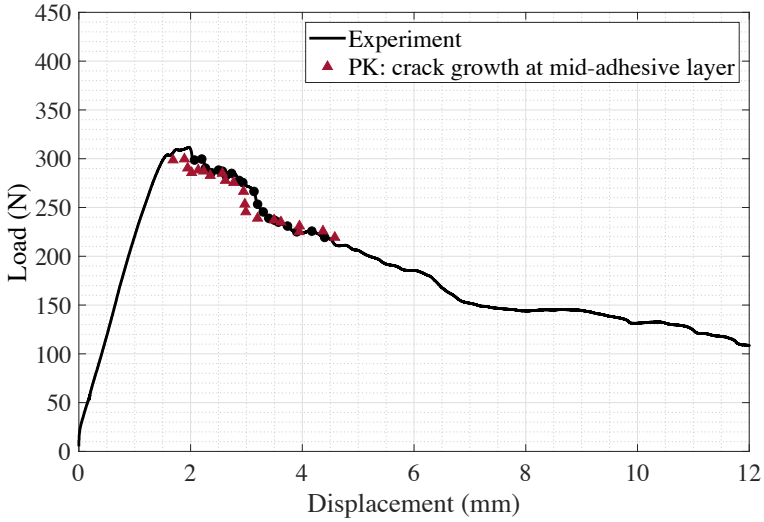

(a) Single-material steel-steel adhesive joint.

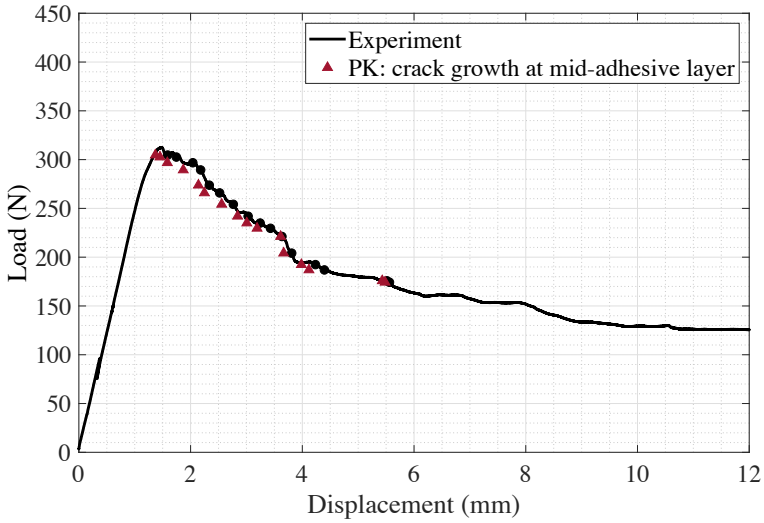

(b) Bi-material steel-GFRP adhesive joint.

Figure 5.8: Representative adhesive joints with thin adhesive layer: load-displacement curves.

gion (approximately up to 3 mm of displacement), and further away propagation region (displacement higher than 3 mm). In the initial propagation region, the PK model resembles the experimental case as there is no adhesive in the unbonded part of the specimen. Therefore, good agreement between the experimental and theoretical results is obtained. By considering the real crack path, the theoretical results are more accurate as the contribution of the adhesive to the opening displacement of the specimen is properly determined. However, in the further away propagation region, the stiffness of the adhesive layer in the unbonded part of the specimen (i.e. in the cracked portion of the specimen) is not included in the model. The flexural stiffness of the specimen is thus underestimated, resulting in higher theoretical displacement. Moreover, the alternating crack path gives an indication that the propagation occurred most likely under mixed mode conditions as shown

in [25], which is not accounted in the model.

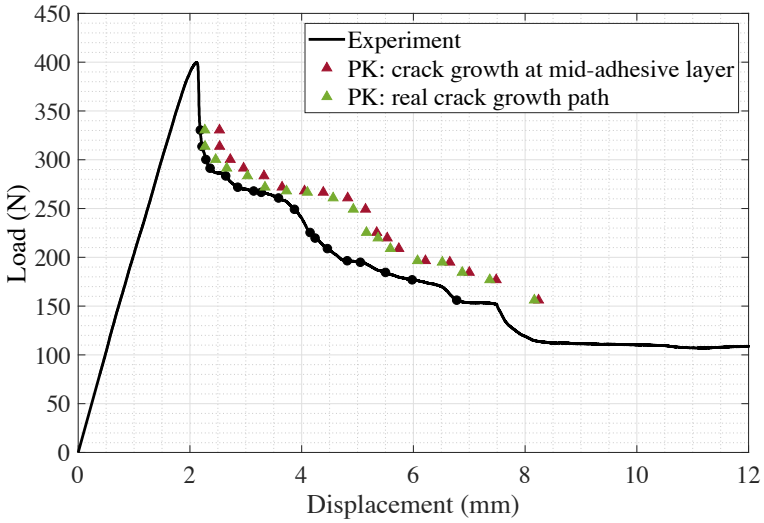

(a) Single-material steel-steel adhesive joint.

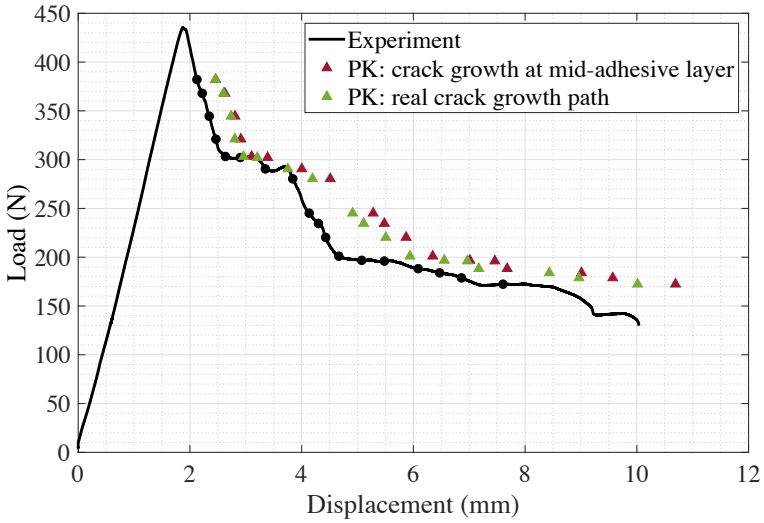

(b) Bi-material steel-GFRP adhesive joint.

Figure 5.9: Representative adhesive joints with thick adhesive layer: load-displacement curves.

As previously described in section 5.3, in the PK model, the process zone at the crack tip is not disregarded. The flexibility of the adhesive at the crack tip is accounted for the specimen displacement, which implies that the geometric (such as the bond-line thickness) and mechanical properties (such as the adhesive Young's modulus) of the adhesive are used as parameters of the model. The reasonably good theoretical results, even though the visually measured crack length is used as input, shown in Figs. 5.8 and 5.9, show the relevance of the PK model to address the mode I fracture behaviour of adhesive joints. Therefore, the PK model is used to calculate the mode I strain energy release rate of the investigated adhesive joints. The failure is assumed to be perfectly cohesive, i.e. at the mid-thickness of the adhesive layer.

5.4.3. *Resistance*-curves

Figs. 5.10 and 5.11 present the *Resistance*-curves of the representative specimens of the steel-steel and steel-GFRP bonded joint types with thin and thick adhesive layers, respectively. For each representative *Resistance*-curve, the longitudinal and transverse crack path profiles are shown in the length and width directions. These crack path profiles are taken from the 3D optical scans at specific locations at the specimen width, B'={5, 12.5, 20 mm}, and at arbitrary crack lengths, $\{a_1, a_2, a_3\}$.

G_{I} of the single-material DCB configurations is calculated by Eq. 5.11, while Eq. 5.13 is used to calculate the mode I strain energy release rate of the bi-material DCB configuration. G_{I} is calculated for each data set: experimental load P_i and visually measured crack length a_i, where i is the number of data points available for each specimen. Both longitudinal and transverse crack path profiles in Figs. 5.10 and 5.11 show that the crack did not grow uniformly along the specimen width, regardless the adhesive joint type and adhesive layer thickness. Therefore, the failure surfaces are not symmetric along the width, which makes it difficult to accurately identify the crack tip position and to determine the crack length.

The *Resistance*-curves show the evolution of the mode I strain energy release rate, G_{I}, as a function of the visually measured crack length. These curves are characterized by an oscillatory behaviour around a mean G_{I} value. In fact, the crack path profiles in Figs. 5.10 and 5.11 show that the crack did not always propagate along the same adhesive height, regardless of the joint configuration and the adhesive bond-line thickness. The changes in the crack path position lead to alternating crack paths, which result in experimental load-displacement curves characterized by a non-smooth behaviour, as shown in Figs. 5.8 and 5.9. The non-smooth behaviour indicates that the crack locus direction has changed several times during the crack growth process, potentially affecting the plastic zone, forming ahead of the crack tip. As energy dissipation mainly occurs in the plastic zone, no steady-state, self-similar regime in the *Resistance*-curves is expected, as it is corroborated by Figs. 5.10 and 5.11. Therefore, G_{I} is not constant throughout the crack growth process.

Moreover, the overall trend of the *R*-curves of the joints with thin adhesive bond-line is as expected, and while the value seems to increase during the crack growth, such could be treated as inherent property of the DCB as shown in [26].

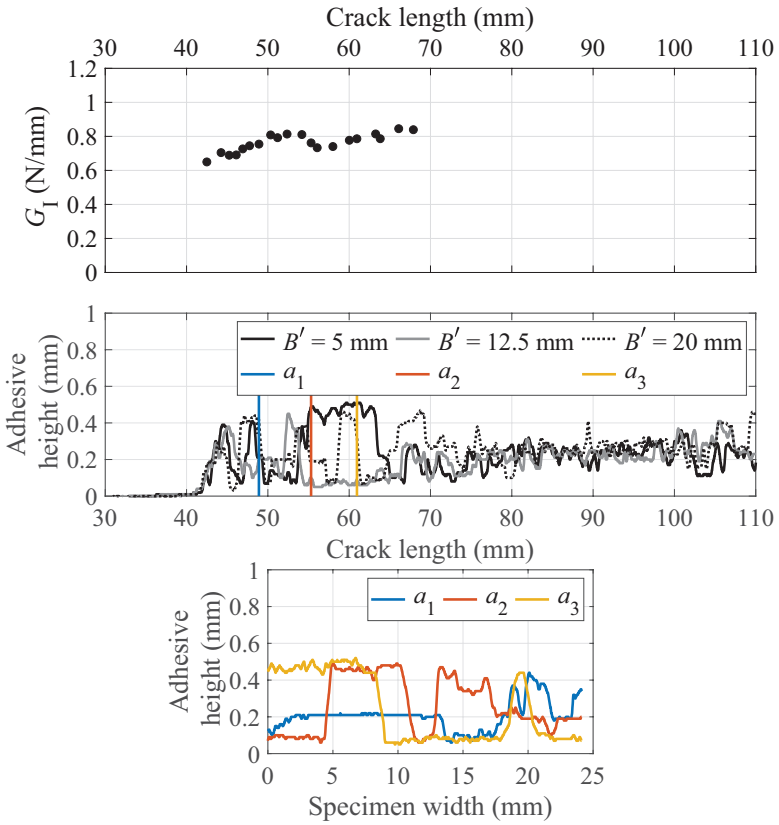

(a) Single-material steel-steel adhesive joint. The adhesive height profiles are taken from Arm 1 shown in Fig. 5.4(a).

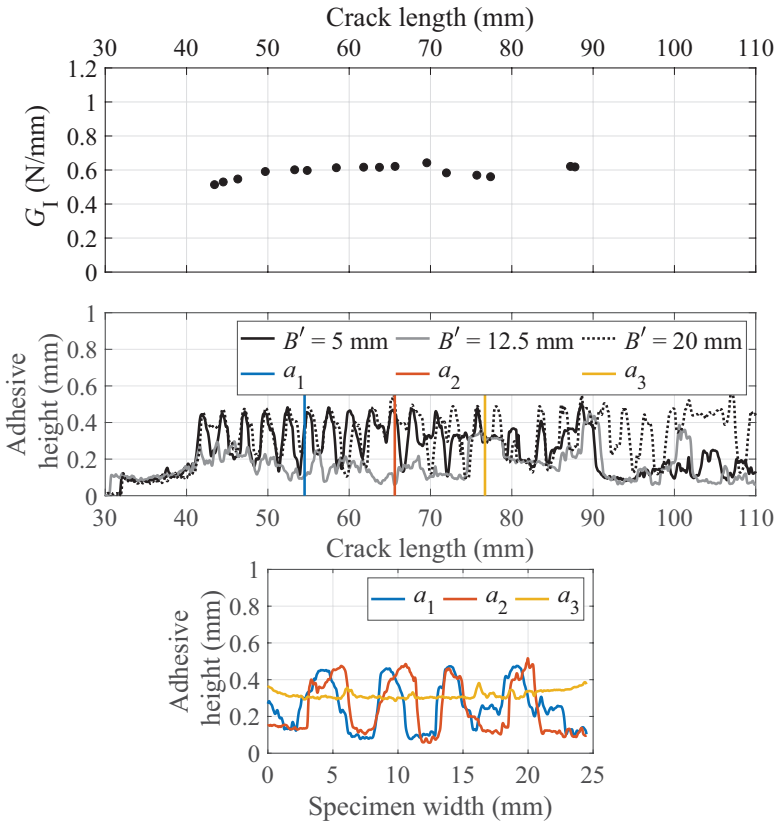

(b) Bi-material steel-GFRP adhesive joint. The adhesive height profiles are taken from Arm 1 shown in Fig. 5.4(c).

Figure 5.10: Representative adhesive joints with thin adhesive layer: *Resistance*-curves and height of adhesive remaining in one of the fracture surfaces (the crack length measurements correspond to data gathered from the image acquisition system).

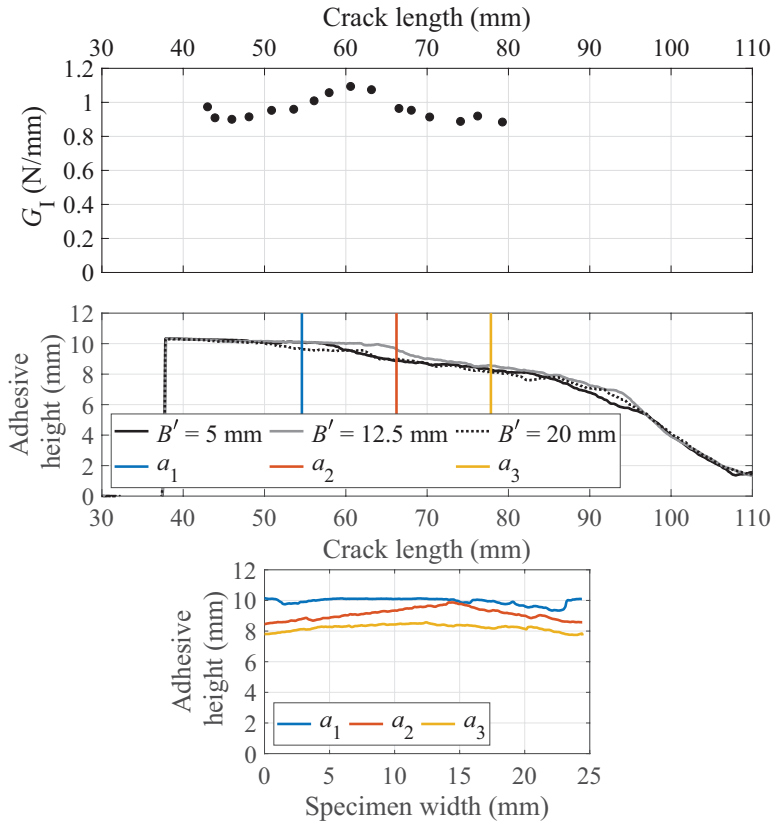

(a) Single-material steel-steel adhesive joint. The adhesive height profiles are taken from Arm 2 shown in Fig. 5.5(a).

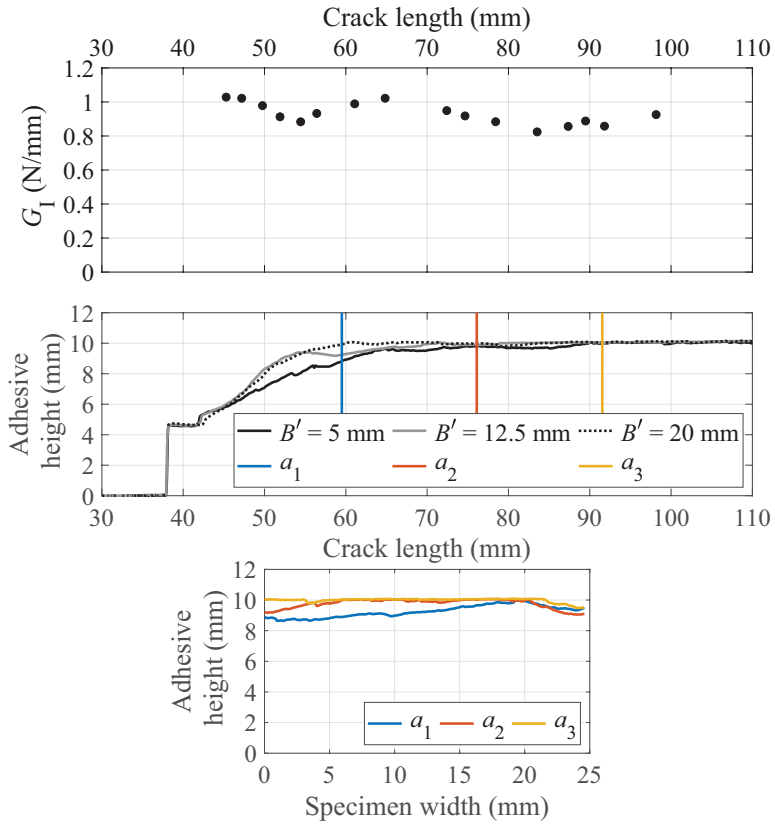

(b) Bi-material steel-GFRP adhesive joint. The adhesive height profiles are taken from Arm 2 shown in Fig. 5.5(c).

Figure 5.11: Representative adhesive joints with thick adhesive layer: *Resistance*-curves and height of adhesive remaining in one of the fracture surfaces (the crack length measurements correspond to data gathered from the image acquisition system).

5.5. Critical mode I fracture energy: results and discussion

In Fig. 5.12, the mode I strain energy release rate is plotted against the adhesive bond-line thickness. The results of the three studied configurations are shown: steel-steel, GFRP-GFRP, and steel-GFRP. The maximum, $\triangle$, and minimum, ∇, values of G_{I} of every specimen are plotted against the average thickness of the corresponding bond-line. For each adhesive joint type and nominal bond-line thickness, two error bars are shown, representing the scatter of the bond-line thickness and G_{I} results. The critical mode I fracture energy, G_{Ic}, is given by • and corresponds to the mean of all G_{I} points (maximum and minimum) and it is plotted against the average bond-line thickness of each adhesive joint type. Table 5.4 gathers the minimum, maximum as well as the average values of the bond-line thickness and G_{I} of all joint types.

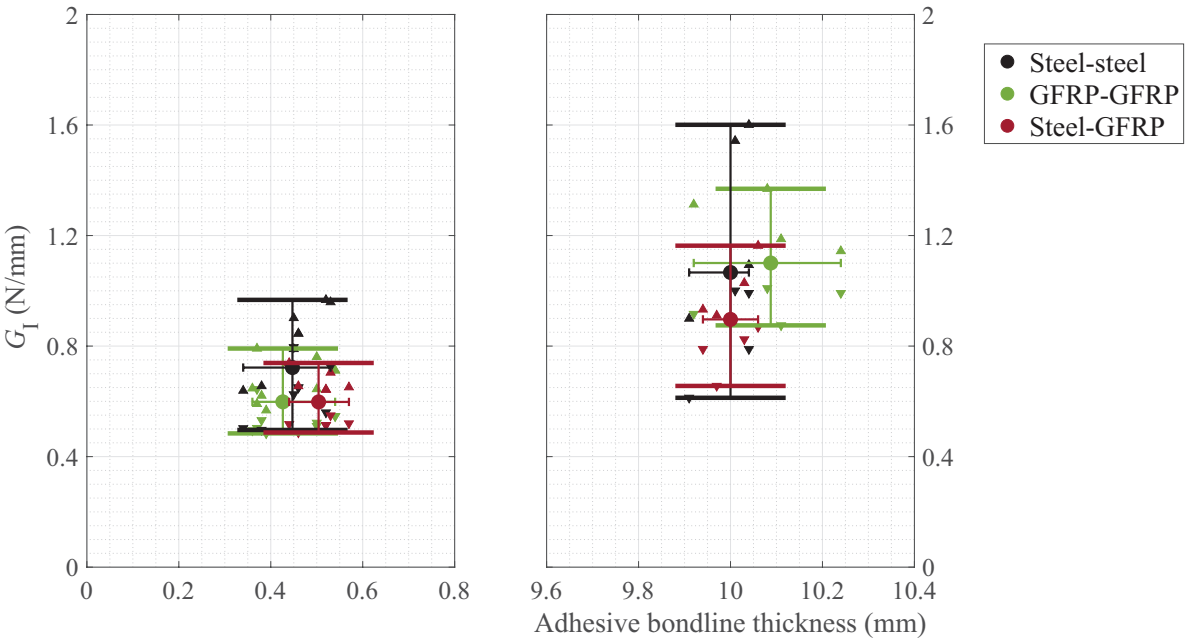

Figure 5.12: Mode I strain energy release rate vs. adhesive bond-line thickness of all joint types.

The results in Fig. 5.12 and Table 5.4 show that, for this set of adhesive joints and bond-line thicknesses, the critical mode I fracture energy is globally independent of the adherend material, even though the fracture surfaces are different. Concerning the joints with the thinner adhesive bond-line, G_{Ic} varies between 0.60-0.72 N/mm, being the lower limit given by the GFRP-GFRP and steel-GFRP configurations and the upper limit given by the steel-steel configuration. Concerning the bonded joints with the thicker adhesive bond-line, G_{Ic} varies between 0.90-1.10 N/mm, being the lower limit given by the steel-GFRP configuration and the upper limit given by the GFRP-GFRP and steel-steel configurations.

In order to better understand the independence of G_{Ic} on the adherend material, the region ahead of the crack tip ($-\infty \leqslant x \leqslant 0$) is analytically and experimen-

Table 5.4: Minimum, average and maximum values of the bond-line thickness (in mm) and the mode I strain energy (in N/mm) of all studied adhesive joints.

Bond-line	Thin			Thick		
Joint type	GFRP-GFRP	Steel-steel	Steel-GFRP	GFRP-GFRP	Steel-steel	Steel-GFRP
$2t_{\text{a-min}}$	0.36	0.34	0.44	9.92	9.91	9.94
$2t_{\text{a-av.}}$	0.43	0.45	0.50	10.09	10.00	10.00
$2t_{\text{a-max}}$	0.54	0.53	0.57	10.24	10.04	10.06
$G_{\text{I min}}$	0.48	0.50	0.49	0.88	0.61	0.66
G_{Ic}	0.60	0.72	0.60	1.10	1.07	0.90
$G_{\text{I max}}$	0.79	0.97	0.74	1.37	1.60	1.16

tally analysed, as shown in Fig. 5.13. More specifically, Fig. 5.13(a) shows the displacement of the PK model in the bonded region, w_{bon} from Eq. 5.4, of the single-material joints with thin and thick adhesive layers. Cohesive propagation at the mid-thickness of the bond-line is assumed. One representative curve is shown in Fig. 5.13(a) for each adhesive joint type and bond-line thickness. Fig. 5.13(b) presents representative experimental results of normalised longitudinal strain, ε_{xx}, from instrumented GFRP-GFRP and steel-GFRP DCB joints. ε_{xx} is normalised by the instantaneous applied force, P, and by the strain gauges position, $a_{\text{strain gauge}}$. The x-axis is shifted to superimpose the experimental curves. Please note that the experimental results are from strain gauges placed at the same position in both adherends (i.e. Arm 1 or Arm 2). The analytical solutions are derived from,

$$\frac{\varepsilon_{xx}}{P a_{\text{strain gauge}}} = \frac{h_{\text{adher}}}{2P a_{\text{strain gauge}}} \frac{d^2 w}{dx^2} \text{ for } -\infty \leqslant x \leqslant 0. \tag{5.14}$$

The length of the plastic region is estimated in Chapter 4 and is approximately 1 mm, considering plane strain conditions. This means that the two bond-line thicknesses considered lay in two different regions: the theoretical estimated plastic region is larger than the thin bond-line, but smaller than the thick bond-line. Therefore, the physical constraint of the adherends is higher in the thin adhesive layer rather than in the thick one, resulting in different crack paths and fracture surfaces as shown in Figs. 5.10-5.11 and 5.4-5.5, respectively.

In Fig. 5.13(a), the segments of the curves with positive values of w_{bon} are highlighted and labelled as $L_{\text{GFRP or Steel, 0.4 or 10.1 mm}}$, depending on the adherend material and the bond-line thickness of the adhesive joint. $L_{\text{GFRP or Steel, 0.4 or 10.1 mm}}$ provides a length scale of the portion of the adhesive in the bonded region that is being deformed: part of the adhesive within the length $L_{\text{GFRP or Steel, 0.4 or 10.1 mm}}$ is in the plastic regime, while the other fraction is in the elastic regime. Regardless the bond-line thickness, higher values of $w_{\text{bon GFRP}}$ and L_{GFRP} than $w_{\text{bon Steel}}$ and L_{Steel} are seen in Fig. 5.13(a). The low E_y^{GFRP} results in higher flexibility at the crack tip (see Eqs. 5.6-5.8), which explains the higher $w_{\text{bon GFRP}}$ in the bonded region for GFRP adherends in comparison with steel adherends. In addition, the high flexural stiffness of the GFRP adherend results in positive $w_{\text{bon GFRP}}$ extended along a larger

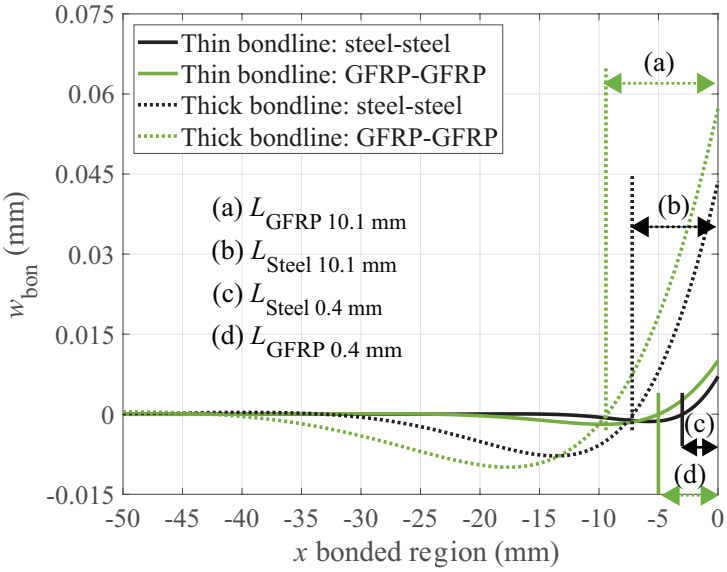

(a) Displacement of PK model in the bonded region, Eq. 5.4.

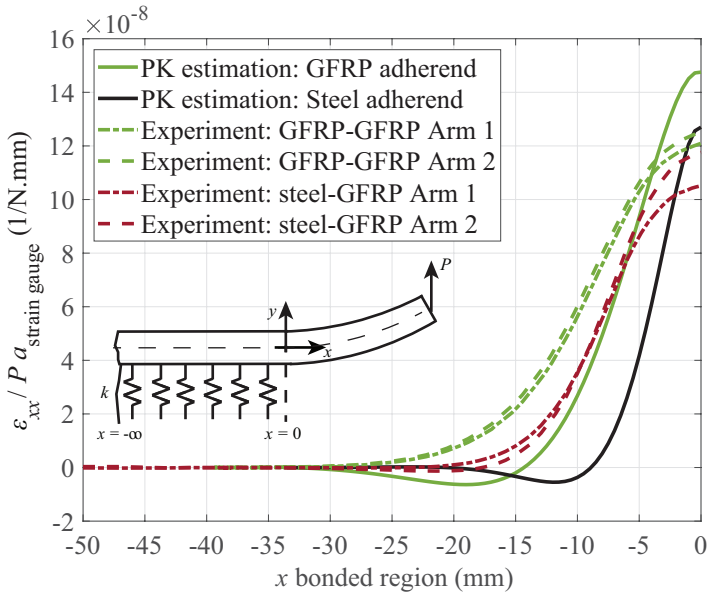

(b) Experimental results and analytical solutions for normalised longitudinal strain, ε_{xx}, of instrumented DCB joints.

Figure 5.13: Analysis of the region ahead of the crack tip ($-\infty \leqslant x \leqslant 0$): analytical approach - via PK model, and experimental approach - via strain gauges bonded in the outer face of the adherends.

distance ahead of the crack tip. A similar observation on the effect of the flexural stiffness on the extent of length L was made in [16].

The experimental results in Fig. 5.13(b) show that the process zone is clearly evidenced by the strain gauges bonded in the outer face of the adherends. For each adhesive joint type, when comparing the normalised strain of two gauges that are bonded to the upper adherend and to the lower one, good superimposition of nor-

malised strain in the bonded part is found. This is an indication of the symmetry of the tests, i.e. both adherends could uniformly deform in the longitudinal direction, resulting in pure mode I loading conditions. Moreover, the normalised strain results of the GFRP-GFRP joint are higher than the steel-GFRP results in the entire extent of the bonded region, which is in accordance with the analytical results shown in Fig. 5.13(a). Concerning the normalised strain, the steel-steel configuration is expected to appear close to the lower bound of the steel-GFRP experimental results. Finally, the PK estimation follows the tendency of the experimental curves, regardless of the adherend material. However, the region near to the crack tip, $x = 0$, is overestimated, while the extension of the positive part of the normalised strain curves is underestimated. It should be noted that the adhesive is elastically modelled, while in reality part of the adhesive in the region ahead of the crack tip is in the plastic regime. In fact, if a tangential modulus, approximately one quarter of the initial linear modulus of the adhesive, would be consider, the analytical results of the normalised strain would get closer to the experimental ones. The stress-strain curve of the adhesive is shown in Chapter 4.

The high flexural stiffness of the adherends, due to either the high stiffness of the steel or the relatively thick GFRP laminate, created similar constraint degree in the adhesive. This is demonstrated by the experimental normalised strain curves present in Fig. 5.13(b). Indeed, the intensity of the normalised strain is of the same magnitude regardless of the adherend material. Therefore, it can be concluded that the constraint imposed by the adherends to the adhesive is the same. It has been proved by other researchers [21] that the intensity of plasticity ahead of the crack tip is more important than the extension of adhesive undertaking deformation for the critical fracture energy. By having a plastic region length of 1 mm, only a small portion of the segment L near $x = 0$ is in fact in the plastic regime. As energy dissipation mainly occurs in this region and as the intensity of the normalised strain is similar regardless the joint type, similar values of the critical mode I fracture energy should be expected.

Several researchers [16–23] have shown that the constraint effect of the adherends decreases with increasing bond-line thickness, in case of cohesive propagation. In fact, this can be shown by the analytical results present in Fig. 5.13(a). The ratio $\frac{L_{GFRP}}{L_{Steel}}$ was determined for both bond-line thicknesses. This ratio gives an indication of the effect of the adherend material on the length L for each bond-line thickness. It is interesting to notice that, for the thinner bond-line, $\frac{L_{GFRP}}{L_{Steel}}$ is equal to 183%, whilst for the thicker bond-line a ratio of 138% is obtained. By increasing the bond-line thickness (from 0.4 mm to 10.1 mm), there is a reduction of almost 50% of the ratio $\frac{L_{GFRP}}{L_{Steel}}$.

Nevertheless, in the experiments of the joints with thick adhesive layer (of approximately 10.1 mm), the crack propagated asymmetrically regardless of the joint type. As explained in sub-section 5.4.1, the asymmetric propagation occurred either along a remote plane from the mid-adhesive thickness, or in an alternating way within the bond-line, although closer to one interface than the other in some segments of the bonded areas (see Fig. 5.5). Although the propagation was asymmetric,

overlapping values of G_I were found, as shown in Fig. 5.12. Overall, it seems that the adhesive could deform similarly in the joints with the thick bond-line, although the crack has been constrained in one side by different types of adherends (i.e. either by a steel- or GFRP-adherend).
As mentioned in sub-section 5.4.1, in the GFRP-GFRP and bi-material steel-GFRP adhesive joints, the crack grew close to one of the adhesive-adherend interfaces, but within the adhesive layer (see Figs. 5.5(b) and 5.5(c)). In the bi-material case, that interface was the adhesive-steel one due to the higher stiffness mismatch between the adhesive layer and the steel adherend. The higher the stiffness mismatch of the materials in the region of the interface, the higher the local stresses [12, 13], which leads to faster crack propagation and, thus, to lower critical fracture energy. Therefore, the lower range of G_I values of the steel-GFRP joints in comparison with the GFRP-GFRP joints is related with the crack growth location within the bond-line. The fracture of the GFRP-GFRP and the bi-material joints with thick adhesive layer was similar in all specimens, resulting in a small range of G_I values (see Fig. 5.12). In the steel-steel joints, the trend of fracture was rather different. Although the crack grew closer to one interface than the other, an alternating crack path behaviour was observed. This means that the crack travelled during the test from one interface to the other. The energy needed for crack propagation in a region close to the interface or in the bulk adhesive is different, resulting in the larger range of G_I values found in Fig. 5.12.

5.6. Conclusions

The primary objective of this chapter was to investigate the effect of the material of the adherends on the mode I fracture behaviour of adhesive joints. Single-material (i.e. steel-steel and GFRP-GFRP) and bi-material (i.e. steel-GFRP) joints bonded with a structural epoxy adhesive were tested under DCB fracture test conditions. Moreover, two different adhesive bond-line thicknesses were considered: 0.4 mm (thin bond-line) and 10.1 mm (thick bond-line). Some specimens were instrumented with strain gauges to assess the crack growth process. The Penado-Kanninen (PK) reduction scheme was outlined and applied to evaluate the mode I strain energy release rate, G_I. The morphology of the fracture surfaces was examined by a 3D optical profiler and their chemical composition was analysed by ATR-FTIR technique.
The failure was cohesive in all adhesive joints. Overall, the fracture surfaces of the joints with the thinner adhesive layer were characterized by peaks and valleys, revealing a non-smooth crack propagation. Asymmetric crack growth (i.e. no geometric symmetry during crack growth) always occurred on the thicker adhesive joints. By assuming perfectly cohesive propagation (i.e. at the mid-thickness of the adhesive layer), the PK model appeared to be suitable to predict the experimental displacement of the thinner adhesive joints, regardless the adhesive joint type. For the joints with thick bond-line, the PK model provided a reasonable approximation of the experimental load-displacement curve, even though the crack propagated asymmetrically. An improvement on the theoretical estimations was obtained when considering the real crack path as an input in the model.

The critical mode I fracture energy, G_{Ic}, showed to be independent of the adherend type and joint configuration (i.e. single- or bi-material). For the joints with a thin adhesive layer, G_{Ic} presented average values between 0.60-0.72 N/mm, while for the bonded joints with a thick adhesive layer average values between 0.90-1.10 N/mm were determined. In the joints with thin adhesive layer, the results from the strain gauges revealed a similar degree of constraint imposed to the adhesive by the high-modulus (i.e. steel) and/or relatively thick (i.e. composite) adherends. The similar constraint degree contributed to a similar strain field in the plastic region and, therefore, to similar G_{Ic} values for all joint configurations with a thin adhesive layer. In all adhesive joints with thick adhesive layer, the crack grew within the adhesive but closer to the adhesive-adherend interface with the highest stiffness mismatch. In the bi-material adhesive joints, the crack grew nearby the region of the adhesive-steel interface. The similar results of the critical mode I fracture energy showed that the adhesive could deform similarly, although the crack has been constrained in one side by different types of adherends (i.e. either by a steel- or GFRP-adherend).

5.7. Data availability

The data required to reproduce these findings are available at:
https://doi.org/10.4121/uuid:870395b1-92f5-4953-aa5d-aca27ef4bbc2

References

[1] R. Lopes Fernandes, S. Teixeira de Freitas, M. K. Budzik, J. A. Poulis, and R. Benedictus, *Role of adherend material on the fracture of bi-material composite bonded joints,* Composite Structures **252** (2020), 10.1016/j.compstruct.2020.112643.

[2] *ISO 527: Plastics - Determination of tensile properties,* (2012).

[3] A. K. Kaw, *Mechanics of composite materials*, 2nd ed. (CRC Press, 2006).

[4] F. E. Penado, *A closed form solution for the energy release rate of the sou-ble cantilever beam specimen with an adhesive layer,* Journal of Composite Materials **27**, 383 (1993).

[5] M. F. Kanninen, *An augmented double cantilever beam model for studying crack propagation and arrest,* International Journal of Fracture **9**, 83 (1973).

[6] S. Heide-Jørgensen and M. K. Budzik, *Crack growth along heterogeneous interface during the DCB experiment,* International Journal of Solids and Structures **120**, 1339 (2017).

[7] D. R. Lefebvre, D. A. Dillard, and H. F. Brinson, *The development of a modified double-cantilever-beam specimen for measuring the fracture energy of rubber to metal bonds,* Experimental Mechanics **28**, 38 (1988).

[8] M. B. Ouezdou, A. Chudnovsky, and A. Moet, *Re-evaluation of adhesive fracture energy,* The Journal of Adhesion **25**, 169 (1988).

[9] M. Budzik, J. Jumel, and M. E. R. Shanahan, *Adhesive compliance effect in mode I separation: profilometry approach,* International Journal of Adhesion and Adhesives **31**, 135 (2011).

[10] M. Budzik, J. Jumel, K. I. Imielińska, and M. E. R. Shanahan, *Effect of adhesive compliance in the assessment of soft adhesives with the wedge test,* Journal of Adhesion Science and Technology **25**, 131 (2011).

[11] M. W. Hyer and T. W. Knott, *Analysis of the end-fitting-induced strains in axially loaded glass-epoxy cylinders,* in *Composite struts for SMES plants (NISTIR 5024)*, edited by R. P. Reed and J. D. McColskey (1994) arXiv:arXiv:1011.1669v3 .

[12] D. B. Bogy, *On the problem of edge-bonded elastic quarter-planes loaded at the boundary,* International Journal of Solids and Structures **6**, 1287 (1970).

[13] J. P. M. Gonçalves, M. F. S. F. de Moura, and P. M. S. T. de Castro, *A three-dimensional finite element model for stress analysis of adhesive joints,* International Journal of Adhesion and Adhesives **22**, 357 (2002).

[14] W. Wang, R. Lopes Fernandes, S. Teixeira de Freitas, D. Zarouchas, and R. Benedictus, *How pure mode I can be obtained in bi-material bonded DCB joints: a longitudinal strain-based criterion,* Composites Part B: Engineering **153**, 137 (2018).

[15] G. Qin, J. Na, W. Mu, W. Tan, J. Yang, and J. Ren, *Effect of continuous high temperature exposure on the adhesive strength of epoxy adhesive, $CFRP$ and adhesively bonded $CFRP$-aluminum alloy joints,* Composites Part B: Engineering **154**, 43 (2018).

[16] S. S. Wang, J. F. Mandell, and F. J. McGarry, *An analysis of the crack tip stress field in DCB adhesive fracture specimens,* International Journal of Fracture **14**, 39 (1978).

[17] A. J. Kinloch and S. J. Shaw, *The fracture resistance of a toughened epoxy adhesive,* The Journal of Adhesion **12**, 59 (1981).

[18] D. L. Hunston, A. J. Kinloch, and S. S. Wang, *Micromechanics of fracture in structural adhesive bonds,* The Journal of Adhesion **28**, 103 (1989).

[19] H. R. Daghyani, L. Ye, and Y. W. Mai, *Mode-I fracture behaviour of adhesive joints. Part I. Relationship between fracture energy and bond thickness,* The Journal of Adhesion **53**, 149 (1995).

[20] H. R. Daghyani, L. Ye, and Y. W. Mai, *Mode-I fracture behaviour of adhesive joints. Part II. Stress analysis and constraint parameters,* The Journal of Adhesion **53**, 163 (1995).

[21] V. Cooper, A. Ivankovic, A. Karac, D. McAuliffe, and N. Murphy, *Effects of bond gap thickness on the fracture of nano-toughened epoxy adhesive joints,* Polymer **53**, 5540 (2012).

[22] S. R. Ranade, Y. Guan, D. C. Ohanehi, J. G. Dillard, R. C. Batra, and D. A. Dillard, *A tapered bondline thickness double cantilever beam (DCB) specimen geometry for combinatorial fracture studies of adhesive bonds,* International Journal of Adhesion and Adhesives **55**, 155 (2014).

[23] K. J. Maloney, *Micro-architected adhesive joints*, Ph.D. thesis, University of Cambridge (2016).

[24] R. Lopes Fernandes, S. Teixeira de Freitas, M. K. Budzik, J. A. Poulis, and R. Benedictus, *From thin to extra-thick adhesive layer thicknesses : fracture of bonded joints under mode I loading conditions,* Engineering Fracture Mechanics **218** (2019), 10.1016/j.engfracmech.2019.106607.

[25] B. Chen and D. A. Dillard, *Numerical analysis of directionally unstable crack propagation in adhesively bonded joints,* International Journal of Solids and Structures **38**, 6907 (2001).

[26] S. Heide-Jørgensen and M. K. Budzik, *Effects of bondline discontinuity during growth of interface cracks including stability and kinetic considerations,* Journal of the Mechanics and Physics of Solids **117**, 1 (2018).

6

Crack onset and path stability in “extra-thick” adhesive joints

In Chapter 2 the special case of adhesive joints with “extra-thick” bond-lines under mode I loading conditions is presented and discussed. With “extra-thick” adhesive bond-lines, a weakness to be recognized, from both scientific and applied points of view, is the stress gradient at bi-material edges and corners, exacerbated by differences in materials properties. This chapter aims to investigate the fracture onset and crack deflection in adhesive joints with 10 mm thick bond-lines under mode I loading. The role of adherend-adhesive modulus mismatch and pre-crack length are scrutinized. The parameters controlling the crack path directional stability are also discussed. Single-material (i.e. steel-steel and GFRP-GFRP) and bi-material (i.e. steel-GFRP) double-cantilever beam joints bonded with a structural epoxy adhesive are tested. The joints are modelled analytically, considering a beam on elastic-plastic foundation, to include characteristic length scales of the problem (e.g. adhesive thickness, plastic zone) and numerically using FEM. An empirical relation, in terms of geometrical and material properties of the joints, that defines the transition between cohesive close to the interface and cohesive adhesive mid-thickness fracture onset is found. Above a specific pre-crack length, the stress singularity at pre-crack tip rules over the stress singularity near bi-material corners, resulting in cohesive adhesive mid-thickness fracture onset. However, the cracking direction rapidly deflects out from the adhesive layer centre-line. Positive T-stress along the crack tip is found to be one of the factors for the unstable crack path.

Parts of this chapter have been published in Composite Structures **266**, 113687 (2021) [1].

6.1. Introduction

In this chapter, the geometry under consideration is shown in Fig. 6.1. Two adherends with finite thickness are bonded together with an adhesive of thickness $2t_a \approx 10$ mm. A pre-crack of length Δa is cut at mid-thickness of the adhesive bond-line. With such adhesive bond-line thickness, stress gradient arises at bi-material edges and corners. Length Δa plays a critical role on fracture onset locus in current approach. The definition of Δa follows the idealization of unloaded region of material adjacent to the crack surfaces in an infinite homogeneous plate with a crack as postulated by Griffith [2, 3]. The unloaded region is approximated by a triangle with the base length corresponding to Δa and a height of $2\pi\Delta a$. Δa must be sufficiently large so the corners near the interfaces are unloaded, as illustrated in Fig. 6.1 by the red diffusion lines. In other words, Δa must be sufficiently large to create a singular stress field around the pre-crack tip, in which the threshold stress is first attained rather than at bi-material edges and corners, resulting in fracture onset at the pre-crack tip.

The primary objective of this study is to investigate the fracture onset and crack deflection in adhesive joints with 10 mm thick bond-lines under mode I loading conditions. More specifically, the role of adherend-adhesive modulus mismatch and the role of pre-crack length, Δa, are scrutinized. The parameters controlling the crack path directional stability are also discussed. Single-material (i.e. steel-steel and GFRP-GFRP) and bi-material (i.e. steel-GFRP) DCB joints bonded with a structural epoxy adhesive are tested. The tests are aided by a 3D image acquisition system. Moreover, the fracture tests are modelled analytically by considering a beam on elastic-plastic foundation - Yamada [4]. To link the experimental findings to existing theoretical models, the behaviour of the different joints is also assessed numerically.

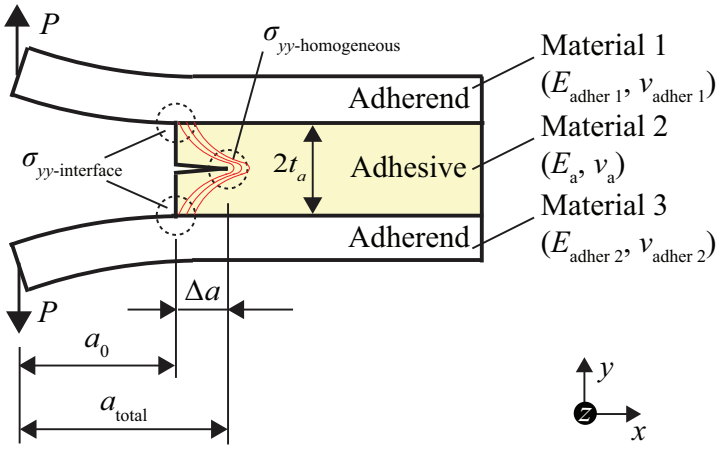

Figure 6.1: Current approach: influence of Δa length on fracture onset in adhesive joint with finite thickness adherends under mode I loading conditions.

6.2. Experimental

6.2.1. Materials and preparation

Materials used

Fig. 6.2 shows the three DCB configurations tested. The adherends were made of either S690 steel, with a thickness of 3.0 mm, or glass fibre reinforced polymer (GFRP) laminate, with a thickness of 8.6 mm. The adherends were bonded with a structural two-component epoxy paste adhesive, Araldite 2015 (Huntsman®) with a bond-line thickness of 10 mm.

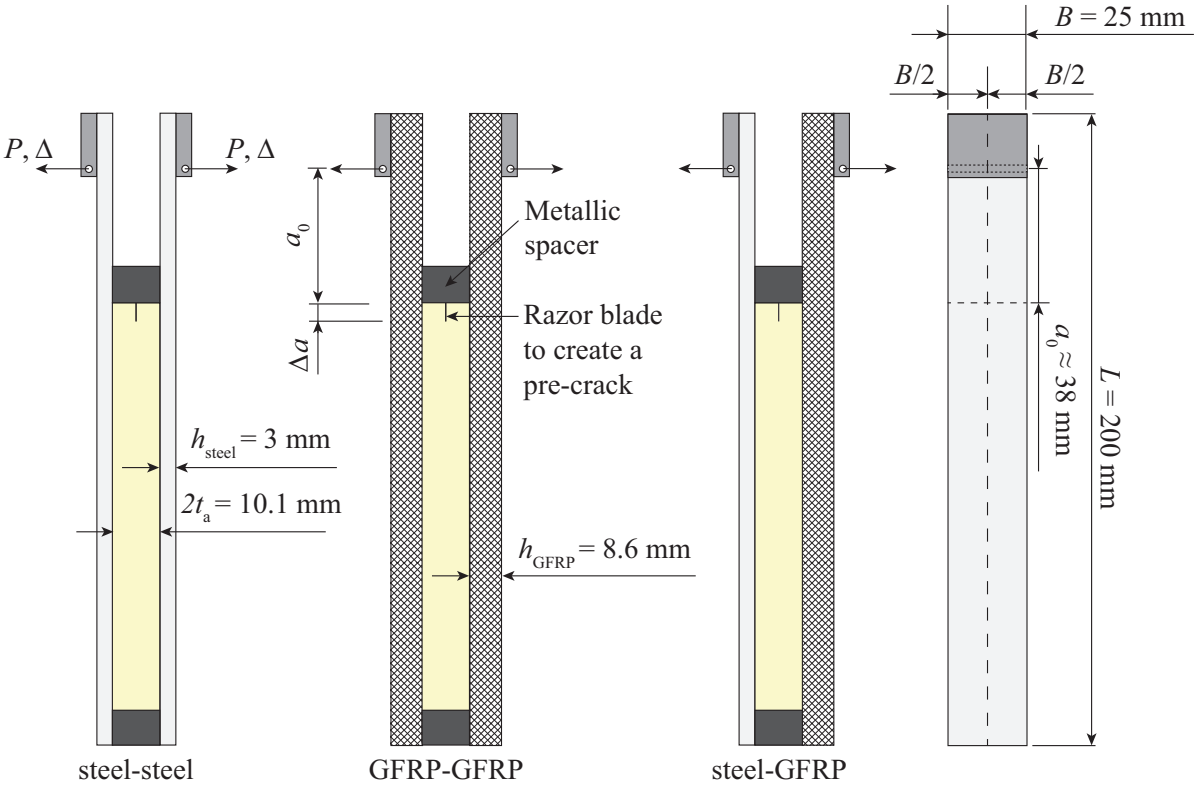

Figure 6.2: DCB specimen: the three tested configurations.

Table 6.1: Mechanical properties of the UD-0° lamina.

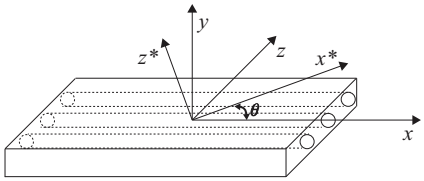

E_{xx} (MPa)	E_{zz} (MPa)	G_{xz} (MPa)	G_{xy} (MPa)	G_{zy} (MPa)	ν_{xz}
37861	12047	5003	4125	3692	0.252

The mechanical properties of the UD-0° lamina were experimentally determined and are given in Table 6.1. The mechanical properties of the steel S690 and the

epoxy adhesive are listed in Table 6.2. The steel properties were taken from the supplier's technical data-sheet, while the adhesive's mechanical properties were experimentally measured from tensile dog bone specimens with a thickness of 2 mm in accordance with ISO 527 [5].

Table 6.2: Mechanical properties of steel S690 and epoxy adhesive Araldite 2015.

Material	E (MPa)	ν	σ_y^{***} (MPa)	$\sigma_{ultimate}$ (MPa)
Steel S690	210000	0.30	770	832
Epoxy adhesive*	2000 ± 300	0.33**	16.1 ± 1.9	28.8 ± 0.7

* experimentally measured from dog bone specimens cured 1 hour at 80°C

** supplier's technical data-sheet

*** Steel: yield strength 0.2% offset; Adhesive: yield strength 0.1% offset

Assumption concerning symmetry of the bi-material specimen

The bi-material steel-GFRP DCB specimens were manufactured by following the longitudinal strain based criterion developed in Chapter 3 to guarantee pure mode I loading at the crack tip. The strain based criterion is given by,

$$E_x^{\text{f-adher 1}} h_{\text{adher 1}}^2 = E_x^{\text{f-adher 2}} h_{\text{adher 2}}^2, \tag{6.1}$$

where $E_x^{\text{f-adher 1,2}}$ is the flexural modulus of adherend 1 and 2, respectively. For the steel adherend, $E_x^{\text{f-Steel}}$ is equal to material Young's modulus (see Table 6.2). The effective flexural modulus of the GFRP laminate, $E_x^{\text{f-GFRP}}$, is calculated by applying the classical lamination theory (CLT). In the case of a non-symmetric lay-up, $E_x^{\text{f-GFRP}}$ is equal to,

$$E_x^{\text{f-GFRP}} = \frac{12}{h_{\text{GFRP}}^3 J_{44}}, \tag{6.2}$$

where J_{44} component is obtained from matrix $[J]$,

$$[J] = \left[\begin{array}{c|c} A & B \\ \hline B & D \end{array}\right]^{-1}. \tag{6.3}$$

The $[A]$, $[B]$, and $[D]$ are the extensional, coupling and flexural matrices of the GFRP laminate, respectively [6].

By considering the steel adherend thickness, h_{steel}, equal to 3 mm, the GFRP adherend is designed to meet the longitudinal strain based criterion. The lay-up of the GFRP laminate is given in Table 6.3 as well as $E_x^{\text{f-GFRP}}$ and the final thickness of the laminate after post-curing. For more details about the strain based criterion and laminate stacking definition, the interested reader is referred to Chapter 3.

Table 6.3: GFRP laminate: lay-up based on the strain based criterion (the lay-up is defined from the bottom to the top of the laminate).

Lay-up	h^*_{GFRP} (mm)	$E_x^{f\text{-}GFRP}$ (MPa)
$[0° +45° 90° -45°]_5/[+45° 90° -45° 0°]_5$	8.60	21996

h^*_{GFRP} - final thickness of the laminate after post-cure cycle

Surface preparation and bonding

The details of surface preparation and bonding are described in Chapter 3, sub-section 3.3.1. Here, a recall is made. Metallic spacers with a sharp razor blade of approximately 10 mm were used to obtain an uniform adhesive bond-line, as shown in Fig. 6.2. While the metallic strips designated the length of initially unbonded zone and the distance from the load application point - a_0, the razor blade placed in between the metallic strips created an additional pre-crack of length Δa at the mid-thickness of the adhesive bond-line. After curing the specimens, in some cases, the length Δa of the existing pre-crack was extended. Finally, prior to testing, to enable digital image correlation (DIC) evaluation, a thin layer of white paint was applied to the side of the specimens with the black speckles painted on top.

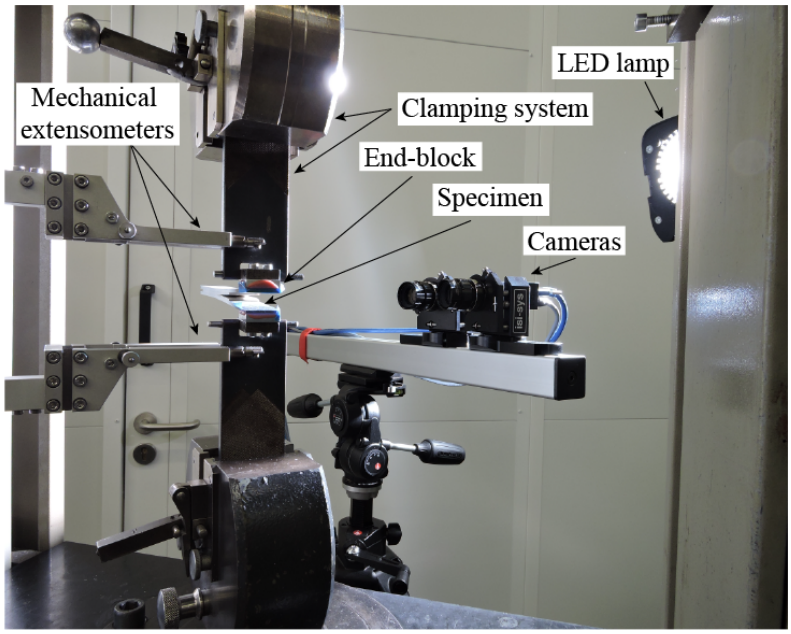

Figure 6.3: Test set-up.

6.2.2. Test set-up

The details of test set-up are described in Chapter 3, sub-section 3.3.2. Here, a recall is made. A 3D image acquisition system was used instead of a camera (VIC-3D system by Correlated Solutions, Inc.), with pictures taken every second after the load application (Fig. 6.3). The use of the 3D image acquisition system was twofold: (i) monitoring of the crack growth throughout the test and, (ii) to

obtain full-field displacement and strain fields over the specimen's surface using DIC technique. The speckle images were processed using Vic-3D 8 software. A parametric study of the effect of the subset and step size on the displacement and strain results was performed. The subset size was set to 29 and the step size was set to 7 pixels.

6.3. Modelling methods

6.3.1. Beam on elastic-plastic foundation

Incorporating relevant length scales, the adhesive thickness, the elastic stress field and the plastic fields can be tedious when using full three-dimensional continuum approach. Instead, this work uses an extension of the known Kanninen model [7] for the DCB geometry. Yamada [4] extended Kanninen's model by including adhesive plasticity effects at the crack tip. This model is followed by assuming elastic/perfectly plastic response of the adhesive while the beam remains elastic. The physical model and mathematical formulation are split into three domains/regions as seen in Fig. 6.4:

- Region 1, (deflection w_1), is the free part of the beam;
- Region 2, (deflection w_2), is the part of the beam which is supported by a perfectly plastic foundation due to the yielding of the adhesive. The stress condition at the crack tip is dominated by a vertical component. Therefore, within the yield plastic zone, an uniform uni-axial stress is assumed;
- Region 3, (deflection w_3), is the part of the beam which is supported by an elastic foundation.

The DCB specimen is assumed to be symmetric about the x-axis along the centreline of the adhesive layer. Only half of the specimen is represented in Fig. 6.4 (bond-line of thickness t_a).

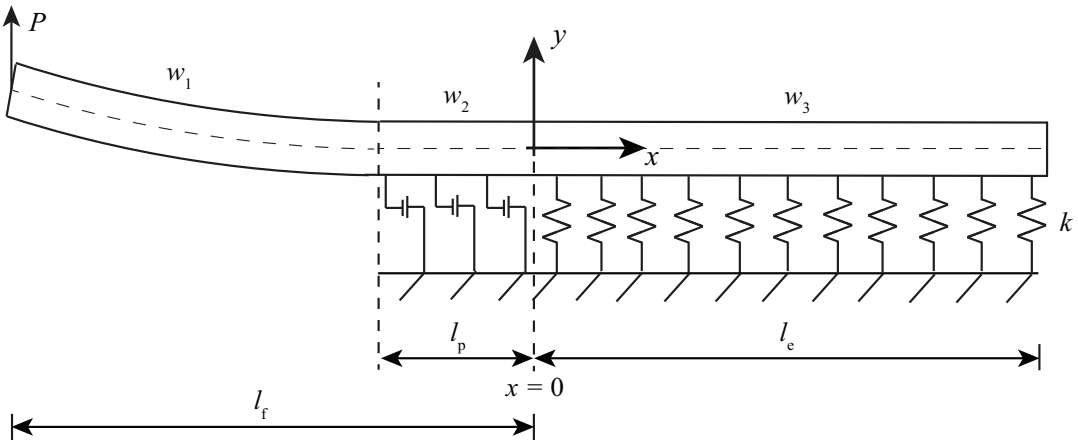

Figure 6.4: DCB specimen modelled according to Yamada's model [4]: elastic-plastic foundation.

The governing equations of the structural response are,

$$E_x^{\mathrm{f}} I \frac{d^2 w_1}{dx^2} = P(l_{\mathrm{f}} + x),\ -l_{\mathrm{f}} \leqslant x < -l_{\mathrm{p}} \tag{6.4}$$

$$E_x^{\mathrm{f}} I \frac{d^4 w_2}{dx^4} = -\sigma_{\mathrm{y}} B,\ -l_{\mathrm{p}} \leqslant x < 0 \tag{6.5}$$

$$E_x^{\mathrm{f}} I \frac{d^4 w_3}{dx^4} = -k w_3,\ 0 \leqslant x < l_{\mathrm{e}} \tag{6.6}$$

in which $E_x^{\mathrm{f}} I$ is the flexural stiffness of the beam ($I = \frac{B h_{\mathrm{adher}}^3}{12}$, being h_{adher} the thickness of the beam), w_i is the deflection in region i ($i = 1, 2, 3$), x is the location in reference to the boundary of elastic and plastic regions, l_{f} is the length between the loading point and the origin, l_{p} is the plastic zone length, P is the applied force, σ_{y} is the yield strength of the adhesive, B is the width of the specimen. Finally, k is the foundation stiffness defined by,

$$k = m_{\mathrm{q}} \frac{E_{\mathrm{a}} B}{t_{\mathrm{a}}}, \tag{6.7}$$

where m_{q} is parameter of order one, t_{a} is the thickness of the foundation (half the thickness of adhesive bond-line), E_{a} is the Young's modulus of the adhesive. Constant m_{q} (q $= 1, 2$) allows for arbitrary formulation of the stress state at the crack tip. Specifically, m_{q} is expressed as,

$$m_1 = 1, \tag{6.8}$$

assuming plane-stress in both out-of-plane and in-plane directions [8], and as,

$$m_2 = \frac{(1 - \nu_{\mathrm{a}})}{(1 - 2\nu_{\mathrm{a}})(1 + \nu_{\mathrm{a}})}, \tag{6.9}$$

assuming plane-strain in both out-of-plane and in-plane directions [9], where ν_{a} is the Poisson's ratio of the adhesive.
The solution to the differential equations reads as,

$$w_1(x) = \frac{P}{6E_x^{\mathrm{f}} I} x^3 + \frac{P l_{\mathrm{f}}}{2E_x^{\mathrm{f}} I} x^2 + R_1 x + R_2, \tag{6.10}$$

$$w_2(x) = -\frac{\sigma_{\mathrm{y}} B}{24E_x^{\mathrm{f}} I} x^4 + \frac{C_1}{6} x^3 + \frac{C_2}{2} x^2 + C_3 x + C_4, \tag{6.11}$$

$$\begin{aligned} w_3(x) = {} & K_1 \cos(\lambda x) \cosh(\lambda x) + K_2 \cos(\lambda x) \sinh(\lambda x) \\ & + K_3 \sin(\lambda x) \sinh(\lambda x) + K_4 \sin(\lambda x) \cosh(\lambda x), \end{aligned} \tag{6.12}$$

with R_{1-2}, C_{1-4}, K_{1-4} being constants of integration to be found through a boundary value problem and in which λ, defined by,

$$\lambda^4 = \frac{k}{4E_x^{\mathrm{f}} I}, \tag{6.13}$$

is the wave number, the inverse of which defines the elastic process zone length. The process zone length, λ^{-1}, in the context of the elastic foundation is interpreted as the distance (from the crack tip) over which the positive peel stress is distributed. The λ^{-1} length exits beyond of the crack tip due to the finite rigidity of the adhesive. Expanding and substituting for k and I, Eq. 6.13 can be rewritten in a non-dimensional form as,

$$\lambda^4 t_{\mathrm{a}} h_{\mathrm{adher}}^3 = 3m_{\mathrm{q}} \frac{E_{\mathrm{a}}}{E_x^{\mathrm{f}}} \tag{6.14}$$

which reveals the relation between the bonded structure characteristic length scales (left hand side) and adherend/bond-line material mismatch (right hand side).
The results of the constants of integration and the plastic zone length for the case where the bonded region is sufficiently long appear in Appendix I. Please note that once l_{p} approaches zero in Eqs. 6.4-6.6, the problem turns into elastic foundation only, i.e. Kanninen model [10]. Additionally, once l_{e} approaches zero, there will be no characteristic length λ^{-1} and the beam is treated as fixed at the crack tip like in Benbow and Roesler studies [11].

6

6.3.2. Finite element (FE) model

The proposed analytical methodology is aimed in indicating and including characteristic length scales of the problem. However, the problem at hand involves additional, local phenomena of e.g. three-dimensional (3D) nature, beyond its capability and intention. While the asymptotic analysis is involved later for discussion, for better comprehension, a 3D model of the DCB adhesive joints was built in Abaqus®. The joints were modelled using 8 node linear brick elements (C3D8). The adherends were modelled as linear elastic, using the material properties given in Tables 6.1 and 6.2. The adhesive was modelled as elastic-plastic, using the data from Chapter 4. The number of elements through-the-thickness direction of the GFRP adherends was defined by one element per lay-up layer. For the steel adherends, 10 elements were used in thickness direction. When needed, a seam crack embedded in the adhesive part was included in the model. The mesh was refined in the areas of interest, i.e. crack tip region and adherend-adhesive interfaces. A coarser mesh was applied in the rest of the model. A mesh convergence study was performed to guarantee mesh in-dependency of the numerical results. In order to simulate the real constraints during a DCB test, the following boundary conditions and loading were applied: 1) the left end of the lower edge of the bottom adherend was constrained from all displacements, rotations were not constrained; 2) the left end of the top edge of the top adherend was constrained from displacement in longitudinal direction; 3) a load was applied on the left end of the upper edge of the top adherend, equal to the load taken from the experimental tests. A mesh overview with the applied boundary conditions is shown in Fig. 6.5.

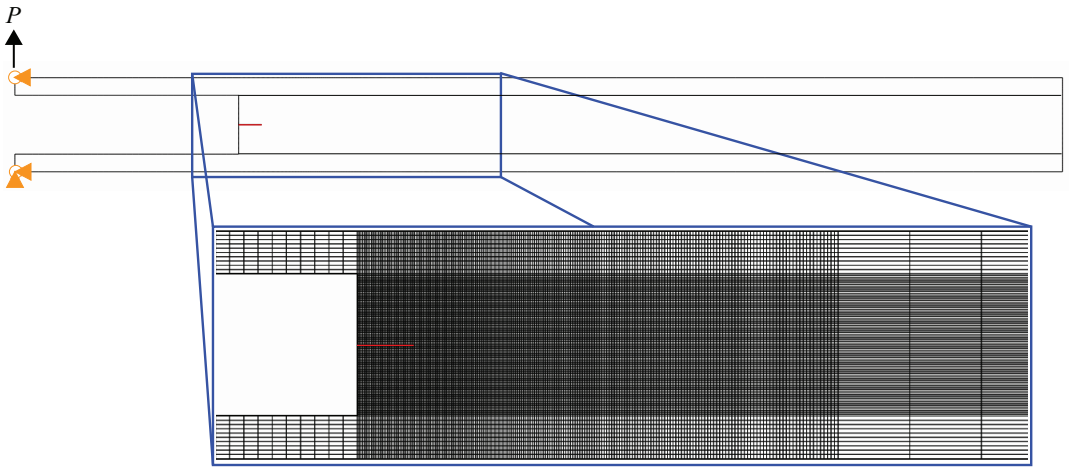

Figure 6.5: Typical mesh details with applied boundary conditions (steel-steel joint as an example).

6.4. Experimental results and models validation

6.4.1. Normalized load vs. displacement curves: stiffness during loading

Figs. 6.6(a), 6.6(c) and 6.6(e) show the representative load vs. displacement ($P - 2\Delta$) curves of the three tested configurations: steel-steel, GFRP-GFRP and steel-GFRP, respectively. Two curves for different values of Δa are presented per joint configuration because length Δa influences fracture onset locus. In each configuration, the difference in specimens' compliance is expected as the initial total crack length, $a_{0\,\text{total}} = a_{\text{init}} = a_0 + \Delta a$, as shown in Fig. 6.1, is not the same in all specimens. Moreover, $a_{0\,\text{total}}$ also affects the maximum load of each specimen. The load-displacement curves show an initial linear region, followed by a smooth transition before crack propagation. This transition is result of plastic effect. The propagation region is initially characterized by a drop on the applied load. After that, the load decreases gradually with increasing displacement up to final failure. The smooth propagation region gives evidence that the fracture process zone was similarly throughout the test.

In Fig. 6.6(a) is also plotted a representative curve of steel-steel joints with a bond-line of approximately 0.4 mm (data taken from Chapter 4). The results show that the stiffness of the adhesive joints is affected by the bond-line thickness as well as the maximum load, i.e. the joint with 0.4 mm thick bond-line is stiffer than the joints with 10 mm thick bond-line, but it withstands lower loads before fracture onset. In fact, in the specimens with an adhesive bond-line of 10 mm, the adhesive is able to deform more and becomes responsible for the dissipation of the majority of the external loading.

In addition, Figs. 6.6(b), 6.6(d) and 6.6(f) show the normalized load vs. displacement ($\tilde{P} - 2\tilde{\Delta}$) curves of the three tested configurations. For the sake of simplicity, the normalization is performed by following the simple beam theory [12],

$$\tilde{P} = \frac{2Pa_{0\,\text{total}}^2}{3E_x^{\text{f}}I}, \tag{6.15}$$

$$2\tilde{\Delta} = \frac{2\Delta}{a_{0\,\text{total}}}. \tag{6.16}$$

In the bi-material joints, the flexural stiffness of both adherends must be taken separately,

$$\tilde{P}_{\text{bi-mat}} = \frac{Pa_{0\,\text{total}}^2}{3}.S, \tag{6.17}$$

where S is given by,

$$S = \frac{1}{E_{x\text{-steel}}^{\text{f}}I_{\text{steel}}} + \frac{1}{E_{x\text{-GFRP}}^{\text{f}}I_{\text{GFRP}}}. \tag{6.18}$$

This normalization allows the comparison of initially linear part of the experimental curves with any other adhesive joints, regardless the materials and joint geometry (for instance, $a_{0\,\text{total}}$ length and adherends thickness), so that differences between the observed and calculated slopes can be attributed to the finite through-the-thickness stiffness of the adherend and the adhesive bond-line [10], as these parameters are not taken into consideration in the performed normalization.

The normalized curves of the experimental steel-steel adhesive joints show the same initial slope, regardless of the initial crack length, as expected (Fig. 6.6(b)). In the GFRP-GFRP and steel-GFRP adhesive joints (Figs. 6.6(d) and 6.6(f), respectively) the trend is different and the slopes of the initial linear part of the curves do not overlap. In fact, the ratio $\frac{a_{0\,\text{total}}}{h_{\text{GFRP}}}$ is approximately 4, corresponding to the stubby beam geometry, whilst its value is higher than 10 when considering the steel adherend. Therefore, the shear deformation of the GFRP adherends should be included in the normalization procedure to obtain overlapping results. For this case, the force normalization is given by,

$$\tilde{P}_{\text{shear}} = \frac{2Pa_{0\,\text{total}}^2}{3E_x^{\text{f}}I} + \frac{3P}{BG_{\text{adher}}h_{\text{adher}}}, \tag{6.19}$$

where G_{adher} is the shear modulus of the adherend. In the case of bi-material joints,

$$\tilde{P}_{\text{shear, bi-mat}} = \frac{Pa_{0\,\text{total}}^2}{3}.S + \frac{3P}{2BG_{\text{steel}}h_{\text{steel}}} + \frac{3P}{2BG_{\text{GFRP}}h_{\text{GFRP}}}. \tag{6.20}$$

Fig. 6.7 shows the normalized $\tilde{P} - 2\tilde{\Delta}$ curves of all adhesive joints without and with the shear deformation of the adherends - Figs. 6.7(a) and 6.7(b), respectively. The results corroborate the explanation given in previous paragraph. The GFRP-GFRP specimen with $\Delta a = 0.8$ mm is the only exception. In fact, this result is unexpected. The only reason found for the difference is the presence of a kink in the initial linear part of the curve.

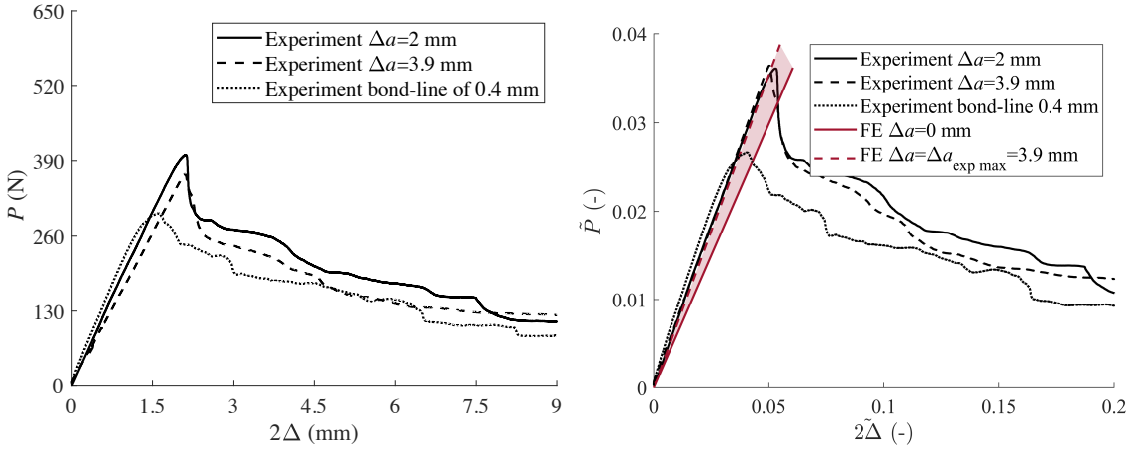

(a) Steel-steel joints: $P - 2\Delta$.

(b) Steel-steel joints: $\tilde{P} - 2\tilde{\Delta}$.

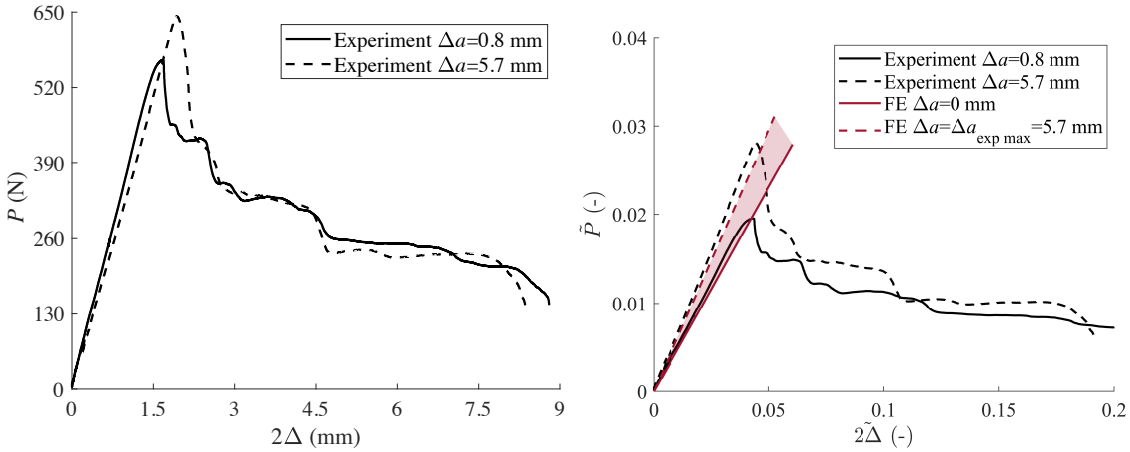

(c) GFRP-GFRP joints: $P - 2\Delta$.

(d) GFRP-GFRP joints: $\tilde{P} - 2\tilde{\Delta}$.

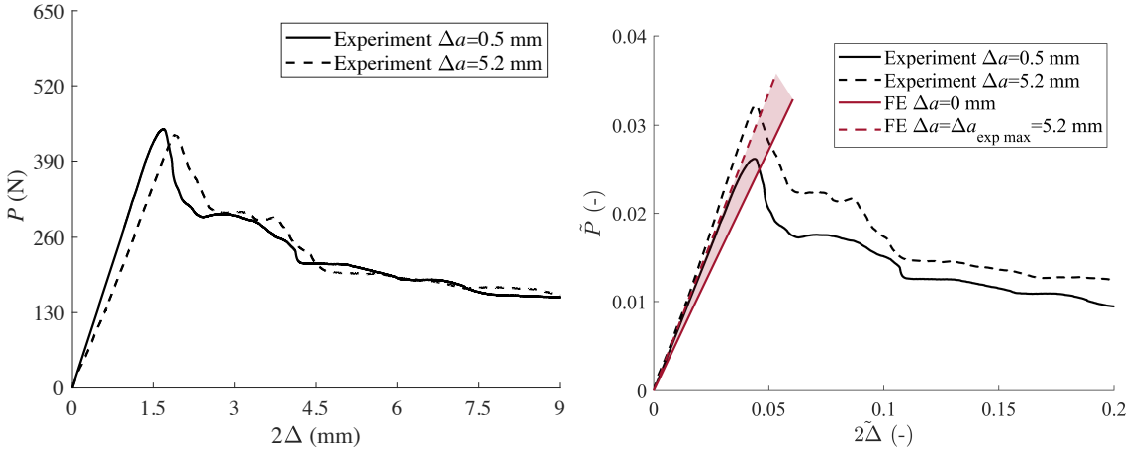

(e) Steel-GFRP joints: $P - 2\Delta$.

(f) Steel-GFRP joints: $\tilde{P} - 2\tilde{\Delta}$.

Figure 6.6: Experimental load vs. displacement curves: raw ($P - 2\Delta$) and normalized results ($\tilde{P} - 2\tilde{\Delta}$).

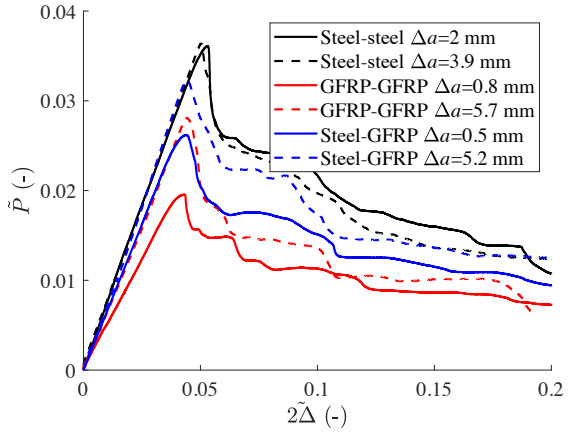

(a) No shear taken into account.

(b) Shear taken into account.

Figure 6.7: Normalized load vs. displacement curves: the effect of shear deformation of the adherends.

In Figs. 6.6(b), 6.6(d) and 6.6(f), the linear part of $\tilde{P} - 2\tilde{\Delta}$ curves with the highest Δa is compared with the linear part of the results obtained from the finite element analysis. Although there is a better agreement between the experimental and numerical results of the steel-steel joints, the difference between the experimental and numerical results in the other two configurations is less than 15%. Moreover, FE results for the case $\Delta a = 0$ mm are also plotted in Figs. 6.6(b), 6.6(d) and 6.6(f). This way, one can observe the spectrum of the structural response of the adhesive joints from $\Delta a = 0$ up to $\Delta a = \Delta a_{\text{exp max}}$, where $\Delta a_{\text{exp max}}$ is the largest Δa experimentally implemented.

6.4.2. Normalized critical force at fracture onset

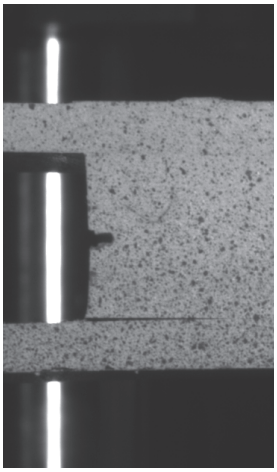

(a) Cohesive close to interface fracture onset.

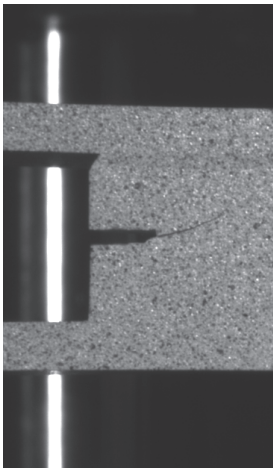

(b) Cohesive adhesive mid-thickness fracture onset.

Figure 6.8: Fracture onset locus.

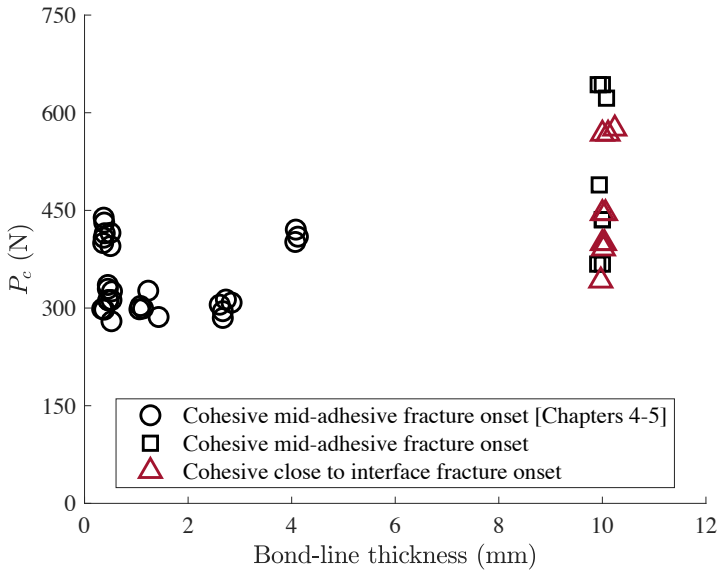

(a) P_c vs. bond-line thickness.

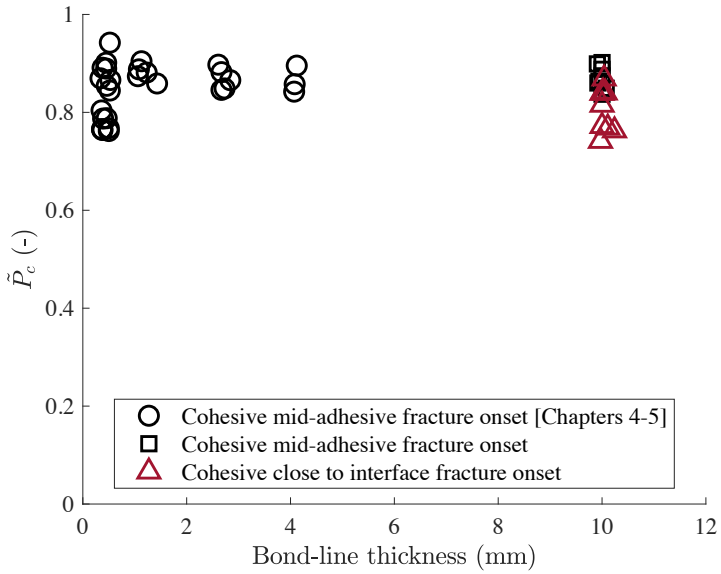

(b) $\tilde{P}_c$ vs. bond-line thickness.

Figure 6.9: Critical load, P_c, vs. normalized critical load, $\tilde{P}_c$, as a function of bond-line thickness.

The critical force at fracture onset, P_c, is analysed and a normalization is performed, being the critical force equal to the maximum load, P_{max}. Distinction is made between cohesive close to interface and cohesive adhesive mid-thickness fracture onset - see Fig. 6.8, regardless of joint configuration. The normalization is done by following the simple beam theory [12, 13]. The critical fracture onset energy, $G_{Ic\text{-}onset}$, and normalized P_c, $\tilde{P}_c$, are given by,

$$G_{Ic\text{-}onset} = \frac{P_c^2}{BE_x^f I}\left(\frac{3\Delta E_x^f I}{P_c}\right)^{\frac{2}{3}}, \tag{6.21}$$

$$\tilde{P}_{\mathrm{c}} = \frac{P_{\mathrm{c}}.a_{0\ \mathrm{total}}}{\sqrt{G_{\mathrm{Ic\text{-}onset}} B E_x^{\mathrm{f}} I}}. \tag{6.22}$$

For the bi-material joints,

$$G_{\mathrm{Ic\text{-}onset,\ bi\text{-}mat}} = \frac{P_{\mathrm{c}}^2}{2B}.S\left(\frac{2\Delta}{\frac{P_{\mathrm{c}}}{3}.S}\right)^{\frac{2}{3}}, \tag{6.23}$$

$$\tilde{P}_{\mathrm{c,\ bi\text{-}mat}} = \frac{P_{\mathrm{c}}.a_{0\ \mathrm{total}}}{\sqrt{2G_{\mathrm{Ic\text{-}onset,\ bi\text{-}mat}} B}}.\sqrt{S}. \tag{6.24}$$

Fig. 6.9 shows the critical force at fracture onset (Fig. 6.9(a)) and the normalized critical force (Fig. 6.9(b)) as a function of bond-line thickness. The results for the bond-line thickness range 0.4 - 4 mm were taken from Chapters 4 and 5. This normalization allows the comparison of fracture onset, regardless the material and geometric properties of adhesive joints.
Similar values of $\tilde{P}_{\mathrm{c}}$ are observed in Fig. 6.9(b), regardless of the bond-line thickness and fracture onset type. Looking into more detail to the results of adhesive joints with approximately 10 mm thick bond-line, the $\tilde{P}_{\mathrm{c}}$ difference between cohesive adhesive mid-thickness and cohesive close to interface fracture onset is, in average, less than 10%. The similar results of $\tilde{P}_{\mathrm{c}}$ indicate that the adhesive was able to deform as a response to the external loading, even though in some cases the critical stress was first attained in a region close to one of the adherend-adhesive interfaces due to materials modulus mismatch ratio, as it is explained in a later stage. Moreover, these results also show that the surface pre-treatments were suitable and led to good adhesion at the interfaces, without interfering with the overall performance of the joints, i.e no adhesive failure occurred.

6.4.3. Deflection in bonded region

To evaluate the applicability of Yamada's model and to further validate the FE models, the experimental deflection curves in the bonded region are compared with the analytical and numerical results. The experimental results are obtained by the DIC technique with pictures taken from the region close to the adherend-adhesive interfaces. Figs. 6.10 and 6.11 show curves representative for the steel-steel specimens with $\Delta a = 2$ and 3.9 mm, respectively, Figs. 6.12 and 6.13 show the deflection curves representative for the GFRP-GFRP and steel-GFRP specimens with $\Delta a = 5.7$ and 5.2 mm, respectively, corresponding to the two different stages of loading: the linear elastic region, and at the moment of fracture onset, i.e. at the maximum load. Both plane-stress and plane-strain conditions are considered in the analytical model (Eqs. 6.8 and 6.9), while the numerical results are taken from both the side and the centre ($B = \pm$ 12.5 mm and $B = 0$ mm, respectively) of the model at the adherend-adhesive interfaces. The curves are shifted from $x = -l_{\mathrm{p}}$ to $x = 0$ for visualization purpose.

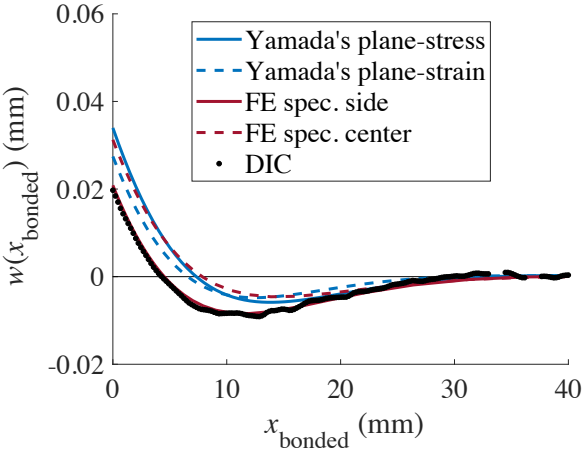

(a) Linear elastic region.

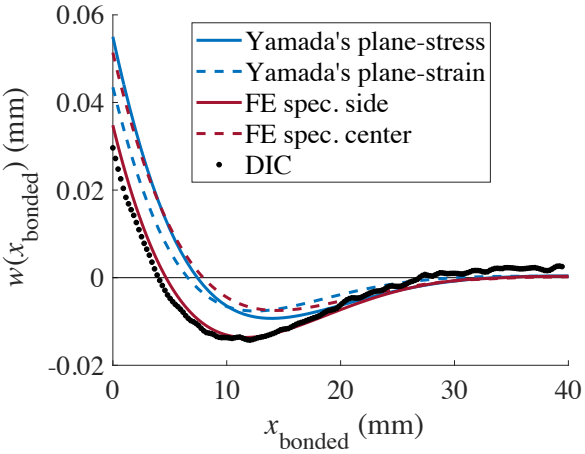

(b) Fracture onset moment.

Figure 6.10: Deflection in bonded region of steel-steel joint: Δa = 2 mm.

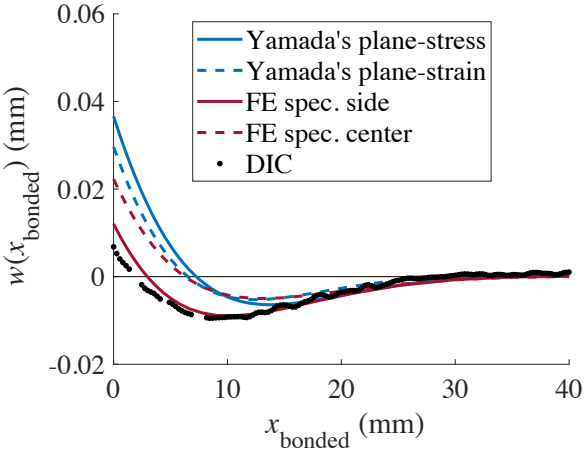

(a) Linear elastic region.

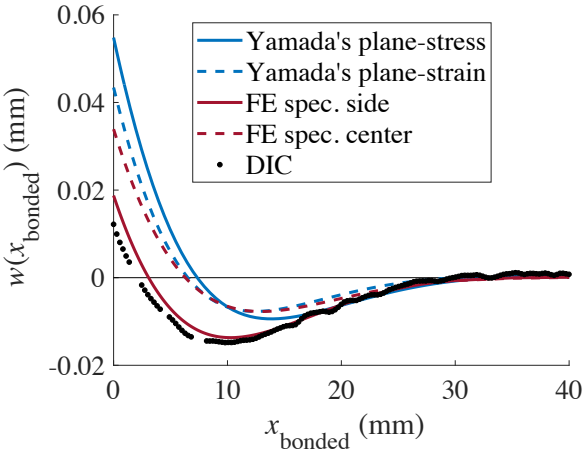

(b) Fracture onset moment.

Figure 6.11: Deflection in bonded region of steel-steel joint: Δa = 3.9 mm.

The agreement between different approaches is very encouraging, specially that no parameter fitting or adjustment was performed and entire models rely on properties measured through either tensile or flexural testing of constituents. Besides, both the analytical and the FE models are based on a single value of the crack length, which cannot be treated as unique due to the crack front curvature [14–16] established at the fracture onset. Excellent agreement is observed between the experimental DIC and the FE results once comparing deflection as evaluated at the specimen side. At the same time, a very good agreement exists between the FE results for deflection along the specimen centre-line and the analytical model. The analytical results considering plane-stress conditions are higher than when considering plane-strain conditions. In the plane-stress case, in general, the adhesive bond-line appears too "soft". Please note that the plane-strain and plane-stress conditions are only applied to the adhesive. Effects, such as anticlastic curvature of the adherends, are not included in the analytical model.

One can observe that the analytical model stays in better agreement with the ex-

perimental deflection in bonded region for smaller values of Δa (Fig. 6.10). In fact, the analytical model does not consider Δa (i.e. it does not take into account the fact that Δa is inside the thick bond-line) and local effects due to Δa, and thus, in general, the crack front stress singularities cannot be captured. Therefore, the case of $\Delta a = 0$ corresponds to the “foundation” representation. Here, however, one need to acknowledge, that such effects should be limited due to the development of the plastic zone at the crack tip.

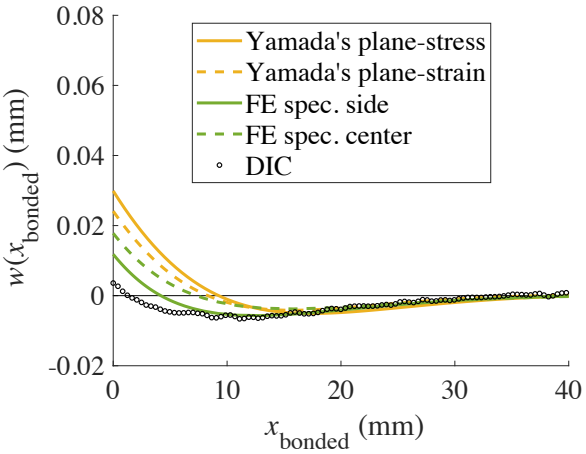

(a) Linear elastic region.

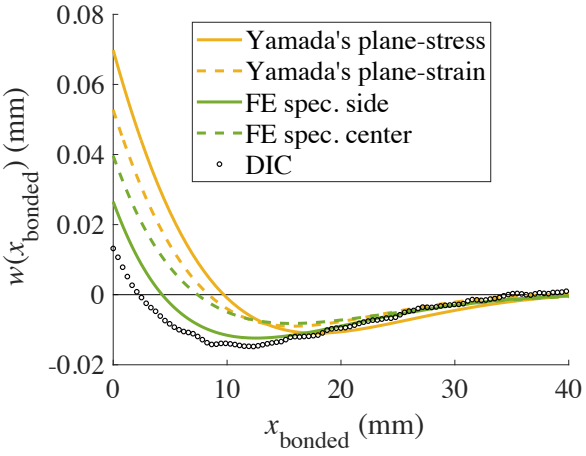

(b) Fracture onset moment.

Figure 6.12: Deflection in bonded region of GFRP-GFRP joint: Δa = 5.7 mm.

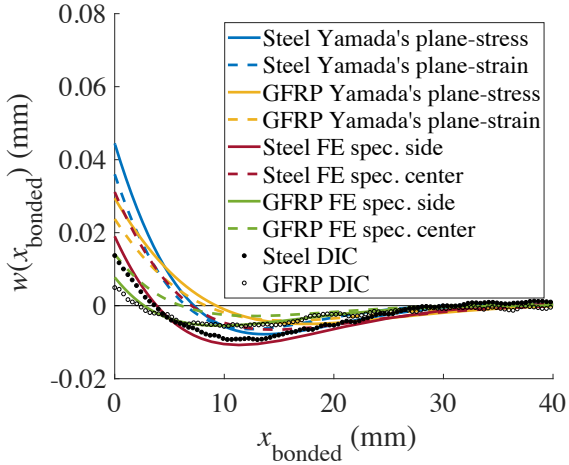

(a) Linear elastic region.

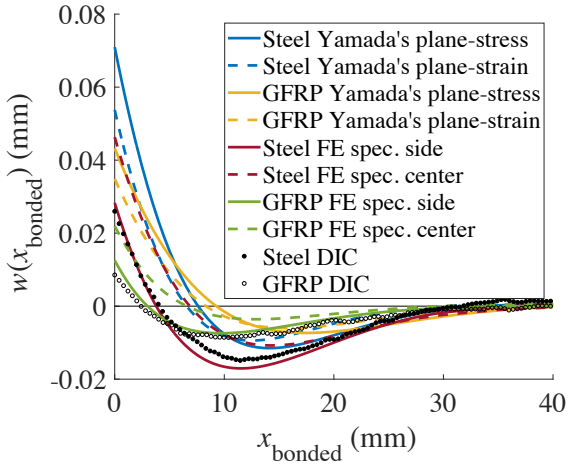

(b) Fracture onset moment.

Figure 6.13: Deflection in bonded region of steel-GFRP joint: Δa = 5.2 mm.

6.5. Discussion

6.5.1. Fracture onset

The role of adherend-adhesive modulus mismatch

In an adhesive joint with dissimilar adherends, in the case of near-interface fracture onset, the adherends-adhesive modulus mismatches dictate the point of fracture initiation, i.e. the fracture onset locus is determined by the highest adherend-adhesive modulus mismatch [17, 18].

At the adherend-adhesive edge, singular stress is produced due to material mismatch and the the threshold value is dependent upon material and geometrical properties, as shown by Dundurs and Bogy [19, 20]. The material mismatch is evaluated from Dundurs parameters α and β, which are given by,

$$\alpha = \frac{G_{\text{adher}}(k_{\text{a}} + 1) - G_{\text{a}}(k_{\text{adher}} + 1)}{G_{\text{adher}}(k_{\text{a}} + 1) + G_{\text{a}}(k_{\text{adher}} + 1)}, \tag{6.25}$$

$$\beta = \frac{G_{\text{adher}}(k_{\text{a}} - 1) - G_{\text{a}}(k_{\text{adher}} - 1)}{G_{\text{adher}}(k_{\text{a}} + 1) + G_{\text{a}}(k_{\text{adher}} + 1)}, \tag{6.26}$$

where the subscripts "adher" and "a" refer to the materials for the adherend and adhesive, respectively. G_{adher} and G_{a} are the shear moduli, $k_i = 3 - 4\nu_i$ for plane strain and $k_i = (3 - \nu_i)/(1 + \nu_i)$ for plane stress (ν_i are the Poisson's ratios with $i =$ adher, a). The parameter α can be interpreted as a measure of the dissimilarity in stiffness of the two materials. The adherend material is rigid relative to the adhesive as $\alpha > 0$ and compliant as $\alpha < 0$. The parameter β, as will be clear soon, is responsible for the near-crack tip oscillatory behavior at the bi-material interface [21].

There have been a lot of studies on the characterisation of the stresses at the adherend-adhesive corners of various joint geometries [20–24]. Within the framework of linear elasticity, the asymptotic stress component normal to the the bi-material corner of many adhesive joints is of the form,

$$\sigma_{yy\text{-interfacial}} = Kr^{\gamma-1} \ (r \to 0), \tag{6.27}$$

where r is the radial distance from the corner, K is the interface corner stress intensity factor and the $\gamma - 1$ is the order of the singularity. Both K and γ depend on geometric and material properties of the joint. An increase of the singular stress is expected with a large mismatch between the two materials [18, 24]. Depending on joint configuration, γ can be real or complex. For the problem of a crack at the interface between two dissimilar homogeneous materials, $\gamma = 1/2 + i\epsilon$ [21, 22], resulting in,

$$\sigma_{yy\text{-interfacial}} = \Re(Kr^{-1/2+i\epsilon}), \tag{6.28}$$

$$\epsilon = \frac{1}{2\pi} \ln\left(\frac{1-\beta}{1+\beta}\right). \tag{6.29}$$

Please note that Eqs. 6.27 and 6.28 are brought here to only illustrate how the stress field is affected by the materials mismatch at bi-material interfaces (parameter ϵ defined in Eq. 6.29).
In the special case of $\beta = 0$, the asymptotic stress component normal to the crack tip has exactly the same form as that for homogeneous materials, i.e.,

$$\sigma_{yy\text{-homogeneous}} = Kr^{-1/2}. \tag{6.30}$$

Although experimental evidence corroborates the effect of the modulus mismatch, as reported in Chapter 5, FE analysis was carried out to further investigate this effect. Three adhesive joints were modelled: steel-steel, GFRP-GFRP and steel-GFRP with adhesive bond-line of 10 mm. For comparison, two important features were kept the same in all models, i.e. no pre-crack in the adhesive layer ($\Delta a = 0$ mm) and same applied load (P_c of representative steel-steel joint with $\Delta a = 2$ mm, cohesive close to interface fracture onset).
The strain ε_{yy} contours of the three models are shown in Fig. 6.14. The adhesive joints with two equal adherends show symmetric strain distribution, having the highest strain values at the corners as shown in Figs. 6.14(a) and 6.14(b). However, in the case of dissimilar adherends, the strain distribution is not symmetric and the highest strain values are found in the region close to the adherend-adhesive interface with the higher modulus mismatch, i.e. steel-adhesive interface as can been seen in Fig. 6.14(c). In fact, the steel-adhesive modulus ratio is 105, while a ratio of approximately 6 is obtained when considering the GFRP adherend.
The Dundurs parameters for each adherend-adhesive pair are listed in Table 6.4. Due to the adhesive bond-line thickness, the joint response to external loading is dominated by the adhesive and, thus, the adhesive plays a major role in the fracture onset process. Therefore, plane-strain conditions are considered. The positive α values show that both adherends are stiffer than the adhesive. As typically, β is approximately $\alpha/4$. As aforementioned, an increase of the singular stress is expected with a large mismatch between the two materials [18, 24]. Therefore, the steel-epoxy interface is more prone to failure under condition that $\Delta a = 0$, as both Dundurs parameters are higher for this pair of materials. This is corroborated by the results in Fig. 6.14(c) and by experimental evidence. In the steel-GFRP adhesive joints, for the cases of cohesive close to interface fracture onset, the locus of failure was always nearby the steel-adhesive interface. More on that later in sub-section 6.5.2.

Table 6.4: Dundurs parameters for different material combinations under plane-strain conditions.

Adherend/Adhesive	G_{adher} (MPa)	G_a (MPa)	ν_{adher} (-)	ν_a (-)	α (-)	β (-)
Steel/Epoxy	80769	752	0.300	0.33	0.98	0.25
GFRP/Epoxy	3897	752	0.252	0.33	0.65	0.15

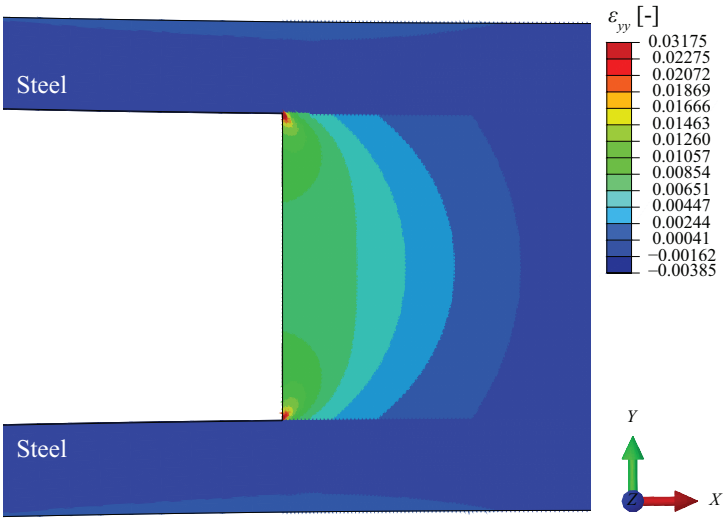

(a) Steel-steel adhesive joint.

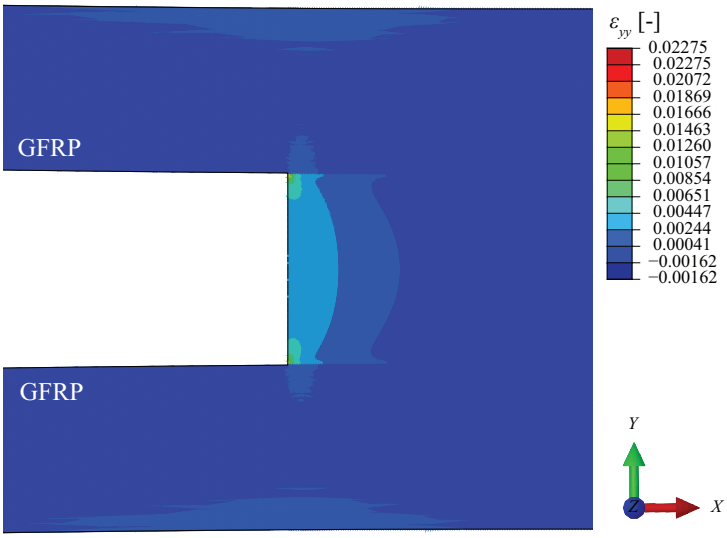

(b) GFRP-GFRP adhesive joint.

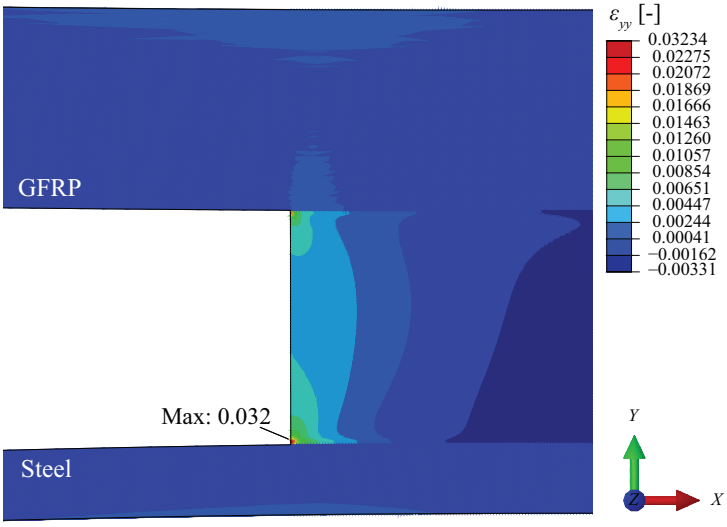

(c) Steel-GFRP adhesive joint.

Figure 6.14: Evolution of strain field, ε_{yy}, for different adhesive joint configurations and corresponding adherends-adhesive modulus mismatches. No pre-crack is modelled, Δa = 0 mm, and same load is applied in all models. The results are taken along the mid-width of the model (B = 0 mm).

The role of pre-crack length, Δa: crack tip singularity, diffusion lines and corner singularities

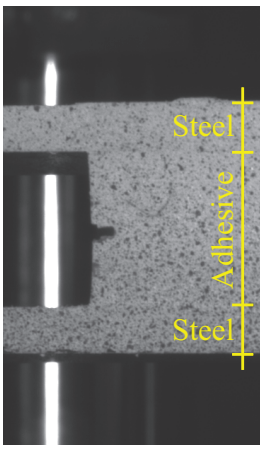

$\Delta a \approx 2.0$ mm
Cohesive close to interface fracture onset

(a) Steel-steel adhesive joint.

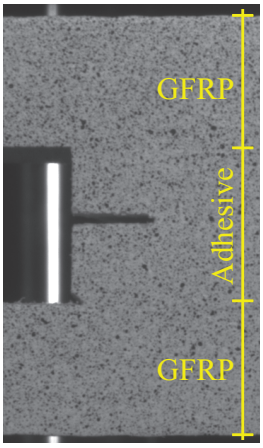

$\Delta a \approx 5.7$ mm
Cohesive adhesive mid-thickness fracture onset

(b) GFRP-GFRP adhesive joint.

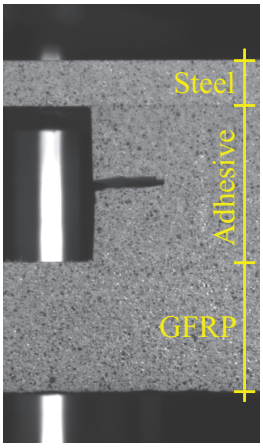

$\Delta a \approx 4.8$ mm
Cohesive adhesive mid-thickness fracture onset

(c) Steel-GFRP adhesive joint.

Figure 6.15: Examples of experimentally investigated Δa's.

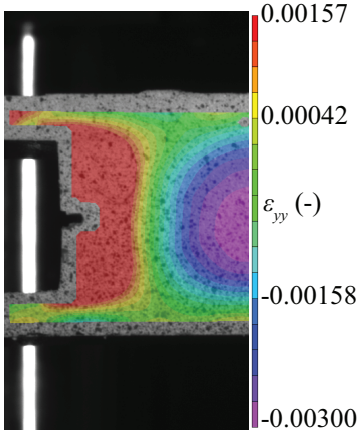

(a) Steel-steel adhesive joint.

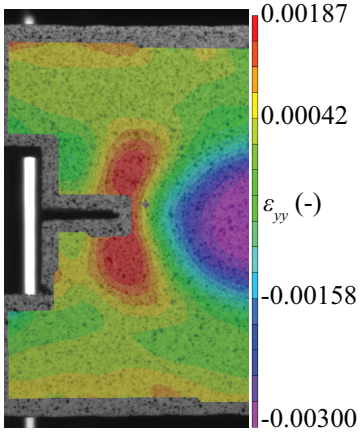

(b) GFRP-GFRP adhesive joint.

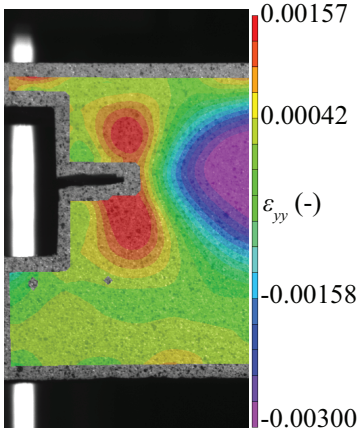

(c) Steel-GFRP adhesive joint.

Figure 6.16: Strain, ε_{yy}, contour at fracture onset moment for three different specimens.

As explained in sub-section 6.2.1, a pre-crack of length Δa is created during the bonding procedure at the mid-thickness of the adhesive bond-line in all specimens. The total crack length is equal to a_{total} and it is defined as the straight and horizontal line distance between the P load line and the pre-crack tip, as illustrated in Fig. 6.1. The fracture onset is dominated by the singular stress field around the existing pre-crack tip up to a certain bond-line thickness. For higher bond-line thicknesses, geometric discontinuities, such as corners, and material discontinuities, such as adherend-adhesive interfaces, create local singularities where the threshold stress is attained first. To overcome this situation, a critical pre-crack length must be defined, $\Delta a_{\text{crit.}}$.

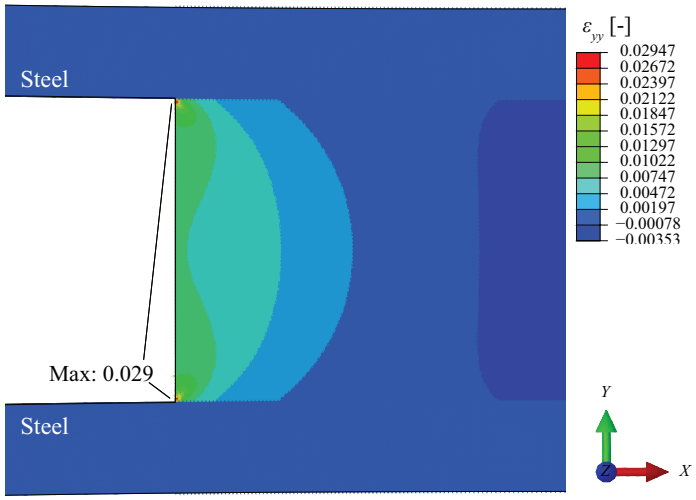

(a) Δa = 0 mm.

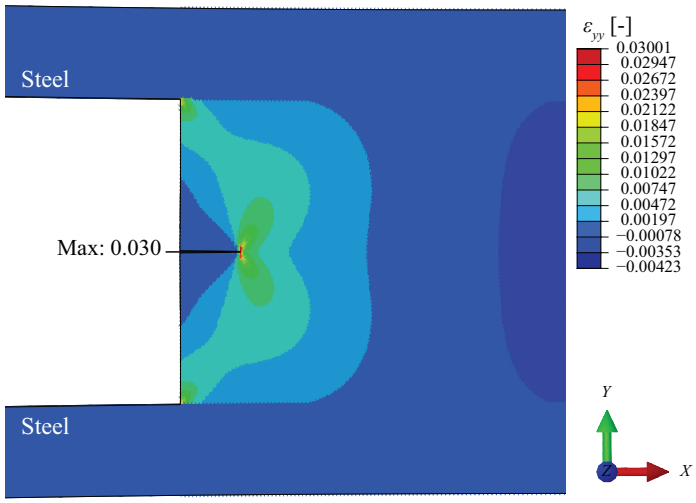

(b) Δa = 2 mm.

Figure 6.17: Evolution of strain field, ε_{yy}, in steel-steel joint with increasing Δa. The results are taken along the mid-width of the model (B = 0 mm).

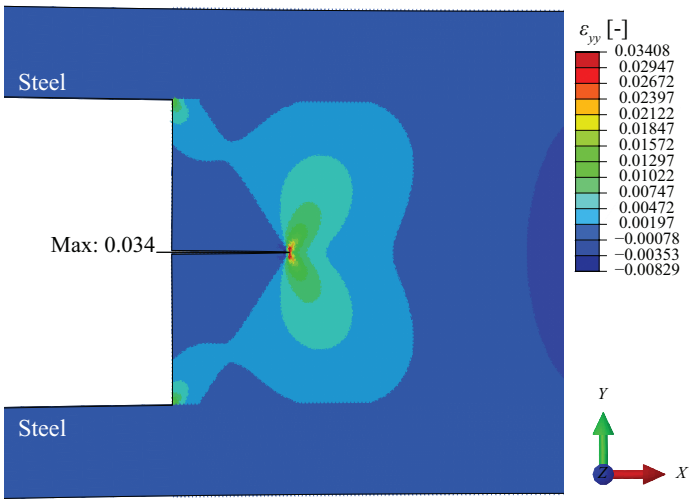

(a) $\Delta a_{\text{exper.}}$ = 3.9 mm.

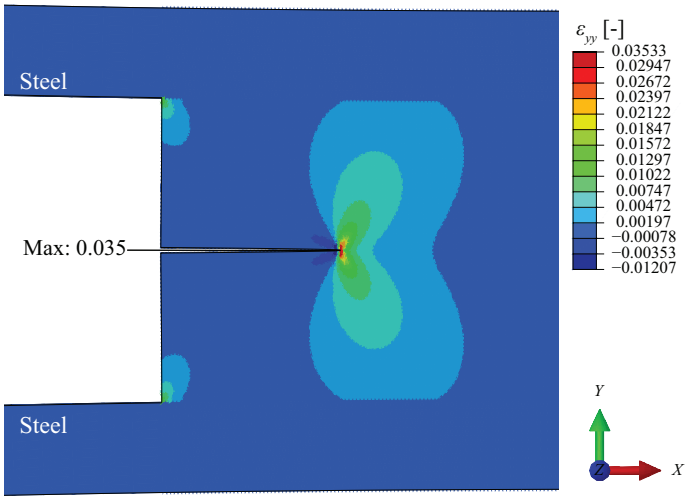

(b) Δa = 6 mm.

Figure 6.18: *Continuation...* Evolution of strain field, ε_{yy}, in steel-steel joint with increasing Δa. The results are taken along the mid-width of the model (B = 0 mm).

As postulated by Griffith [3], when a crack has grown into a homogeneous solid to a specific depth, a region of material adjacent to the free surfaces is unloaded. The criterion to define Δa should be similar to Griffith's diffusion line approach, i.e. Δa must be sufficiently large so the corners near the interfaces are unloaded, as illustrated in Fig. 6.1 by the red diffusion lines. In other words, Δa must be sufficiently large so the stress threshold is first attained at the crack tip than at the corners. In the infinite plate with a crack, the unloaded region is approximated by an triangle with the base length corresponding to Δa and a height of $2\pi\Delta a$ [2]. This, for the problem at hand, would imply that as long as the adhesive thickness fulfil the criterion $2t_a \geqslant 2.(2\pi\Delta a)$, the corners are unloaded and the crack can only onset from the crack tip. It is clear that the critical length Δa depends on the bond-line thickness.

Therefore, the effect of the length of Δa on the fracture onset locus was experimentally investigated. Two types of bonded joints with 10 mm thick adhesive bond-line were studied: 1) single-material: steel-steel and GFRP-GFRP, 2) bi-material: steel-GFRP. Fig. 6.15 shows three examples of specimens with different Δa lengths and the corresponding strain, ε_{yy}, contours at fracture onset are shown in Fig. 6.16. Regardless of the joint type, the strain contour distribution demonstrates clearly a change in the location of the region with high strain values, indicated with red colour, as the length of Δa is increased. For a small Δa of approximately 2 mm (Fig. 6.16(a)), the strain contour shows a red region that expands all over the bond-line thickness up to the adherend-adhesive interfaces, resulting in fracture onset close to one of the adherend-adhesive interfaces. However, for longer Δa's (Figs. 6.16(b) and 6.16(c)), the highest strains are concentrated around the pre-crack tip, leading to cohesive adhesive mid-thickness fracture onset. These results strongly support Δa as a length that determine the point of fracture onset.

In order to better show the strain contour evolution for increasing values of Δa, numerical simulations were ran. The load correspondent to fracture onset moment of a representative steel-steel adhesive joint with $\Delta a = 3.9$ mm was applied on FE models with varying Δa length from 0 up to 6 mm. The results are shown in Figs. 6.17 and 6.18, and were taken at the mid-width of the specimen ($B \pm 0$ mm). One should observe that the numerical and experimental strain contours should only be compared qualitatively. In fact, the FE model represents sharp bi-material corners and pre-crack tip unlike the experiments, in which finite radii exist at those regions.

For $\Delta a = 0$ mm, one can observe a singularity at the corners of the bond-line in Fig. 6.17(a). By increasing Δa from 2 up to 6 mm, one can observe a change in the location of the singularity, i.e. the higher values of the strain are found in the pre-crack tip region as shown in Figs. 6.17(b), 6.18(a) and 6.18(b). Moreover, an increase of Δa leads to larger unloaded areas, indicated by the dark blue colour in the cracked adhesive region. However, the corners do not need to be completely unloaded to have cohesive adhesive mid-thickness fracture onset, as shown in Fig. 6.18(a) where $\Delta a_{\text{exper.}}$ is considered and has resulted in cohesive adhesive mid-thickness fracture in the experimental tests. For cohesive adhesive mid-thickness fracture onset, the stress threshold must be first attained at the pre-crack tip region rather than at the bi-material corners.

From the proposed elastic-plastic model, two length scales are identified. The first one, l_{p}, in some cases can be interpreted as crack tip plastic radius, thus, solely associated with the material properties, including yield stress and critical fracture energy of the adhesive material [3]. However, the process zone can further extend above the plastic radius depending on the second length scale. The second characteristic dimension, associating distribution of the stress field along the joint with overall joint geometry and material properties, emerges as λ^{-1}. The parameter λ^{-1} is the characteristic length defined to solve the differential equation of a beam supported by an elastic medium. This parameter is function of the geometry and mechanical properties of the adhesive bond-line and adherends [10], as given by Eq. 6.13. Importantly, it is a parameter that is measurable and corresponds to the distance over which $\sigma_{yy} \geq 0$. We postulate existence of two non-dimensional

parameters which can be used to craft an adhesive joint failure map:

- Case 1: $\frac{r_p}{t_a} > 1$ and $\Delta a = 0$ - the plastic regions builds up through the entire bond-line thickness and the joint will most likely fail in cohesive manner.
- Case 2: $\frac{r_p}{t_a} > 1$ and $\Delta a > 0$ - the joint will most likely fail in cohesive manner.
- Case 3: $\frac{r_p}{t_a} < 1$ and $\Delta a = 0$ - the joint will fail at or close the interface with the highest material mismatch.
- Case 4: $\frac{r_p}{t_a} < 1$ and $\Delta a > 0$ then another parameter needs to be taken into account - $\frac{\lambda^{-1}}{\Delta a}$. This parameter can be treated as a more general case of Griffith's diffusion line approach, which should enable capturing effects of bond-line confinement [25]. In specific, for the plate made from a single material $\lambda^{-1} \to \infty$ and the $\frac{\lambda^{-1}}{\Delta a} \to \infty$, implying that the stress is applied to the specimen remotely, i.e. $\sigma_{yy} = \sigma_{yy}^{\infty}$ and the original diffusion lines argument applies. In an adhesive joint, some transition Δa, defined as $\Delta a_{\text{crit.}}$, must exist at which the failure will change from interfacial (singular field at the corner/edge) to cohesive (singular stress field at the pre-crack tip), possibly resulting in diffusion lines as illustrated in Fig. 6.1.

All experiments carried out in this study correspond to case 4. An estimation of $2r_p \approx 1$ mm under plane-strain conditions is reported in Chapter 4. Therefore, $r_p < t_a$. Besides, in all joints was created a pre-crack at the mid-thickness of the adhesive bond-line during the manufacturing procedure, i.e. $\Delta a > 0$. From the experimental results, it was found out that, that regardless of the joint type, a ratio of $\frac{\lambda^{-1}}{\Delta a_{\text{crit.}}} \leqslant 2$ leads to cohesive adhesive mid-thickness fracture onset, considering both plane-strain and plane-stress conditions. Table 6.5 summarizes the experimental Δa's considered for all joint types as well as the ratio $\frac{\lambda^{-1}}{\Delta a}$ and corresponding failure type at fracture onset. The empirical relation for cohesive adhesive mid-thickness fracture onset can also be expressed as $(8E_a B/E_x^f I).(\Delta a_{\text{crit.}})^4 \geqslant 2t_a$, so that for a given material mismatch $(\Delta a_{\text{crit.}}/h_{\text{adher}})^4 \sim (t_a/h_{\text{adher}})$ is the scaling relation for transition into cohesive adhesive mid-thickness fracture onset.

6.5.2. Crack path selection

The issue of crack path selection and stability depends upon local, crack tip loading and can be addressed in terms of the asymptotic stress field around the crack tip [18, 26, 27]. Let (r,θ) be polar coordinates centred at the crack tip of a crack in a homogeneous material. The stresses ahead of the crack tip ($\theta = 0$) are given by,

$$\begin{bmatrix} \sigma_{xx} & \sigma_{xy} \\ \sigma_{xy} & \sigma_{yy} \end{bmatrix} = \frac{K_I}{\sqrt{2\pi r}} \begin{bmatrix} 1 & 0 \\ 0 & 1 \end{bmatrix} + \frac{K_{II}}{\sqrt{2\pi r}} \begin{bmatrix} 0 & 1 \\ 1 & 0 \end{bmatrix} + \begin{bmatrix} T & 0 \\ 0 & 0 \end{bmatrix} + O(\sqrt{r}), \tag{6.31}$$

Table 6.5: Empirical relation between λ^{-1} and Δa under plane-strain conditions.

Joint type	t_a (mm)	Δa (mm)	$\frac{\lambda^{-1}_{steel}}{\Delta a}$ (-)	$\frac{\lambda^{-1}_{GFRP}}{\Delta a}$ (-)	Fracture onset
Steel-steel	5.0	0.6	12.5	-	Cohesive close to interface
	5.0	2.0	3.9		Cohesive close to interface
	5.0	**3.9**	**1.9**		**Cohesive adhesive mid-thickness**
GFRP-GFRP	5.1	0.8	-	11.8	Cohesive close to interface
	5.0	**5.1**		**1.8**	**Cohesive adhesive mid-thickness**
	5.0	**5.7**		**1.6**	**Cohesive adhesive mid-thickness**
Steel-GFRP	5.0	0.5	15.1	18.9	Cohesive close to interface
	5.0	**4.8**	**1.5**	**1.9**	**Cohesive adhesive mid-thickness**
	5.0	**5.2**	**1.4**	**1.8**	**Cohesive adhesive mid-thickness**

where K_{I} and K_{II} are the stress intensity factors of opening and shear modes, respectively, T is a stress acting parallel to the crack plane and $O(\sqrt{r})$ represents higher order terms. Please note that Eq. 6.31 is brought here to show how physically the T-stress term contributes to the stress field ahead of the crack tip. The T-stress is determined in the following sub-section.

According to Cotterell and Rice [28], if a straight crack advancing in a homogeneous material with $K_{\mathrm{II}} = 0$ is perturbed due to some micro-heterogeneity, a positive T-value drives the crack away from the straight trajectory while a negative T-value drives the crack back to initial trajectory. Fleck et al. [26] and Chen et al. [27, 29, 30] concluded that, similarly to the homogeneous materials, the magnitude of T-stress plays an important role in the directional stability of cracks in adhesive joints (stable cracks grow in a straight, non-wavy manner). The T-stress decreases with the thickness of the adhesive, resulting in higher probability of stable crack propagation if the thickness of the adhesive layer decreases. On the other hand, as the adherend thickness decreases, the T-stress increases due to the effect of adherend bending. Moreover, the T-stress also depends on the residual stress originating from joint manufacturing, due to the mismatch of the coefficients of thermal expansion and shrinkage.

Fig. 6.19 shows the representative crack growth paths in case of cohesive adhesive mid-thickness fracture onset for the adhesive joints investigated in this study. One of the features, observed by naked eye, of crack onset and growth in these joints is the deflection of the crack from the straight trajectory along the centre of the

adhesive thickness. The adherends constraint effects in thick bond-lines are relieved to some extent and, thus, the adhesive bond-line is not entirely constrained. In the absence of stabilizing factor of compressive stresses (which are at a large distance from the crack tip, of order λ^{-1}, if compared to the asymptotic field), the crack is found to rapidly deflect out from the mid-adhesive thickness. Therefore, parameters such as the local crack tip loading, which may not be predominantly in mode I, and the T-stress control the unstable crack growth [26, 27, 30]. To better understand this behaviour, in the following sub-section, the T-stress at the crack tip is analysed for two different bond-line thicknesses considering steel-steel joints. Moreover, the overall shape of the crack path per joint configuration is discussed thereafter.

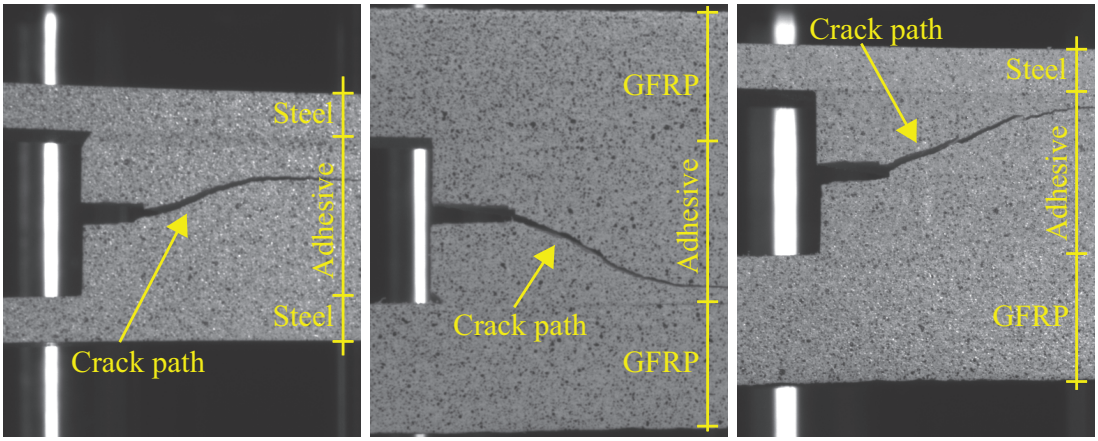

(a) Steel-steel joint. (b) GFRP-GFRP joint. (c) Steel-GFRP joint.

Figure 6.19: Examples of crack growth paths in adhesive joints with 10 mm thick adhesive bond-line.

The role of T-stress

To quantify the T-stress in steel-steel DCB specimens with varying bond-line thickness (4 and 10 mm), finite element analysis was carried out. Both the adhesive and adherends were modelled as elastic materials (T-stress is calculated based on the load level and linear elastic material properties). The overall description of the 3D-models and material properties can be found in sub-sections 6.3.2 and 6.2.1, respectively. As the T-stress depends on the residual stress in the adhesive, a thermal gradient representative of the cooling part of the curing cycle (from curing temperature, 80°C, to laboratory temperature, 23°C) was also included in the models. The coefficients of thermal expansion used in the models are listed in Table 6.6. The calculation of T-stress along the crack front is conducted within ABAQUS® program. Five contours were used in the analyses as a good independence of the T-stress distribution was obtained. Therefore, only the T-stress distributions taken from the outer contour (contour number 5) are shown.

Fig. 6.20 shows the results of the T-stress distribution along the crack tip for two different bond-line thicknesses: 4 and 10 mm. The first moment of crack growth visually identified during the experimental tests was picked as the loading case – points highlighted in Figs. 6.20(a) and 6.20(b). As shown in Fig. 6.20(c), the T-

Table 6.6: Coefficients of thermal expansion (CTE).

Material	CTE (x10^{-5} °C^{-1})	Reference
Steel	1.17	[6]
Araldite 2015	9.5	Supplier's technical data-sheet
GFRP	0.86 (longitudinal)	[6]
	2.21 (transverse)	[6]

stress increases with increasing bond-line thickness. These results are in agreement with the findings of Chen et al. [29]. Therefore, it seems that non-straight crack paths are more likely to occur in joints with a 10 mm thick adhesive bond-line than in joints with a bond-line of 4 mm. Fleck et al. [26] reported that the presence of mode II loading component and positive T-stress at the crack tip leads to crack kinking towards the interface.

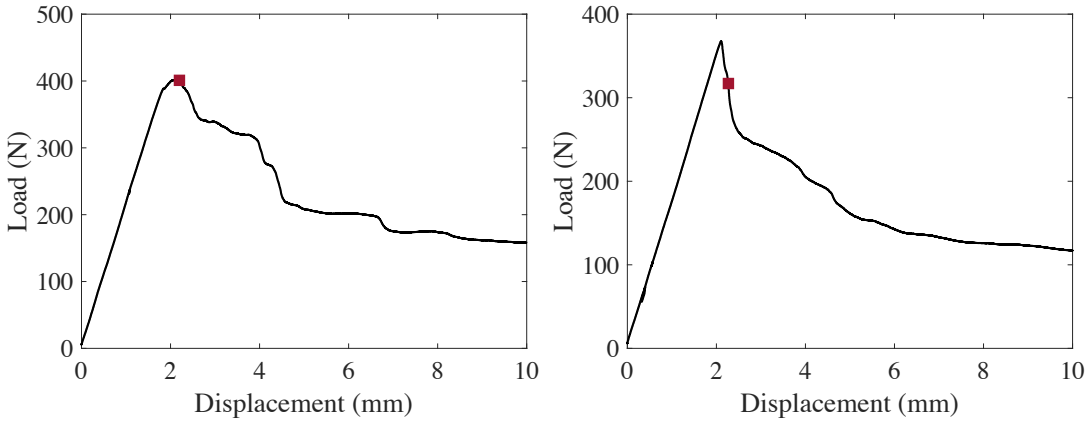

(a) $P-2\Delta$: $2t_a$ = 4 mm, a_{total} = 40.6 mm (b) $P-2\Delta$: $2t_a$ = 10 mm, a_{total} = 43.1 mm. (data taken from Chapter 4).

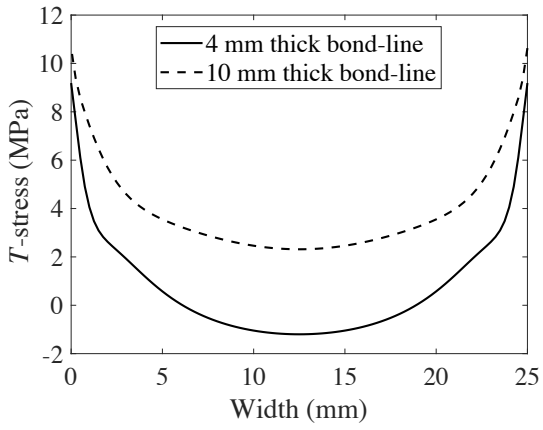

(c) T-stress distribution along the crack tip.

Figure 6.20: Experimental load vs. displacement ($P-2\Delta$) curves and T-stress distribution at crack tip for DCB steel-steel specimens with different bond-line thicknesses.

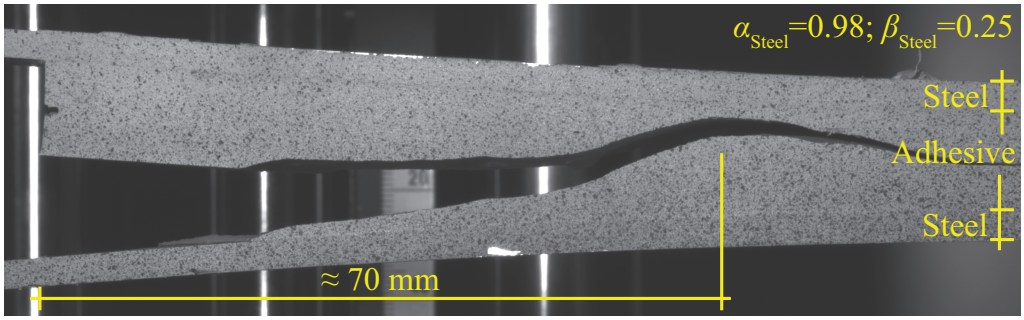

(a) Crack trajectory in steel-steel joint - cohesive close to adhesive-adherend interface fracture onset.

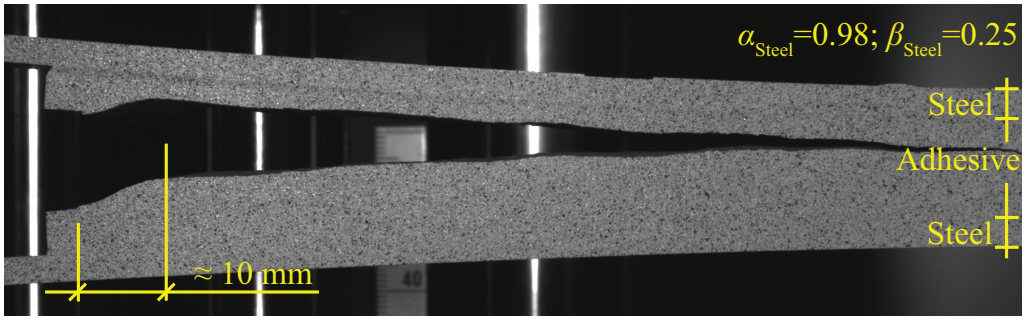

(b) Crack trajectory in steel-steel joint - cohesive adhesive mid-thickness fracture onset.

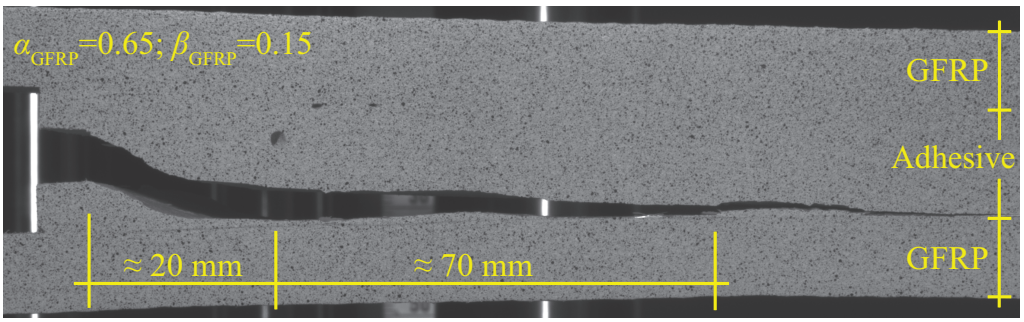

(c) Crack trajectory in GFRP-GFRP joint - cohesive adhesive mid-thickness fracture onset.

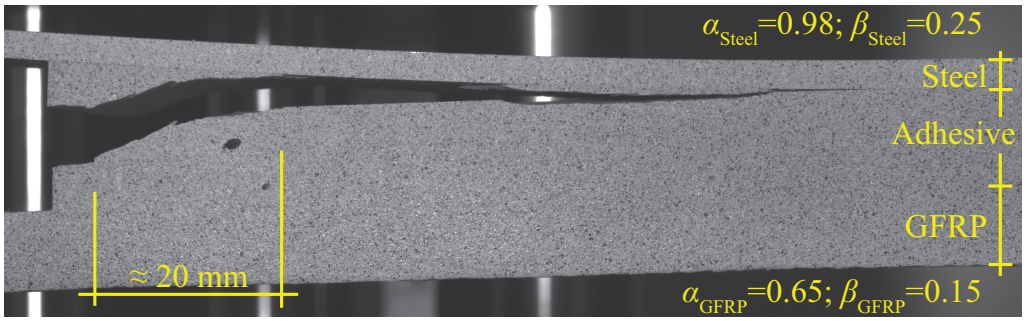

(d) Crack trajectory in steel-GFRP joint - cohesive adhesive mid-thickness fracture onset.

Figure 6.21: Representative crack trajectories of different adhesive joint configurations with 10 mm thick bond-line.

Characteristic length of unstable propagation

Representative crack trajectories of each joint type investigated in this study are presented in Fig. 6.21. These trajectories can be analysed in terms of initial Δa length:

- In case of $\Delta a < \Delta a_{\text{crit.}}$, the fracture onset locus occurred close to one of the adhesive-adherend interfaces (Fig. 6.21(a)). In the steel-GFRP joints, that interface was the adhesive-steel one. Afterwards, two different crack propagation behaviours were observed: i) asymmetric propagation along a remote plane from the mid-adhesive thickness – GFRP-GFRP and steel-GFRP joints, ii) alternating propagation within the bond-line, although closer to one interface than the other in some segments of the bonded area – steel-steel joints.

- In case of $\Delta a \geqslant \Delta a_{\text{crit.}}$, the fracture onset was cohesive at adhesive mid-thickness (Figs. 6.21(b), 6.21(c) and 6.21(d)). Afterwards, the direction of cracking was towards one of the adherends. In the steel-GFRP joints, the crack always steered away towards the steel adherend. The crack propagation occurred then along a remote plane from the adhesive centre-line up to the final failure.

According to Chen et al. [27, 30], the energy available for the crack to grow decreases as the crack approaches an adhesive-adherend interface due to the rigid boundary of the adherend. As the adherends are tougher than the adhesive, the crack does not normally propagate into them. Instead, the crack follows the direction with the lowest critical fracture energy, being in the present study a straight path remote from the adhesive mid-thickness. Fleck et al. [26] found out that under remote mode I load, for some material combinations, there is an additional straight path, satisfying $K_{\text{II}} = 0$, off the adhesive centre-line, near one of the interfaces.
Chen et al. [27] numerically predicted the crack trajectories of directionally unstable cracks in DCB specimens for different values of adhesive thickness and different material systems characterized by Dundurs parameter α, Eq. 6.25. According to the authors, the crack trajectories for different material combinations are similar in shape, although the characteristic length, i.e. the horizontal distance in which the crack alternates its location from a region near to one adhesive-adherend interface to a region near to the opposite interface, decreases as the Dundurs parameter α increases. Both the critical local mixed-mode loading and the T-stress at the crack tip are found to occur at smaller crack lengths for higher material mismatch and, consequently, the characteristic length is predicted to be smaller.
In the present study, only the steel-steel joints with $\Delta a < \Delta a_{\text{crit.}}$ presented alternating crack propagation within the adhesive bond-line (Fig. 6.21(a)). By comparing these crack trajectories with the predictions of Chen et al. [27], one can conclude that there is a qualitative agreement between both, but not a quantitative one. The numerically predicted characteristic length (around 20-30 mm) is smaller than the experimental one (approximately 70 mm). These results may be explained by the fact that a load was applied horizontally to maintain a positive T-stress level in the

numerical models, which might have resulted in higher values of T-stress and, thus, in more directionally unstable crack propagation (i.e. more wavy pattern) [26]. For the GFRP-GFRP and steel-GFRP, it seems that the critical loading conditions and stresses at crack tip did not reach the critical values, and the cracking direction along the remote plane off the adhesive centre-line was kept.

6.6. Conclusions

This study aimed in investigating the fracture onset and crack deflection in adhesive joints with “extra-thick” bond-lines (10 mm) under mode I loading conditions. Single-material (i.e. steel-steel and GFRP-GFRP) and bi-material (i.e. steel-GFRP) double-cantilever beam joints bonded with a structural epoxy adhesive were tested. The joints were modelled analytically. To link the experimental findings to existing theoretical models, the behaviour of the different joints was also assessed numerically.

The Yamada's analytical model (based on the Euler-Bernoulli beam theory and on a beam supported by an elastic-plastic foundation for the free and the bonded regions of the adhesive joint, respectively) gives fairly good agreements with the experimental results, specially taking into account that no parameter fitting or adjustment was performed and the entire models rely on properties measured through either tensile or flexural testing of constituents.

Both the initially linear part of the experimental load-displacement curves and the critical force at fracture onset were normalized by following the simple beam theory. These steps allow the comparison of the results here presented with the results of any other adhesive joints, regardless the materials and joint geometry.

The normalization of the critical force at fracture onset was made by considering joints with varying adhesive bond-line thickness (from 0.4 to 10 mm) and by distinguishing between cohesive adhesive mid-thickness and cohesive close to interface fracture onset (both failure types only happened for 10 mm thick bond-line). Similar values of the normalized critical force at fracture onset were found, regardless of the bond-line thickness. The difference between cohesive adhesive mid-thickness and cohesive close to interface fracture onset was less than 10% for the joints with a bond-line of 10 mm. This indicates that the adhesive was able to deform as a response to the external loading, even though in some cases the critical stress was first attained in a region close to one of the adherend-adhesive interfaces.

For “extra-thick” adhesive bond-lines, such as 10 mm thick ones, geometric discontinuities, such as corners, and material discontinuities, such as adherend-adhesive interfaces, create local singularities where the threshold stress for fracture onset is attained first. To overcome this situation, a critical pre-crack length must be defined, $\Delta a_{\text{crit.}}$. The definition of $\Delta a_{\text{crit.}}$ follows the idealization of unloaded region near crack surfaces in an infinite homogeneous plate with a crack as postulated by A.A. Griffith.

For the case $r_{\text{p}} < t_{\text{a}}$ and $\Delta a > 0$, an empirical relation, in terms of geometrical and material properties of the joints, that defines the transition between cohesive close to the interface and cohesive adhesive mid-thickness fracture onset was found - for a given material mismatch, the scaling relation is $(\Delta a_{\text{crit.}}/h_{\text{adher}})^4 \sim (t_{\text{a}}/h_{\text{adher}})$. For

$\Delta a < \Delta a_{\text{crit.}}$: the stress singularity near the bi-material corner rules over the stress singularity at the pre-crack tip. The bi-material corner with the highest modulus mismatch, characterized by the highest Dundurs parameters, dictates the region of fracture initiation; for $\Delta a \geqslant \Delta a_{\text{crit.}}$: the stress singularity at the pre-crack tip is dominant, resulting in cohesive adhesive mid-thickness fracture onset.
In all joints with cohesive adhesive mid-thickness fracture onset, the cracking direction rapidly deflected out from the adhesive layer centre-line. Positive T-stress along the crack tip was numerically found considering 10 mm thick bond-line, being one of the factors for the unstable crack path. The crack propagation occurred then along a remote plane from the adhesive centre-line up to the final failure.

6.7. Appendix I

Ten unknown coefficients and the plastic zone size are obtained by satisfying boundary conditions at $x = l_{\text{e}}$,

$$\frac{d^3 w_3}{dx^3} = 0, \tag{6.32}$$

$$\frac{d^2 w_3}{dx^2} = 0, \tag{6.33}$$

and continuity conditions at $x = -l_{\text{p}}$,

$$w_1 = w_2, \tag{6.34}$$

$$\frac{dw_1}{dx} = \frac{dw_2}{dx}, \tag{6.35}$$

$$\frac{d^2 w_1}{dx^2} = \frac{d^2 w_2}{dx^2}, \tag{6.36}$$

$$\frac{d^3 w_1}{dx^3} = \frac{d^3 w_2}{dx^3}, \tag{6.37}$$

and at $x = 0$,

$$w_2 = w_3, \tag{6.38}$$

$$\frac{dw_2}{dx} = \frac{dw_3}{dx}, \tag{6.39}$$

$$\frac{d^2 w_2}{dx^2} = \frac{d^2 w_3}{dx^2}, \tag{6.40}$$

$$\frac{d^3 w_2}{dx^3} = \frac{d^3 w_3}{dx^3}, \tag{6.41}$$

$$\frac{d^4 w_2}{dx^4} = \frac{d^4 w_3}{dx^4}. \tag{6.42}$$

The mathematical details of the solution procedure appear in [4]. The results for the case where the bonded region is sufficiently long are,

$$\gamma_1 = \frac{P\lambda}{\sigma_y B}, \tag{6.43}$$

$$\gamma_2 = \frac{(l_f - l_p)P\lambda^2}{\sigma_y B}, \tag{6.44}$$

$$\gamma_3 = \frac{\sigma_y B}{E_x^f I \lambda^3}, \tag{6.45}$$

$$\lambda l_p = \gamma_1 - 1 + \sqrt{\gamma_1^2 + 2\gamma_2}, \tag{6.46}$$

$$C_1 = \gamma_3 \lambda^2 (\gamma_1 - \lambda l_p), \tag{6.47}$$

$$C_2 = \gamma_3 \lambda \left(\gamma_2 - \frac{1}{2}\lambda^2 l_p^2 + \gamma_1 \lambda l_p \right), \tag{6.48}$$

$$C_3 = (K_2 + K_4)\lambda, \tag{6.49}$$

$$C_4 = K_1, \tag{6.50}$$

$$K_1 = \frac{\sigma_y B}{4E_x^f I \lambda^4}, \tag{6.51}$$

$$K_2 = -K_1, \tag{6.52}$$

$$K_3 = \frac{C_2}{2\lambda^2}, \tag{6.53}$$

$$K_4 = -K_3, \tag{6.54}$$

$$R_1 = \frac{\gamma_3}{6}(\lambda l_p)^3 + C_3, \tag{6.55}$$

$$R_2 = \frac{\gamma_3}{24\lambda}[(\lambda l_p)^4 + 6]. \tag{6.56}$$

When l_p is not positive, the plastic zone does not exist. Though Eq. 6.51 is no longer valid, the set of equations Eqs. 6.43, 6.44, 6.45, 6.47, 6.48, 6.52, 6.53 and 6.54 can still be solved by setting $l_p = 0$ and eliminating Eq. 6.42,

$$C_1 = \frac{P}{E_x^{\mathrm{f}} I}, \tag{6.57}$$

$$C_2 = \frac{(l_{\mathrm{f}} - l_{\mathrm{p}})P}{E_x^{\mathrm{f}} I}, \tag{6.58}$$

$$K_1 = \frac{P}{2E_x^{\mathrm{f}} I\lambda^3} + \frac{(l_{\mathrm{f}} - l_{\mathrm{p}})P}{2E_x^{\mathrm{f}} I\lambda^2}, \tag{6.59}$$

$$K_2 = -K_1, \tag{6.60}$$

$$K_4 = -K_3, \tag{6.61}$$

$$R_1 = -(K_1 - K_4)\lambda, \tag{6.62}$$

$$R_2 = K_1. \tag{6.63}$$

6.8. Data availability

The data required to reproduce these findings are available at:
https://doi.org/10.4121/13148441

References

[1] R. Lopes Fernandes, M. K. Budzik, R. Benedictus, and S. Teixeira de Freitas, *Multi-material adhesive joints with thick bond-lines: crack onset and crack deflection,* Composite Structures **266** (2021), 10.1016/j.compstruct.2021.113687.

[2] Z. P. Bazant and L. Cedolin, *Stability of structures: elastic, inelastic, fracture and damage theories* (World Scientific, 2010).

[3] N. Perez, *Fracture mechanics* (Springer, 2017).

[4] S. E. Yamada, *Elastic/plastic fracture analysis for bonded joints,* Engineering Fracture Mechanics **27**, 315 (1987).

[5] *ISO 527: Plastics - Determination of tensile properties,* (2012).

[6] A. K. Kaw, *Mechanics of composite materials*, 2nd ed. (CRC Press, 2006).

[7] M. F. Kanninen, *An augmented double cantilever beam model for studying crack propagation and arrest,* International Journal of Fracture **9**, 83 (1973).

[8] C. L. Chow, C. W. Woo, and J. L. Sykes, *On the determination and application of cod to epoxy-bonded aluminium joints,* Journal of Strain Analysis **14**, 37 (1979).

[9] J. Jumel, M. K. Budzik, and M. E. R. Shanahan, *Beam on elastic foundation with anticlastic curvature: application to analysis of mode I fracture tests,* Engineering Fracture Mechanics **78**, 3253 (2011).

[10] F. E. Penado, *A closed form solution for the energy release rate of the souble cantilever beam specimen with an adhesive layer,* Journal of Composite Materials **27**, 383 (1993).

[11] J. J. Benbow and F. C. Roesler, *Experiments on controlled fractures,* Proceedings of the Physical Society B **70**, 201 (1957).

[12] *ASTM D 5528 - Standard test method for mode I interlaminar fracture toughness of unidirectional fiber-reinforced polymer matrix composites,* (2013).

[13] R. Lopes Fernandes, S. Teixeira de Freitas, M. K. Budzik, J. A. Poulis, and R. Benedictus, *From thin to extra-thick adhesive layer thicknesses : fracture of bonded joints under mode I loading conditions,* Engineering Fracture Mechanics **218** (2019), 10.1016/j.engfracmech.2019.106607.

[14] B. D. Davidson and R. A. Schapery, *Effect of finite width on deflection and energy release rate of an orthotropic double cantilever specimen,* Journal of Composite Materials **22**, 640 (1988).

[15] A. Møberg, M. K. Budzik, and H. M. Jensen, *Crack front morphology near the free edges in double and single cantilever beam fracture experiments,* Engineering Fracture Mechanics **175**, 219 (2017).

[16] M. K. Budzik and S. Heide-Jørgensen, *Branching and softening of loading path during onset of crack at elastic-brittle interface,* Mechanics of Materials **127**, 1 (2018).

[17] D. B. Bogy, *Edge-bonded dissimilar orthogonal elastic wedges under normal and shear loading,* Journal of Applied Mechanics **35**, 460 (1968).

[18] M. K. Budzik, J. Jumel, and M. E. R. Shanahan, *4-Point beam tensile test on a soft adhesive,* Materials and design **46**, 134 (2013).

[19] J. Dundurs, *Discussion: "Edge-bonded dissimilar orthogonal elastic wedges under normal and shear loading" (Bogy, D. B., 1968, ASME J. Appl. Mech., 35, pp. 460–466),* Journal of Applied Mechanics **36**, 650 (1969).

[20] D. B. Bogy, *On the problem of edge-bonded elastic quarter-planes loaded at the boundary,* International Journal of Solids and Structures **6**, 1287 (1970).

[21] Z. Suo and J. W. Hutchinson, *Sandwich test specimens for measuring interface crack toughness,* Materials Science and Engineering: A **107**, 135 (1989).

[22] J. W. Hutchinson, M. E. Mear, and J. R. Rice, *Crack paralleling an interface between dissimilar materials,* Journal of Applied Mechanics **54**, 828 (1987).

[23] E. D. Reedy and T. R. Guess, *Interface corner failure analysis of joint strength: effect of adherend stiffness,* International Journal of Fracture **88**, 305 (1997).

[24] A. R. Akisanya and C. S. Meng, *Initiation of fracture at the interface corner of bi-material joints,* Journal of the Mechanics and Physics of Solids **51**, 27 (2003).

[25] T. Pardoen, T. Ferracin, C. M. Landis, and F. Delannay, *Constraint effects in adhesive joint fracture,* Journal of the Mechanics and Physics of Solids **53**, 1951 (2005).

[26] N. A. Fleck, J. W. Hutchinson, and Z. Suo, *Crack path selection in a brittle adhesive layer,* International Journal of Solids and Structures **27**, 1683 (1991).

[27] B. Chen and D. A. Dillard, *Numerical analysis of directionally unstable crack propagation in adhesively bonded joints,* International Journal of Solids and Structures **38**, 6907 (2001).

[28] B. Cotterell and J. R. F. Rice, *Slightly curved or kinked cracks,* International Journal of Fracture **16**, 155 (1980).

[29] B. Chen and D. A. Dillard, *The effect of the T-stress on crack path selection in adhesively bonded joints,* International Journal of Adhesion and Adhesives **21**, 357 (2001).

[30] B. Chen, D. A. Dillard, J. G. Dillard, and R. L. Clark Jr., *Crack path selection in adhesively-bonded joints: the role of material properties,* The Journal of Adhesion **75**, 405 (2001).

7

Conclusions and future work

7.1. Summary of main findings

The emergence of composite materials in shipbuilding and civil industries has driven research into structural adhesive bonding technology. However, the application of adhesive bonding in these industries presents a critical difference in comparison with the reference industries, i.e. aerospace and automotive. The efficient production of large structures leads to high engineering tolerances, which corresponds in practice to adhesive bond-lines of up to 10 mm. These "extra-thick" adhesive bond-lines take the use of epoxy-based structural adhesives to a new chapter.

The geometrical length scale of the adhesive bond-line thickness imposed by shipbuilding and civil industries opens a series of questions in terms of reliability and performance of bi-material joints with thick adhesive bond-lines. There is still a long path to go through for certification of adhesive bonding as a primary joining method in these industries. The work developed in this document gives a contribution in that direction.

This dissertation deals with adhesive joints with "extra-thick" bond-lines and their fracture behaviour under mode I loading conditions. The main research question is broken down into four smaller research questions, which results in the studies presented in Chapters 3 to 6. The studies involve analytical and/or numerical work supported by laboratory experiments.

The first research question is pursued in Chapter 3 and it is formulated as "How can pure opening mode be characterized in bi-material adhesive joints?". A new design criterion for characterization of mode I fracture behaviour of bi-material DCB adhesive joints is developed, which consists of matching the longitudinal strain distributions of the dissimilar adherends at the bond-line, instead of matching their flexural stiffness. The results and conclusions provided by this research question are as follows:

- It is identified that matching the longitudinal strain distributions of the dissim-

ilar adherends at the bond-line, instead of matching their flexural stiffness, eliminates mode II fracture component at the crack front;

- Both experimental and numerical longitudinal strain distributions are quite similar on both adherends by following the longitudinal strain based criterion, whilst a great discrepancy in the longitudinal strain distributions of the two adherends is found when using the flexural stiffness based criterion. The discrepancy in the strain distributions in the region in front of the crack tip gives the indication that the adhesive was loaded under shear mode when applying the flexural stiffness based criterion;
- The fractography analysis shows that the fracture surfaces of the longitudinal strain based specimen comprise mode I fracture features, while the fracture surfaces of the flexural stiffness based specimen comprise mixed-mode features as indicated by the occurrence of titled crack growth into the adhesive;
- The mixed-mode ratio at the crack front is reduced by a factor of 5 when using the proposed longitudinal strain based criterion in comparison with the flexural stiffness based criterion;
- The new design criterion proposed has high potential to be included in a test standard for characterization of mode I fracture behaviour of bi-material DCB adhesive joints.

The second research question is pursued in Chapter 4 and it is formulated as "What is the effect of the bond-line thickness on the fracture behaviour of adhesive joints under opening loading conditions?". The effect of the adhesive bond-line thickness on the mode I fracture behaviour of epoxy-based steel-steel adhesive joints is investigated. A wide range of bond-line thicknesses is studied, from 0.4 to 10 mm. The following results and conclusions are drawn from this research question:

- The critical fracture energy of the adhesive joints with different bond-line thickness is affected by: a) the constraint from the adherends, which controls the stress state and the deformation field of the adhesive material around the crack tip and the resultant crack path, b) the morphology of the fracture surfaces;
- It is shown analytically that the constraint applied by the adherends on the adhesive material decreases with increasing bond-line thickness. Therefore, in the joints with the thinnest adhesive bond-line thickness (of 0.4 mm), the crack front is more constrained and the local peel stresses are the highest;
- By increasing the bond-line thickness, the constraint effect from the adherends is reduced. Stresses at the crack tip are lower for larger bond-line, which means that the adhesive undergoes more plastic deformation. Therefore, a gradual increase of the critical fracture energy with increasing bond-line thickness is expected. However, the critical fracture energy is influenced by the crack path. In case of wavy crack path, the stress state ahead of the crack

tip varies with crack tip location and, thus, influences the development of the plastic zone size;

- For thicker adhesive bond-lines, the stabilizing factor of crack growth (i.e. the adherends constraint effect) is relieve to some extent and the crack path rapidly deflects out from the mid-adhesive thickness. Overall, wavy crack paths are observed;
- The fracture surfaces with higher frequency of peaks are expected to lead to higher critical fracture energy as the total surface area is larger and, thus, more external work is needed for crack growth;
- In the adhesive bond-line thickness range of 0.4-2.6 mm, the morphology of the fracture surfaces and the stress state ahead of the crack tip (related with wavy crack path) vary with the bond-line thickness in such a manner that the critical fracture energy remains approximately the same;
- For the joints with adhesive layers of thickness of 4.1 and 10.1 mm, though the crack propagates in a wavy way (always within the adhesive layer), the lower stresses at the crack due to increased bond-line thickness result in higher adhesive plastic deformation. However, the adhesive joints critical mode I fracture energy decreases with increasing bond-line thickness from 4.1 to 10.1 mm. It is thought that the for 4.1 mm thick adhesive bond-line, the adherends offer enough constraint to enhance the plastic zone size, while for the 10.1 mm case only one of the adherends constrains the crack tip, reducing the size of the plastic zone.

The third research question is investigated in Chapter 5 and it is formulated as "How is the fracture behaviour of adhesive joints under opening loading conditions affected by the material of the adherends?". The effect of the material of the adherends on the mode I fracture behaviour of adhesive joints is pursued. The following epoxy-based adhesive joint configurations are investigated: steel-steel, GFRP-GFRP, steel-GFRP. Moreover, each configuration is produced with adhesive layer of 0.4 mm (thin bond-line) and 10.1 mm (thick bond-line). The results and conclusions provided by this research question are as follows:

- The critical mode I fracture energy shows to be independent of the adherend type and joint configuration (i.e. single- or bi-material) for each bond-line thickness;
- In the joints with thin bond-line, experimental strain results reveal a similar degree of constraint imposed to the adhesive by the high-modulus (i.e. steel) and/or relatively thick (i.e. composite) adherends. The similar constraint degree contributed to a similar strain field ahead of the crack tip and, thus, to similar critical fracture energy values;
- In the joints with thick bond-line, the crack grows in general along a plane close to the adhesive-adherend interface characterized by the highest material

stiffness mismatch. The critical mode I fracture energy independence shows that the adhesive deforms similarly, even though the crack tip is constrained in one side by different types of adherends (i.e. either by a steel- or GFRP-adherend).

Finally, the fourth and last research question is pursued in Chapter 6 and it is formulated as "What are the parameters controlling the fracture onset locus and crack growth path in single- and bi-material joints with "extra-thick" adhesive bond-lines?". The fracture onset and crack deflection in adhesive joints with 10 mm thick bond-lines under mode I loading are investigated. The following results and conclusions are drawn from this research question:

- For "extra-thick" adhesive bond-lines, such as 10 mm thick ones, geometric discontinuities, such as corners, and material discontinuities, such as adherend-adhesive interfaces, create local singularities where the threshold stress for fracture onset is attained first. To overcome this situation, a critical pre-crack length must be defined, $\Delta a_{\text{crit.}}$. The definition of $\Delta a_{\text{crit.}}$ follows the idealization of unloaded region near crack surfaces in an infinite homogeneous plate with a crack as postulated by Griffith;
- For the case $r_{\text{p}} < t_{\text{a}}$ and $\Delta a > 0$, an empirical relation that defines the transition between cohesive close to the interface and cohesive adhesive mid-thickness fracture onset is found - for a given material mismatch, the scaling relation is $(\Delta a_{\text{crit.}}/h_{\text{adher}})^4 \sim (t_{\text{a}}/h_{\text{adher}})$;
- For $\Delta a < \Delta a_{\text{crit.}}$: the stress singularity near the bi-material corner rules over the stress singularity at the pre-crack tip. The bi-material corner with the highest modulus-mismatch, characterized by the highest Dundurs parameters, dictates the region of fracture initiation;
- For $\Delta a \geqslant \Delta a_{\text{crit.}}$: the stress singularity at the pre-crack tip is dominant, resulting in cohesive adhesive mid-thickness fracture onset;
- The experiments show that, when cohesive adhesive mid-thickness fracture onset occurs, the cracking direction rapidly deflects out from the adhesive layer centre-line. Positive T-stress along the crack tip is one of the factors for unstable crack path.

7.2. Recommendations for further work

This dissertation deals with adhesive joints with "extra-thick" bond-lines, which are relevant for shipbuilding and civil industries, and their fracture behaviour under mode I loading conditions. A natural extension to the work developed in Chapters 4 and 5 would be to investigate the fracture behaviour of the same adhesive joint types under pure mode II or mixed-mode loading conditions, in order to determine the fracture envelope. Moreover, in Chapter 6, the logical step would be to model the "extra-thick" adhesive joints with extended finite element method (XFEM) to fully understand the crack path selection and stability.

In the work developed in this dissertation, non-aged test campaigns are carried out. The next logical step would be to include the effects of environmental harsh conditions, representative of in-service conditions of civil and shipbuilding applications. Factors such as temperature and moisture affect the performance of any adhesive joint. Therefore, this step is essential for assessing the durability of real life bonded structures.

The interfaces in an adhesive joint are a critical point. Due to the high surface energies of the surfaces of the adherends, water molecules can accumulate along the interface. In a bi-material composite-metal adhesively bonded joint, the degradation mechanisms and the water diffusion process that occur at the adhesive-composite interface are different from those that occur at the adhesive-metal interface. The qualitative and quantitative characterization of the water diffusion process is well advanced for adhesive-metal interfaces. However, the scenario is different for adhesive-composite interfaces. Research on the characterization of the water diffusion process in adhesive-composite would be interesting.

For a reliable application of the adhesive bonding technology in shipbuilding and civil industries, more reliable non-destructive inspection techniques are needed to quantify the bonded regions strength throughout their service lifetime in order to prevent catastrophic fracture. Furthermore, better prediction models are needed for the behaviour of adhesive joints under multi-axial loading and harsh environmental conditions. So far, no predictive model has been developed that is sufficiently reliable and generally applicable to allow certification of adhesive bonding as a primary joining method.

Acknowledgements

I would like to express my gratitude to my supervisors Dr. Sofia Teixeira de Freitas, Dr. Michal Budzik and Dr. Johannes Poulis, without whom none of this would have been possible. I owe them a debt of gratitude for their invaluable guidance, encouragement and continuous support through the past years. I would also like to acknowledge my promotor Prof.Dr.ir. Rinze Benedictus.

I would like to acknowledge everyone involved in Durabond project - M2i and TNO colleagues, and all industrial partners. Thank you very much for the fruitful consortium meetings and for giving me the opportunity of sharing my research findings in the cluster meetings and M2i conferences.

I am grateful to Dr. Michal Budzik for receiving me as a visiting scholar in his research group at the University of Aarhus. I would like to thank all the people in the Mechanics of Interfaces and Adhesion Research Group for welcoming me with open arms and making my stay enjoyable.

Thank you Ilias, John-Alan and Niels for welcoming me so well at the office. Thank you Bram, Chantal, Chelsey, Chirag, Cornelis, Fabricio, Hongwei, Leila, Lucas, Maria, Mario, Maro, Megan, Mohamed, Nicolas, Nikos, Pap, Wandong, Xi for your friendly vibe and for the relaxing coffee-breaks. I would like to thank some special fellows - Carlitos, Clarissa, Franscisco, Julian, Nestor, Nikas, Pedro, Timo, Violeta - for all the lovely moments of friendship.

I would like to give a very special thanks to my dearest boyfriend Tiago. He gave me his support from the day that I found out about the PhD vacancy up to the day of the doctoral defence. He was always there to give me constructive feedback and to share his expertise. He was also always there to listen to my boring PhD-related existential crises. His unconditional love brought a special light into my life and made this journey much easier.

Last but not least, I would like to thank my dearest parents Isabel and Faustino, and my dearest sisters Cheila, Sabrina and Daniela for their love and support.

List of Publications

(4) **R. Lopes Fernandes**, M. K. Budzik, R. Benedictus, S. Teixeira de Freitas, *Multi-material adhesive joints with thick bond-lines: crack onset and crack deflection*, Composite Structures **266**, 113687 (2021).

(3) **R. Lopes Fernandes**, S. Teixeira de Freitas, M. K. Budzik, J. A. Poulis, R. Benedictus, *Role of adherend material on the fracture of bi-material composite bonded joints*, Composite Structures **252**, 112643 (2020).

(2) **R. Lopes Fernandes**, S. Teixeira de Freitas, M. K. Budzik, J. A. Poulis, R. Benedictus, *From thin to extra-thick adhesive layer thicknesses: fracture of bonded joints under mode I loading conditions*, Engineering Fracture Mechanics **218**, 1-22 (2019).

(1) **R. Lopes Fernandes**[*], W. Wang[*], S. Teixeira de Freitas, D. Zarouchas, R. Benedictus, *How can pure Mode I fracture be obtained in bonded composite-metal DCB joints: a longitudinal strain-based criterion*, Composites Part B: Engineering **153**, 137-148 (2018).
[*]co-first author